Model Reduction for Flight Dynamics using Computational Fluid Dynamics

Thesis submitted in accordance with the requirements of
the University of Liverpool for the degree of Doctor in Philosophy
by
Giampaolo Pagliuca

August 2018

In every century people have thought they understood the universe at last, and in every century they were proved to be wrong. It follows that the one thing we can say about our modern "knowledge" is that it is wrong.

The Relativity of Wrong,
Isaac Asimov,
1988

Abstract

The coupling of computational fluid dynamics and rigid body dynamics promises enhanced multidisciplinary simulation capability for aircraft design and certification. Industrial application of such coupled simulations is limited however by computational cost. In this context, model reduction can retain the fidelity of the underlying model while decreasing the overall computational effort. Thus, investigation of such coupled model reduction is presented in this thesis. The technique described herein relies on an expansion of the full order non-linear residual function in a truncated Taylor series and subsequent projection onto a small modal basis. Two procedures are outlined to obtain modes for the projection. First, flight dynamics eigenmodes are obtained with an operator-based identification procedure which is capable of calculating the global modes of the coupled Jacobian matrix related to flight dynamics without computing all the modes of the system. Secondly, proper orthogonal decomposition is used as a data-based method to obtain modes representing the coupled system subject to external disturbances such as gusts. Benefits and limitations of the two methods are investigated by analysing results for both initial and external disturbance simulations. Three test cases of increasing complexity are presented. First, an aerofoil, free to translate vertically and rotate, is investigated with aerodynamics based on the Euler equations. Secondly, a two-dimensional wing-tail configuration is studied for longitudinal dynamics. Aerodynamics is modelled with Reynolds-averaged Navier–Stokes equations and Spalart–Allmaras turbulence model. Thirdly, a three-dimensional industrial use case, which concerns a large civil aircraft, is investigated and longitudinal as well as lateral dynamics are both taken into account. Overall, reduced order models relying on both operator-based and data-based identifications are able to retain the accuracy of the high-fidelity tools to predict accurately flight dynamics responses and loads while reducing the computational cost by up to two orders of magnitude. If adopted, these techniques are expected to speed-up aircraft design and lowering certification costs with the final aim of reduced expense for airlines and, as a consequence, for flying passengers.

Acknowledgements

I would like to acknowledge my supervisors Dr Sebastian Timme and Professor Ken Badcock for their assistance and support. I particularly wish to thank Dr Sebastian Timme for his invaluable advice and much appreciated help. Thanks also to the other members of the Computational Fluid Dynamics Laboratory at the University of Liverpool, both past and present.

My family shall not be forgotten for their support and patience[1]. A special thanks to Gilda, who has been supporting (and sometimes tolerating) me for many years now. I would also like to thank all of my friends for their supportive attitude which helped me to achieve my goal.

A particular acknowledgement goes to Archer Supercomputing Service which enabled me to perform large-scale simulations. The work was sponsored by Innovate UK as part of the Enhanced Fidelity Transonic (EFT) wing project in collaboration with Airbus Operations Ltd.

---

[1] Un grazie veramente sentito ai miei genitori e fratelli che, nonostante la grande distanza, mi sono sempre vicini e pronti ad aiutarmi.

Declaration

I confirm that the thesis is my own work, that I have not presented anyone else's work as my own and that full and appropriate acknowledgement has been given where reference has been made to the work of others.

Giampaolo Pagliuca
August 2018

List of Publications

Refereed journals:

- Thormann, R., Pagliuca, G. and Timme, S. [2018], 'Influence of gust modelling on free-flight aerofoils', submitted to *Aerospace Science and Technology.*
- Pagliuca, G. and Timme, S. [2017], 'Model reduction for flight dynamics simulations using computational fluid dynamics', *Aerospace Science and Technology*, 69, 15-26. doi: 10.1016/j.ast.2017.06.013

Conference papers:

- Pagliuca, G., Bekemeyer, P., Thormann, R. and Timme, S. [IFASD-2017-148, 2017], Model reduction for gust load analysis of free-flying aircraft, in 'International Forum on Aeroelasticity and Structural Dynamics' (IFASD), Como, Italy.
- Thormann, R., Pagliuca, G. and Timme, S. [IFASD-2017-195, 2017], Influence of gust modelling on free-flight aerofoils, in 'International Forum on Aeroelasticity and Structural Dynamics' (IFASD), Como, Italy.
- Pagliuca, G. and Timme, S. [AIAA 2016-3850, 2016], Flight Dynamics Mode Identification and Model Reduction using Computational Fluid Dynamics, in '16th AIAA Aviation Technology', Washington, D.C.
  Winner of the *Best Atmospheric Flight Mechanics Student Paper* award.
  doi: 10.2514/6.2016-3850

Presentations without proceedings:

- Model Reduction for Longitudinal Flight Dynamics Using CFD, at 'DiPaRT Conference - Loads and aeroelastics', Bristol, United Kingdom, November 2016
- Progress on Flight Dynamics Reduced Order Model Development, at 'DiPaRT Conference - Loads and aeroelastics', Bristol, United Kingdom, November 2015

Table of Contents

List of Figures

List of Tables

List of Symbols

b	Longitudinal reference length
C_D, C_L, C_M	Coefficients of drag, lift and moment
c_p	Pressure coefficient
E	Total internal energy
F_x, F_y, F_z	Force components in horizontal, lateral and vertical direction
i	Imaginary unit $i = \sqrt{-1}$
m	Number of modes for model reduction
M_y	Moment in longitudinal plane
n	Number of degrees-of-freedom for coupled system $(n = n_f + n_r)$
n_f	Number of aerodynamic degrees-of-freedom
n_r	Number of flight dynamics degrees-of-freedom
p	Static pressure
q	Rate of change of pitch rotation, $q = \frac{\mathrm{d}\theta}{\mathrm{d}\tau}$
r_α	Non-dimensional rotational parameter
T	Static temperature

Vectors

$\boldsymbol{n}$	Normal vector
$\boldsymbol{R}$	Non-linear residual of system involving aerodynamics and flight dynamics
$\boldsymbol{R}_f$	Non-linear residual of aerodynamic subsystem
$\boldsymbol{R}_r$	Non-linear residual of flight dynamics subsystem

$\boldsymbol{u}_c$	Input vector for control deflection
$\boldsymbol{u}_d$	Input vector for disturbance
$\boldsymbol{V}$	Velocity vector
$\boldsymbol{x}$	Vector of grid point locations
$\boldsymbol{w}$	Vector containing unknowns of coupled system
$\boldsymbol{z}$	Vector containing unknowns of reduced order model, $\boldsymbol{z} \in \mathbb{C}^m$

Matrices

A	Jacobian matrix of coupled system
A_{ff}	Jacobian matrix of aerodynamic subsystem
A_{fr}	Matrix containing partial derivatives of fluid unknowns with respect to flight dynamics unknowns
A_{rf}	Matrix containing partial derivatives of flight dynamics unknowns with respect to fluid unknowns
A_{rr}	Jacobian matrix of flight dynamics subsystem
I	Identity matrix
M	Mass matrix
Q	Matrix of dynamic derivatives for aerodynamics

Greek letters

β	Weighting factor
ϵ	Infinitesimal increment
$\boldsymbol{\eta}$	Vector of modal coordinates
γ	Ratio of specific heats
λ	Complex-valued eigenvalue, $\lambda \in \mathbb{C}$
μ	Non-dimensional mass ratio
$\boldsymbol{\phi}$	Direct eigenvector. It is split into flight dynamics and aerodynamic parts, $\boldsymbol{\phi}_r$ and $\boldsymbol{\phi}_r$, respectively, with $\boldsymbol{\phi} = [\boldsymbol{\phi}_f, \boldsymbol{\phi}_r]^T$.
Φ	Modal basis for right multiplication
$\boldsymbol{\psi}$	Adjoint eigenvector. It is split into flight dynamics and aerodynamic parts, $\boldsymbol{\psi}_r$ and $\boldsymbol{\psi}_r$, respectively, with $\boldsymbol{\psi} = [\boldsymbol{\psi}_f, \boldsymbol{\psi}_r]^T$.

Ψ	Modal basis for left multiplication
ρ	Density
τ	Non-dimensional time
θ	Rigid rotation in pitch degree-of-freedom

Operators

$\bar{{\color{gray}\bullet}}$	Complex conjugate of ${\color{gray}\bullet}$
${\color{gray}\bullet}^T$	Transpose of ${\color{gray}\bullet}$
${\color{gray}\bullet}^H$	Hermitian of ${\color{gray}\bullet}$, ${\color{gray}\bullet}^H = \bar{{\color{gray}\bullet}}^T$
$\langle {\color{gray}\bullet}, \bullet \rangle$	Hermitian inner product of ${\color{gray}\bullet}$ and $\bullet$, $\langle {\color{gray}\bullet}, \bullet \rangle = {\color{gray}\bullet}^H \bullet$
$\lvert\lvert {\color{gray}\bullet} \rvert\rvert$	Euclidean norm of ${\color{gray}\bullet}$
$\Re({\color{gray}\bullet})$	Real part of ${\color{gray}\bullet}$
$\Im({\color{gray}\bullet})$	Imaginary part of ${\color{gray}\bullet}$

Subscripts

${\color{gray}\bullet}_f$	Fluid dynamics part of ${\color{gray}\bullet}$
${\color{gray}\bullet}_r$	Rigid-body part of ${\color{gray}\bullet}$

List of Acronyms

ALE	Arbitrary Lagrangian-Eulerian
AOA	Angle of attack
CFD	Computational fluid dynamics
CSD	Computational structural dynamics
DLM	Doublet lattice method
DLR	German Aerospace Center
EASA	European aviation safety agency
EMD	Eigenmode decomposition
FD	Fight dynamics
FEM	Finite element method
GAF	Generalised aerodynamic force
LFD	Linearised frequency domain
NACA	National Advisory Committee for Aeronautics
NS	Navier–Stokes
POD	Proper orthogonal decomposition
QS	Quasi steady state
RANS	Reynolds-averaged Navier–Stokes
RBF	Radial basis function
ROM	Reduced order model
SA	Spalart–Allmaras
URANS	Unsteady Reynolds-averaged Navier–Stokes

Chapter 1

Introduction

On the 17th of December 1903 the age of powered, heavier-than-air aircraft began [8]. Such epoch was signed by an inexorable development in all aeronautics fields ranging from sophisticated aerodynamic theories to material improvements [6]. However, it was also signed by fatal accidents since safety was not a major concern for pioneers who were developing the ability to fly for the first time. Airworthiness regulations aiming to promote safer flight were gradually proposed as early as 1919 when the idea of type certificate was introduced in the United Kingdom with the Air Navigation Regulations [2, 36]. A century later, meeting certification requirements at any stage of flight mission is an essential prerequisite to declare any civil aircraft capable of flying [57]. A flight envelope is defined by relating loads to flight speed. As an example, a typical flight envelope for a large civil aircraft is shown in Fig. 1.1 where the aerodynamic loads are related to the aircraft weight and given in terms of load factor.

Certification requires that the aircraft is able to fly safely at any point enclosed by the flight envelope even if it is subject to external disturbances. One of the critical conditions to be investigated is represented by gust encounter [57]. It consists of sudden changes in the wind direction and intensity which alter lift, drag and moment. Such changes represent the air turbulence and they belong to the category of weather-related phenomena. Although current numbers of fatal accidents are low [24], gust encounter can still cause serious problems and lead to fatalities [62]. Gusts represent the most dangerous atmospheric hazard for large civil aircraft, as shown in Fig. 1.2, where wind and turbulence are identified as responsible for the majority of accidents. When it comes to certification, safety during a gust encounter is ensured by defining a conventional gust shape called ‘1-cos’ to model the atmospheric turbulence and by asking aircraft manufacturers to test the aircraft behaviour against it [57]. The ‘1-cos’ gust shape was born from the idea of discrete gust introduced by Küssner [89]. Although atmospheric turbulence is a random continuous problem [136], the aircraft response must be investigated for discrete gusts. In fact, continuous turbulence can be decomposed in a sequence of discrete pulse excitations [2, 29]. This approach has

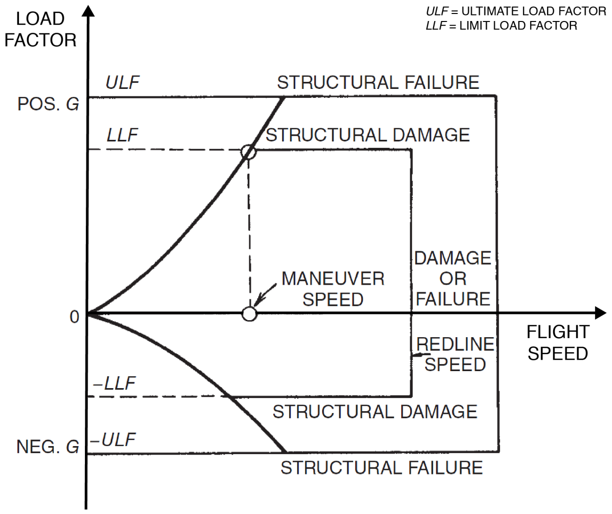

Figure 1.1: Typical flight envelope (adapted from [50, p. 235]).

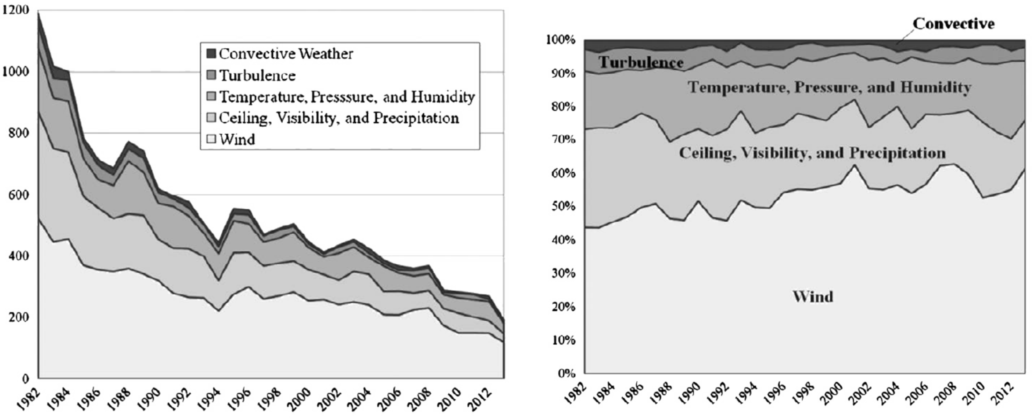

(a) Absolute number of accidents and causes (b) Yearly contribution in percentage of total

Figure 1.2: Flight accidents due to weather-related phenomena (taken from [62]).

proven to be a good trade-off when compared to continuous models [158] and the current regulation is based on the theoretical work presented in [112]. The ‘1-cos’ gust shape is defined as function of time depending on two parameters, specifically gust length and amplitude as shown for a vertical (also known as longitudinal) gust in Fig. 1.3. The intensity is defined according to altitude, gust length and flight speed [57]. Although the ‘1-cos’ shape represents a mathematical idealisation of natural phenomena, a physical interpretation is provided. The gust disturbance consists of small variations in the flow field which can alter either the angle of attack or dynamic pressure [76, Ch. 1]. It moves towards the aircraft at free-stream velocity and interacts with body surfaces producing changes in aerodynamic forces. Lift, drag and moment build-up causes vertical and rotational aircraft motions [76]. As a consequence, the resulting loads are a combination

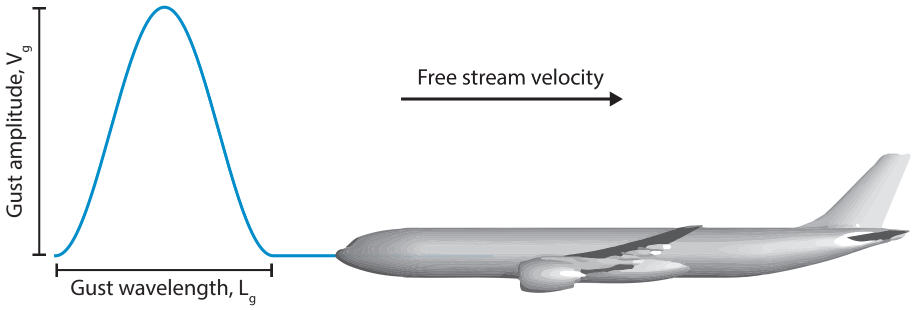

Figure 1.3: Shape and defining parameters for '1-cos' gust.

of various effects such as force increment given by the disturbance itself, aircraft motion as well as the mutual interaction between aircraft and gust.

In practice, certification regulations require evaluations of gust responses for a sufficient number of gust lengths for each mass case and flight point in order to identify the worst-case scenario and investigate the aircraft's limit loads. Nowadays, this is partly achieved by means of computer simulations which help the design process. The trend, set by all major players in the aircraft market, is to achieve certification by analysis in order to reduce time and cost. Regulation authorities work side-by-side with manufacturers and results from computer simulations will produce safer and cheaper products. This has been demonstrated for instance in [49, 90]. However, research is still needed when it comes to high-fidelity gust encounter simulations, particularly if free flight effects are included to describe physics more accurately. Their main limitation is represented by high computational cost. Certification by analysis concerning gust loads and flight dynamics promises to further reduce time and cost of the overall design process, especially if applied during early design stages in a fast and reliable way. In addition, this will be an enabling technology for designing novel configurations in the upcoming years.

In the next sections, the status for gust certification by analysis based on simulations including flight dynamics effects is described and limitations of the current practice are highlighted. Focus is on aircraft design and the main obstacles to increased use of this type of high-fidelity simulations are discussed.

1.1 Application Requirements

Current industrial practice for aircraft design relies on low fidelity simulations for gust loads evaluations. The need for fast results during the design exploration is satisfied with linear potential aerodynamic methods which offer low fidelity at affordable computational cost [116]. Flight dynamics effects are usually not included and the aircraft is considered static, not moving, while the disturbances hit the surfaces [116]. However, the next steps towards more accurate gust loads estimation are multidisciplinary simulations involving aerodynamics and flight dynamics among other disciplines [131]. This leads to

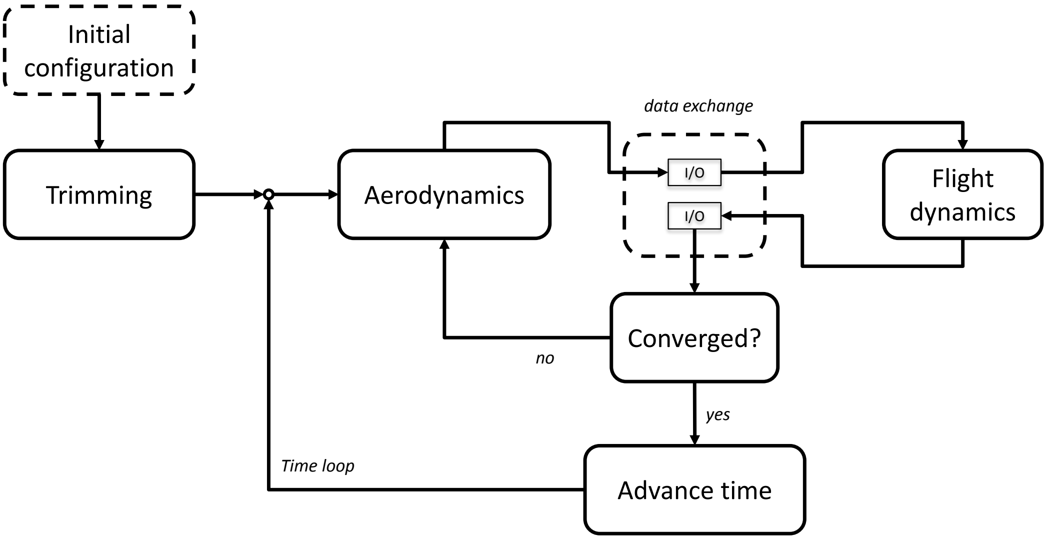

Figure 1.4: Block diagram representing a multidisciplinary approach to couple aerodynamics and flight dynamics in an unsteady loop.

multidisciplinary problems which must be addressed with methods developed on purpose. Two approaches are commonly adopted to couple aerodynamics and flight dynamics.

The first one is based on aerodynamic tables computed with computational fluid dynamics (CFD) [65]. Such approach is usually adopted to assess flight dynamics performance as well as to provide physical insight for flight simulators [67, 126] and its accuracy can be compared to wind tunnel experiments in some circumstances [40]. Aerodynamic tables include data for aerodynamic forces and moments as function of state variables such as angle of attack and Mach number. Tables cannot be computed with CFD in real time because of the computational cost and Kriging interpolation applied to pre-computed data was proposed as a remedy to lower computational requirements [146]. This approach is considered quasi-steady since the flight path during a manoeuvre is pre-defined. This leads to problems when fast motion is involved, as reported in [146], because the mutual interaction of aerodynamics and flight dynamics is computed only at steady state and then frozen.

The second approach relies on the assumption that each discipline involved in the process requires input which depends on others. Specifically, the interaction is mutual since flight dynamics states depend on aerodynamic forces and vice versa. This multidisciplinary approach is well explained in [37] and summarised in Fig. 1.4 with a block diagram. One of the disciplines is advanced in time first and its output is then used as input for the next block which produces a new output as well. These intermediate results are used iteratively and they represent a new input for the previous block in order to obtain results at a fixed time step. The loop is repeated until convergence and the system then moves to the next time step. Phenomena such as gusts are included in the aerodynamic block. The resulting system might be computationally expensive if high-fidelity results are provided by each subsystem. This modular approach has proven to be reliable in the multidisciplinary context [96] and it will be used as guideline in this work as well. An example of coupling blocks representing flight dynamics, flexible structures and unsteady aerodynamics for gust response analysis was achieved, for instance, in [54] using unsteady lifting line theory in the subsonic regime. Similar solutions were proposed for gust analysis of HALE (High Altitude, Long Endurance) configurations [35, 127] since flight dynamics effects are essential to predict accurately those systems' behaviour. Coupling can also be achieved directly in the linear aerodynamics equations with correction terms accounting for body acceleration, as suggested in [110, 119]. Although the work described so far summarises the industrial practice based on fast methods, it exclusively relies on low fidelity aerodynamic models to perform multidisciplinary simulations.

Application in the transonic regime requires high-fidelity aerodynamics based on CFD, which can describe non-linear flow phenomena like shock waves. One of the earliest attempts to model transonic aerodynamics with CFD for a free-flight test case is reported in [59] for a fighter aircraft solving CFD Euler equations. The multidisciplinary model was based on a modular approach composed of two interacting subsystems which concern aerodynamics and flight dynamics. Simulations were performed advancing in time and exchanging information between the two subsystems at each time-step. The need to perform such computations using a computer cluster was the main limitation reported whereas efficient programming solutions were suggested for the data exchange. Similarly, an example of a simulation for a manoeuvring aircraft in transonic flow is presented in [115], running a CFD Euler solver alongside a structural modal solver in a closed loop. The manoeuvre was pre-defined so that time-varying flight dynamics parameters such as angle-of-attack are imposed onto the CFD solver at each time-step. A similar approach based on two distinct and interacting subsystems was also applied in [108] to cope with large static displacements in transonic flow.

These studies provide an effective way to cope with pre-defined manoeuvres or static problems but an extension to unsteady gust encounter in viscous and transonic flow is needed. Although gust disturbances are pure aerodynamic phenomena and they are included in the aerodynamic block, particular care must be taken when introducing them in time-domain coupled simulations. For such cases, flight dynamics unknowns must be calculated at each time-step using the most recent values of aerodynamic forces which, in turn, depend also on the gust disturbance. Moreover, aerodynamics also depends on flight dynamics unknowns, leading to a two-way coupled problem. This mutual interaction was investigated in [140] for free-flying aerofoils using CFD based on Reynolds-averaged Navier–Stokes (RANS) equations and applying two techniques. First, gust is simulated using a resolved approach. The disturbance propagates starting from the boundary upwind and reaches the aerofoil by downstream propagation. This approach resembles the natural phenomenon but it requires a fine and Cartesian mesh in order to avoid an excessive numerical dissipation of disturbances and excessive cost.

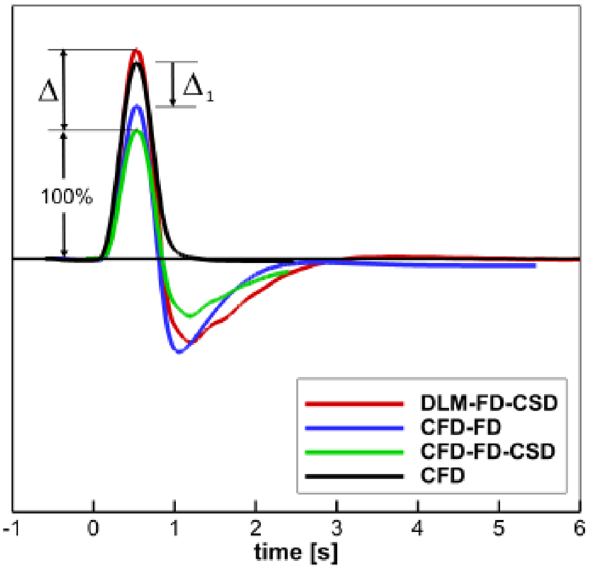

Figure 1.5: Effects of including flight dynamics when performing gust encounter simulations (adapted from [117]).

Such requirements translate into a high computational cost to be paid which makes the adoption of such solution infeasible for large test cases. The second technique for gust modelling is called disturbance velocity method and it introduces the gust in the domain by altering the grid velocity [109]. It is based on the equivalence between an aerodynamic body moving in a steady flow and a steady body surrounded by a moving fluid. When it comes to gusts, the motion of the fluid is defined by the shape of gust disturbance, i.e. '1-cos' . In practice, velocity values at grid points are altered by adding velocity terms which depend on the intensity of the gust at the specific point. Effects such as loads alteration and rigid-body motion produced by the gust are simulated but the disturbance alterations due to the body are ignored. However, good agreement between two methods was obtained despite the reduced computational cost [140]. Similar results are discussed in [73] where the disturbance velocity method and the resolved technique are compared for a lateral gust encounter of a three-dimensional test case. The aircraft was considered static, i.e. not moving, and matching results are provided for loads only since no motion is simulated. The disturbance velocity method was exploited in [117] to perform gust encounter simulation of free-flying aircraft in transonic flow and aerodynamics modelled with RANS equations. An interesting comparison in terms of load factor for a gust encounter is shown in this study, and reproduced in Fig. 1.5. The CFD curve corresponds to a static aircraft whereas the CFD-FD curve shows results for the same simulation including flight dynamics effects. Peak values are lowered and the difference Δ_1 between the resulting load factors is clear. This suggests that flight dynamics should be included for gust simulations in order to avoid overestimation of loads. The additional two curves labelled CFD-FD-CSM and DLM-FD-CSM show results from simulations including flexible structures as well as flight dynamics with aerodynamics modelled using either CFD or doublet lattice method (DLM). The difference Δ between them highlights the limitations of the current industrial practice based on DLM and shows the improved accuracy of the multidisciplinary approach based on CFD. A similar solution based on coupling modules for CFD aerodynamics and flight dynamics and introducing gust with disturbance velocity method is adopted in the current work to provide reference data.

With feasibility for an industry-scale adoption of multidisciplinary analyses based on CFD already demonstrated, the main obstacle remains computational cost. A first reduction has been achieved using linearised frequency domain (LFD) formulations. For such methods, the CFD equations are linearised around a steady state and harmonic excitation as well as harmonic response are assumed. Thus, a complex-valued system of linear equations is obtained and its solution depends on the excitation frequency. In practice, responses to harmonic disturbances are obtained solving the resulting linear system. The left-hand side of such system is composed of the Jacobian matrix arising from the CFD linearisation with a complex shift to account for frequency and damping. The right-hand side is defined by the disturbance instead. LFD methods were first developed for turbomachinery applications involving Euler flows as a short-cut towards unsteady aerodynamics [69]. Other applications in the aerodynamic field benefit from LFD [141] and it has been successfully applied to fluid-structure interaction problems in the field of aeroelasticity as well [9, 142]. In such cases, disturbances are represented by structural deformation expressed by means of mode shapes. The complex-valued interaction terms relating changes in the aerodynamic forces due to structural motions are then efficiently computed with LFD. The technique was scaled to industrial cases by improving the solution procedure based on iterative linear solvers with the adoption of better preconditioning [97] and better algorithms [156]. The improvements led to a reduction in the computational cost by an order of magnitude [97]. An interesting application of LFD is the calculation of dynamic derivatives which are needed for flight dynamics studies [41]. Traditionally, quasi-steady derivatives were obtained applying a forced periodic motion to the aerodynamic body during wind tunnel experiments or, alternatively, dynamic derivatives were calculated with unsteady time-marching CFD simulations. The LFD formulation allows for a quicker evaluation of such derivatives as reported in [150] for an aircraft in a viscous transonic flow.

Recently, LFD has been applied to the evaluation of gust loads. In fact, harmonic disturbances forming the right-hand side of the linear system can represent other phenomena besides structural motion. In [82] airloads were calculated with the same tools for both structural deformations and sinusoidal gusts. The phase difference between different locations in the domain, which characterises the gust disturbance, translates into complex numbers for the right-hand-side. Gust loads evaluation using LFD has been scaled to industrial cases and expanded for the ‘1-cos’ gust using Fourier decomposition

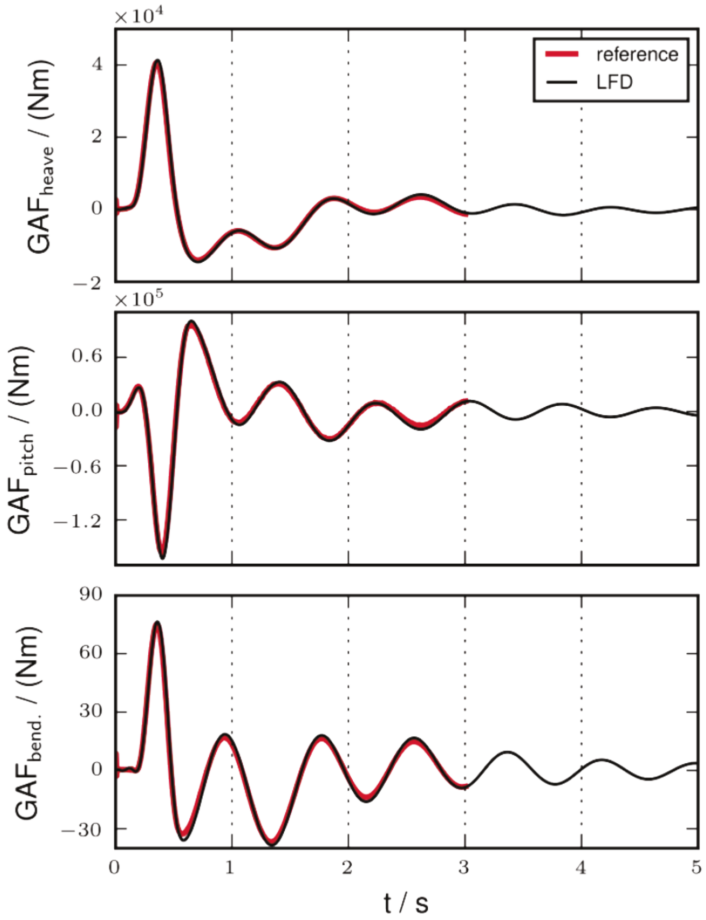

Figure 1.6: Comparison of results produced with linearised frequency domain method and time-domain method for coupled system (taken from [81]).

in [17] where a comparison between this approach and the traditional time-domain formulation is provided in terms of both computational cost and accuracy. It is possible to exploit LFD for coupled problems including CFD, flight dynamics and structures as described in [81] for a large civil aircraft subject to gust encounter. In that paper, three degrees-of-freedom were considered, specifically rigid rotation, vertical translation and a flexible wing bending mode. Dynamic derivatives relating aerodynamic forces to the three degrees-of-freedom were calculated as function of frequency using LFD. Similarly, gust derivatives were obtained by calculating the aerodynamic responses to sinusoidal gusts and projecting the complex-valued LFD solutions onto the degrees-of-freedom of motion. Response to a '1-cos' gust is calculated expanding the gust shape in a Fourier series and superimposing the results. Such methodology produces results matching the time-domain reference solution as reported in Fig. 1.6 by plotting the generalised aerodynamic forces. The methodology represents the extension towards CFD of methods traditionally based on DLM. However, the computational effort required to compute the dynamic derivatives with LFD and then reconstruct the unsteady response exceed the cost of the corresponding time-domain simulation by a factor of 6 [81]. Focus of the study is on the aeroelastic subsystem since results are provided for the flight dynamics, structural degrees-of-freedom and generalised aerodynamic forces. Paradoxically, most of the information concerning the flow field, which is included in the LFD solutions and required a large portion of computational time, is not reconstructed from the reduced model. An alternative method, which further decreases the computational time needed by multidisciplinary simulations based on CFD while retaining the high-fidelity accuracy, is needed for a wider adoption of such tools.

Summarising, it is useful to highlight the link between LFD, dynamic derivatives and gust predictions which was described in this section by referring to literature studies. The LFD method enables the rapid computation of flow responses to sinusoidal excitations with small amplitudes. This is achieved by linearising the CFD equations around a steady-state and solving them in the frequency-domain. A saving in terms of computational cost is, thus, obtained. In practice, the resulting aerodynamic forces are complex-valued numbers which represent the sinusoidal response to the excitation. Dynamic derivatives are found by relating the output (aerodynamic forces) to the input (the sinusoidal excitation). Precisely, they are equal to the ratios between aerodynamic force and the excitation, both expressed as complex numbers. Traditionally, this approach was employed for sinusoidal structural motions (i.e. pitch rotation, plunge translation, bending deformation and so on) in the field of aeroelasticy. When it comes to gusts, the external disturbance is a sinusoidal alteration of the velocity field in the fluid domain.

Overall, high-fidelity aerodynamics is needed to produce more efficient and innovative aircraft designs but computational cost limits its adoption. Fast methods, which are able to retain high-fidelity accuracy while lowering the time for simulations, are highly desirable. In addition, multidisciplinary studies for gust loads evaluation involving flight dynamics represent a further improvement for simulation fidelity. The application of fast methods in this multidisciplinary context would combine the benefits of multiple disciplines and high-fidelity aerodynamics. This aspect is investigated in this work.

1.2 Reduced Order Modelling

In this context, reduced order models (ROMs) of high-fidelity methods represent a promising approach for simulations coupling flight dynamics and aerodynamics. The aim is to reduce the system's complexity while retaining a very similar accuracy of the original model [14]. The idea of model reduction has been applied in many fields ranging from microelectromechanical systems [14] to aerospace applications [135] in order to reduce computational cost or achieve a better understanding of the system's behaviour. Often, reduction techniques are not applied directly to the non-linear full order model since a linearisation is performed prior the reduction. In such cases, linear ROMs are used [14]. In general, formulations for non-linear reduced models exist and they rely on modelling the

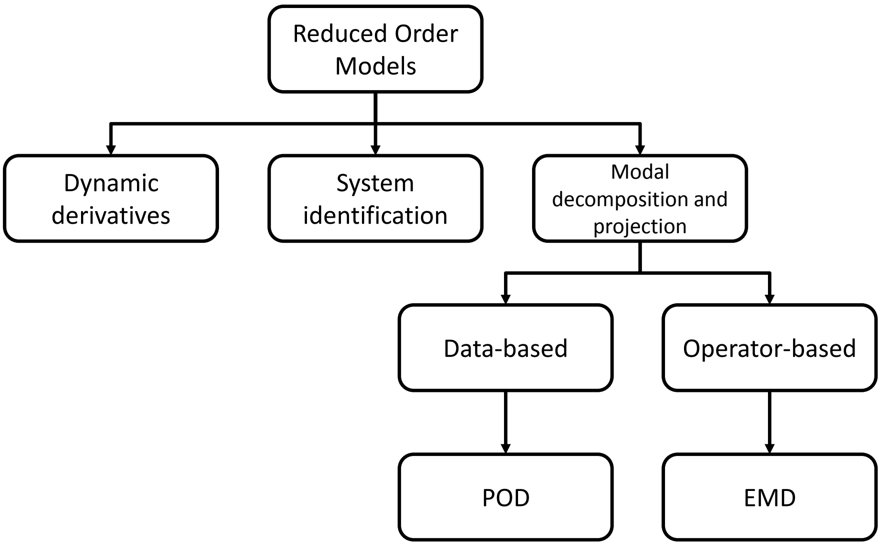

Figure 1.7: A classification of model reduction techniques.

non-linearities with a polynomial of low degree [14]. However, they are outside the scope of this work which focuses on linear reduced models instead. A schematic representation of the most popular model reduction techniques is given in Fig. 1.7 with a tree-structure. For sake of simplicity, the classification is not exhaustive and limited to methods which relate to the current work and that are, therefore, described in this section.

A typical approach for multidisciplinary reduced models is borrowed from the aeroelastic practice [72]. Owing to the fact that flight dynamics equations are of low dimension, aerodynamics is typically represented with dynamic derivatives [134]. Flight dynamics response is then obtained by integrating the equations of motion in time and interpolating the pre-computed dynamic derivatives at each time-step. The flow field information is somehow hidden by such method which focuses mainly on the flight dynamics response. This is the usual approach but additional techniques are available in literature [53] and they are usually based on low-fidelity aerodynamics [22]. However, such reduction techniques, which were first developed using low-fidelity aerodynamics, are applicable in general to larger higher-fidelity systems as well. A comprehensive review is provided in [53] for general fluid-structure interaction problems and in [66] for the specific problem of including flight dynamics. Reduced models can be grouped in families according to their mathematical formulation.

System identification methods use a time-domain formulation [53], with Volterra series representing one of the most popular implementations. For example, an application is available in [129]. The system is assumed to be a black-box and a limited set of inputs and outputs is defined a priori. The relationships between input parameters and output variables are determined by sampling the system response to training excitations [128]. However, a recalculation of the model is needed if an additional output variable is requested. Furthermore, this approach hides the complexity of the underlying aerodynamic model, and flow details, which are necessarily computed, are discarded as noted in [53].

Another family of methods is based on the projection of the linearised system onto a small modal basis. They are called model decomposition and projection methods [95]. The crucial point for them is the calculation of the modal basis since it should contain all the information needed to rebuild full order results. Among the methods belonging to this family, two are particularly promising. The first one is in the category of the data-based methods and it is called proper orthogonal decomposition (POD) [95, 135], also known as the snapshots method [70] or Karhunen-Loeve expansion [130]. It is based on a sampling procedure performed either in time or frequency domain with applications in almost every field of aeronautical engineering ranging from steady CFD computations [3] to unsteady flows [93]. The system is sampled at discrete points in time or frequency and the solutions are stored as columns of a snapshot matrix. A saving in memory can be achieved by storing the solution for areas of interest only, for example just for the domain points closest to the body surfaces as described in [3]. Using the snapshot matrix, a number of POD modes equal to the number of snapshots is calculated by means of a small eigenvalue problem. The model reduction is performed projecting the original system onto modal bases populated with such modes. In addition, POD modes can be sorted by their energy content [130]. This allows a further reduction if only few POD modes are retained for the projection [70]. POD method offers insight for a better understanding of the system as well. For example, in [130] such method was used to identify coherent structures in the fluid flow from both experiments and simulations [135] and, in general, it provides a way for pattern recognition [61]. Multidisciplinary reduced order models using POD in frequency domain can be found in [70] where it is used in conjunction with an LFD linearisation of the underlying CFD aerodynamics. The data-based ROM is used in such work to reproduce the aerodynamic responses to an aerofoil's sinusoidal motions. The structural block of the multidisciplinary workflow is not reduced while high-fidelity CFD is used only to compute the POD modes and it is replaced in the coupling loop by the reduced model. Another example of multidisciplinary model is proposed in [44] as a way to reduce computational cost. The aerodynamic model is replaced with a reduced model based on POD and uses a linearised form for the equation of motion for the rigid motions.

In the context of gust encounter, POD has been applied in [12] to evaluate the variations of surface pressure during the gust. The snapshots were obtained from time-domain simulations for sharp-edge gusts. Solutions for arbitrary gust shapes were calculated applying the convolution integral and exploiting POD to reconstruct the spatial distribution of pressure. Recently, research focused on POD reduced models to perform gust encounter simulations and evaluate airloads directly. The method was applied in [19] in conjunction with LFD for transonic CFD aerodynamics based on RANS equations. The variations of aerodynamic loads produced by '1-cos' gusts were reproduced accurately by the reduced model for linear gust amplitudes. Such application was scaled in [18] to a large civil aircraft and expanded to include flexible structures. The work described so far used POD to reduce the aerodynamic model only. An application for coupling flight dynamics and CFD in a single monolithic reduced model is still needed. Ideally, POD modes would be computed for the whole original system which includes aerodynamics as well flight dynamics. However, the main limitation of POD is highlighted in [153] where it is pointed out that POD-based reduced models can be unstable even though the underlying full model is stable.

Remaining in the family of projection methods, another category gathers formulations which are based on the eigenmode decomposition (EMD) of the underlying system [53] and they are called hereafter operator-based methods [135]. A description of the methodology to obtain the reduced model is given in [53] and summarised in this paragraph. The eigenvalue problem for the linearised system is solved and eigenpairs obtained. Note that this task is computationally expensive even for small cases when high-fidelity aerodynamics is adopted. The reduced model is built by projecting the small system onto modal bases which are assembled with a small number of eigenvectors. This projection method produces a versatile ROM which facilitates a comprehensive study of the coupled system. Previous applications include the simulation of coupled structural and aerodynamic systems using linear potential aerodynamics for gust encounter analysis and robust control [39, 42]. The operator-based reduction methods can be applied easily to multidisciplinary models for which eigenvectors from the coupled system should be used for more accurate results [154]. However, as noted in [53], eigensolutions are tied to the specific flight condition for which they are calculated and they must be recomputed when flight parameters change. An analytical formulation for the operator-based model reduction is provided in [45]. It is highlighted that one of the benefits of the method is that the Jacobian matrix of the reduced model has the same dominant eigenvalues and eigenvectors of the original system [45]. However, the method relies on computing the full set of eigenpairs for the system in order to identify the dominant ones. This represents a fundamental limitation when it comes to applications to large systems while it is trivial problem for small matrices [53].

A possible solution is provided by the reduced models based on the Schur decomposition [124, 143] also known in literature as the Schur complement method. They focus on a small set of unknowns and modes for the projection are obtained with the Schur decomposition of the partitioned Jacobian matrix. The decomposition can be applied to both direct and adjoint formulations. The resulting modes form bi-orthogonal bases if modes belonging to direct and adjoint eigenspaces of the original system are used [124]. In addition, the transformation from the full to the reduced model is stable when bi-orthogonal bases are used for the projection [124].

In the field of aeroelasticity, the Schur complement method led to successful applications regarding flutter analysis using CFD aerodynamics [143]. An iterative procedure

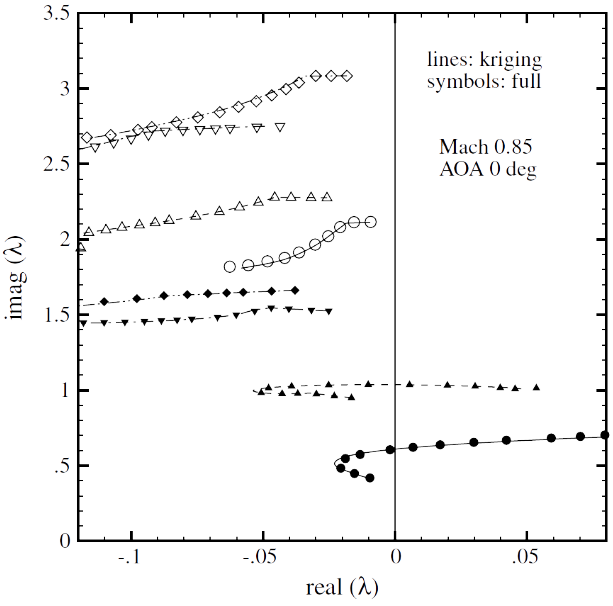

Figure 1.8: Tracing procedure for eigenvalues originating in structure performed with Schur complement method (taken from [143]).

was proposed for which the eigenpairs related to the structural degrees-of-freedom were traced during their evolution in the complex plane. The tracing starts from in-vacuum eigensolutions, which correspond to solutions of the eigenvalue problem for the structural model only, and continues until they become eigenpairs of the aeroelastic system. Their difference from structural modes is clear when the eigenvalues are compared. The structural ones have non-zero frequency and zero damping (apart from the structural one) whereas the aeroelastic ones have both frequency and damping arising from the coupling with fluid. In [143] the tracing is performed changing flight altitude and starting from a large value of it. At the beginning, this corresponds to an almost decoupled system because the density value is very low. The altitude is decreased in steps and new eigensolutions are calculated. Flutter condition is identified when one or more eigenvalues, which are computed iteratively, show a positive real part. The tracing procedure can then continue beyond the flutter point.

Figure 1.8 is taken from [143] to illustrate the tracing for a Goland wing at Mach number of 0.85 and zero degree angle-of-attack. Horizontal and vertical axes correspond to real and imaginary parts of eigenvalues, respectively. Each line set illustrates the tracing for a single structural mode, for a total of 8 modes. The tracing is performed with the Schur method (symbols in the figure) and an approximate formulation based on Kriging interpolation (dashed and continuous lines). It is interesting to note that the part of eigenpairs belonging to the coupled system and related to the structural degrees-of-freedom are available at every stage of the procedure. From a different point of view, this suggests that a small number of eigenpairs of the coupled system can be calculated with the Schur tracing without the need to compute the whole spectrum, which is an almost impossible task for large systems. This information was exploited in [142] where the Schur complement method was used to produce direct and adjoint eigenvectors suitable for operator-based model reduction. This allowed the identification of just few eigenpairs of the large eigenvalue problem arising from aeroelastic applications based on CFD. The problem of identifying eigenvectors for the projection was thus overcome and the resulting reduced model was exploited for gust encounter simulations. Recently, the method was expanded for structural non-linearities [64] as well using linear aerodynamics. Regarding gust encounter simulations, the operator-based approach has shown promising results for flexible structures [18, 20]. Application of this method to trace flight dynamics modes with the final purpose of gust encounter simulations is particularly challenging. In fact, when the eigenspectrum is considered, eigenvalues related to aerodynamics are situated in a dense cloud. Eigenvalues corresponding to flight dynamics modes can be located inside that cloud where they are closely surrounded by fluid eigenvalues. This makes the identification of flight dynamics modes difficult and this problem will be investigated in this work.

1.3 Aim of Work and Outline of Thesis

The aim of this work is to investigate model reduction techniques applied to multidisciplinary simulations involving CFD and flight dynamics, particularly in the context of aircraft gust encounter in the transonic regime. This is proposed as solution to reduce computational cost while retaining the accuracy of the underlying model, thus enabling the use of high-fidelity aerodynamics early during the aircraft design. The ultimate goal is to contribute to the long-term vision of certification-by-simulation for greener, more efficient aircraft.

Focus is on three research areas for which no study is available in literature. First, a novel operator-based identification for flight dynamics modes is developed. Secondly, the data-based method is applied to the coupled system treated as a monolithic entity in frequency domain. Thirdly, the theoretical framework for the model reduction is presented in a generic way so that it is applicable to modes coming from both data-based and operator-based identification.

Theory for both full and reduced models are given in the next two chapters. Specifically, an overview of the full order model is given in Chapter 2. It is composed of two modules, specifically aerodynamics, which is based on RANS or Euler equations, and flight dynamics. It is used to produce reference results and it is the target of the model reduction which is described in Chapter 3. It is based on an expansion of the full order non-linear residual function in a truncated Taylor series and subsequent projection of the Jacobian matrix onto a small modal basis. Two methods are proposed to provide modes for the projection. The first one belongs to the family of operator-based methods and it is a novel extension of the Schur complement method to flight dynamics problems which require particular care for the tracing. The second one is a data-based approach which involves POD applied to the multidisciplinary system. Both methods promise an effective reduction in terms of computational cost and time, when compared to the full order model.

These model reduction techniques are exploited for the reduction of a two-dimensional test case in Chapter 4. In particular, the test case is composed of a NACA 0012 aerofoil free to move in the vertical direction and to rotate rigidly. Aerodynamics is modelled with Euler equations. The small size of the problem allows for a detailed assessment of the two reduction methods. Limitations are highlighted and remedies proposed.

Reduction techniques are scaled towards a larger, albeit two-dimensional, test case in Chapter 5. Aerodynamics is modelled with RANS equations while full longitudinal flight dynamics is adopted. The test case involves two aerofoils representing wing and tail sections, respectively. A trimming procedure is introduced so that non-trivial starting conditions are taken into account. Both operator-based and data-based methods are applied to the test case while the tracing procedure for the former is further improved to identify flight dynamics eigenvalues inside the cloud of fluid eigenvalues.

In Chapter 6 an application of the model reduction techniques to an industrial-size test case is presented. The test case is a large civil aircraft which translate and rotate rigidly in the three-dimensional space. RANS equations are adopted for aerodynamics whereas flight dynamics is implemented with a modal approach. The size of the model makes the application of both operator-based and data-based methods a challenging task. Overall, both techniques proved to be an effective way for the reduction of computational cost for high-fidelity multidisciplinary simulations.

To summarise, three objectives are pursued in this work with the long-term ambition of certification by simulation. First, the development of a fast and reliable model reduction technique for coupled systems involving CFD and flight dynamics. The objective is composed of three novel contributions, specifically the operator-based identification for flight dynamics modes, the monolithic approach to the data-based identification in frequency domain and the generic theoretical framework to perform the reduction. This is described in Chapter 3 using the full order model introduced in Chapter 2. Secondly, the reduction method is assessed with two-dimensional applications in Chapters 4 and 5. Thirdly, the objective of speeding up gust encounter simulations for aircraft design is met in Chapter 6 with an industry-relevant case which is based on a large three-dimensional aircraft. The two- and three-dimensional test cases presented in this work are the first applications, to the author's best knowledge, of a projection reduced order model for a coupled system composed of CFD aerodynamics and flight dynamics with modes identified applying either the operator-based or the data-based technique.

Chapter 2

Full Order Modelling

Theory of the full order model and numerical methods adopted for its implementation are described in this chapter. The coupling of aerodynamics and flight dynamics is achieved by implementing the two disciplines as two distinct subsystems. The first part of the chapter focuses on the mathematical formulation of aerodynamic and flight dynamics models. The former is modelled with computational fluid dynamics (CFD) which is based on Navier–Stokes equations. Solving such equations for high Reynolds numbers is a challenging task since it requires considerable computational power. So, a reduction in computational cost is achieved by solving Reynolds-averaged Navier–Stokes (RANS) equations which are obtained with a time-averaging procedure from the Navier–Stokes ones. A further reduction, leading to Euler equations, is obtained by neglecting viscosity and heat-transfer terms in the Navier–Stokes equations.

The mathematical background for flight dynamics is then presented. Equations of motion are derived from first principles and they describe the capability of bodies to move in space when subject to external forces. Two formulations of the equations are presented, specifically deriving from Newton's laws and Lagrange's equations. Equations for the coupled model contain both aerodynamic and flight dynamics subsystems. A non-linear residual function, which takes into account both aerodynamic and flight dynamics non-linear residuals, is derived. In addition, linearised frequency domain (LFD) methods are presented. Numerical aspects of the implementation are discussed in the second part of the chapter. An overview of numerical methods used for flight dynamics is given. Similarly, numerical procedures for CFD are reported and a detailed description of the gust modelling in CFD is provided. The information regarding body motions is transferred from the flight dynamics subsystem to the aerodynamic one with grid deformation based on radial basis function (RBF) interpolation.

The last part of the chapter describes the two CFD solvers used in the thesis, an in-house software and DLR-TAU, respectively. The first one is a research code which computes flow solutions by discretising RANS or Euler equations on a set of points distributed in the computational domain. It is used for two-dimensional test cases. The second one is a well-known finite volume code, DLR-TAU, from the German Aerospace Center (DLR). It has been employed for test cases ranging from aerofoil to large aircraft configurations. It is adopted for three-dimensional cases in the thesis.

2.1 Equations of Aerodynamics

Aerodynamics is modelled with Navier–Stokes equations which describe the behaviour of fluid flows. Their derivation from first principles is a complex task and it is described in detail in Appendix A. Their integral form is reported hereafter since it is usually adopted for the implementation of finite volume codes. Equation for conservation of mass is

$$\frac{\partial}{\partial t}\iiint_{\mathcal{V}} \rho \, \mathrm{d}\mathcal{V} + \iint_{S} \rho(\boldsymbol{V}\cdot\boldsymbol{n}) \, \mathrm{d}S = 0 \tag{2.1}$$

where $\mathcal{V}$ is the finite control volume, S is the control surface, $\boldsymbol{n}$ is the normal vector, $\boldsymbol{V}$ is the velocity vector and ρ is the density. The momentum equation, which is derived from Newton's second law,

$$\begin{split}\frac{\partial}{\partial t}\iiint_{\mathcal{V}} \rho\boldsymbol{V} \, \mathrm{d}\mathcal{V} + \iint_{S} \rho\boldsymbol{V}(\boldsymbol{V}\cdot\boldsymbol{n}) \, \mathrm{d}S = \\ \iiint_{\mathcal{V}} \rho\boldsymbol{f}_{ext} \, \mathrm{d}\mathcal{V} - \iint_{S} p\boldsymbol{n} \, \mathrm{d}S + \iint_{S} \overline{\overline{\tau}}\cdot\boldsymbol{n} \, \mathrm{d}S\end{split} \tag{2.2}$$

introduces static pressure p and external body forces per unit mass $\rho\boldsymbol{f}_{ext}$. This is a vector equation and the stress is expressed by means of the second order tensor $\overline{\overline{\tau}}$. Conservation of energy is given for total energy per unit mass E,

$$\begin{split}\frac{\partial}{\partial t}\iiint_{\mathcal{V}} \rho E \, \mathrm{d}\mathcal{V} + \iint_{S} \rho E(\boldsymbol{V}\cdot\boldsymbol{n}) \, \mathrm{d}S - \iint_{S} k(\boldsymbol{\nabla} T\cdot\boldsymbol{n}) \, \mathrm{d}S = \\ \iiint_{\mathcal{V}} (\rho\boldsymbol{f}_{ext}\cdot\boldsymbol{V} + \dot{q}) \, \mathrm{d}\mathcal{V} - \iint_{S} p\boldsymbol{V}\cdot\boldsymbol{n} \, \mathrm{d}S + \iint_{S} (\overline{\overline{\tau}}\cdot\boldsymbol{V})\cdot\boldsymbol{n} \, \mathrm{d}S\end{split} \tag{2.3}$$

where T is the temperature, k is fluid's conductivity coefficient and $\dot{q}$ accounts for possible heat sources. The set of Eqs. (2.1-2.3) is an integral form of Navier–Stokes equations which are written for a control volume and using a Eulerian reference frame [7, 23].

The Navier–Stokes equations in differential form are reported here as well using a Lagrangian reference frame [7, 23]. They can be derived from the integral formulation since they are mathematically equivalent

$$\frac{\mathrm{D}\rho}{\mathrm{D}t} = -\rho\boldsymbol{\nabla}\cdot\boldsymbol{V} \tag{2.4}$$

$$\rho\frac{\mathrm{D}\boldsymbol{V}}{\mathrm{D}t} = -\boldsymbol{\nabla}p + \boldsymbol{\nabla}\overline{\overline{\tau}} + \rho\boldsymbol{f}_{ext} \tag{2.5}$$

$$\rho\frac{\mathrm{D}}{\mathrm{D}t}\left(e + \frac{\boldsymbol{V}^2}{2}\right) = \rho\dot{q} + \boldsymbol{\nabla}\cdot(k\boldsymbol{\nabla}T) - \boldsymbol{\nabla}\cdot(p\boldsymbol{V}) + \boldsymbol{\nabla}\cdot\left(\overline{\overline{\tau}}\boldsymbol{V}\right) + \rho\boldsymbol{f}_{ext}\cdot\boldsymbol{V} \tag{2.6}$$

Specifically, Eq. (2.4) expresses mass conservation, Eq. (2.5) is the momentum equation and Eq. (2.6) imposes energy conservation. Although integral and differential forms are mathematically equivalent, one can be preferred over the other for implementation purposes [7].

When moving reference frames need to be taken into account, a formulation of Navier–Stokes equations called Arbitrary Lagrangian-Eulerian (ALE) must be adopted [51, 75]. ALE equations were developed specifically for fluid-structure interaction problems [51] and they have been successfully applied to fluid dynamics involving rigid-body motions [52, 55]. The velocity of the reference frame is denoted $\boldsymbol{U}$ and Eq. (2.1) turns into

$$\frac{\partial}{\partial t}\iiint_{\mathcal{V}}\rho\,\mathrm{d}\mathcal{V} - \iint_S \rho(\boldsymbol{U}-\boldsymbol{V})\cdot\boldsymbol{n}\,\mathrm{d}S = 0 \tag{2.7}$$

which describes balance of mass. Similarly, the momentum Eq. (2.2) becomes

$$\begin{aligned}\frac{\partial}{\partial t}\iiint_{\mathcal{V}}\rho\boldsymbol{V}\,\mathrm{d}\mathcal{V} - \iint_S \rho\boldsymbol{V}(\boldsymbol{U}-\boldsymbol{V})\cdot\boldsymbol{n}\,\mathrm{d}S &= \\ \iiint_{\mathcal{V}}\rho\boldsymbol{f}_{ext}\,\mathrm{d}\mathcal{V} - \iint_S p\boldsymbol{n}\,\mathrm{d}S + \iint_S \overline{\overline{\tau}}\cdot\boldsymbol{n}\,\mathrm{d}S\end{aligned} \tag{2.8}$$

and the conservation of energy is satisfied by rewriting Eq. (2.3) as

$$\begin{aligned}\frac{\partial}{\partial t}\iiint_{\mathcal{V}}\rho E\,\mathrm{d}\mathcal{V} - \iint_S \rho E(\boldsymbol{U}-\boldsymbol{V})\cdot\boldsymbol{n}\,\mathrm{d}S - \iint_S k(\boldsymbol{\nabla}T\cdot\boldsymbol{n})\,\mathrm{d}S &= \\ \iiint_{\mathcal{V}}(\rho\boldsymbol{f}_{ext}\cdot\boldsymbol{V} + \dot{q})\,\mathrm{d}\mathcal{V} - \iint_S p\boldsymbol{V}\cdot\boldsymbol{n}\,\mathrm{d}S + \iint_S (\overline{\overline{\tau}}\cdot\boldsymbol{V})\cdot\boldsymbol{n}\,\mathrm{d}S\end{aligned} \tag{2.9}$$

When $\boldsymbol{U} = \boldsymbol{V}$, the reference frame moves at the same speed of the flow and formulation is Lagrangian. Conversely, when $\boldsymbol{U} = 0$, it is not moving. The formulation is then Eulerian and Eqs. (2.7-2.9) reduce to Eqs. (2.1-2.3). Similarly, ALE equations can be written in a differential form which is analogous to Eqs. (2.4-2.6). Such equations are not reported here for sake of brevity and they are available in literature [52].

Navier–Stokes equations in either integral or differential form are composed of five equations with seven variables, specifically density ρ, velocity vector $\boldsymbol{V}$ with three components, static pressure p, internal energy e and temperature T. Two additional equations, thus closing the system, are obtained by assuming a perfect gas model [31]. Pressure and specific internal energy are related to the temperature,

$$p = \rho R T \tag{2.10}$$

$$e = c_v T \tag{2.11}$$

where R is perfect gas constant and c_v is the specific heat capacity at constant volume. Pressure is expressed with total energy E by substituting Eq. (2.11) into Eq. (2.10) and applying the definition of total energy $E = e + \frac{\boldsymbol{V}^2}{2}$,

$$p = (\gamma - 1)\rho \left(E - \frac{\boldsymbol{V}^2}{2} \right) \tag{2.12}$$

where $\gamma = 1 + \frac{R}{c_v}$ is the ratio of specific heats whose value depends on the gas. To complete the thermodynamic model, usually the Sutherland equation is adopted to calculate the dynamic viscosity μ of the fluid as a function of the temperature T,

$$\mu = \mu_0 \frac{T_0 + C}{T + C} \left(\frac{T}{T_0} \right)^{\frac{3}{2}} \tag{2.13}$$

where T_0 is the reference temperature, μ_0 is the reference viscosity at reference temperature and C is Sutherland's constant for the gas.

Regarding the second order stress tensor $\overline{\overline{\tau}}$ that appears in both momentum and energy equations, it is composed of 9 parameters which must be determined in order to obtain a solution for the Navier–Stokes equations. Denote u, v and w the three components of velocity vector $\boldsymbol{V} = [u, v, w]$ in the directions x, y and z, respectively. The tensor is defined as

$$\overline{\overline{\tau}} = \begin{bmatrix} \sigma_x & \tau_{xy} & \tau_{xz} \\ \tau_{yx} & \sigma_y & \tau_{yz} \\ \tau_{zx} & \tau_{zy} & \sigma_z \end{bmatrix} \tag{2.14}$$

where each component represents a scalar value. The shear stresses are denoted with τ and the double subscript indicates the two directions of each shear stress. For example, τ_{xy} is the stress in the y direction on a plane perpendicular to the x axis. The principal stresses are denoted with σ instead and they represents stresses in the orthogonal directions x, y and z. A first simplification is made when the tensor components are considered proportional to the velocity ratio under the assumption of Newtonian fluid [23],

$$\begin{array}{lll} \sigma_x = \lambda \boldsymbol{\nabla} \cdot \boldsymbol{V} + 2\mu \frac{\partial u}{\partial x} & \tau_{xy} = \mu \left(\frac{\partial u}{\partial y} + \frac{\partial v}{\partial x} \right) & \tau_{xz} = \mu \left(\frac{\partial u}{\partial z} + \frac{\partial w}{\partial x} \right) \\ \tau_{yx} = \tau_{xy} & \sigma_y = \lambda \boldsymbol{\nabla} \cdot \boldsymbol{V} + 2\mu \frac{\partial v}{\partial y} & \tau_{yz} = \mu \left(\frac{\partial v}{\partial z} + \frac{\partial w}{\partial y} \right) \\ \tau_{zx} = \tau_{xz} & \tau_{zy} = \tau_{yz} & \sigma_z = \lambda \boldsymbol{\nabla} \cdot \boldsymbol{V} + 2\mu \frac{\partial w}{\partial z} \end{array} \tag{2.15}$$

with λ and μ representing the second viscosity and dynamic viscosity coefficients, respectively. The expression for principal stresses is further simplified with the Stoke's hypothesis [30], $\lambda = -\frac{2}{3}\mu$. Finally, the value of μ must be determined with empirical assumptions.

So far, we focused on Navier–Stokes equations, thermodynamic model of perfect gas and Newtonian fluid. The last aspect to be analysed in order to completely define a CFD problem is boundary conditions [7]. Only two types of boundary conditions are presented here since they were used in the thesis. A detailed analysis about boundary conditions is out of the scope of this work and it can be found in [23]. The distinction is made between solid wall and far field. The first one, called also non-slip condition, imposes a zero relative velocity at the interface between fluid and solid walls [46]. Mathematically, it corresponds to a Dirichlet boundary condition since the solution is specified along the boundary [16]. Similarly, the far field condition imposes the value of velocity at far field which is a region considered far from every solid body [15]. The equations for boundary conditions are

$$\boldsymbol{V}|_w = 0 \qquad \boldsymbol{V}|_F = \boldsymbol{V}_\infty \tag{2.16}$$

where subscripts w and F indicate the wall and the far field, respectively, and $\boldsymbol{V}_\infty$ is the free-stream velocity vector. Regarding the wall temperature, the fluid near the wall should be in thermal equilibrium with the body and an additional condition on the heat-flux near body surface must be imposed [23],

$$\left. \frac{\partial T}{\partial n} \right|_{\boldsymbol{n}} = -\frac{\dot{q}}{k} \tag{2.17}$$

where $\boldsymbol{n}$ is the surface normal and k is the fluid thermal conductivity.

Direct solution of Navier–Stokes equations is an area of active research [94, 157] and so far it is possible just for small, academic cases [102]. Main limitation is the requirement in terms of computational resources and applications to industrial cases are decades away [102, 147]. Specifically, the whole ranges of both spacial and temporal scales must be resolved to describe accurately the turbulent phenomena. Thus, a very fine computational grid is required and its spacing ultimately depends on the non-dimensional Reynolds number $\mathrm{Re} = \frac{\rho U_{\mathrm{ref}} L_{\mathrm{ref}}}{\mu}$ which is defined as function of reference velocity U_{ref} and reference length L_{ref}. An idea of the problem to overcome is given by the computational memory which would be needed to store flow solutions [33]. The memory required for each flow solution is proportional to the number of grid points which, in turn, depends on $\mathrm{Re}^{2.25}$. Reynolds numbers usually associated to industrial applications are roughly $10^6 - 10^8$ and they are far from the one (10^3) reached by the most computationally expensive direct simulation performed so far [78]. An additional problem is the computational speed for dealing with such large simulations which will not be available for the foreseeable future [33]. Hence, simplified formulations are employed instead. Two sets of equations, which can be derived from Navier–Stokes equations by making some simplifying assumptions, are commonly adopted by the aerospace community and described in the following paragraphs.

2.1.1 Reynolds-averaged Navier–Stokes Equations

When it comes to turbulent flows, solving the Reynolds-averaged Navier–Stokes (RANS) equations [32, 60] is the de-facto standard adopted by the industry community [1, 102]. Such equations, which were first derived by O. Reynolds in 1895 [118], rely on the Reynolds's decomposition [1] to divide flow variables into average values and fluctuations. Hence, a scalar quantity U is expressed as

$$U = \overline{U} + \widetilde{U} \tag{2.18}$$

where $\overline{U}$ is the ensemble-averaged value of U and $\widetilde{U}$ is its fluctuation with respect to the mean. The application of Eq. (2.18) to the Navier–Stokes equations is not a trivial process [137]. An additional stress tensor term, which is called Reynolds tensor $\overline{\overline{\tau}}^R$, is found as a result [23]. It depends on velocity fluctuations since its components are defined for an incompressible flow as

$$\tau_{ij}^R = -\rho \overline{\widetilde{V}_i \widetilde{V}_j} \tag{2.19}$$

where $\widetilde{V}_i$ and $\widetilde{V}_j$ are the fluctuations in the i and j components of the velocity vector $\boldsymbol{V}$, respectively, with $i, j \in [1, 3]$. Besides $\overline{\overline{\tau}}^R$, an additional term originates from the averaging procedure, specifically a heat-flux tensor which is added to the diffusive heat term [23]. RANS equations allow for a quicker calculation of flow solutions if compared to the Navier–Stokes equations. However, they need a turbulence model for the Reynolds stress tensor in order to define a closed problem.

Turbulence models are an area of active research and a comprehensive overview is available in [151]. They are catalogued into main families, according to the order of the closure [23]. In practice, first order closures are usually adopted since equations for higher order ones are difficult to solve. They rely on a single scalar value to calculate the Reynold stress tensor. The Boussinesq hypothesis models the transfer of momentum caused by turbulent eddies using a scalar eddy viscosity μ_T by analogy with molecular viscosity which models momentum transfer caused by molecular motion [25, 26]. The components of $\overline{\overline{\tau}}^R$ in Eq. (2.19) become

$$\tau_{ij}^R = -\rho\overline{\widetilde{V}_i\widetilde{V}_j} = -\mu_T\left(\frac{\partial \boldsymbol{V}_i}{\partial x_i} + \frac{\partial \boldsymbol{V}_j}{\partial x_j} - \frac{2}{3}\frac{\partial \boldsymbol{V}_i}{\partial x_i}\delta_{ij}\right) - \frac{2}{3}\rho k\delta_{ij} \tag{2.20}$$

where δ_{ij} is the Kronecker delta. Turbulence models provide the value of μ_T. In the category of first order closures, they are classified according to the number of equations adopted [91, 152].

The one-equation Spalart-Allmaras model [132] is widely adopted for research and extensively exploited in this work as well since it is designed for aerospace applications. The complete derivation is available in [132] whereas the resulting equations are reported here. The turbulent eddy viscosity is defined with the Spalart-Allmaras variable $\widetilde{\nu}$,

$$\mu_T = \rho\widetilde{\nu}f_{v1}(\widetilde{\nu}) \tag{2.21}$$

A transport equation is solved to provide values of $\widetilde{\nu}$,

$$\begin{aligned}\frac{\mathrm{D}\widetilde{\nu}}{\mathrm{D}t} =& c_{b1}\left(1 - f_{t2}\right)\widetilde{S}\widetilde{\nu}\\ &+ \frac{1}{\sigma}\left\{\boldsymbol{\nabla}\cdot\left(\left(\nu + \widetilde{\nu}\right)\nabla\widetilde{\nu}\right) + c_{b2}\left(\nabla\widetilde{\nu}\right)^2\right\}\\ &- \left(c_{w1}f_w - \frac{c_{b1}}{k^2}f_{t2}\right)\left(\frac{\widetilde{\nu}}{d}\right)^2 + f_{t1}\boldsymbol{V}^2\end{aligned} \tag{2.22}$$

with the right-hand side depending on the distance d from the closest wall as well as the flow velocity $\boldsymbol{V}$ at the field point. It is completely defined with the auxiliary quantities,

$$\begin{array}{lll} \chi = \frac{\widetilde{\nu}}{\nu} & f_{v1} = \frac{\chi^3}{\chi^3 + c_{v1}^3} & f_{v2} = 1 - \frac{\chi}{1 + \chi f_{v1}} \\ \widetilde{S} = S + \frac{\widetilde{\nu}}{k^2 d^2}f_{v2} & r = \frac{\widetilde{\nu}}{\widetilde{S}k^2 d^2} & g = r + c_{w2}\left(r^6 - r\right) \\ f_w = g\left(\frac{1 + c_{w3}^6}{g^6 + c_{w3}^6}\right)^{\frac{1}{6}} & f_{t1} = c_{t1}g_t e^{-c_{t2}\frac{\omega_t}{\boldsymbol{V}^2}\left(d^2 + g_t^2 d_t^2\right)} & f_{t2} = c_{t3}e^{-c_{t4}\chi^2} \end{array}$$

where S is the magnitude of the vorticity and values for the constants can be found in reference [132]. Solving Eq. (2.22) is achieved imposing Dirichlet boundary conditions with

$$\widetilde{\nu}|_{\boldsymbol{n}} = 0 \tag{2.23}$$

so that the value of Spalart-Allmaras variable $\widetilde{\nu}$ is zero on the solid wall.

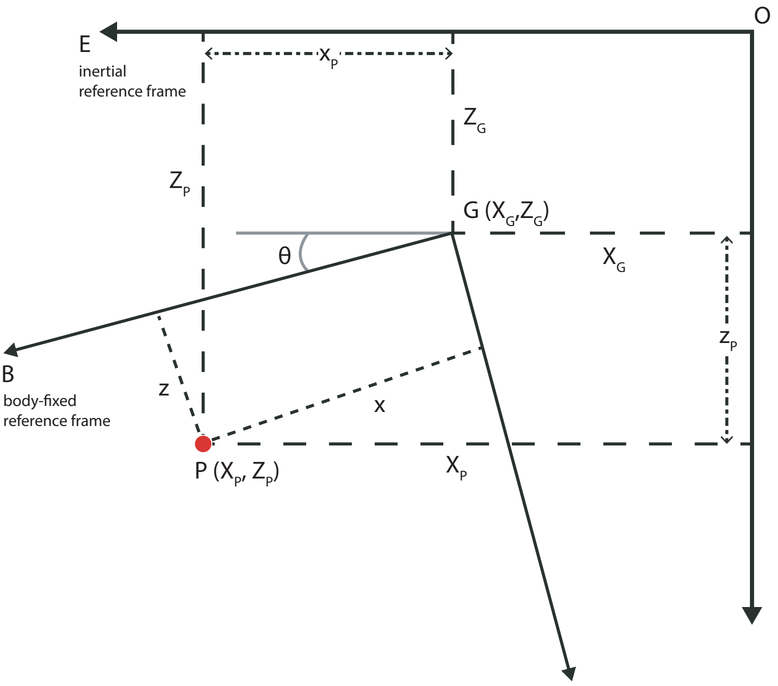

Figure 2.1: Reference frames for derivation of longitudinal dynamics equations.

2.1.2 Euler Equations

Another set of aerodynamic equations, which is exploited in this work, is composed of the so-called Euler equations [23, 58]. They can be derived from the Navier–Stokes equations by assuming an adiabatic and inviscid fluid as described in Appendix A. They represent a simplification of Navier–Stokes ones which completely discards viscous effects. It is a valid assumption when applied to cases, for example, of fluid flows with very high Reynolds numbers for which the boundary layer is very thin [23]. Shock waves are still captured by solving Euler equations. However, interesting phenomena such as interaction of boundary layer with shock waves cannot be simulated.

With a constantly increasing computational capability, Euler equations are almost superseded by RANS ones. However, they still have an important role in the research community as a fast method for preliminary results [71] or as a test bench for new methods.

2.2 Equations of Flight Dynamics

So far, focus was on the aerodynamic part of the full order model. In this section, the theoretical background is given for flight dynamics. Various approaches have been proposed in literature [155] to derive the flight dynamics equations and the classical approach based on Newton's law is shown in this section for longitudinal dynamics. The aim is to obtain differential equations describing the relative, rigid motion between the flying body and an inertial coordinate system. Two reference frames are defined for the derivation and they are depicted in Fig. 2.1. The first is denoted with the letter E. It is Earth centred and it is assumed to be an inertial reference frame. The second one is a body-fixed frame denoted with B. Its origin corresponds to the barycentre[1] (also known as centre of mass) of the body and it moves together with it. The pitch angle θ is defined as the angle which is needed to overlap the inertial reference frame to the body-fixed one with a counter-clockwise rotation. Note that two different orientations are usually adopted for reference frames when it comes to flight dynamics and CFD. Specifically, the direction which is perpendicular to the free-stream flow is assumed positive downward for flight dynamics but negative for CFD.

The derivation is composed of three steps leading to flight dynamics equations formulated in the body-fixed reference frame. First, the barycentre G is assumed to move in the inertial frame E. A generic point P belonging to the body is chosen. It moves with respect to the origin O of the inertial frame while its relative position referred to the barycentre G does not change. Secondly, the acceleration of the generic point P is calculated in the inertial frame. Thirdly, Newton's second law is applied and the resulting equations are translated into the body-fixed reference frame.

The location (X_P, Z_P) of the generic point P in the inertial frame is

$$\begin{aligned} X_P &= X_G + x_P \\ Z_P &= Z_G + z_P \end{aligned} \tag{2.24}$$

where (X_G, Z_G) is the barycentre position. The quantities x_P and z_P represent the relative distance between P and the barycentre G in the inertial reference frame. Such distance can be calculated in the body-fixed reference frame as well. Specifically, the coordinates of P in the body-fixed reference frame (x, z) are rotated by θ with respect to the inertial frame and Eq. (2.24) becomes

$$\begin{aligned} X_P &= X_G + x\cos\theta + z\sin\theta \\ Z_P &= Z_G - x\sin\theta + z\cos\theta \end{aligned} \tag{2.25}$$

The derivatives with respect to time of Eq. (2.25) provide the velocity of P in the inertial frame,

$$\begin{aligned} \frac{\mathrm{d}X_P}{\mathrm{d}t} &= \frac{\mathrm{d}X_G}{\mathrm{d}t} + \frac{\mathrm{d}x}{\mathrm{d}t}\cos\theta - x\sin\theta\frac{\mathrm{d}\theta}{\mathrm{d}t} + \frac{\mathrm{d}z}{\mathrm{d}t}\sin\theta + z\cos\theta\frac{\mathrm{d}\theta}{\mathrm{d}t} \\ \frac{\mathrm{d}Z_P}{\mathrm{d}t} &= \frac{\mathrm{d}Z_G}{\mathrm{d}t} - \frac{\mathrm{d}x}{\mathrm{d}t}\sin\theta - x\cos\theta\frac{\mathrm{d}\theta}{\mathrm{d}t} + \frac{\mathrm{d}z}{\mathrm{d}t}\cos\theta - z\sin\theta\frac{\mathrm{d}\theta}{\mathrm{d}t} \end{aligned} \tag{2.26}$$

---

[1] Note that barycentre and centre of gravity coincide for a body subject to uniform gravitational field.

The barycentre velocity $\frac{\mathrm{d}X_G}{\mathrm{d}t}$ and $\frac{\mathrm{d}Z_G}{\mathrm{d}t}$ are expressed in the body-fixed reference frame with a rotation of θ as

$$\begin{aligned}\frac{\mathrm{d}X_G}{\mathrm{d}t} =& U\cos\theta + W\sin\theta \\ \frac{\mathrm{d}Z_G}{\mathrm{d}t} =& -U\sin\theta + W\cos\theta\end{aligned} \tag{2.27}$$

where the unknowns U and W are the barycentre horizontal and vertical velocity in the body-fixed reference frame, respectively. Equation (2.27) will be later exploited to calculate the flight path in the inertial frame by integration of body-fixed quantities. The velocity of P in the body-fixed reference frame are named v_x and v_z, respectively. They are obtained by rotating the velocity pair $\left(\frac{\mathrm{d}X_P}{\mathrm{d}t}, \frac{\mathrm{d}Z_P}{\mathrm{d}t}\right)$ by the angle θ.

$$\begin{aligned}v_x =& \frac{\mathrm{d}X_P}{\mathrm{d}t}\cos\theta - \frac{\mathrm{d}Z_P}{\mathrm{d}t}\sin\theta \\ v_z =& \frac{\mathrm{d}X_P}{\mathrm{d}t}\sin\theta + \frac{\mathrm{d}Z_P}{\mathrm{d}t}\cos\theta\end{aligned} \tag{2.28}$$

Substituting Eqs. (2.26) and (2.27) into Eq. (2.28) and defining $q = \frac{\mathrm{d}\theta}{\mathrm{d}t}$ leads to

$$\begin{aligned}v_x =& U + zq + \frac{\mathrm{d}x}{\mathrm{d}t} \\ v_z =& W - xq + \frac{\mathrm{d}z}{\mathrm{d}t}\end{aligned} \tag{2.29}$$

where the derivatives of x and z are $\frac{\mathrm{d}x}{\mathrm{d}t} = \frac{\mathrm{d}z}{\mathrm{d}t} = 0$ by definition of rigid bodies.

The acceleration of P in the inertial frame is obtained by differentiating Eq. (2.26) with respect to time.

$$\begin{aligned}\frac{\mathrm{d}^2X_P}{\mathrm{d}t^2} =& \frac{\mathrm{d}^2X_G}{\mathrm{d}t^2} - xq^2\cos\theta - x\sin\theta\frac{\mathrm{d}q}{\mathrm{d}t} - zq^2\sin\theta + z\cos\theta\frac{\mathrm{d}q}{\mathrm{d}t} \\ \frac{\mathrm{d}^2Z_P}{\mathrm{d}t^2} =& \frac{\mathrm{d}^2Z_G}{\mathrm{d}t^2} + xq^2\sin\theta - x\cos\theta\frac{\mathrm{d}q}{\mathrm{d}t} - zq^2\cos\theta - z\sin\theta\frac{\mathrm{d}q}{\mathrm{d}t}\end{aligned} \tag{2.30}$$

Similarly, the acceleration of the barycentre is obtained by differentiating Eq. (2.27). This leads to

$$\begin{aligned}\frac{\mathrm{d}^2X_G}{\mathrm{d}t^2} =& \frac{\mathrm{d}U}{\mathrm{d}t}\cos\theta + \frac{\mathrm{d}W}{\mathrm{d}t}\sin\theta - Uq\sin\theta + Wq\cos\theta \\ \frac{\mathrm{d}^2Z_G}{\mathrm{d}t^2} =& -\frac{\mathrm{d}U}{\mathrm{d}t}\sin\theta + \frac{\mathrm{d}W}{\mathrm{d}t}\cos\theta - Uq\cos\theta - Wq\sin\theta\end{aligned} \tag{2.31}$$

The acceleration of P in the body-fixed reference frame is then calculated by rotating the pair $\left(\frac{\mathrm{d}^2X_P}{\mathrm{d}t^2}, \frac{\mathrm{d}^2Z_P}{\mathrm{d}t^2}\right)$ by θ,

$$
\begin{aligned}
a_x =& \frac{\mathrm{d}^2X_P}{\mathrm{d}t^2}\cos\theta - \frac{\mathrm{d}^2Z_P}{\mathrm{d}t^2}\sin\theta \\
a_z =& \frac{\mathrm{d}^2X_P}{\mathrm{d}t^2}\sin\theta + \frac{\mathrm{d}^2Z_P}{\mathrm{d}t^2}\cos\theta
\end{aligned}
\tag{2.32}
$$

Substituting Eqs. (2.30) and (2.31) into Eq. (2.32) leads to

$$
\begin{aligned}
a_x =& \frac{\mathrm{d}U}{\mathrm{d}t} + Wq - xq^2 + z\frac{\mathrm{d}q}{\mathrm{d}t} \\
a_z =& \frac{\mathrm{d}W}{\mathrm{d}t} - Uq - zq^2 - x\frac{\mathrm{d}q}{\mathrm{d}t}
\end{aligned}
\tag{2.33}
$$

which is the acceleration expressed in the inertial reference frame with body-fixed quantities. Newton's second law is applied next. It links acceleration to force by means of geometric parameters such as mass and inertia.

The expressions for the acceleration in Eq. (2.33) are used to apply Newton's second law to the body dynamics

$$
\begin{aligned}
\int a_x \mathrm{d}m =& F_x \\
\int a_z \mathrm{d}m =& F_z \\
\int (a_x z - a_z x)\,\mathrm{d}m =& M_y
\end{aligned}
\tag{2.34}
$$

where the symbols F_x, F_z and M_y represent external forces. They include aerodynamic as well as volumetric forces such as gravity. Substituting Eq. (2.33) into Eq. (2.34), leads to the equations of motion

$$
\begin{aligned}
\frac{\mathrm{d}U}{\mathrm{d}t}\int \mathrm{d}m + Wq\int \mathrm{d}m - q^2\int x\mathrm{d}m + \frac{\mathrm{d}q}{\mathrm{d}t}\int z\mathrm{d}m =& F_x \\
\frac{\mathrm{d}W}{\mathrm{d}t}\int \mathrm{d}m - Uq\int \mathrm{d}m - q^2\int z\mathrm{d}m - \frac{\mathrm{d}q}{\mathrm{d}t}\int x\mathrm{d}m =& F_z \\
\frac{\mathrm{d}U}{\mathrm{d}t}\int z\mathrm{d}m + Wq\int z\mathrm{d}m + \frac{\mathrm{d}q}{\mathrm{d}t}\int \left(x^2+z^2\right)\mathrm{d}m - \frac{\mathrm{d}W}{\mathrm{d}t}\int x\mathrm{d}m + Uq\int x\mathrm{d}m =& M_y
\end{aligned}
\tag{2.35}
$$

The terms involving $\int x\mathrm{d}m$ and $\int z\mathrm{d}m$ are static moments with respect of the centre of mass and their value is zero by definition of the centre of mass. The total mass and the moment of inertia are defined as $\int \mathrm{d}m = m$ and $\int \left(x^2+z^2\right)\mathrm{d}m = I_\theta$, respectively. Note that both m and I_θ are computed in the longitudinal plane and they are referred to one unit of length in the third dimension. The resulting equations of motion involve four flight dynamics state variables, specifically U, W, q and θ

$$\begin{aligned} &\frac{\mathrm{d}U}{\mathrm{d}t} + Wq = \frac{F_x}{m} && \frac{\mathrm{d}W}{\mathrm{d}t} - Uq = \frac{F_z}{m} \\ &\frac{\mathrm{d}q}{\mathrm{d}t} = \frac{M_y}{I_\theta} && \frac{\mathrm{d}\theta}{\mathrm{d}t} = q \end{aligned} \tag{2.36}$$

The equations of motion in Eq. (2.36) can be linearised around an equilibrium state so that values of flight dynamics variables are the sum of equilibrium values and fluctuations. Usually the equilibrium condition is calculated with a trimming procedure for steady, straight flight conditions. This implies that variations of the state vector are assumed small around the trim configuration. The flight dynamics unknowns are defined as $U = U_0 + \widetilde{u}$, $W = W_0 + \widetilde{w}$, $q = q_0 + \widetilde{q}$ and $\theta = \theta_0 + \widetilde{\theta}$. Specifically, U_0 and W_0 are the horizontal and vertical flight speed of the body at the equilibrium. They are related to flight speed U_∞ and angle-of-incidence α_0 since $U_0 = U_\infty \cos\alpha_0$ and $W_0 = U_\infty \sin\alpha_0$. The terms $\widetilde{u}$, $\widetilde{w}$, $\widetilde{q}$ and $\widetilde{\theta}$ are fluctuations with respect to the equilibrium conditions. Attitude θ_0 and angular velocity q_0 at equilibrium are assumed zero for level flight. Thus, $q = \widetilde{q}$ and $\theta = \widetilde{\theta}$ for the derivation reported thereafter. The linearised equations of motion are

$$\begin{aligned} &\frac{\mathrm{d}\widetilde{u}}{\mathrm{d}t} + W_0 q = \frac{F_x}{m} && \frac{\mathrm{d}\widetilde{w}}{\mathrm{d}t} - U_0 q = \frac{F_z}{m} \\ &\frac{\mathrm{d}\widetilde{q}}{\mathrm{d}t} = \frac{M_y}{I_\theta} && \frac{\mathrm{d}\widetilde{\theta}}{\mathrm{d}t} = q \end{aligned} \tag{2.37}$$

and they will be extensively used in this work together with the CFD model for the aerodynamic components which provides aerodynamic external forces. The integration in time of Eq. (2.37) results in time histories for the flight dynamics unknowns. The flight path can be calculated by integrating Eq. (2.27) as a post-processing step.

The properties of the system are expressed by two non-dimensional quantities, specifically $r_\theta = \sqrt{I_\theta/(mb^2)}$ and mass ratio $\mu = m/(\pi\rho b^2)$, where ρ is the fluid density. This is achieved by defining a reference length b, which is assumed to be the wing semi-chord $b = \frac{c}{2}$ in this work according to the convention in [22] for longitudinal dynamics, and a non-dimensional time $\tau = tU_\infty/b$. The forces are expressed by means of force coefficients $F_x = \frac{1}{2}\rho c U_\infty^2 C_x = \rho b U_\infty^2 C_x$, $F_z = \rho b U_\infty^2 C_z$, $M_y = 2\rho b^2 U_\infty^2 C_m$. As a consequence, non-dimensional equations are derived from Eq. (2.37),

$$\begin{aligned} \frac{\mathrm{d}u^*}{\mathrm{d}\tau} + W_0^* q^* &= \frac{C_x}{\pi\mu} \qquad & \frac{\mathrm{d}w^*}{\mathrm{d}\tau} - U_0^* q^* &= \frac{C_z}{\pi\mu} \\ \frac{\mathrm{d}q^*}{\mathrm{d}\tau} &= \frac{2C_m}{\pi\mu r_\alpha^2} \qquad & \frac{\mathrm{d}\theta^*}{\mathrm{d}\tau} &= q^* \end{aligned} \tag{2.38}$$

where u^*, w^*, q^*, U_0^* and W_0^* are non-dimensional quantities. Please, note that when θ is expressed in radians, the equality $\theta = \theta^*$ holds. The flight path in the inertial reference frame is calculated with the corresponding non-dimensional formulation of Eq. (2.27)

$$\begin{aligned} \frac{\mathrm{d}X_G^*}{\mathrm{d}\tau} &= (U_0^* + u^*)\cos\theta^* + (W_0^* + w^*)\sin\theta^* \\ \frac{\mathrm{d}Z_G^*}{\mathrm{d}\tau} &= -\,(U_0^* + u^*)\sin\theta^* + (W_0^* + w^*)\cos\theta^* \end{aligned} \tag{2.39}$$

where X_G^* and Z_G^* are the non-dimensional coordinates. Equation (2.39) is obtained by substituting $U = U_0 + \widetilde{u}$ and $W = W_0 + \widetilde{w}$ into Eq. (2.27) and then applying the non-dimensionalisation procedure, already presented, with reference length b and non-dimensional time $\tau = tU_\infty/b$.

These equations can be further simplified by focusing on the short-term response of the system. The horizontal velocity u of the body is assumed constant and its corresponding degree-of-freedom is removed.

$$\begin{aligned} \frac{\mathrm{d}w^*}{\mathrm{d}\tau} - U_0^* q^* &= \frac{C_z}{\pi\mu} \\ \frac{\mathrm{d}q^*}{\mathrm{d}\tau} &= \frac{2C_m}{\pi\mu r_\alpha^2} \\ \frac{\mathrm{d}\theta^*}{\mathrm{d}\tau} &= q^* \end{aligned} \tag{2.40}$$

This assumption is valid when dealing with fast phenomena such as gusts since changes in the horizontal speed are assumed to be negligible.

So far, equations of flight dynamics have been derived for longitudinal motion and they will be exploited in this form for two-dimensional test cases. A generalisation to three-dimensional dynamics is available in literature [77, 122]. Equations for translation and rotation are expressed with matrix notation as

$$\begin{aligned} M_b\left(\frac{\mathrm{d}\boldsymbol{V}}{\mathrm{d}t} + \boldsymbol{\Omega} \times \boldsymbol{V}\right) &= \boldsymbol{F}_e \\ I_b\frac{\mathrm{d}\boldsymbol{\Omega}}{\mathrm{d}t} + \boldsymbol{\Omega} \times (I_b\boldsymbol{\Omega}) &= \boldsymbol{M}_e \end{aligned} \tag{2.41}$$

where M_b is the diagonal matrix containing the body's mass, $\boldsymbol{V}$ is the velocity vector, $\boldsymbol{\Omega}$ is the vector of angular velocities and I_b is the 3×3 inertia matrix in the body-fixed reference frame. Three-dimensional forces and moments are contained in the vector $\boldsymbol{F}_e$ and $\boldsymbol{M}_e$, respectively. Dynamics described by Eq. (2.41) is complex because degrees-of-freedom are not decoupled [34, Ch. 4]. A linearised, decoupled formulation of three-dimensional equations can be obtained with a modal formulation. Its benefits are a simplified mathematical model and a final form of equations which is very similar to aeroelastic one. This allows reusing aeroelastic software tools for flight dynamics problems.

The equations of motion for rigid-body dynamics are derived in modal form using Lagrange's equation [155, Ch. 14]. Denote $\boldsymbol{\eta} = [\eta_1, \eta_2, \eta_3, \eta_4, \eta_5, \eta_6]^T$ as the vector containing six generalised coordinates. In the specific case of flight dynamics, they will correspond to the rigid-body degrees-of-freedom in a three-dimensional space (3 translations and 3 rotations). The kinetic energy K of the system is

$$K = \frac{1}{2}\sum_{j=1}^{6} M_j \left(\frac{\mathrm{d}\eta_j}{\mathrm{d}t}\right)^2 \tag{2.42}$$

where M_j is the generalised mass associated with the generalised coordinate η_j. The elastic potential energy is zero since rigid-body degrees-of-freedom have no stiffness by definition. Gravity on the other hand contributes to the total potential energy U. Gravity acceleration is decomposed into six components g_j corresponding to directions η_j and leading to

$$U = -\sum_{j=1}^{6} M_j g_j \eta_j \tag{2.43}$$

with $j \in [1, 6]$. Defining $L = K - U$, Lagrange's equation is written as

$$\frac{\mathtt{d}}{\mathtt{d}t}\left(\frac{\partial L}{\partial \dot{\eta}_j}\right) - \frac{\partial L}{\partial \eta_j} = Q_j \qquad \forall j \in [1, 6] \tag{2.44}$$

where Q_j takes into account aerodynamic forces in the direction of η_j. Substituting Eqs. (2.42) and (2.43) into Eq. (2.44) results in a set of 6 equations which describe the rigid-body dynamics

$$M_j \frac{\mathrm{d}^2\eta_j}{\mathrm{d}t^2} = Q_j - M_j g_j = F_j \qquad \forall j \in [1, 6] \tag{2.45}$$

The aerodynamic forces Q_j are calculated using CFD while the gravity forces are obtained from the mass of the aircraft. The resulting external force is denoted with F_j. Equation (2.45) assumes no explicit coupling between the rigid-body modes and this is the case when the reference frame is anchored to the body mean axis [155]. However, a decoupled modal system is not guaranteed when another reference frame is adopted for flight dynamics [155]. Equation (2.45) resembles the modal equation for structural dynamics and it can be similarly written in a matrix form

$$M\frac{\mathrm{d}^2\boldsymbol{\eta}}{\mathrm{d}t^2} = \boldsymbol{F} \tag{2.46}$$

where M is a diagonal mass matrix with entries M_j and $\boldsymbol{F}$ the vector containing generalised forces.

The six coordinates η_j and their related generalised masses in Eq. (2.46) are usually obtained from an in-vacuum eigenvalue analysis of the unconstrained finite element model. Each degree-of-freedom η_j is associated with a mass-normalised mode shape vector which contains the relative displacement of the FEM grid points in an arbitrary reference frame. These modal shape vectors are splined to the CFD surface point distribution and results stored in the vectors $\boldsymbol{\xi}_j$, $\forall j \in [1, 6]$. The total displacement $\boldsymbol{x}$ of the surface is given by

$$\boldsymbol{x} = \Xi\boldsymbol{\eta} \qquad \Xi = [\boldsymbol{\xi}_1, \boldsymbol{\xi}_2, \boldsymbol{\xi}_3, \boldsymbol{\xi}_4, \boldsymbol{\xi}_5, \boldsymbol{\xi}_6] \tag{2.47}$$

Rigid-body motions are obtained as superposition of mode shapes amplified by the modal amplitudes. In general, rigid-body modes coming from the eigenvalue analysis do not correspond exactly to directions in the body-fixed reference frame such as vertical or horizontal translations. In particular, each mode can be a linear combination of translations and rotations and only the final superposition in Eq. (2.47) provides the total displacement. This is shown in Fig. 2.2 with a representative mode shape resulting from an eigenvalue analysis of a large civil aircraft. It is clearly composed of both vertical translation and roll rotation so that the corresponding generalised coordinate is a superposition of both motions.

Although this does not represent an issue for either the theoretical framework or the numerical model, a link to the physical quantities traditionally adopted for flight dynamics is not immediately available. A possible solution is to apply a transformation and translate results using a new modal basis. Regarding flight dynamics, a new set of pure translational and rotational modes Υ is artificially created. Denoting horizontal, lateral and vertical translations in the inertial reference frame as x_I, y_I and z_I, respectively, and the roll, pitch and yaw rotations as ϕ, θ and ψ, the vector $\boldsymbol{\chi} = [x_I, y_I, z_I, \phi, \theta, \psi]^T$ contains the modal amplitudes for this new set of modes. Since the same physical rigid motion $\boldsymbol{x}$ can now be obtained with those two sets of modes, we can write

$$\Upsilon\boldsymbol{\chi} = \boldsymbol{x} = \Xi\boldsymbol{\eta} \tag{2.48}$$

Mapping modal displacement $\boldsymbol{\eta}$ to physical quantities $\boldsymbol{\chi}$ is achieved using a pseudo-inverse matrix [111] with

$$\boldsymbol{\chi} = \left(\Upsilon^T\Upsilon\right)^{-1}\Upsilon^T\Xi\boldsymbol{\eta} = T\boldsymbol{\eta} \tag{2.49}$$

Figure 2.2: Mode shape resulting from eigenvalue analysis. It is a linear combination of both translation and rotation.

where a 6×6 transformation matrix $T = \left(\Upsilon^T \Upsilon\right)^{-1} \Upsilon^T \Xi$ is introduced. The transformation matrix T is pre-computed once and used to provide physical insights about the system.

2.3 Equations of Coupled Model

Rigid-body dynamics is described in this work by either Eqs. (2.38) or (2.46) according to the specific implementation. Denoting $\boldsymbol{w}_r$ as the vector containing n_r flight dynamics unknowns and $\boldsymbol{R}_r$ as the corresponding residual function, the flight dynamics equations are formulated as a first order ordinary differential equation in time t,

$$\frac{\mathrm{d}\boldsymbol{w}_r}{\mathrm{d}t} = \boldsymbol{R}_r(\boldsymbol{w}_f, \boldsymbol{w}_r) \tag{2.50}$$

with the vector $\boldsymbol{w}_f$ containing the n_f fluid unknowns. Specifically, the residual vector $\boldsymbol{R}_r$ is written in a general form as

$$\boldsymbol{R}_r(\boldsymbol{w}_f, \boldsymbol{w}_r) = \boldsymbol{f}_e(\boldsymbol{w}_r) + C\boldsymbol{f}_a(\boldsymbol{w}_f, \boldsymbol{w}_r) \tag{2.51}$$

with $\boldsymbol{f}_a$ representing aerodynamic forces. The formulation of the vector function $\boldsymbol{f}_e$ depends on the specific set of equations which is adopted. Specifically, $\boldsymbol{f}_e = 0$ for the modal formulation in Eq. (2.46), whereas it is defined as

$$\boldsymbol{f}_e = \begin{bmatrix} 0 & 0 & -W_0^* & 0 \\ 0 & 0 & U_0^* & 0 \\ 0 & 0 & 0 & 0 \\ 0 & 0 & 1 & 0 \end{bmatrix} \begin{bmatrix} u^* \\ w^* \\ q^* \\ \theta^* \end{bmatrix} \tag{2.52}$$

when the formulation in Eq. (2.38) is adopted. The matrix C contains information about geometric properties of the system. The non-linear equations describing Euler or Navier–Stokes aerodynamics are similarly written in a semi-discrete form as

$$\frac{\mathrm{d}\boldsymbol{w}_f}{\mathrm{d}t} = \boldsymbol{R}_f(\boldsymbol{w}_f, \boldsymbol{w}_r, \boldsymbol{u}_d, \boldsymbol{u}_c) \tag{2.53}$$

where $\boldsymbol{R}_f$ is the non-linear residual corresponding to the fluid unknowns, $\boldsymbol{u}_d$ represents a possible external disturbance such as gusts and $\boldsymbol{u}_c$ introduces inputs such as control surface deflections.

Denoting $\boldsymbol{w} = [\boldsymbol{w}_f^T, \boldsymbol{w}_r^T]^T$ as the vector of unknowns of the coupled system, the state-space equations of dimension $n = n_f + n_r$ can be combined as

$$\frac{\mathrm{d}\boldsymbol{w}}{\mathrm{d}t} = \boldsymbol{R}(\boldsymbol{w}, \boldsymbol{u}_d, \boldsymbol{u}_c) \tag{2.54}$$

where $\boldsymbol{R}$ is the corresponding coupled non-linear residual vector. Reference solutions are obtained by integrating in time the full order model (FOM) defined in Eq. (2.54). In addition, a frequency domain formulation of full order equations is exploited in this work and presented next.

Linearised frequency domain (LFD) formulation provides unsteady results by manipulating the governing equations [41]. In this work, LFD is used to speed-up calculations which are needed to produce reduced order models. Hereafter the derivation is presented for the coupled system and the underlying aerodynamic and/or flight dynamics model is not specified since it does not affect the formulation. Governing equations of the coupled system in Eq. (2.54) are considered. Without affecting the generality, the dependency on control surface deflection $\boldsymbol{u}_c$ is dropped for sake of clarity. As a result, the residual $\boldsymbol{R}$ depends on the solution $\boldsymbol{w}$ and the disturbance $\boldsymbol{u}_d$

$$\frac{\mathrm{d}\boldsymbol{w}}{\mathrm{d}t} = \boldsymbol{R}(\boldsymbol{w}, \boldsymbol{u}_d) \tag{2.55}$$

Define $\boldsymbol{w}(t) = \boldsymbol{w}_0 + \widetilde{\boldsymbol{w}}(t)$ and accordingly $\boldsymbol{u}_d(t) = \boldsymbol{u}_{d0} + \widetilde{\boldsymbol{u}}_d(t)$. The residual $\boldsymbol{R}$ is expanded in a Taylor series truncated at first order around a linearisation point $\boldsymbol{R}(\boldsymbol{w}_0, \boldsymbol{u}_{d0}) \approx 0$

$$\frac{\mathrm{d}\widetilde{\boldsymbol{w}}}{\mathrm{d}t} = \frac{\partial \boldsymbol{R}}{\partial \widetilde{\boldsymbol{w}}}\widetilde{\boldsymbol{w}} + \frac{\partial \boldsymbol{R}}{\partial \boldsymbol{u}_d}\widetilde{\boldsymbol{u}}_d + \mathcal{O}\left(|\widetilde{\boldsymbol{w}}|^2, |\widetilde{\boldsymbol{u}}_d|^2\right) \tag{2.56}$$

Note that all the residual derivatives must be computed at the equilibrium point which is obtained with an iterative trimming procedure split into two steps. First, equilibrium conditions, i.e. sum of forces and moments equal to zero, define the state of the flight dynamics subsystem, i.e. velocity and attitude. Secondly, an aerodynamic steady state solution is computed at the equilibrium point. The matrix $\frac{\partial \boldsymbol{R}}{\partial \widetilde{\boldsymbol{w}}} = A$ is the Jacobian matrix of the coupled system

$$\frac{\mathrm{d}\widetilde{\boldsymbol{w}}}{\mathrm{d}t} = A\,\widetilde{\boldsymbol{w}} + \frac{\partial \boldsymbol{R}}{\partial \boldsymbol{u}_d}\widetilde{\boldsymbol{u}}_d \tag{2.57}$$

The equation resulting from the linearisation is translated into Laplace domain assuming complex harmonic variation for $\widetilde{\boldsymbol{w}} = \widehat{\boldsymbol{w}}e^{\lambda t}$ and $\widetilde{\boldsymbol{u}}_d = \widehat{\boldsymbol{u}}_d e^{\lambda t}$ with $\lambda \in \mathbb{C}$

$$\lambda\widehat{\boldsymbol{w}} = A\,\widehat{\boldsymbol{w}} + \frac{\partial \boldsymbol{R}}{\partial \boldsymbol{u}_d}\widehat{\boldsymbol{u}}_d \tag{2.58}$$

Right-hand and left-hand sides of the equation are simplified by isolating unknowns and external disturbance

$$\left(A - \lambda I\right)\widehat{\boldsymbol{w}} = -\frac{\partial \boldsymbol{R}}{\partial \boldsymbol{u}_d}\widehat{\boldsymbol{u}}_d \tag{2.59}$$

The right-hand side contains partial derivatives of $\boldsymbol{R}$ with respect to the disturbance, specifically $\frac{\partial \boldsymbol{R}}{\partial \boldsymbol{u}_d}$. Although an analytical expression for such term can be formulated, a common method for its evaluation is finite differences. In particular, a central difference scheme can be used for which

$$\frac{\partial \boldsymbol{R}}{\partial \boldsymbol{u}_d} = \frac{\boldsymbol{R}(\boldsymbol{w}_0, \boldsymbol{u}_{d0} + \epsilon) - \boldsymbol{R}(\boldsymbol{w}_0, \boldsymbol{u}_{d0} - \epsilon)}{2\epsilon} \tag{2.60}$$

Once the right-hand side is defined, solving Eq. (2.59) is possible by using iterative linear solvers [123, 156] for large, sparse systems or direct methods for small ones. The result is the complex-valued solution vector $\widehat{\boldsymbol{w}}$.

The assumption of linear behaviour around the equilibrium point allows the superposition of results. This is particularly useful when non-harmonic phenomena, like '1-cos' gusts, must be investigated. In such cases, the disturbance $\widetilde{\boldsymbol{u}}_d$ is expanded in a Fourier series

$$\widetilde{\boldsymbol{u}}_d(t) \approx \widetilde{\boldsymbol{u}}_N(t) = \sum_{n=-N}^{N} \widehat{\boldsymbol{u}}_{d_n} e^{i\frac{2\pi n}{P}t} + \varepsilon \tag{2.61}$$

with P defining its period, N the number of harmonics considered and ε the error. The final result is then obtained by superposing a solution of Eq. (2.59) for each harmonic. The number N of harmonics should be chosen to minimise the difference between the original signal $\widetilde{\boldsymbol{u}}_d(t)$ and the approximated one $\widetilde{\boldsymbol{u}}_N(t)$. The process of expanding a '1-cos' gust disturbance in a Fourier series is depicted in Fig. 2.3 with an increasing number of harmonics. Using $N = 1$, the '1-cos' is approximated with

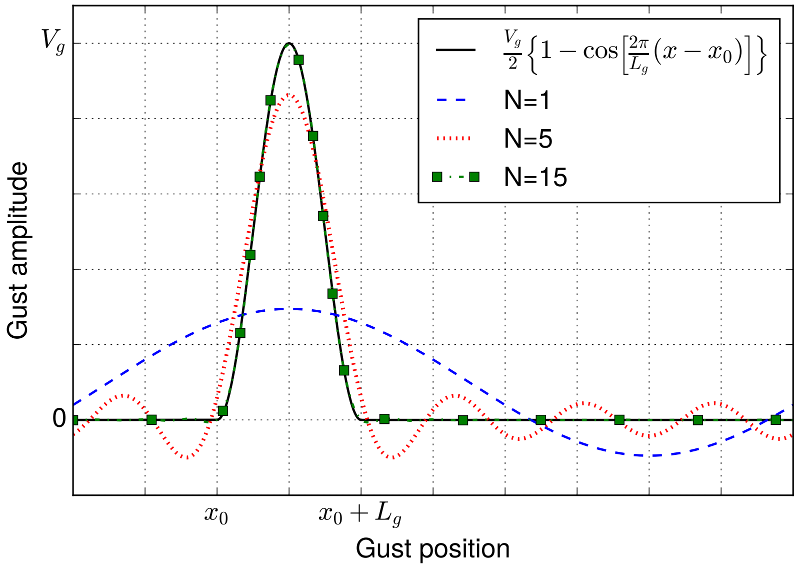

Figure 2.3: Fourier decomposition of a '1-cos' gust with an increasing number of harmonics.

one simple harmonic disturbance. This is not sufficient for a proper reconstruction of the original '1-cos' curve. Increasing N to $N = 5$ brings the curve closer to the original one. Some differences and wobbling are still present. However, when a number $N = 15$ of harmonics is used, the reconstructed curve is undistinguishable from the reference. In addition, choosing a value N in Eq. (2.61) for a given '1-cos' gust defines the frequencies for which Eq. (2.59) must be solved.

When the focus is on the aerodynamic response only, the non-linear residual $\boldsymbol{R}_f$ in Eq. (2.53) is considered. Although the derivation is similar to the one for the coupled system, focus is here on the aerodynamic subsystem only. The resulting LFD formulation is very useful when computing the aerodynamic response to variation in the flight dynamics degrees-of-freedom. Equation (2.53) is expanded in Taylor series truncated at the first order around an equilibrium point $\boldsymbol{R}_f(\boldsymbol{w}_{f_0}, \boldsymbol{w}_{r_0}, \boldsymbol{u}_{d0}) \approx 0$,

$$\frac{\mathrm{d}\widetilde{\boldsymbol{w}}_f}{\mathrm{d}t} = \frac{\partial \boldsymbol{R}_f}{\partial \widetilde{\boldsymbol{w}}_f}\,\widetilde{\boldsymbol{w}}_f + \frac{\partial \boldsymbol{R}_f}{\partial \widetilde{\boldsymbol{w}}_r}\,\widetilde{\boldsymbol{w}}_r + \frac{\partial \boldsymbol{R}_f}{\partial \widetilde{\boldsymbol{u}}_d}\,\widetilde{\boldsymbol{u}}_d + \mathcal{O}\left(|\widetilde{\boldsymbol{w}}_f|^2, |\widetilde{\boldsymbol{w}}_r|^2, |\widetilde{\boldsymbol{u}}_d|^2\right) \tag{2.62}$$

with $\boldsymbol{w}_f(t) = \boldsymbol{w}_{f_0} + \widetilde{\boldsymbol{w}}_f(t)$, $\boldsymbol{w}_r(t) = \boldsymbol{w}_{r_0} + \widetilde{\boldsymbol{w}}_r(t)$ and $\boldsymbol{u}_d(t) = \boldsymbol{u}_{d_0} + \widetilde{\boldsymbol{u}}_d(t)$. The equation is translated into Laplace domain assuming $\widetilde{\boldsymbol{w}}_f = \widehat{\boldsymbol{w}}_f e^{\lambda t}$, $\widetilde{\boldsymbol{w}}_r = \widehat{\boldsymbol{w}}_r e^{\lambda t}$, $\widetilde{\boldsymbol{u}}_d = \widehat{\boldsymbol{u}}_d e^{\lambda t}$,

$$\left(\frac{\partial \boldsymbol{R}_f}{\partial \boldsymbol{w}_f} - \lambda I\right)\widehat{\boldsymbol{w}}_f = -\frac{\partial \boldsymbol{R}_f}{\partial \boldsymbol{w}_r}\widehat{\boldsymbol{w}}_r - \frac{\partial \boldsymbol{R}_f}{\partial \boldsymbol{u}_d}\widehat{\boldsymbol{u}}_d \tag{2.63}$$

and fluid dynamics unknowns are isolated. This equation can be exploited in two ways. A first application is the computation of dynamic derivatives by assuming $\boldsymbol{u}_d = 0$

$$\left(\frac{\partial \boldsymbol{R}_f}{\partial \boldsymbol{w}_f} - \lambda I\right)\widehat{\boldsymbol{w}}_f = -\frac{\partial \boldsymbol{R}_f}{\partial \boldsymbol{w}_r}\widehat{\boldsymbol{w}}_r \tag{2.64}$$

Such equation is particularly useful to compute aerodynamic responses $\widehat{\boldsymbol{w}}_f$ to complex harmonic excitations in the flight dynamics degrees-of-freedom $\widehat{\boldsymbol{w}}_r$. Further details about their computation and comparisons with time-domain results are provided in the next Chapter 3. A second application of Eq. (2.63) is obtained when $\boldsymbol{w}_r = 0$. This corresponds to calculating aerodynamic responses to aerodynamic disturbances such as gusts

$$\left(\frac{\partial \boldsymbol{R}_f}{\partial \boldsymbol{w}_f} - \lambda I\right) \widehat{\boldsymbol{w}}_f = -\frac{\partial \boldsymbol{R}_f}{\partial \boldsymbol{u}_d} \widehat{\boldsymbol{u}}_d \tag{2.65}$$

In particular, when Eq. (2.65) is solved for a specific frequency and imposing no damping, the complex-valued flow solution $\widehat{\boldsymbol{w}}_f$ is the flow response to a sinusoidal gust. Investigation for a static, not moving, aircraft during a '1-cos' gust encounter can be performed expanding the disturbance in a Fourier series, similarly to the process described for the coupled system.

2.4 Numerical Methods

Numerical integration in time of the coupled model is performed for flight dynamics with Eq. (2.50) and for fluid equations with Eq. (2.53) in a strongly-coupled loop using dual time-stepping [79]. Data is exchanged between the two subsystems at each inner iteration and solution updated.

Focusing first on flight dynamics equations, their integration is usually achieved by means of two well-known numerical schemes, specifically the backward finite difference scheme and the β-Newmark method [104]. The former is based on approximating the time-domain derivative in Eq. (2.50) with a second order finite difference scheme,

$$\frac{\mathrm{d}\boldsymbol{w}_r^{(i)}}{\mathrm{d}t} = \frac{1}{\Delta t}\left(\frac{3}{2}\boldsymbol{w}_r^{(i)} - 2\boldsymbol{w}_r^{(i-1)} + \frac{1}{2}\boldsymbol{w}_r^{(i-2)}\right) \tag{2.66}$$

where Δt is the time step and the superscripts (i), $(i-1)$ and $(i-2)$ represent the current and previous two time steps, respectively. Substituting Eq. (2.66) into Eq. (2.50) provides an update to $\boldsymbol{w}_r^{(i)}$,

$$\boldsymbol{w}_r^{(i)} = \frac{2\Delta t \boldsymbol{R}_r^{(i)} + 4\boldsymbol{w}_r^{(i-1)} - \boldsymbol{w}_r^{(i-2)}}{3} \tag{2.67}$$

This is performed when integrating flight dynamics with Eq. (2.38). Regarding the β-Newmark scheme, it is widely adopted by the structural community to integrate modal equations. Applying the scheme to Eq. (2.46) with $\beta = 1/4$ and $\gamma = 1/2$, an update of the generalised coordinates and their time derivatives is

$$\boldsymbol{\eta}^{(i)} = \boldsymbol{\eta}^{(i-1)} + \Delta t \frac{\mathrm{d}\boldsymbol{\eta}}{\mathrm{d}t}^{(i-1)} + \frac{\Delta t^2}{2} M^{-1} \boldsymbol{F} \tag{2.68}$$

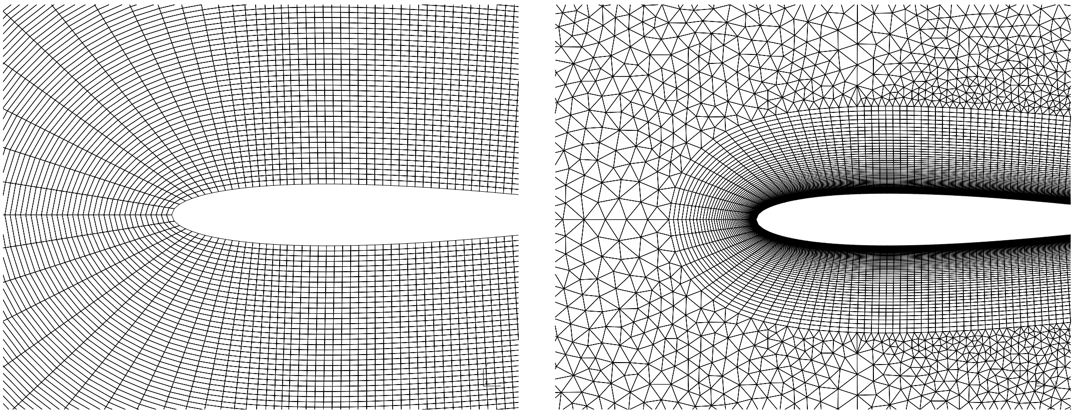

(a) Example of body-fitted, structured grid (b) Example of hybrid grid

Figure 2.4: Example of structured and hybrid grid.

$$\frac{\mathrm{d}\boldsymbol{\eta}^{(i)}}{\mathrm{d}t} = \frac{\boldsymbol{\eta}^{(i)} - \boldsymbol{\eta}^{(i-1)}}{\Delta t} - \frac{\mathrm{d}\boldsymbol{\eta}^{(i-1)}}{\mathrm{d}t} \tag{2.69}$$

Focusing on the aerodynamics subsystem, a solution is obtained following a two-steps procedure [23]. First, a number of grid points is placed in the physical space with a body-fitted approach so that the point distribution follows the body shape. Two kinds of computational grids (also known as meshes) can be obtained from the points distribution and they are called structured and unstructured grids, respectively. Regarding the former, lines connecting grid points form quadrilaterals for two-dimensional structured grids as shown in Fig. 2.4(a). The regular structure leads to very fast computations, simpler programming algorithms and a well-banded Jacobian matrix. However, structured grids require long time to be produced because human involvement is often needed [23]. Conversely, unstructured grids have lines forming triangles as well as quadrilaterals for two-dimensional geometries and they can be automatically generated. However, particular care must still be paid to geometric elements closer to solid wall in order to get good quality flow solutions in the boundary layer [23]. A trade-off is provided by hybrid approaches where the region close to the body wall is structured and the remaining domain is unstructured, as shown in Fig. 2.4(b) for a two-dimensional test case. Hybrid grids are used in this work for all test cases.

Once the spatial discretisation is ready, the calculation is performed with a numerical method. The most popular ones are finite difference [114], finite element [145] and finite volume [98]. The latter one is the most popular method of the three and it is adopted in this work for three-dimensional test cases. Physical space is discretised in polyhedral volumes and the conservation laws are solved in an integral form. In addition, some advanced techniques which are referred to as meshless [13] are adopted in this work for two-dimensional test cases. They do not require the grid points to be connected by lines and are based on point clouds to solve the differential form of governing equations. Thus, volumes are not calculated explicitly. Meshless methods are very promising for complex geometries since the number of points around a sensitive target such as spoilers or gaps can be increased arbitrarily. However the main drawback is the conservation of mass, momentum and energy which is not guaranteed because of lack of the telescopic property [85].

2.4.1 Radial Basis Function Interpolation for Grid Deformation

Grid deformation is used in this work to couple aerodynamics and flight dynamics. In particular, the rigid body motions calculated by the flight dynamics module are transferred to the CFD solver by means of grid deformation. This is performed with radial basis function (RBF) interpolation [47, 100]. Note that exact values of displacement are available for boundary points (i.e. points on body surfaces and far field) since they are computed as a combination of rigid-body motions by the flight dynamics solver. Interpolation affects points in the flow domain only. The displacement $S(\boldsymbol{x})$ of points in the flow domain is related to the position $\boldsymbol{x}_b$ of the boundary points,

$$S(\boldsymbol{x}) = p(\boldsymbol{x}) + \sum_{j=1}^{n_b} \alpha_j \phi\left(||\boldsymbol{x} - \boldsymbol{x}_{b_j}||\right) \tag{2.70}$$

where n_b is the number of boundary points, $\phi(||\boldsymbol{x} - \boldsymbol{x}_{b_j}||)$ the radial basis function used as interpolator and $p(\boldsymbol{x}) = \boldsymbol{\beta} \cdot \boldsymbol{x}$ a polynomial accounting for rigid-body motions. The coefficient vectors $\boldsymbol{\alpha}$ and $\boldsymbol{\beta}$ are unknown and they must be calculated. The interpolating functions are chosen among various formulations given in the literature. They are divided in two categories, specifically global and compact support. The deformation is applied to all the grid points when a function with global support is used and a summary of global radial basis functions is given in Table 2.1. Conversely, functions with compact support are applied to a certain area only and involve fewer points [47].

The calculation of the interpolating coefficients is based on two conditions. The first is that the displacement at boundary points is exactly $\boldsymbol{d}_b$,

$$S(\boldsymbol{x}_b) = \boldsymbol{d}_b \tag{2.71}$$

In addition, all the polynomials q with degree less than p should meet the following requirement [47]:

$$\sum_{j=1}^{n_b} \alpha_j q\left(x_{b_j}\right) = 0 \tag{2.72}$$

Limiting the derivation to two-dimensional problems with no loss of generality, we can derive the RBF equation for two degrees-of-freedom x and y. The polynomial p can be chosen as $p(x, y) = \beta_1 + \beta_2 x + \beta_3 y$ to take into account rigid motions in

Table 2.1: Most common types of radial basis functions.

Function ϕ	**Name**
$e^{-\rho^2}$	Gaussian
$\sqrt{1+\rho^2}$	Multiquadratic
$\frac{1}{1+\rho^2}$	Inverse quadratic
$\rho^k \log(\rho) \quad k \in \mathbb{N}^+$	Polyharmonic spline
$\rho^2 \log(\rho)$	Thin plate spline

The distance ρ is usually the Euclidean norm $\rho = ||\boldsymbol{x}_A - \boldsymbol{x}_B||$ between vectors $\boldsymbol{x}_A$ and $\boldsymbol{x}_B$.

the x and y direction and in-plane rotations. Numbering the boundary points from 0 to n_b, the system in Eq. (2.73) gives the values of $\boldsymbol{\alpha}$ and $\boldsymbol{\beta}$

$$\begin{bmatrix} d_{b_1} \\ \vdots \\ d_{b_{n_b}} \\ 0 \\ 0 \\ 0 \end{bmatrix} = \begin{bmatrix} & & & 1 & x_{b_1} & y_{b_1} \\ & M_b & & 1 & \vdots & \vdots \\ & & & 1 & x_{b_{n_b}} & y_{b_{n_b}} \\ 1 & 1 & 1 & 0 & 0 & 0 \\ x_{b_1} & \dots & x_{b_{n_b}} & 0 & 0 & 0 \\ y_{b_1} & \dots & y_{b_{n_b}} & 0 & 0 & 0 \end{bmatrix} \begin{bmatrix} \alpha_i \\ \vdots \\ \alpha_{n_b} \\ \beta_1 \\ \beta_2 \\ \beta_3 \end{bmatrix} \tag{2.73}$$

The submatrix M_b is calculated applying the radial basis function to each pair of boundary points as follow

$$M_b = \begin{bmatrix} \phi(0) & \phi(\rho_{1,2}) & \dots & \phi(\rho_{1,n_b}) \\ \phi(\rho_{2,1}) & \phi(0) & \dots & \phi(\rho_{2,n_b}) \\ \vdots & \vdots & \phi(0) & \vdots \\ \phi(\rho_{n_b,1}) & \phi(\rho_{n_b,2}) & \dots & \phi(0) \end{bmatrix} \tag{2.74}$$

with $\rho_{i,j} = \sqrt{(x_{b_i} - x_{b_j})^2 + (y_{b_i} - y_{b_j})^2}$. The thin plate spline radial basis function $\phi(\rho) = \rho^2 \log \rho$ is a good trade-off between high-accuracy and computational cost [47]. It was chosen to perform grid deformation in this work and its application to a 10 degrees flap deflection is shown in Fig. 2.5. Note that the deformation at boundary points is exact, while locations of all other points are proportionally modified.

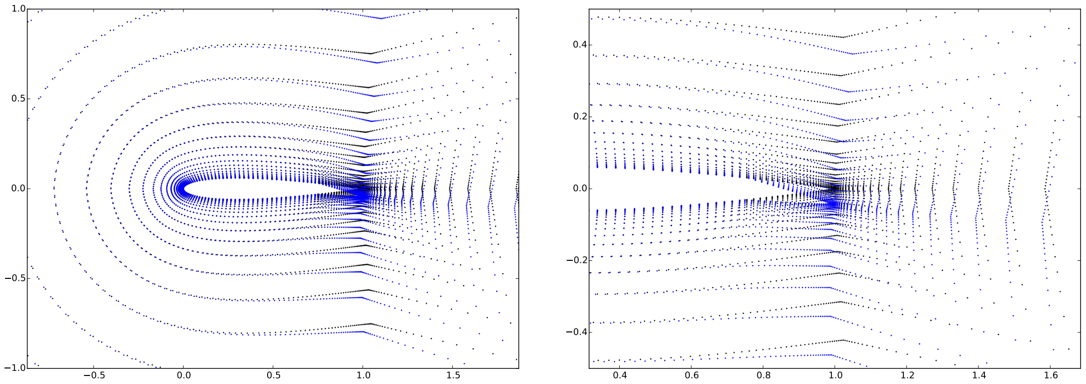

(a) Aerofoil

(b) Trailing edge

Figure 2.5: Grid deformation using RBF interpolation for aerofoil with a $\delta = 10$ deg flap deflection.

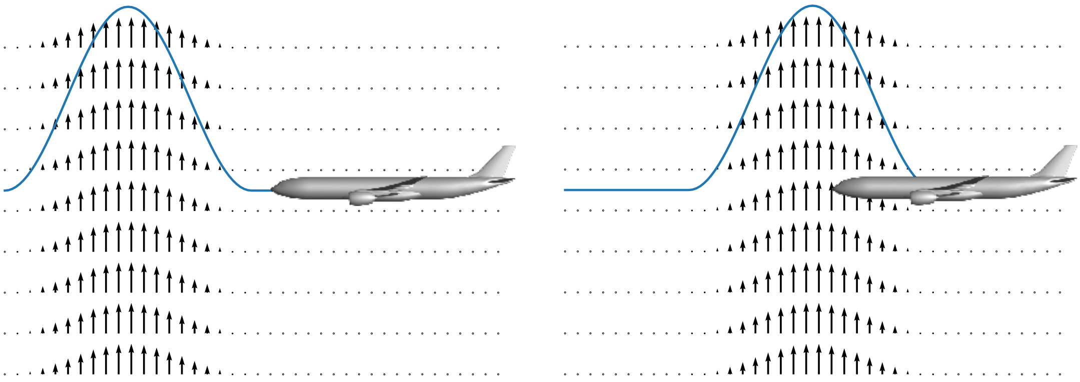

(a) Beginning of simulation

(b) Updated gust position

Figure 2.6: Disturbance velocity method for gust simulations.

2.4.2 Disturbance Velocity Method for Gusts

Gusts are assumed to be disturbances in the flow velocity only and they are modelled with disturbance velocity method [73]. It relies on the existing space discretisation to alter the velocity of grid points according to the gust shape. Hence, gust velocity is mathematically treated like grid velocity and an additional term is added to unsteady residual calculation for the disturbance. In practice, this is achieved by altering the velocity $\boldsymbol{U}$ in Eqs. (2.7-2.9) for every grid point according to the gust shape. The process is illustrated in Fig. 2.6 with a simple two-dimensional schema representing CFD grid points, prescribed gust shape and grid point velocities. At the beginning of the simulation, grid point velocities are altered upwind the aircraft as shown in Fig. 2.6(a). They depend on the gust location as defined by certification regulations for longitudinal gusts [57]. Specifically, only points which are located inside the gust length are altered for a '1-cos' shape. Since no dependence on the points' vertical positions is specified by regulation, velocities are altered between the top and bottom domain boundaries. This is represented in Fig. 2.6(a) because the disturbance is propagated vertically everywhere in the region which falls between the gust's horizontal beginning and end. When the simulation advances in time, the region to alter is updated as well by assuming that disturbances travel with free-stream velocity. This simulates a travelling gust which depends on time as well as spatial coordinates. When the gust hits the body surface, the disturbance is applied to the surface grid points as well. This situation is represented in Fig. 2.6(b) where the aircraft is depicted surrounded by the disturbance. Although its most common applications are longitudinal gusts, the disturbance velocity method has been adopted to simulate lateral gusts as well [73]. In such cases, the alteration concerns the lateral velocity and it depends on the lateral coordinate while the disturbance is propagated everywhere in the horizontal and longitudinal directions.

When the system's gust response is concerned, the disturbance velocity method provides the right-hand side of LFD computations. Focus is on aerodynamics only since the residual $\boldsymbol{R}_f$ in Eq. (2.65) becomes a function of grid point velocities,

$$\boldsymbol{R}_f = \boldsymbol{R}_f(\boldsymbol{w}_f, \boldsymbol{w}_r, \dot{\boldsymbol{x}}) \tag{2.75}$$

where $\dot{\boldsymbol{x}}$ is the vector of grid point velocities and $\boldsymbol{x}$ the corresponding point locations. Thus, the right-hand side in Eq. (2.65) is formulated with the complex-value variable λ and the LFD equation becomes

$$\left(\frac{\partial \boldsymbol{R}_f}{\partial \boldsymbol{w}_f} - \lambda I\right) \widehat{\boldsymbol{w}}_f = -\lambda \frac{\partial \boldsymbol{R}_f}{\partial \dot{\boldsymbol{x}}} \widehat{\boldsymbol{x}} \tag{2.76}$$

with $\boldsymbol{x} = \widehat{\boldsymbol{x}} e^{\lambda t}$. The partial derivative $\frac{\partial \boldsymbol{R}_f}{\partial \dot{\boldsymbol{x}}}$ is calculated with finite differences by altering grid point velocities,

$$\frac{\partial \boldsymbol{R}_f}{\partial \dot{\boldsymbol{x}}} = \frac{\boldsymbol{R}_f(\boldsymbol{w}_{f_0}, \boldsymbol{w}_{r_0}, \dot{\boldsymbol{x}}_0 + \epsilon) - \boldsymbol{R}_f(\boldsymbol{w}_{f_0}, \boldsymbol{w}_{r_0}, \dot{\boldsymbol{x}}_0 - \epsilon)}{2\epsilon} \tag{2.77}$$

Note that the flight dynamics subsystem is not affected by gusts directly and its residual does not depend on grid velocities, $\frac{\partial \boldsymbol{R}_r}{\partial \dot{\boldsymbol{x}}} = 0$. Thus, if the partial derivative of the coupled residual $\frac{\partial \boldsymbol{R}}{\partial \dot{\boldsymbol{x}}}$ is needed, for example to solve Eq. (2.59), it can be obtained by padding the partial derivative of the aerodynamic one with the appropriate number of zeros, $\frac{\partial \boldsymbol{R}}{\partial \dot{\boldsymbol{x}}} = \left[\frac{\partial \boldsymbol{R}_f}{\partial \dot{\boldsymbol{x}}}, 0\right]^T$. The disturbance velocity method has proved to be effective when compared to a resolved gust approach for both fluid-only [73] and multidisciplinary simulations [140]. Influence of the body on gust disturbances is neglected and this assumption has proved to be valid for all the gust lengths required by certification [140].

2.4.3 Computational Fluid Dynamics Software

Two CFD solvers are used throughout this work. The first is an in-house code and it uses a meshless scheme to solve Euler, laminar and Reynolds-averaged Navier–Stokes equations (with the Spalart–Allmaras turbulence model) [85, 86]. The computational domain is populated with a cloud of points and a preprocessor is in charge of identifying a number of so-called star points, i.e. points where fluid unknowns are stored. A stencil of neighbouring points is build for each star point in order to perform spatial discretisation. Osher's approximate Riemann solver is used to evaluate the convective fluxes between each point and the points in its stencil. The gradients of the flow variables are reconstructed with the least squares method and used to provide a higher order reconstruction of the interface values for the Riemann problem. A fully implicit scheme is applied using local time stepping for steady-state convergence acceleration, while the unsteady, time-dependent equations are solved with a dual-time integration scheme. The LFD formulation in the in-house CFD code has previously been verified for the aerodynamic subsystem in [17, 139]. It is based on a first-discretise-then-linearise, matrix-forming approach with an analytical, hand-differentiated Jacobian matrix. The iterative solver used for linear systems resulting from both the fully-implicit scheme and to perform LFD computations is the generalised minimal residual solver (GMRES) with complex arithmetic [123]. Preconditioning uses block incomplete lower-upper factorisation. Gusts are introduced with the disturbance velocity method [73].

The second CFD solver is DLR-TAU from the German Aerospace Centre (DLR). It is based on the finite volume method and it is widely used in the European aerospace sector. Validation of the code is available in the literature for steady [125, 133] and unsteady cases [103, 133]. RANS equations in conjunction with the Spalart-Allmaras turbulence model [132] are solved. Inviscid fluxes are discretised applying a central scheme with scalar artificial dissipation of Jameson, Schmidt and Turkel [80]. Exact gradients used for viscous and source terms are computed using the Green-Gauss approach. Steady-state solutions are obtained using backward Euler method with lower-upper Symmetric-Gauss-Seidel iterations [56] and local time-stepping. Convergence is accelerated by applying a geometric multigrid scheme. Unsteady simulations are performed with a dual-stepping method combined with a second order backward Euler scheme. Regarding LFD, the Jacobian matrix is hand-differentiated and a generalised conjugate residual solver with deflated restarting is used to solve arising linear systems [156]. Preconditioning is provided with a block incomplete lower-upper factorisation of the Jacobian matrix with zero level of fill-in applied. Similar to the in-house code, gusts are introduced with the disturbance velocity method.

Chapter 3

Reduced Order Modelling

The model reduction technique is described in this chapter. Starting from the full order equations, a smaller model is obtained which contains all the information needed to reconstruct the behaviour of the full order model at a fraction of the original computational cost. The reduction is performed by projecting the Jacobian matrix of the coupled system onto a small modal basis. Regarding the reduced model construction, modes to populate the basis are calculated with either one of two techniques, specifically operator-based and data-based mode identification.

Operator-based identification is based on eigenmode decomposition of the Jacobian matrix. Eigenvectors related to flight dynamics are extracted from the system without computing the whole set of eigensolutions. The procedure is performed for both adjoint and direct eigenproblems. The second data-based approach relies on the snapshot method. The coupled system is sampled at discrete frequencies and a snapshot matrix is assembled with the results. Proper orthogonal decomposition (POD) is applied to the matrix and modes representing the system's response are obtained.

3.1 Model Reduction with Matrix Projection

The system in Eq. (2.54) is expanded in a first order Taylor series around an equilibrium state with $\boldsymbol{R}(\boldsymbol{w}_0, \boldsymbol{u}_{d0}, \boldsymbol{u}_{c0}) \approx 0$,

$$\frac{\mathtt{d}\boldsymbol{w}}{\mathtt{d}t} = \boldsymbol{R}(\boldsymbol{w}, \boldsymbol{u}_d, \boldsymbol{u}_c) = A\,\widetilde{\boldsymbol{w}} + \frac{\partial \boldsymbol{R}}{\partial \boldsymbol{u}_d}\widetilde{\boldsymbol{u}}_d + \frac{\partial \boldsymbol{R}}{\partial \boldsymbol{u}_c}\widetilde{\boldsymbol{u}}_c + \mathcal{O}\left(|\widetilde{\boldsymbol{w}}|^2, |\widetilde{\boldsymbol{u}}_d|^2, |\widetilde{\boldsymbol{u}}_c|^2\right) \tag{3.1}$$

where $\boldsymbol{w}(t) = \boldsymbol{w}_0 + \widetilde{\boldsymbol{w}}(t)$ and accordingly $\boldsymbol{u}_d(t) = \boldsymbol{u}_{d0} + \widetilde{\boldsymbol{u}}_d(t)$ and $\boldsymbol{u}_c(t) = \boldsymbol{u}_{c0} + \widetilde{\boldsymbol{u}}_c(t)$. The matrix $\frac{\partial \boldsymbol{R}}{\partial \boldsymbol{u}_d}$ is referred to as gust matrix and the product $\frac{\partial \boldsymbol{R}}{\partial \boldsymbol{u}_d}\widetilde{\boldsymbol{u}}_d$ is used to introduce gusts modelled with the disturbance velocity approach as described in Section 2.4.2. In particular, the vector $\widetilde{\boldsymbol{u}}_d$ depends on the gust shape to be simulated since it represents the phase lag between points due to the excitation. The flight dynamics residual does not directly depend on the gust disturbance and $\frac{\partial \boldsymbol{R}}{\partial \boldsymbol{u}_d}$ is padded with zeros accordingly.

Similarly, the term $\frac{\partial \boldsymbol{R}}{\partial \boldsymbol{u}_c}$ is calculated with finite differences and it models the effect of control surface deflections on the aerodynamic residual.

The Jacobian matrix A of dimension $n \times n$, with $n = n_f + n_r$, is partitioned into blocks

$$A = \begin{pmatrix} A_{ff} & A_{fr} \\ A_{rf} & A_{rr} \end{pmatrix} \tag{3.2}$$

with

$$\begin{aligned} A_{ff} = &\ \frac{\partial \boldsymbol{R}_f}{\partial \boldsymbol{w}_f}, \quad & A_{fr} = &\ \frac{\partial \boldsymbol{R}_f}{\partial \boldsymbol{w}_r} \\ A_{rf} = &\ C\frac{\partial \boldsymbol{f}_a}{\partial \boldsymbol{w}_f}, \quad & A_{rr} = &\ \frac{\partial \boldsymbol{f}_e}{\partial \boldsymbol{w}_r} + C\frac{\partial \boldsymbol{f}_a}{\partial \boldsymbol{o}}\frac{\partial \boldsymbol{o}}{\partial \boldsymbol{w}_r} \end{aligned} \tag{3.3}$$

The diagonal blocks A_{ff} and A_{rr} are fluid and flight dynamics Jacobian matrices, respectively, whereas the off-diagonal blocks describe the coupling terms. Specifically, the matrix A_{rf} describes the dependence of the integrated aerodynamic forces on the fluid unknowns and A_{fr} represents fluid excitation due to the flight dynamics degrees-of-freedom. The term $\frac{\partial \boldsymbol{f}_a}{\partial \boldsymbol{o}}$ relates a change of aerodynamic forces to a rotation of surface normals $\boldsymbol{o}$ while keeping the flow variables fixed. The overall term $C\frac{\partial \boldsymbol{f}_a}{\partial \boldsymbol{o}}\frac{\partial \boldsymbol{o}}{\partial \boldsymbol{w}_r}$ is neglected in the current investigation since it is small in comparison to $\frac{\partial \boldsymbol{f}_e}{\partial \boldsymbol{w}_r}$ which contains structural mass and moment of inertia [9]. Both aerodynamic and structural blocks, specifically A_{ff} and A_{rr}, are square and the former is the largest one since $n_f \ggg n_r$. The off-diagonal blocks A_{fr} and A_{rf} are rectangular with shape $n_f \times n_r$ and $n_r \times n_f$, respectively. Note that the size in terms of state variables of the aerodynamic subsystem is $\mathcal{O}(n_f) \geqslant 10^7$ when using CFD while the size of the flight dynamics one is much smaller, $\mathcal{O}(n_r) = 10$.

The model reduction is obtained by projecting the Taylor series in Eq. (3.1) onto a smaller modal basis [39]. Specifically, right and left bases are used and they are named Φ and Ψ, respectively. They are built by choosing m appropriate modes,

$$\begin{aligned} \text{right: } \Phi &= \begin{pmatrix} \boldsymbol{\phi}^{(1)}, & \boldsymbol{\phi}^{(2)}, & \dots, & \boldsymbol{\phi}^{(m)} \end{pmatrix} \\ \text{left: } \Psi &= \begin{pmatrix} \boldsymbol{\psi}^{(1)}, & \boldsymbol{\psi}^{(2)}, & \dots, & \boldsymbol{\psi}^{(m)} \end{pmatrix} \end{aligned} \tag{3.4}$$

scaled to satisfy the conditions

$$\langle \boldsymbol{\phi}^{(j)}, \boldsymbol{\phi}^{(j)} \rangle = 1 \qquad \text{and} \qquad \langle \boldsymbol{\psi}^{(j)}, \boldsymbol{\phi}^{(j)} \rangle = 1 \qquad \forall j \in [1, m] \tag{3.5}$$

where the Hermitian inner product $\langle \boldsymbol{x}, \boldsymbol{y} \rangle$ is defined as $\boldsymbol{x}^H \boldsymbol{y}$. The projection is performed with the transformation of variable

$$\widetilde{\boldsymbol{w}} = \Phi \boldsymbol{z}, \qquad \boldsymbol{z} \in \mathbb{C}^m \tag{3.6}$$

and pre-multiplying with the left modal basis Ψ. Thus, the vector $\boldsymbol{z}$ contains the reduced order unknowns. Including complex conjugate pairs in the modal basis in Eq. (3.4) gives a real-valued vector $\widetilde{\boldsymbol{w}}$ in Eq. (3.6). This simplifies reconstructing physical quantities from the reduced model while doubling its negligible computational cost. The reduced order model (ROM) is then expressed as

$$\Psi^H \Phi \frac{\mathrm{d}\boldsymbol{z}}{\mathrm{d}t} = \Psi^H A \Phi\, \boldsymbol{z} + \Psi^H \frac{\partial \boldsymbol{R}}{\partial \boldsymbol{u}_d}\, \widetilde{\boldsymbol{u}}_d + \Psi^H \frac{\partial \boldsymbol{R}}{\partial \boldsymbol{u}_c}\, \widetilde{\boldsymbol{u}}_c \tag{3.7}$$

and integrated in time to obtain time-domain response $\boldsymbol{z}(t)$. Initial conditions for the integration are computed inverting the transformation in Eq. (3.6) with

$$\boldsymbol{z} = \left(\Psi^H \Phi\right)^{-1} \Psi^H \widetilde{\boldsymbol{w}} \tag{3.8}$$

Note that if bi-orthogonal bases are used for which $\Psi^H \Phi = I$, Eqs. (3.7) and (3.8) can be simplified. That is the case, for example, when direct and adjoint eigenvectors of A populate the right and left modal bases, respectively. However, the assumption of $\Psi^H \Phi = I$ does not apply in general and here a more general formulation is described. Assuming complex harmonic excitation $\widetilde{\boldsymbol{u}}_d = \hat{\boldsymbol{u}}_d e^{\lambda t}$ and $\widetilde{\boldsymbol{u}}_c = \hat{\boldsymbol{u}}_c e^{\lambda t}$ and complex harmonic response $\boldsymbol{z}(t) = \hat{\boldsymbol{z}} e^{\lambda t}$ with $\lambda \in \mathbb{C}$, Eq. (3.7) can also be rewritten in frequency domain,

$$\Psi^H \left(A - \lambda I\right) \Phi \hat{\boldsymbol{z}} = -\Psi^H \frac{\partial \boldsymbol{R}}{\partial \boldsymbol{u}_d}\, \hat{\boldsymbol{u}}_d - \Psi^H \frac{\partial \boldsymbol{R}}{\partial \boldsymbol{u}_c}\, \hat{\boldsymbol{u}}_c \tag{3.9}$$

Exploiting Eq. (3.9) is more convenient for responses to sinusoidal external excitations since it provides a reduced form of Eq. (2.59) directly in frequency domain. Equation (3.7) is adopted for time-domain integration of the ROM. However, results can be translated a posteriori in either time or frequency domain since both equations lead to the same mathematical solution.

The modal bases in Eq. (3.4) must be built from modes representing the dominating system behaviour. Two procedures, named operator-based and data-based modal identification, are proposed in the following to calculate these modes.

3.2 Operator-based Modal Identification

This section describes the first of two identification methods which are employed in this work. The modes provided for the reduction are the ones traditionally considered in the field of flight dynamics, i.e. short period and phugoid in the longitudinal plane for example [34, 155]. They are computed by following the evolution of rigid-body modes when aerodynamics is gradually added to the system. The identification is composed of three steps. First, the flight dynamics subsystem is not coupled with the aerodynamic one. The eigenpairs of the flight dynamics set of equations, which now correspond to in-vacuum rigid-body modes, are easily computed with direct methods. Secondly, the coupling with the aerodynamic subsystem is introduced with a mathematical parameter β which ranges from 0 (uncoupled subsystems) to 1 (fully coupled system). Thirdly, the interval $[0, 1]$ is split into a number of intermediate values and for each one, in turn, a tracing procedure is started from the converged solution at the previous value of β. The tracing is needed because both eigenvalue and eigenvector change when the coupling between flight dynamics and aerodynamic is introduced for $\beta > 0$. The mathematical details are provided thereafter for the identification as well as the tracing procedure which is based on Newton's method.

The system in Eq. (2.54) is expanded by means of Eq. (3.1) and translated into Laplace domain with complex-valued variable $\lambda \in \mathbb{C}$ by assuming $\widetilde{\boldsymbol{w}} = \widehat{\boldsymbol{w}} e^{\lambda t}$.

$$\lambda \widehat{\boldsymbol{w}} = A \widehat{\boldsymbol{w}} \tag{3.10}$$

The external forcing terms are $\boldsymbol{u}_d = \boldsymbol{u}_c = \boldsymbol{0}$ for operator-based identification. Solving Eq. (3.10) leads to the direct and adjoint eigenvalue problems for which the solution vector $\boldsymbol{w}$ is named $\boldsymbol{\phi}^{(j)}$ and $\boldsymbol{\psi}^{(j)}$, respectively

$$\left(A - \lambda^{(j)} I\right) \boldsymbol{\phi}^{(j)} = 0 \qquad \text{and} \qquad \left(A^T - \lambda^{(j)} I\right) \bar{\boldsymbol{\psi}}^{(j)} = 0 \qquad \forall j \in [1, m] \tag{3.11}$$

where $(\lambda^{(j)}, \boldsymbol{\phi}^{(j)})$ and $(\lambda^{(j)}, \boldsymbol{\psi}^{(j)})$ are the corresponding eigenpairs. A subset of m direct and adjoint eigenvectors related to flight dynamics degrees-of-freedom is included in the modal bases for the model reduction. Notice that in this case the conditions in Eq. (3.5) are satisfied due to the bi-orthogonality of eigenvectors,

$$\langle \boldsymbol{\psi}^{(j)}, \boldsymbol{\phi}^{(k)} \rangle = \delta_{jk} \qquad \text{and} \qquad \langle \boldsymbol{\psi}^{(j)}, \bar{\boldsymbol{\phi}}^{(k)} \rangle = 0 \qquad \forall j, k \in [1, m] \tag{3.12}$$

where δ_{jk} is the Kronecker delta. Thus, the projection in Eq. (3.7) is a Petrov-Galerkin one with test base Ψ.

Focusing on the direct problem first, two equations in Laplace domain are obtained by applying the partitioning in Eq. (3.3),

$$\left(A_{ff} - \lambda^{(j)} I\right) \boldsymbol{\phi}_f^{(j)} = -A_{fr} \boldsymbol{\phi}_r^{(j)} \tag{3.13}$$

$$\left(A_{rr} - \lambda^{(j)} I\right) \boldsymbol{\phi}_r^{(j)} = -A_{rf} \boldsymbol{\phi}_f^{(j)} \tag{3.14}$$

A small non-linear eigenvalue problem of dimension n_r is formulated by isolating the flight dynamics part of the direct eigenproblem,

$$\begin{aligned} \left[\left(A_{rr} - \lambda^{(j)} I\right) - \beta A_{rf} \left(A_{ff} - \lambda^{(j)} I\right)^{-1} A_{fr} \right] \boldsymbol{\phi}_r^{(j)} &= \\ S\left(\lambda^{(j)}\right) \boldsymbol{\phi}_r^{(j)} &= 0 \end{aligned} \tag{3.15}$$

where $S\left(\lambda^{(j)}\right)$ is the spectral Schur complement of $\left(A_{ff} - \lambda^{(j)} I\right)$ in $\left(A - \lambda^{(j)} I\right)$. An artificial weighting factor β is introduced to gradually add the coupling effect between aerodynamics and flight dynamics. Specifically, when $\beta = 0$, no aerodynamic influence on the rigid-body motions is taken into account since the interaction term $\beta A_{rf}\left(A_{ff} - \lambda^{(j)} I\right)^{-1} A_{fr} = 0$. Conversely, when $\beta = 1$, the system is fully coupled since the interaction term is taken into account when solving the eigenvalue problem. This provides a way to mathematically tune the influence of aerodynamics on the rigid-body degrees-of-freedom and improve convergence. Newton's method solving for $(\lambda^{(j)}, \boldsymbol{\phi}_r^{(j)})$ is used to trace the evolution of the rigid-body degrees-of-freedom starting at $\beta = 0$ to the coupled eigenvalue at $\beta = 1$. The tracing for flight dynamics modes is not trivial and the details are given in Section 3.2.2. The corresponding fluid part $\boldsymbol{\phi}_f^{(j)}$ of the eigenvector is calculated for the converged solution $(\lambda^{(j)}, \boldsymbol{\phi}_r^{(j)})$ at $\beta = 1$ by solving one additional linear equation per degree-of-freedom

$$\left(A_{ff} - \lambda^{(j)} I\right) \boldsymbol{\phi}_f^{(j)} = -A_{fr} \boldsymbol{\phi}_r^{(j)} \tag{3.13}$$

The computationally expensive part of Eq. (3.15) is the repeated evaluation of the interaction term $A_{rf}\left(A_{ff} - \lambda^{(j)} I\right)^{-1} A_{fr}$ depending on the solution $\lambda^{(j)}$. For small-sized problems, this matrix can be computed with direct solvers whereas iterative methods have to be applied for industrial test cases [156]. This can lead to convergence problems since the eigenspectrum of the system can easily contain millions of eigenvalues and the flight dynamics eigenvalue might be within the cloud of aerodynamic modes. Specifically, when this happens the matrix $\left(A_{ff} - \lambda^{(j)} I\right)$ is almost singular which, in turns, generates convergence issues when computing the interaction term $A_{rf}\left(A_{ff} - \lambda^{(j)} I\right)^{-1} A_{fr}$ or solving Eq. (3.13). A Taylor expansion for $\lambda^{(j)} = \lambda_0^{(j)} + \lambda_\epsilon^{(j)}$ was proposed in [9, 143] to alleviate the problem of tracing eigenpairs related to aeroelastic problems inside the cloud and provide a speed-up. The inverse of $A_{ff} - \lambda^{(j)} I$ becomes

$$\left(A_{ff} - \lambda^{(j)} I\right)^{-1} = \left(A_{ff} - \lambda_0^{(j)} I\right)^{-1} + \lambda_\epsilon^{(j)} \left(A_{ff} - \lambda_0^{(j)} I\right)^{-2} + \mathcal{O}(|\lambda_\epsilon^{(j)}|^2) \tag{3.16}$$

where $\lambda_\epsilon^{(j)}$ represents a small variation of $\lambda^{(j)}$ from a reference value $\lambda_0^{(j)}$. The expansion can proceed with high-order terms but in-house tests have shown that no major benefits are obtained beyond second order. The reference value $\lambda_0^{(j)}$ can be given by a previously converged solution or by the rigid body eigenvalue.

Challenges addressed by the operator-based identification, which might not be clear from the mathematical formulation presented so far, are described next with a schematic eigenspectrum of a coupled Jacobian matrix for a system involving CFD aerodynamics, flight dynamics and elastic structure shown in Fig. 3.1. The tracing of flight dynamics eigenpairs is compared to the one of elastic modes in order to provide a clear explanation since the latter is currently used for industrial and research applications [142]. A

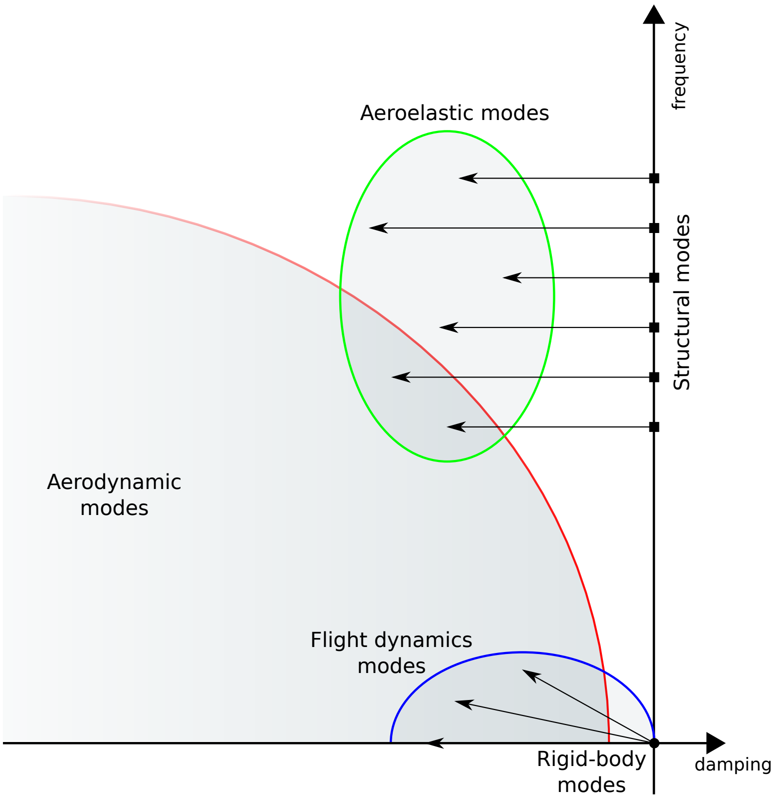

Figure 3.1: Schematic representation of an eigenspectrum for coupled system involving CFD aerodynamics, flight dynamics and structure.

large region of the spectrum in Fig. 3.1 is occupied by aerodynamic eigenvalues. They form a cloud which starts from the origin and spread out in the complex plane with a characteristic dome shape. Assuming no structural damping, structural eigenvalues are located on the imaginary axis since they have a non-zero in-vacuum frequency. When aerodynamics is coupled with elastic structure, structural eigenvalues move from their original location to a new position which has non-zero damping as well as non-zero frequency [143]. Their new location is usually outside the cloud of aerodynamics modes. Their tracing can start from in-vacuum eigenpairs and follow the evolution of the eigenvalues in the complex plane without encountering any fluid eigenvalue. Regarding flight dynamics modes, a different behaviour is expected. They originate from rigid-body modes which all have both zero frequency and damping when aerodynamics is not included in the system. Hence, all eigenvalues related to rigid-body dynamics are located in the origin of the eigenspectrum when no aerodynamics is included. They move to new locations which have both non-zero damping and frequency when aerodynamics is added. Usually, their final positions are inside the cloud of aerodynamic eigenvalues. Two challenges are identified. First, the operator-based identification must be able to trace flight dynamics eigenpairs inside the cloud of aerodynamic modes. This could be a problem for the calculation of the interaction term in Eq. (3.15) since a λ very close to an aerodynamic eigenvalue leads to an almost singular matrix $\left(A_{ff} - \lambda^{(j)} I\right)$. Secondly, the starting point for the tracing is not as clear as for structural modes since all eigenvalues are located in the origin at the beginning of the tracing. Both challenges must be addressed by the operator-based identification for a successful model reduction and solutions are provided in the next chapters.

The description of the operator-based identification proceeds with the adjoint formulation for which the same challenges must be solved. The adjoint eigenvalue problem, the solution of which is needed for the model reduction, is derived from the adjoint formulation in Eq. (3.11)

$$\left(A^T - \lambda^{(j)} I\right) \bar{\boldsymbol{\psi}}^{(j)} = 0 \tag{3.17}$$

for the adjoint vector $\boldsymbol{\psi}^{(j)}$. Note that $\boldsymbol{\psi}^{(j)}$ is also split in fluid and flight dynamics unknowns, $\boldsymbol{\psi} = [\boldsymbol{\psi}_f, \boldsymbol{\psi}_r]^T$, and the matrix A^T is written as

$$A^T = \begin{pmatrix} A_{ff}^T & A_{rf}^T \\ A_{fr}^T & A_{rr}^T \end{pmatrix} \tag{3.18}$$

according to the partitioning in Eq. (3.2). Equation (3.18) is substituted in Eq. (3.17) and a system of two equations in Laplace domain is obtained,

$$\left(A_{ff}^T - \lambda^{(j)} I\right) \bar{\boldsymbol{\psi}}_f^{(j)} = -A_{rf}^T \bar{\boldsymbol{\psi}}_r^{(j)} \tag{3.19}$$

$$\left(A_{rr}^T - \lambda^{(j)} I\right) \bar{\boldsymbol{\psi}}_r^{(j)} = -A_{fr}^T \bar{\boldsymbol{\psi}}_f^{(j)} \tag{3.20}$$

Isolating $\bar{\boldsymbol{\psi}}_f^{(j)}$ in Eq. (3.19) and substituting it into Eq. (3.20) leads to the adjoint equation

$$\left\{ \left(A_{rr}^T - \lambda^{(j)} I\right) - \beta A_{fr}^T \left(A_{ff}^T - \lambda^{(j)} I\right)^{-1} A_{rf}^T \right\} \bar{\boldsymbol{\psi}}_r^{(j)} = 0 \tag{3.21}$$

which is enhanced by introducing the artificial weighting β and solved iteratively with the same techniques adopted for direct eigenpairs. The flight dynamics part of the adjoint eigenvector is obtained when $\beta = 1$. Manipulating the interaction term using the equality $(ABC)^T = C^T B^T A^T$, this equation can equivalently be formulated as

$$\begin{aligned} \left\{ \left(A_{rr}^T - \lambda^{(j)} I\right) - \beta \left[A_{rf} \left(A_{ff} - \lambda^{(j)} I\right)^{-1} A_{fr}\right]^T \right\} \bar{\boldsymbol{\psi}}_r^{(j)} &= \\ S^T \left(\lambda^{(j)}\right) \bar{\boldsymbol{\psi}}_r^{(j)} &= 0 \end{aligned} \tag{3.22}$$

and it is compared to Eq. (3.15). Note that the interaction term, which is the computationally expensive part of the adjoint equation, can be obtained for the adjoint problem from the computations performed for direct eigenvectors. This provides an important way to save computational time by storing the interaction terms when solving Eq. (3.15) and reusing them to solve Eq. (3.22). The fluid part of the left eigenvector is then calculated by solving the adjoint problem in Eq. (3.19).

The derivation so far has previously been described as Schur complement method [9]. The full order CFD solver is rearranged and directly employed during the solution of the small non-linear eigenvalue problem in Eqs. (3.15) and (3.22). The relation to more classical analysis via dynamic derivatives is apparent. This is described next in order to show the equivalence of the interaction term with dynamic derivatives. Substituting the definition of A_{rf} into Eq. (3.15), the interaction term is expressed as

$$A_{rf}\left(A_{ff}-\lambda^{(j)}I\right)^{-1}A_{fr}=C\frac{\partial \boldsymbol{f}_a}{\partial \boldsymbol{w}_f}\left(A_{ff}-\lambda^{(j)}I\right)^{-1}A_{fr} \tag{3.23}$$

The term $\left(A_{ff}-\lambda^{(j)}I\right)^{-1}A_{fr}$ is associated in Eq. (2.63) with the response of the fluid unknowns to excitations in the flight dynamics degrees-of-freedom,

$$C\frac{\partial \boldsymbol{f}_a}{\partial \boldsymbol{w}_f}\left(A_{ff}-\lambda^{(j)}I\right)^{-1}A_{fr}=C\frac{\partial \boldsymbol{f}_a}{\partial \boldsymbol{w}_f}\frac{\partial \boldsymbol{w}_f}{\partial \boldsymbol{w}_r}=C\frac{\partial \boldsymbol{f}_a}{\partial \boldsymbol{w}_r}=CQ \tag{3.24}$$

Thus, the matrix Q describes the transfer function relating flight dynamics motions to the aerodynamic forces by means of complex-valued dynamic derivatives of the aerodynamic system [43, 121]. The direct and adjoint eigenvalue problems in Eqs. (3.15) and (3.22) are then rewritten using dynamic derivatives as

$$\left[\left(A_{rr}-\lambda^{(j)}I\right)+\beta CQ\right]\boldsymbol{\phi}_r^{(j)}=0 \quad\text{and}\quad \left[\left(A_{rr}^T-\lambda^{(j)}I\right)+\beta Q^TC^T\right]\bar{\boldsymbol{\psi}}_r^{(j)}=0 \tag{3.25}$$

Relying on the fact that real and imaginary parts of $\lambda^{(j)}$ correspond to damping and frequency, the dynamic derivatives are pre-computed for a finite number of complex harmonic motions corresponding to points in the complex plane. This can be done directly in Laplace domain by solving Eq. (3.24) or using time-domain methods described in the next section. Interpolation techniques are used to calculate dynamic derivatives for pairs of damping and frequency not sampled. Note that the same derivatives are used for both direct and adjoint problems. In addition, the latter equations are identical to Eqs. (3.15) and (3.22), if Q is computed for each point in the complex plane.

A simplification arises by neglecting the damping during the computation of the aerodynamic influence, similar to the p-k method for flutter analysis [72]. As a consequence, the matrix Q would depend on frequency only and pre-computed for simple harmonic motions.

3.2.1 Dynamic Derivatives from Time-Domain Simulations

When solving Eq. (3.25), a crucial point for accurate results is the pre-computation of dynamic derivatives, i.e. the entries of the matrix Q. Two strategies are employed, specifically in frequency-domain and in time-domain. The former is based on solving Eq. (2.64) in turn for each degree-of-freedom with an LFD solver. This is the standard procedure adopted in this work since it speeds up the computation of the reduced model. Regarding the latter, dynamic derivatives are calculated from time-histories of time-domain forced-motion simulations. Both methods lead to the same results and the latter provides a verification for LFD results. It is described in detail in this section.

In literature, approaches based on the Fourier transform were proposed to calculate the frequency response which links input (forced motion) to output (aerodynamic coefficients) [43]. However, such approaches are limited to pure harmonic motions and they cannot account for damping. So, a different procedure is needed when the matrix Q have to be calculated for points in the complex plane in order to solve, for example, Eq. (3.25). Two parameters are taken into account, decay ratio γ and reduced frequency ω which are real and imaginary part of the complex number $\lambda \in \mathbb{C}$, respectively. Forced motions can have any combination of these two parameters, leading to simulations for simple harmonic motions as well as decaying ones.

The method is described now in detail. The flight dynamics degrees-of-freedom are excited in turns. Denote α as the forced variable. Its time-history is given by

$$\alpha(t) = \alpha_0 e^{(\gamma + i\omega)t} = \alpha_0 e^{\lambda t} \tag{3.26}$$

as function of the time t. In practice, the motion imposed in a forced simulations is

$$\alpha(t) = \alpha_0 e^{\gamma t} \sin\left(\omega t + \frac{\pi}{2}\right) \tag{3.27}$$

which corresponds to the real part of Eq. (3.26). A small amplitude must be chosen for α_0 in order to stay in the linear range. The generic aerodynamic coefficient C_x represents drag, lift or moment coefficient and it is expressed in time-domain using dynamic derivatives as

$$C_x = C_{x0} + C_{x\alpha}\alpha + C_{x\dot{\alpha}}\dot{\alpha} \tag{3.28}$$

with C_{x0}, $C_{x\alpha}$ and $C_{x\dot{\alpha}}$ to be determined. Substituting Eq. (3.26) in Eq. (3.28),

$$C_x = C_{x0} + \alpha_0 \widehat{C}_{x_\alpha}(\lambda) e^{\lambda t} \tag{3.29}$$

$$\widehat{C}_{x_\alpha}(\lambda) = C_{x_\alpha} + \lambda C_{x\dot{\alpha}} \tag{3.30}$$

the complex-valued dynamic derivative $\widehat{C}_{x_\alpha}(\lambda)$ is defined as function of the complex number λ.

The calculation of the dynamic derivative $\widehat{C}_{x_\alpha}$ starts from assembling a matrix D from the time history of the forced motion simulation. It has dimension $n_t \times 3$ with n_t the total number of time steps. Each column contains the coefficient of the three unknowns C_{x0}, C_{x_α} and $C_{x\dot{\alpha}}$ in Eq. (3.28),

$$D = \begin{bmatrix} 1 & \alpha_1 & \dot{\alpha}_1 \\ \vdots & \vdots & \vdots \\ 1 & \alpha_{n_t} & \dot{\alpha}_{n_t} \end{bmatrix} \tag{3.31}$$

Note that the first column is filled with 1 to account for a constant shift whereas α_i and $\dot{\alpha}_i$ represent the value of the flight dynamics variable and its time derivative at the time step i. If not available, the time history of $\dot{\alpha}$ is obtained by differentiating numerically the time history of α. The vector $\boldsymbol{B}$ is then assembled with the time history of the coefficient C_x, $\boldsymbol{B} = [C_{x1}, \ldots, C_{xn_t}]^T$. The condition in Eq. (3.28) must be satisfied for each time step of the forced motion simulation. Thus, a overdetermined linear system is obtained

$$D\boldsymbol{C_x} = \boldsymbol{B} \tag{3.32}$$

with $\boldsymbol{C_x} = [C_{x0}, C_{x_\alpha}, C_{x\dot{\alpha}}]$. The unknown vector $\boldsymbol{C_x}$ is determined using the Moore-Penrose inverse matrix [111],

$$\boldsymbol{C_x} = (D^T D)^{-1} D^T \boldsymbol{B} = D^* \boldsymbol{B} \tag{3.33}$$

with the 3×3 matrix $D^T D$ to be inverted. This approach can be interpreted as a least squares curve fitting of the time-domain data [92]. The dynamic derivative $\widehat{C}_{x_\alpha}$ is then calculated using Eq. (3.30). The calculation of multiple dynamic derivatives is performed by computing the matrix D^* once and changing in turn the vector $\boldsymbol{B}$ for coefficients of drag, lift and moment.

This method was extensively used to calculate the dynamic derivatives from URANS data and compare their values against the corresponding LFD evaluation. The forced motion simulations must have small amplitudes since the ultimate target is a linear reduced order model. A value of 0.01% reference length is chosen as amplitude of forced harmonic motions when computing dynamic derivatives through the thesis. No attempt is made to compare the LFD results to non-linear URANS simulations with large amplitudes. An example to illustrate the computation of a dynamic derivative from time-domain data is provided next. Results from a forced motion simulation for the vertical velocity of a two-dimensional wing-tail configuration is shown in Fig. 3.2(a). The oscillation frequency ω is expressed in a non-dimensional way by defining the reduced frequency $k = {}^{\omega b}/_{U_\infty}$,where U_∞ is the flow-stream velocity and b is the reference length. A value of $k = 0.05$ and an amplitude of 0.0001 chord length were employed to produce the results for Fig. 3.2(a). They show the evolution of lift coefficient when the vertical velocity changes and the phenomenon of hysteresis is clearly visible. The dynamic derivative was estimated as $\widehat{C}_{L_{\dot{z}}} = 12.74\angle 167.5°$ using the method described in this section. This value was confirmed by an application of the Fourier transform

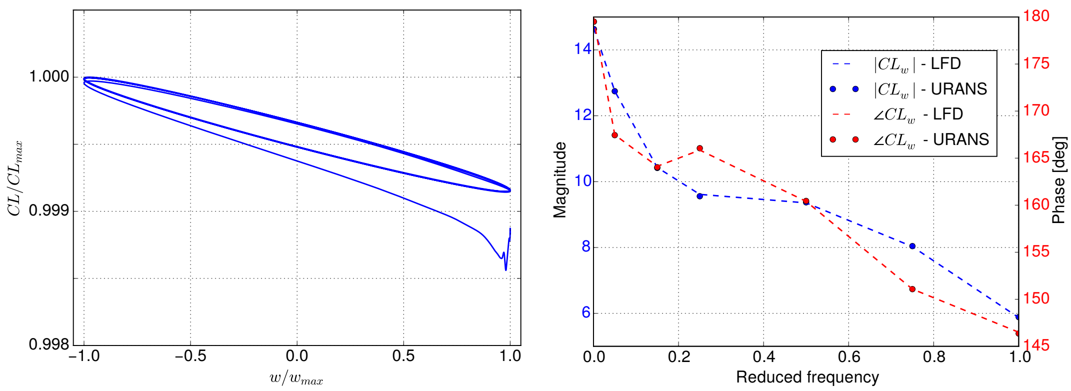

(a) Reduced frequency $k = 0.05$

(b) Comparison of LFD and URANS

Figure 3.2: Dynamic derivatives relating lift coefficient to vertical velocity.

to the time-domain data since no damping was included. The same procedure was repeated for forced motion simulations with the same amplitude but different reduced frequencies in order to show that LFD and time-domain approach lead to the same results as expected. The variation of the dynamic derivative with the reduced frequency is shown in Fig. 3.2(b). LFD results were obtained by solving Eq. (2.64) directly.

3.2.2 Newton's Method for Mode Tracing

Newton's method is the core tool to perform the tracing during the operator-based identification of flight dynamics eigenpairs. Note that, as already stated at the beginning of Section 3.2, the tracing is needed to compute the eigenpairs at a larger value of the coupling parameter β and starting from $\beta = 0$. When the coupling value is increased, i.e. β is increased, the eigenpair evaluated at a smaller coupling provides an initial guess for the computation of the eigenpair at the larger coupling level. The evaluation is performed with Newton's method until convergence is reached. At the end, the converged eigenpair at $\beta = 1$ represents the flight dynamics mode which can be used as one column of the modal basis in Eq (3.4).

In general, Newton's method is particularly suitable to find the root $\boldsymbol{x}^*$ of a vector function, i.e. $\boldsymbol{F}(\boldsymbol{x}^*) = 0$, and it is here described briefly with focus on the solution of Eqs. (3.15) and (3.25). The mathematical formulation of the iterative method is obtained by expanding the function $\boldsymbol{F}$ in a first order Taylor series around a point $\boldsymbol{x}_k$. This leads to

$$\boldsymbol{F}(\boldsymbol{x}_{k+1}) = \boldsymbol{F}(\boldsymbol{x}_k) + \frac{\partial \boldsymbol{F}}{\partial \boldsymbol{x}_k}(\boldsymbol{x}_{k+1} - \boldsymbol{x}_k) \tag{3.34}$$

where $\boldsymbol{x}_{k+1}$ is a generic point in the neighbourhood of $\boldsymbol{x}_k$ and $\frac{\partial \boldsymbol{F}}{\partial \boldsymbol{x}_k}$ is the Jacobian matrix containing the partial derivatives of $\boldsymbol{F}$ with respect to $\boldsymbol{x}$. Assuming $\boldsymbol{F}(\boldsymbol{x}_{k+1}) = 0$, we have a new approximation for the solution $\boldsymbol{x}$,

$$\boldsymbol{x}_{k+1} = \boldsymbol{x}_k - \left(\frac{\partial \boldsymbol{F}}{\partial \boldsymbol{x}_k}\right)^{-1} \boldsymbol{F}(\boldsymbol{x}_k) \tag{3.35}$$

The method works by replacing locally the function with its tangent (subject to the condition of a non-singular Jacobian matrix) and using this assumption to locate the zero [114]. An initial guess $\boldsymbol{x}_0$ for the first iteration must be provided. The methods converges if the initial guess is close to the solution, i.e. it lies in a suitable neighbourhood of the solution $\boldsymbol{x}^*$. Quadratic convergence is obtained if $\boldsymbol{x}_0$ is close to $\boldsymbol{x}^*$ otherwise the method provides linear convergence or diverges. The order of convergence degrades to 1 also in case of solution with multiplicity greater than 1. A relaxation parameter m is included to facilitate convergence so that the equation for the modified Newton's method becomes

$$\boldsymbol{x}_{k+1} = \boldsymbol{x}_k - m \left[\left(\frac{\partial \boldsymbol{F}}{\partial \boldsymbol{x}_k}\right)^{-1} \boldsymbol{F}(\boldsymbol{x}_k)\right] \tag{3.36}$$

and an a priori knowledge of m is required.

In the specific case of flight dynamics mode identification, the tracing procedure for the modes concerns the solution of

$$\boldsymbol{F}(\lambda^{(j)}, \boldsymbol{\phi}_r^{(j)}) = \begin{cases} \left[\left(A_{rr} - \lambda^{(j)} I\right) + \beta C Q\right] \boldsymbol{\phi}_r^{(j)} = 0 \\ \langle \boldsymbol{\phi}_r^{(j)}, \boldsymbol{\phi}_r^{(j)} \rangle = 1 \end{cases} \tag{3.37}$$

according to the workflow depicted in Fig. 3.3. Specifically, Eq. (3.37) represents the direct problem in either Eq. (3.15) or (3.25) with the additional condition of unit norm for the eigenvector. Applying the tracing to the adjoint problem is straightforward once the direct problem is solved. Particular focus is on the evaluation of the Jacobian matrix by means of partial derivatives of interaction term Q. The unknown eigenvalue $\lambda^{(j)}$ and the eigenvector $\boldsymbol{\phi}_r^{(j)}$ are split in real/imaginary part and collected in the vector $\boldsymbol{x} = [\lambda_R, \lambda_I, \boldsymbol{\phi}_R, \boldsymbol{\phi}_I]^T$ with $\lambda_R = \Re(\lambda^{(j)})$, $\lambda_I = \Im(\lambda^{(j)})$, $\boldsymbol{\phi}_R = \Re(\boldsymbol{\phi}_r^{(j)})$ and $\boldsymbol{\phi}_I = \Im(\boldsymbol{\phi}_r^{(j)})$. The set of equations to solve, including the condition for unitary norm of $\boldsymbol{\phi}_r^{(j)}$, becomes

$$\boldsymbol{F}(\lambda_R, \lambda_I, \boldsymbol{\phi}_R, \boldsymbol{\phi}_I) = \begin{cases} (A_{rr} - \lambda_R I + \beta C Q_R)\, \boldsymbol{\phi}_R + (\lambda_I I - \beta C Q_I)\, \boldsymbol{\phi}_I = 0 \\ (A_{rr} - \lambda_R I + \beta C Q_R)\, \boldsymbol{\phi}_I - (\lambda_I I - \beta C Q_I)\, \boldsymbol{\phi}_R = 0 \\ \boldsymbol{\phi}_R^T \boldsymbol{\phi}_R + \boldsymbol{\phi}_I^T \boldsymbol{\phi}_I = 1 \\ \boldsymbol{\phi}_R^T \boldsymbol{\phi}_I - \boldsymbol{\phi}_I^T \boldsymbol{\phi}_R = 0 \end{cases} \tag{3.38}$$

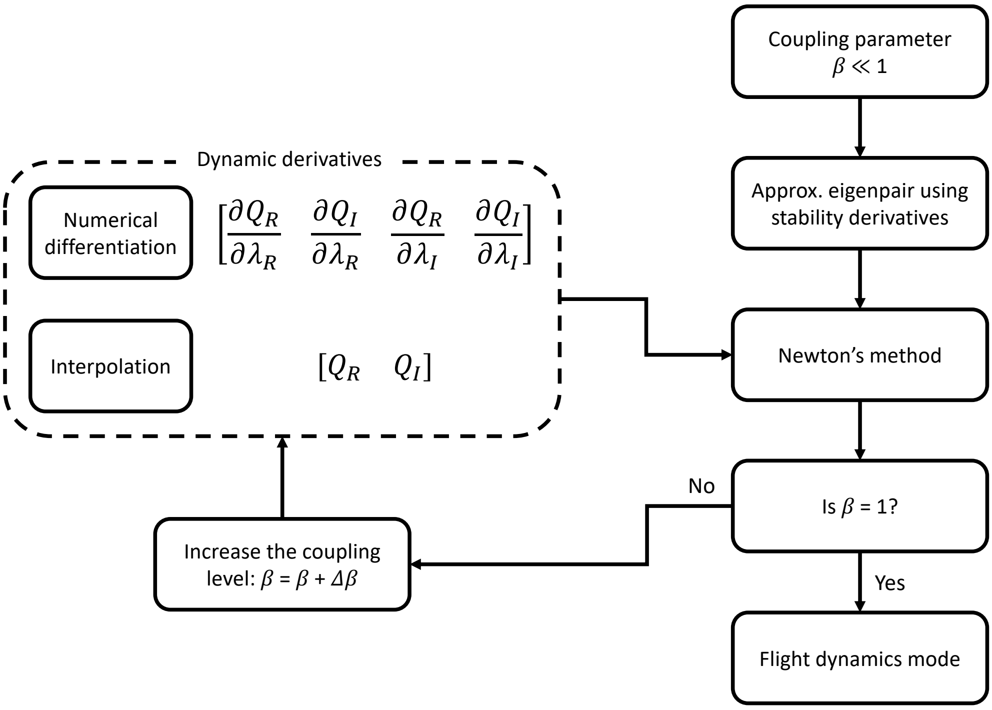

Figure 3.3: Tracing procedure for flight dynamics and the elastic eigenpairs.

with the last equation always satisfied. The Jacobian matrix is derived as

$$\frac{\partial \boldsymbol{F}}{\partial \boldsymbol{x}} = \begin{pmatrix} \frac{\partial \boldsymbol{F}_1}{\partial \lambda_R} & \frac{\partial \boldsymbol{F}_1}{\partial \lambda_I} & A_{rr} - \lambda_R I + \beta C Q_R & \lambda_I I - \beta C Q_I \\ \frac{\partial \boldsymbol{F}_2}{\partial \lambda_R} & \frac{\partial \boldsymbol{F}_2}{\partial \lambda_I} & -\lambda_I I + \beta C Q_I & A_{rr} - \lambda_R I + \beta C Q_R \\ 0 & 0 & 2\boldsymbol{\phi}_R^T & 2\boldsymbol{\phi}_I^T \\ 0 & 0 & \boldsymbol{\phi}_I^T & \boldsymbol{\phi}_R^T \end{pmatrix} \tag{3.39}$$

with derivatives explicitly given as

$$\begin{aligned} \frac{\partial \boldsymbol{F}_1}{\partial \lambda_R} &= \left(-I + \beta C \frac{\partial Q_R}{\partial \lambda_R}\right) \boldsymbol{\phi}_R - \beta C \frac{\partial Q_I}{\partial \lambda_R} \boldsymbol{\phi}_I \\ \frac{\partial \boldsymbol{F}_1}{\partial \lambda_I} &= \beta C \frac{\partial Q_R}{\partial \lambda_I} \boldsymbol{\phi}_R + \left(I - \beta C \frac{\partial Q_I}{\partial \lambda_I}\right) \boldsymbol{\phi}_I \\ \frac{\partial \boldsymbol{F}_2}{\partial \lambda_R} &= \beta C \frac{\partial Q_I}{\partial \lambda_R} \boldsymbol{\phi}_R + \left(-I + \beta C \frac{\partial Q_R}{\partial \lambda_R}\right) \boldsymbol{\phi}_I \\ \frac{\partial \boldsymbol{F}_2}{\partial \lambda_I} &= \left(-I + \beta C \frac{\partial Q_I}{\partial \lambda_I}\right) \boldsymbol{\phi}_R + \beta C \frac{\partial Q_R}{\partial \lambda_I} \boldsymbol{\phi}_I \end{aligned} \tag{3.40}$$

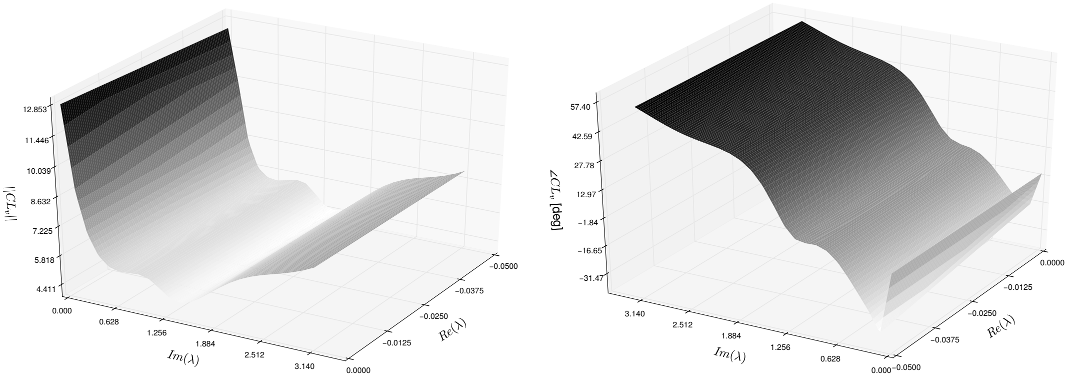

(a) Magnitude

(b) Phase

Figure 3.4: Magnitude and phase of the entry of the matrix Q which relates lift coefficient with vertical velocity.

Splitting complex numbers in real and imaginary parts is needed in order to compute the partial derivatives $\frac{\partial Q_R}{\partial \lambda_R}$, $\frac{\partial Q_R}{\partial \lambda_I}$, $\frac{\partial Q_I}{\partial \lambda_R}$ and $\frac{\partial Q_I}{\partial \lambda_I}$. In fact, no assumption can be made regarding the function $Q(\lambda)$ and, in general, it does not satisfy the Cauchy-Riemann equations to be complex-differentiable so that the existence of the complex-valued derivative $\frac{\partial Q}{\partial \lambda}$ with $\lambda \in \mathbb{C}$ is not guaranteed [88]. The partial derivatives are computed for the Schur formulation in Eq. (3.15) since $CQ = A_{rf}\left(A_{ff} - \lambda^{(j)} I\right)^{-1} A_{fr}$. However, when the dynamic derivatives method is employed, they are usually calculated with finite differences since Q is only available in specific points of the complex plane and reconstructed with two-dimensional interpolation. A complex-valued entry of the matrix Q is presented in Fig. 3.4 as representative entry. Its value depends on the real and imaginary part of the eigenvalue and both magnitude and phase are presented with three-dimensional maps. Specifically, interpolation based on Delaunay triangulation is used in this case [48]. It is clear that the entries of Q do not satisfy the symmetry condition required to be complex-differentiable.

The initial guess, which is needed to start the iteration of the Newton's solver, is evaluated for a given value of β by solving the eigenvalue problem

$$\left(A_{rr} - \lambda^{(j)} I + \beta C Q_s\right) \boldsymbol{\phi}^{(j)} = 0 \tag{3.41}$$

for which the stability derivatives Q_s are used to approximate Q. They can be obtained by either direct calculation or evaluating the dynamic derivatives at frequency zero. This approach leads to successful tracing for both flight dynamics and also for aeroelastic eigenpairs so that the same framework can be used for both problems. A verification of the implementation with a reproduction of bibliographic data is provided in Appendix B.

3.3 Data-based Modal Identification

The snapshot method [130] is adopted to interpolate the response of the coupled system involving CFD and flight dynamics subject to sinusoidal disturbances. A snapshot matrix S of dimension $n \times m$ is obtained by combining m solutions of Eq. (2.59), which is restated here for convenience,

$$(A - \lambda I)\,\widehat{\boldsymbol{w}} = -\frac{\partial \boldsymbol{R}}{\partial \boldsymbol{u}_d}\widehat{\boldsymbol{u}}_d \tag{2.59}$$

for frequencies in the range of interest. The number of snapshots determines the number of possible modes. Producing the snapshots is the computationally expensive part of the method since m complex-valued linear systems with leading dimension n need to be solved. Equation (2.59) involves the coupled Jacobian matrix and it can be solved with the same strategies used for the interaction matrix described above, i.e. direct or iterative methods according to the size of the system. This is in contrast to the usual practice which focuses on the application of Eq. (2.65) for the aerodynamic subsystem only. This coupled formulation allows to use the theoretical framework for the model reduction provided in Eq. (3.9) with modes computed using the data-based identification.

Proper Orthogonal Decomposition (POD) is then applied to the snapshot matrix S with POD modes $\boldsymbol{\phi}^{(j)}$ defined as

$$\boldsymbol{\phi}^{(j)} = S\boldsymbol{v}_j \qquad \forall j \in [1, m] \tag{3.42}$$

where each entry of the vector $\boldsymbol{v}_j$ represents the contribution of the corresponding snapshot to the mode $\boldsymbol{\phi}^{(j)}$. The condition that $\boldsymbol{v}_j$ lie along the principal axes of the space spanned by S leads to the eigenproblem

$$\langle S, S\rangle \boldsymbol{v}_j = \sigma_j \boldsymbol{v}_j \qquad \forall j \in [1, m] \tag{3.43}$$

with larger eigenvalues σ_j corresponding to the dominant modes. Specifically, σ_j^2 is a measure of energy per unit mass as defined traditionally [144] when all entries of S are velocities. That is usually the case of incompressible flows. However, when entries of S have different units, for compressible flows as an example, the dot product $\langle S, S\rangle$ must be redefined to provide a consistent measure of energy [11]. The negligible computational cost of the reduced model can be further decreased by selecting only a subset of modes [17]. However, this additional reduction is not performed herein to avoid the arbitrariness of POD modal selection criteria.

Contrary to the Petrov-Galerkin projection used for the operator-based approach, the Galerkin one is used for the data-based ROMs instead. As a result, both the modal bases Φ and Ψ contain the same POD modes and they satisfy Eq. (3.5). This can lead to numerical issues when integrating the time-domain Eq. (3.7) since the stability of the reduced model is not guaranteed even though the full order model is stable [5]. Solutions proposed in literature to assure a stable ROM range from the redefinition of the inner product $\langle S, S\rangle$ for compressible flow [83] to non-intrusive methods which turn an unstable ROM into a stable one by means of an a posteriori Petrov-Galerkin projection. ROM stability and accuracy can be achieved by increasing the number of snapshots to cover all frequencies of interest as suggested in [11]. However, the stability of the reduced model does not represent an issue when the frequency domain formulation provided in Eq. (3.9) is exploited. In fact, the time-domain integration is avoided and the solution is found by solving a small complex-valued linear system. The method presented here does not depend on the nature of the disturbance $\boldsymbol{u}_d$. However, the POD technique will be applied in the following to gust encounter simulations by computing the right-hand side as described in Section 2.4.2.

3.4 Notes for Finite Volume Formulations

The derivation described so far for the model reduction method does not rely on any assumptions regarding the numerical implementation. However, particular care must be taken when dealing with finite volume codes such as DLR-TAU. Dividing the flow field into a number of finite volumes alters the equations for the model reduction. The solution in every cell is considered constant and equal to the average when a second order scheme is adopted [23]. A diagonal matrix $\mathcal{V}$ is defined so that it contains the cell volumes corresponding to fluid unknowns. An identity matrix fills the diagonal for the flight dynamics degrees-of-freedom. The matrix $\mathcal{V}$ should be calculated directly by the CFD solver since it depends on the specific spatial discretisation. The full order model in Eq. (2.54) becomes

$$\frac{\mathtt{d}\mathcal{V}\boldsymbol{w}}{\mathtt{d}t} = \boldsymbol{R}\left(\boldsymbol{w}, \boldsymbol{u}_d, \boldsymbol{u}_c\right) \tag{3.44}$$

and the presence of $\mathcal{V}$ propagates throughout the derivation. For example, the LFD formulation in Eq. (2.59) becomes

$$\left(A - \lambda\mathcal{V}\right)\widehat{\boldsymbol{w}} = -\frac{\partial \boldsymbol{R}}{\partial \boldsymbol{u}_d}\widehat{\boldsymbol{u}}_d \tag{3.45}$$

The presence of $\mathcal{V}$ leads to two major modifications. The eigenproblem in Eq.(3.43) for the data-based identification must be reformulated as

$$\langle S, \mathcal{V}S\rangle \boldsymbol{v}_j = \sigma_j \boldsymbol{v}_j \qquad \forall j \in [1, m] \tag{3.46}$$

to be consistent with the formulation for finite volumes codes. Similarly, the product in Eq. (3.5) becomes

$$\langle \boldsymbol{\psi}^{(j)}, \mathcal{V}\boldsymbol{\phi}^{(j)} \rangle = 1 \qquad\qquad \forall j \in [1, m] \tag{3.47}$$

to account for the volume matrix $\mathcal{V}$.

Chapter 4

Model Reduction for Short-term Dynamics

Mode identification and model reduction are described in this chapter in detail for a two-dimensional case. Focus is on short-term response of the system to fast phenomena, for example gust encounters, and it is dominated by the short period mode [34, 155]. It describes a damped oscillation of the aerodynamic body which lasts few seconds. The flight speed does not change and the motion concerns mainly rigid rotation and vertical velocity. Since short-term dynamics is dominated by the short period mode, flight dynamics equations are simplified by discarding the horizontal degree-of-freedom. The position of such flight dynamics mode in the eigenspectrum (either inside or outside the cloud of eigenvalues) determines the short-term response of the system and its accurate identification is crucial. The equations for short-term approximation, given in Eq. (2.40), are adopted for flight dynamics. Aerodynamics is modelled with Euler equations for a NACA 0012 aerofoil and an in-house code provided CFD aerodynamics for transonic flow. Both operator-based and data-based identification methods were exploited and results from the reduced order models are compared to the reference provided by the full order model. The small size of the model and the focus on the short-term dynamics allow for a very detailed investigation to identify potential problems arising during the identification procedure and discuss remedies. Results are provided for initial disturbance simulations as well as for responses to external disturbances. The majority of these results have been presented in [106, 107].

4.1 Governing Equations

The equations derived in Section 2.2 for short-term approximation for longitudinal dynamics are used in this chapter. This simplifies the investigation since the added complexity of multiple flight dynamics modes is avoided. Specifically, the relevant set of

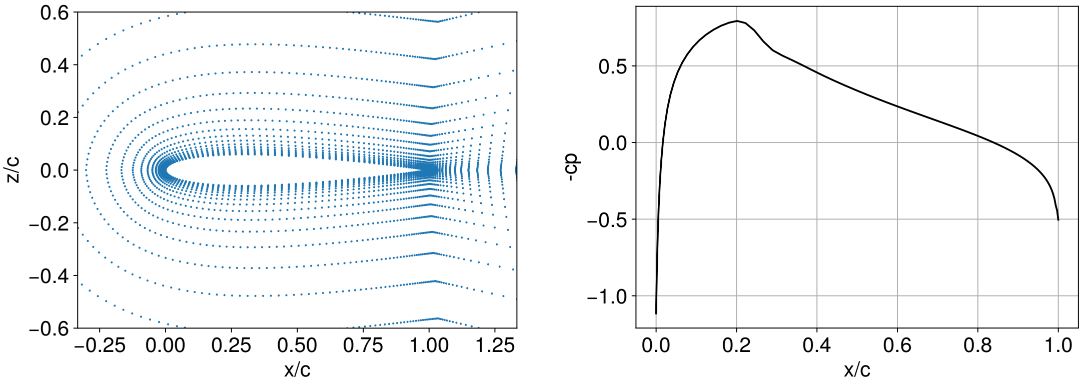

(a) Aerofoil close-up (b) Pressure distribution

Figure 4.1: Point distribution for NACA 0012 aerofoil and pressure coefficient at steady state.

equations is provided in Eq. (2.40) and they are restated here for convenience,

$$\begin{aligned}\frac{\mathrm{d}w^*}{\mathrm{d}\tau} - U_0^* q^* =& \frac{C_z}{\pi\mu}\\ \frac{\mathrm{d}q^*}{\mathrm{d}\tau} =& \frac{2C_m}{\pi\mu r_\alpha^2}\\ \frac{\mathrm{d}\theta^*}{\mathrm{d}\tau} =& q^*\end{aligned} \tag{2.40}$$

The reference length for the test case is defined as the wing semi-chord.

4.2 NACA 0012 Aerofoil

Equation (2.40) was implemented as a module of the in-house CFD solver. The computational domain was discretised with 7860 points and the near field is shown in Fig. 4.1(a). The steady state is calculated at a Mach number of 0.75 and 0 deg angle-of-attack. The resulting symmetric pressure distribution is depicted in Fig 4.1(b) where very weak shock waves are visible. The non-dimensional parameter $r_\theta = 0.5$ and two mass ratios are investigated, as discussed below. The drag is assumed to be constantly balanced by a thrust so that the rate of horizontal speed $\frac{\mathrm{d}u^*}{\mathrm{d}\tau}$ is zero. Without affecting the generality of the approach, the centre of mass is located at the leading edge to have a stable flight dynamics model for many flow conditions. In fact, stability in the longitudinal plane is obtained when the centre of mass, which is the reference point for moment calculations, is located ahead of the aerodynamic centre [87, Ch. 9], which is at the quarter chord point for a thin aerofoil in incompressible flow [84, Ch. 1].

4.3 Operator-based Identification

Regarding the operator-based identification, two flight dynamics modes related to vertical translation and rotation are expected to play a key role [155] since the focus is on the short-term longitudinal motions. The mode corresponding to the horizontal degree-of-freedom contributes only insignificantly to the short-term response of the system and is omitted [34]. It was found that the eigenvalue corresponding to the vertical translation mode remains close to the origin and is thus easy to calculate. The short period mode originating from the rigid rotation on the other hand is more challenging to identify and details are discussed in the next paragraphs. The eigenvalue associated to the short period moves away from the origin of the complex plane for in-vacuum conditions to a new, as yet undefined, position when aerodynamics is imposed.

The two values of mass ratio, $\mu = 100$ and $\mu = 35$, lead to distinct system behaviours. The first value $\mu = 100$ is taken from the *heavy* case in [10]. It is a realistic value of μ for a short-to-medium-range civil aircraft flying at 10000 m altitude. The second one, $\mu = 35$, corresponds to the same aircraft flying at sea level. Identification results are shown with parts of the complete eigenspectrum in Fig. 4.2. Real and imaginary part of eigenvalues are reported on horizontal and vertical axis, respectively. For instance, a stable eigenvalue with a positive frequency is located in the upper left region of the eigenspectrum. Three approximations of flight dynamics eigenvalues provided by operator-based identification as well as an exact solution computed with a direct method are depicted. Note that only the small size of the full order problem allows a direct calculation of the eigenvalues of the coupled Jacobian matrix and this is not the case in general. A number of 250 eigenvalues close to a shift of $0.3i$ were thus extracted using MATLAB®, specifically direct methods implemented in the function `eigs()`.

Regarding the case with mass ratio of 100, presented in Fig. 4.2(a), the eigenvalue corresponding to the short period mode is outside the cloud of fluid eigenvalues. The tracing was performed by solving Eq. (3.15) with the parameter β increasing from zero to one in 20 steps. For each step Newton's method was used to calculate the flight dynamics eigenpair for the new value of β using the previous converged solution as initial guess. At $\beta = 0$, when all the eigenvalues related to the flight dynamics degrees-of-freedom are located in the origin of the complex plane, the selection of the mode to trace relies on a unique rigid-body eigenvector of A_{rr} as initial guess. The Schur complement method provides an exact solution to the eigenvalue problem, as can be seen by comparison with the direct method. In addition, the figure includes the results based on the approximation of the interaction matrix with dynamic derivatives.

For the approach with dynamic derivatives, the matrix Q was pre-computed at 7 reduced frequencies linearly distributed in the interval ranging from 0 to 0.8. This range's upper limit was chosen to include typical frequency values for the short period mode [34]. Linear interpolation is used to evaluate Q for intermediate reduced frequencies. Adding

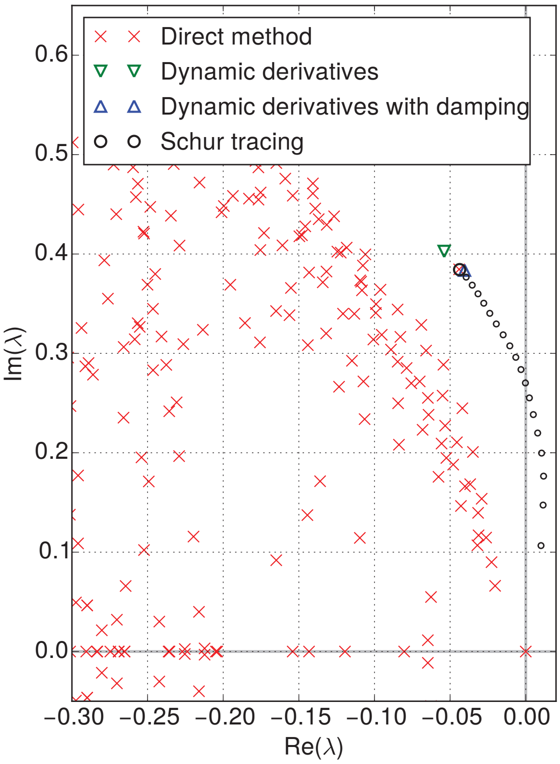

(a) Identification at $\mu = 100$

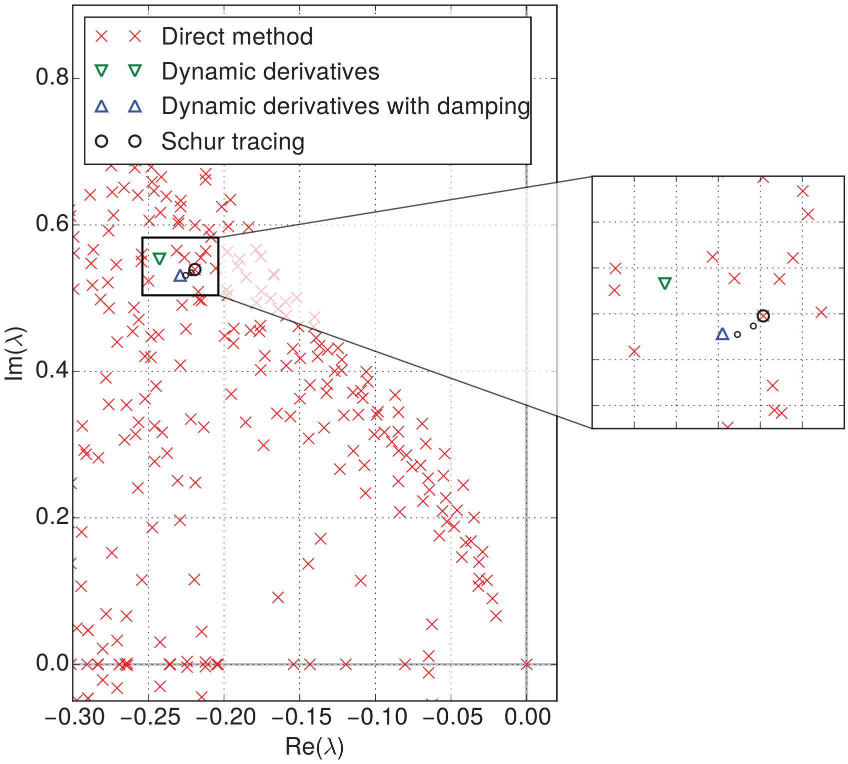

(b) Identification at $\mu = 35$

Figure 4.2: Eigenspectrum for operator-based identification.

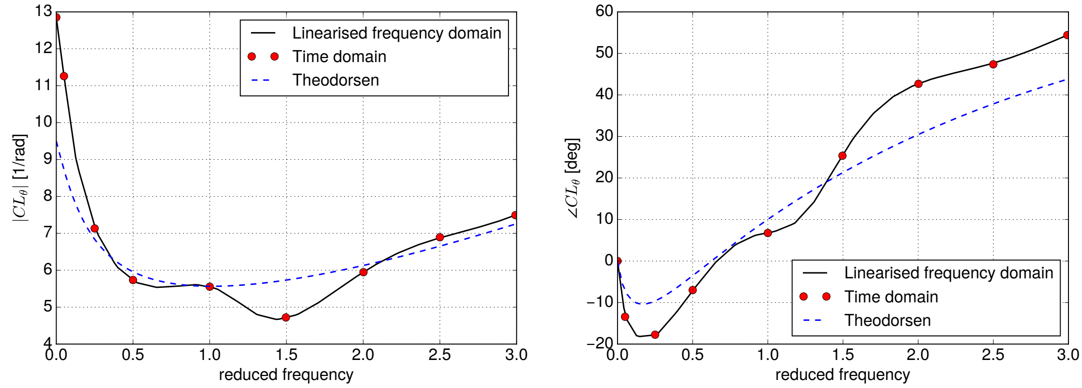

(a) Magnitude

(b) Phase in degrees

Figure 4.3: Magnitude and phase of dynamic derivative $C_{L\theta}$ (i.e. lift coefficient with respect to pitch) shown as representative entry of matrix Q.

more samples does not improve significantly the reconstruction of dynamic derivatives because entries of Q have a monotonic behaviour in such range. The dynamic derivative $C_{L\theta}$ relating the lift coefficient to the pitch angle θ, is shown in Fig. 4.3 as a representative entry of Q for reduced frequencies ranging between 0 and 3. Although all entries of Q are needed for an accurate identification, the derivative $C_{L\theta}$ is the most important one to compute the short period mode, which describes a motion composed of rigid rotation and vertical velocity. The magnitude of the lift coefficient in Fig. 4.3(a) starts from a quasi-steady value of $C_{L_\theta} \approx 12.18$ at zero frequency and it decreases until a minimum around a reduced frequency of 1.5. The trend is then reversed. A similar behaviour is shown for the phase in Fig. 4.3(b) which starts at zero. A few time-domain forced motion simulations were performed as reference and good agreement was found with the LFD calculations for both magnitude and phase. The calculation of dynamic derivatives from such simulations was achieved as described in Section 3.2.1. The good quality of results is confirmed by a comparison to Theodorsen's linear theory [63]. It provides unsteady lift coefficient for a flat plate oscillating in incompressible flow. Prandtl-Galuert correction was applied to take into account compressible effects [68]. The difference between Euler CFD and Theodorsen at zero frequency in Fig. 4.3(a) is due to two factors. First, aerofoil thickness is not taken into account by linear theory and this leads to underestimation of lift coefficient. Secondly, transonic effects are not accounted for by Prandtl-Galuert correction which should not be used for Mach numbers larger than 0.3-0.5. The theoretical value of the dynamic derivative in incompressible flow, $C_{L_\theta} = 2\pi$, becomes $C_{L_\theta} = {}^{2\pi}/\sqrt{1-M^2} \approx 9.5$ at Mach number of $M = 0.75$. As a result, linear theories underestimates the corresponding CFD result which is $C_{L_\theta} \approx 12.18$ instead. However, the qualitative trend of magnitude and phase is comparable and they are similar to results provided in [74] for transonic flows.

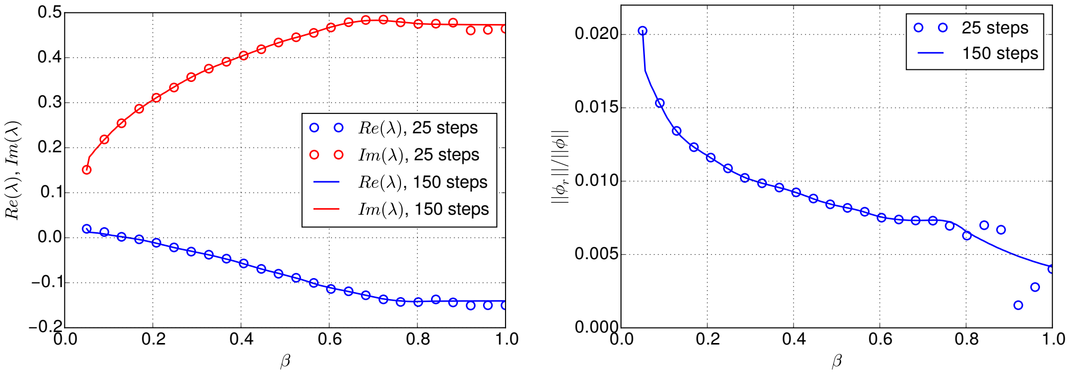

(a) Real and imaginary part of eigenvalue

(b) Norm of flight dynamics part of eigenvector compared to norm of whole eigenvector

Figure 4.4: Evolution of traced eigenpair as function of β for unsuccessful tracing.

The approximation of discarding the damping when calculating the interaction term Q leads to slightly different results compared to the Schur complement method in Fig. 4.2(a). However, the error introduced should be seen in relation to the computational cost which is much lower for the dynamic derivatives method. A trade-off between the two approaches is the inclusion of damping for the calculation of the dynamic derivatives. The pre-computation of Q was augmented to damped harmonic motions corresponding to a finite number of points in the complex plane. The set of 7 samples already available at zero damping was extended calculating the dynamic derivatives at the same frequencies but with a damping corresponding to the eigenvalue solution provided by the basic dynamic derivatives method. Note that this does not represent an optimised strategy which should focus on a refined local sampling instead. Adding local samples of Q and optimisation of the procedure was not attempted since it will eventually lead to the same results of Schur complement method as pointed out in Section 3.2. Two-dimensional linear interpolation was then used for points in the complex plane. The assumption of a linear behaviour of entries of Q with respect to the damping improves the final solution which is now closer to the exact result provided by the Schur complement method.

The case for the lower mass ratio of 35, when the eigenvalue related to the short period resides inside the cloud, as shown in Fig. 4.2(b), is significantly more challenging. The presence of fluid eigenvalues around the target eigenvalue misleads the Schur tracer converging to fluid eigenpairs during the tracing procedure instead. This is particularly critical when iterative methods are used to evaluate the interaction matrix, since the iterative solver might not converge at all. The eigenvalue evolution during an unsuccessful tracing is shown in Fig. 4.4(a). In addition, the relative importance of the flight dynamics part of the eigenvector $\boldsymbol{\phi}_r$ compared to the whole eigenvector $\boldsymbol{\phi}$ is depicted in Fig. 4.4(b). When $\beta \approx 0.8$, the Schur tracer starts iterating around an eigenpair for which the eigenvalue is not changing any more. However, it is clear from

Fig. 4.4(b) that the ratio $\|\phi_r\|/\|\phi\|$ decreases at every iteration for $\beta > 0.8$ while λ is nearly constant. This suggests that the Schur tracer is converging to an eigenvector whose flight dynamics part is becoming less and less important at every iteration. A way to alleviate this problem, while adding to the computational cost, is to increase the number of steps for the tracing. However, also this strategy fails for this case since increasing the number of steps from 25 to 150 does not improve the results. The problem is overcome using the dynamic derivatives method to calculate a first approximation of the solution. This method is not sensitive to the presence of fluid eigenvalues since it uses sample points to reconstruct Q. The resulting eigenvalue and eigenvector were used as initial solution for the Schur complement method which was able to converge to the exact solution in three iterations.

The same techniques for the identification of the short period were applied to the vertical translation mode without encountering any significant difficulty. Once the flight dynamics parts of the eigenvectors and the corresponding eigenvalues are available, the fluid parts were computed to assemble the right modal basis. As representative entry, the pressure component of the direct eigenvector related to the short period at $\mu = 100$ is shown in Fig. 4.5. Fluctuations around the shock positions are shown in Fig. 4.5(a) and they represent the most important feature of the flow field. Differences between the Schur complement and dynamic derivatives method are reported in 4.5(b) for the pressure magnitude. A negative difference was found upwind whereas a region of positive variation is located near upper and lower surfaces. The shock waves are sensitive regions since fluctuations were found. Overall, a difference of less than 0.4% was found in the pressure magnitude between eigenvectors resulting from the Schur complement method and the dynamic derivatives method.

The solutions to the corresponding adjoint problems in Eqs. (3.22) and (3.25) provided the adjoint eigenpairs required for the model reduction. Identifying these eigensolutions is trivial once the direct solution is known. In Fig. 4.5 the pressure component of the adjoint short period eigenvector calculated with the Schur tracing is depicted. The information is mainly distributed in the region surrounding the aerofoil, as shown in Fig. 4.5(c) whereas little information concerns the shock wave position. A comparison between results coming from the Schur tracer and the dynamic derivatives method is given in Fig. 4.5(d). A maximum positive deviation of 0.1% was found and it mainly concerns the upwind flow field since the region close to the aerofoil presents almost no differences.

Similarly, the fluid part of the direct eigenvector concerning the short period mode at $\mu = 35$ was extracted with the Schur complement method and presented in Fig. 4.6 using the pressure component. Regarding the pressure magnitude in Fig. 4.6(a), it looks very similar to the case $\mu = 100$ since the aerofoil's near field, in particular the shock wave region, contains most of the information. A comparison between Schur tracing and dynamic derivatives method is shown in Fig. 4.6(b). A major difference is visible near the shock wave located on the aerofoil's lower surface and another area of difference is

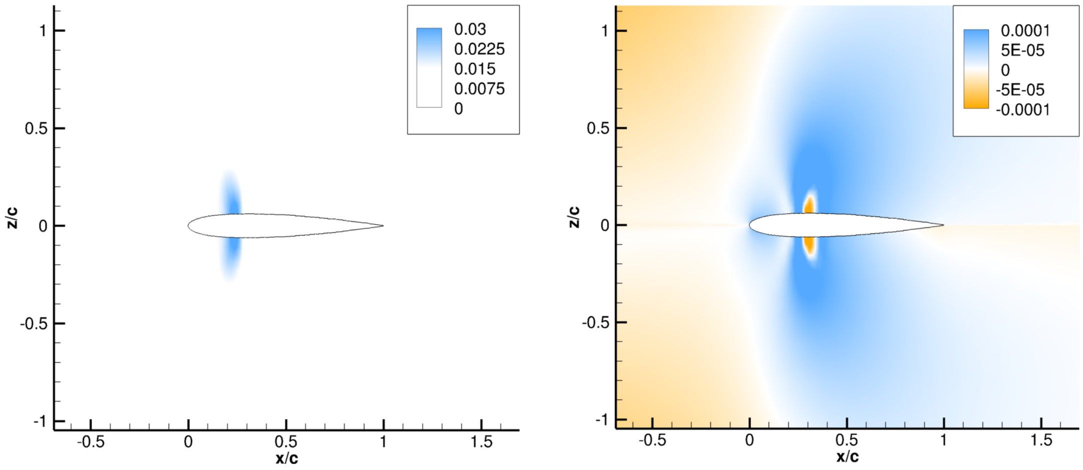

(a) Magnitude of direct eigenvector

(b) Difference due to neglecting damping for direct eigenvector

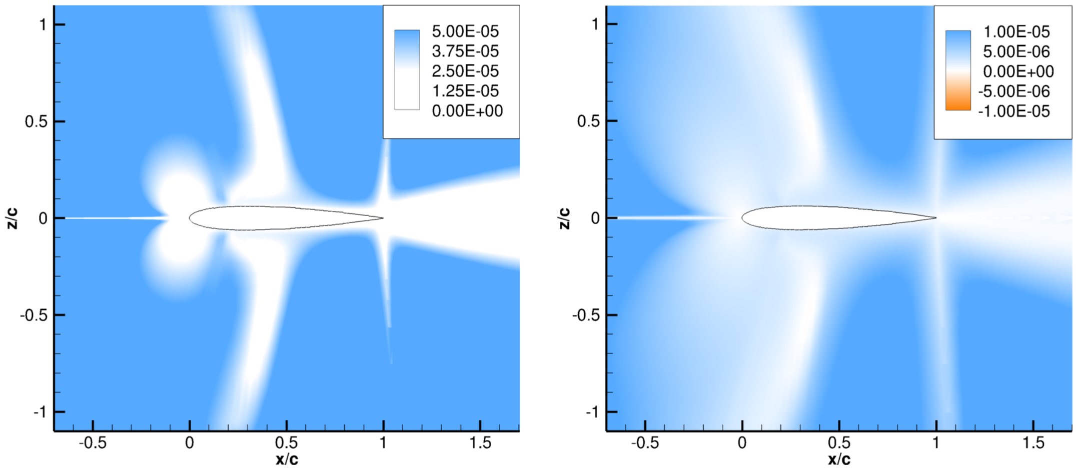

(c) Magnitude of adjoint eigenvector

(d) Difference due to neglecting damping for adjoint eigenvector

Figure 4.5: Pressure component of direct and adjoint fluid eigenvectors computed with Schur complement method and dynamic derivative method at $\mu = 100$.

found around the trailing edge. The corresponding adjoint eigenvector, calculated for the case $\mu = 35$ with the Schur method, is plotted in Fig. 4.7 presenting the pressure component as well. The magnitude in Fig. 4.7(a) shows that most of the information is concentrated in the region surrounding the aerofoil. When compared to results provided by the dynamics derivatives method, differences were found in large areas of the flow field, as shown in Fig. 4.7(b) and the largest difference is smaller than 0.2%. Overall, adjoint eigenvectors, which were computed with the Schur tracer, have a similar pattern for both $\mu = 35$ and $\mu = 100$, as shown in Fig. 4.7(a) and 4.5(c), respectively.

Two ROMs were built using the modes provided by the Schur complement method and the dynamic derivatives approach. Results using dynamic derivatives calculated

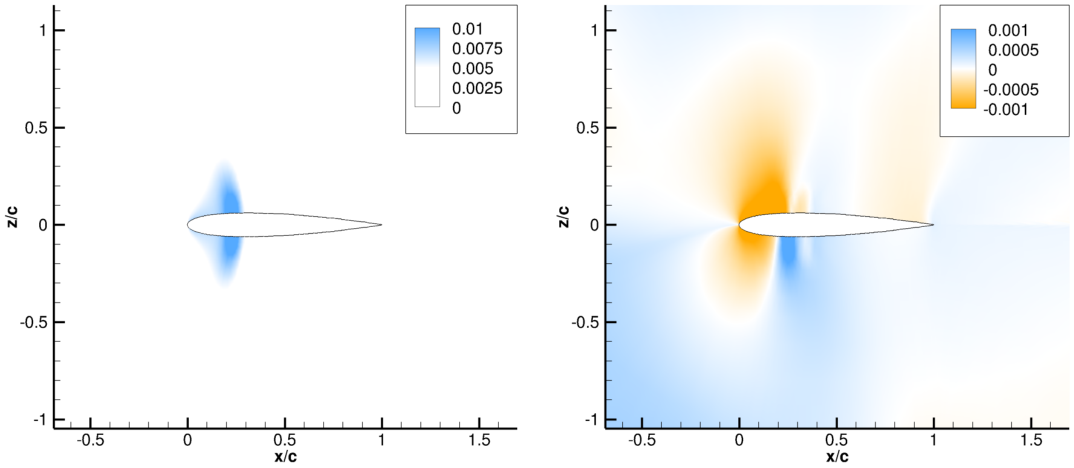

(a) Magnitude (b) Difference due to neglecting damping

Figure 4.6: Pressure component of direct fluid eigenvector computed with Schur complement method and dynamic derivative method at $\mu = 35$.

for damped harmonic motions are not included for sake of brevity since they do not differ significantly from the ones produced with the Schur complement method. Initial disturbance analyses with angular velocity $q^*(t = 0) = 0.1$ deg (per non-dimensional time-unit) were performed for both mass ratios and results are presented in Fig. 4.8. For $\mu = 100$ results from the reduced model based on the Schur complement method matches the reference full order model obtained with Eq. (2.54). Small differences are visible in the first two peak values presumably due to the broadband excitation given by the initial disturbance. This can excite flight dynamics as well as quickly-decaying aerodynamic modes, leaving the system response to the dominant modes. Results from the dynamic derivatives method show an underestimation of peak values and a general frequency shift due to the approximations made. The case for $\mu = 35$ presented in Fig. 4.8(b) provides a stronger damped response as expected from the real part of the short period eigenvalue. The reduced model built with the dynamic derivatives method is less accurate for the transient decay even though the transition to the new equilibrium state, characterized by a return to zero velocity, is captured. The case with $\mu = 35$ is not discussed further at this point since it is outside the scope of the chapter which focuses on a first application of operator-based and data-based identification instead. A case leading to similar results is investigated in detail in the next chapter.

The reduced model was extended by introducing an external excitation to demonstrate its versatility. An application is described for a flap device at $\mu = 100$ for which a deflection law is defined as a time-dependent function. Regarding the full order model, flap rotation is imposed at each physical time-step with radial basis function mesh deformation, as described in Section 2.4.1, applied to the rear 25% of the aerofoil. The flap action is introduced in the reduced model with the term $\Psi^H \frac{\partial \boldsymbol{R}}{\partial \boldsymbol{u}_c} \widetilde{\boldsymbol{u}}_c$ in Eq. (3.7).

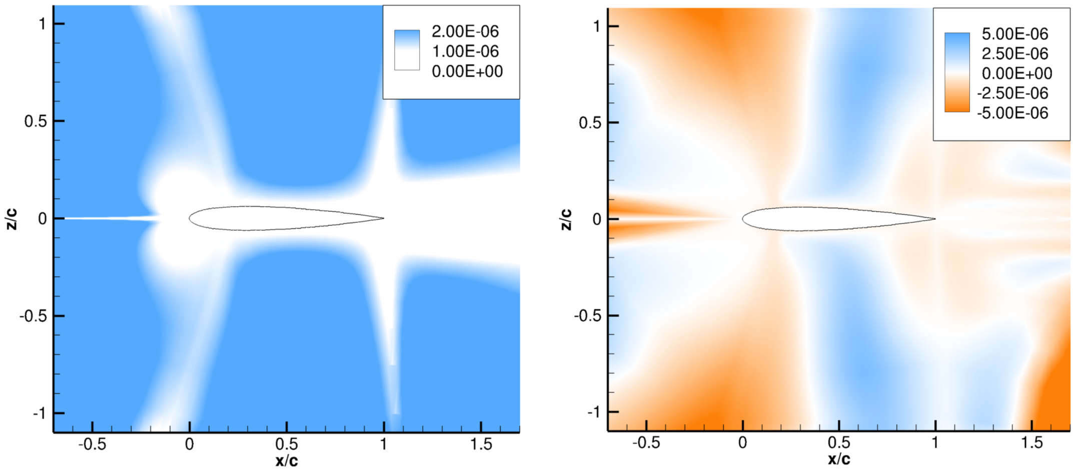

(a) Magnitude (b) Difference due to neglecting damping

Figure 4.7: Pressure component of adjoint fluid eigenvector computed with Schur complement method and dynamic derivative method at $\mu = 35$.

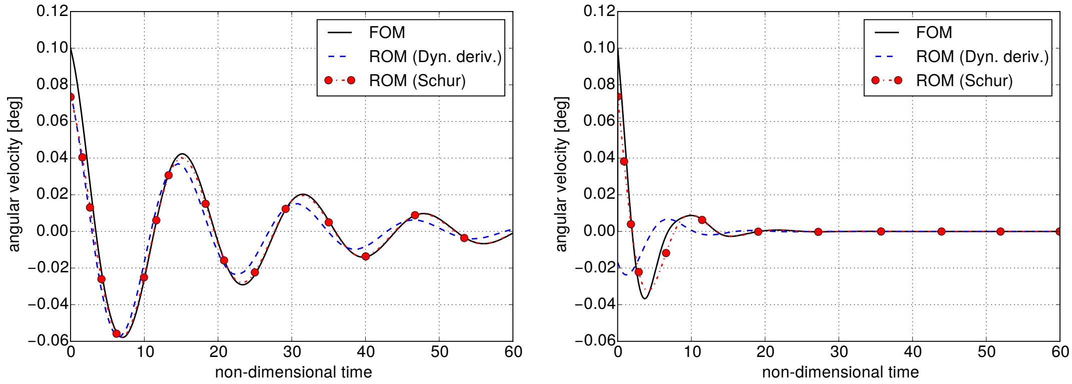

(a) Angular velocity at $\mu = 100$ (b) Angular velocity at $\mu = 35$

Figure 4.8: Response to initial disturbance in angular velocity of $q^* = 0.1$ deg.

Specifically, the deflection law depicted in Fig. 4.9(a) was simulated. The maximum rotation is 2 deg which is reached after 5 non-dimensional time units with an excitation lasting 10 time units in total. A picture of the maximum deformation is also given in Fig. 4.9(a). The results from the reduced model are compared with the reference in Fig. 4.9(b). Angular velocity only is shown since similar behaviours were found for the other flight dynamics quantities. At first, the system moves because of the additional lift and moment increment given by the flap deflection. However, when the flap returns to an undeflected position, the system returns to an equilibrium condition after a few oscillations. The reduced model based on the Schur complement method is capable of reproducing accurately full order results. Both transient and final equilibrium are well represented. Overestimation of peak values is shown for the reduced

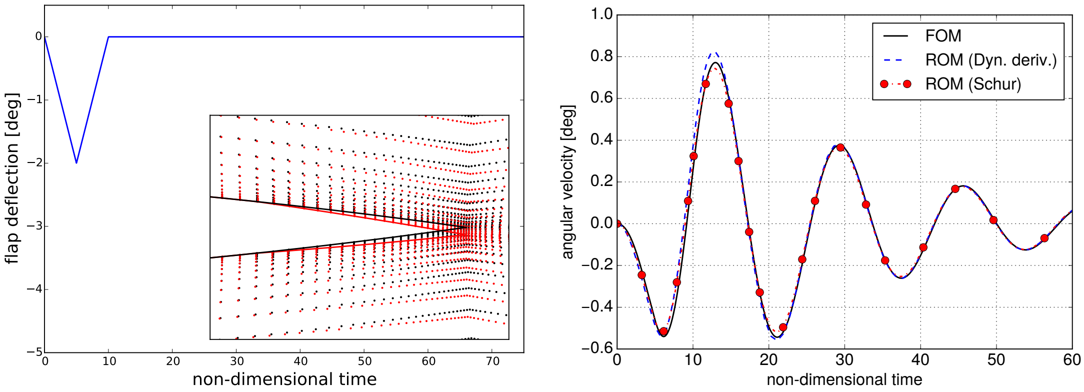

(a) Deflection law and deformed grid

(b) Angular velocity

Figure 4.9: Response to a flap excitation at $\mu = 100$.

model based on the dynamic derivatives. The increment in angular velocity due to the flap deflection is not captured accurately. However, the system's dynamics is well reproduced once the flap has returned to the undeflected position.

The inclusion of external disturbances leads to a reduced model capable of incorporating flight dynamics effects for gust encounter simulations, which is an objective of this work. In particular, gust encounter simulations performed with and without flight dynamics effects lead to different results. The former ones concern a fixed, static, aerofoil which does not move because of the gust. Conversely, the aerofoil is free to rotate and move vertically for the latter. An example produced with the full order model at $\mu = 100$ is given in Fig. 4.10, showing loads for a gust encounter of a travelling '1-cos' gust with amplitude $V_g = 0.1\%$ of free-stream velocity and initial starting point at the aerofoil leading edge. Results for motion are not reported since irrelevant for the fixed, static, aerofoil. Two gust wavelengths with $L_g = 5$ and $L_g = 10$ chords were investigated. Including flight dynamics effects changes the peak values for lift and moment and modifies the general behaviour. Part of the energy from the disturbance goes into the system dynamics. As a results, the peak values are lowered and effects on rigid-body dynamics are significant and still visible after the disturbance has passed the system.

Corresponding simulations were performed with the reduced model as well and results are depicted in Fig. 4.11. Aerodynamic influences contained in the flight dynamics eigenpairs are able to capture the response of the system to external disturbances such as gusts for the two wavelengths considered. The results from the Schur complement method are compared to the full order model showing a general good agreement. Some differences arising in the peak values might depend on a non-complete description of the aerodynamic phenomena. The reduced model built with the dynamic derivatives method shows an underestimation of peak values and a shift in the frequency, when compared to the Schur complement method. The error in the identification of the flight dynamics

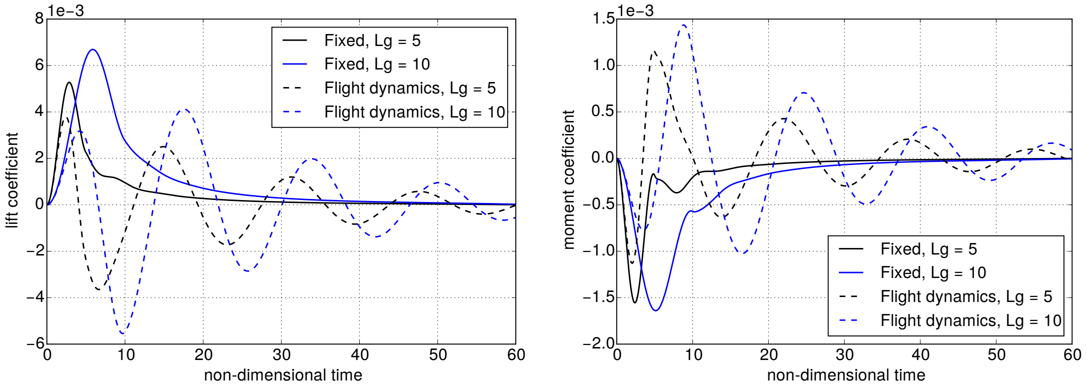

(a) Lift coefficient

(b) Moment coefficient

Figure 4.10: Effects of including flight dynamics when simulating a gust encounter for '1-cos' gust of amplitude $V_g = 0.1\%$ free-stream velocity at $\mu = 100$. with full order model.

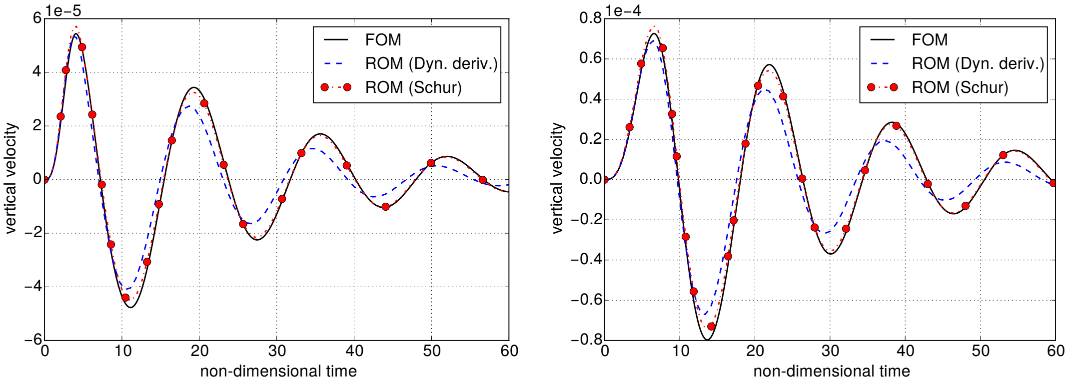

(a) Gust wavelength $L_g = 5$

(b) Gust wavelength $L_g = 10$

Figure 4.11: Gust encounter simulation for '1-cos' gust with amplitude $V_g = 0.1\%$ of free-stream velocity at $\mu = 100$.

eigenpairs, as shown in Fig. 4.2(a) and Fig. 4.5, affects the final results by means of Eq. (3.7). The decay ratio and frequency, linked to the real and imaginary parts of the eigenvalues, are therefore different from exact values given by the Schur complement method. The trend is reproduced for short and long gusts and the differences between reduced and full model increased with the number of oscillations.

4.4 Data-based Identification

Data-based identification was investigated as well by calculating the system response to external disturbances. In particular, the method was applied to gust encounter simulations at $\mu = 100$, when flight dynamics is more relevant to the system and less coupled with aerodynamics. The application of the data-based method requires the

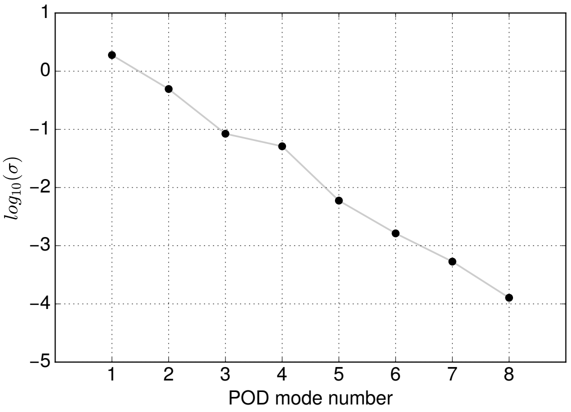

Figure 4.12: POD eigenvalues.

'1-cos' time-domain gust signal to be translated into the frequency domain as sum of sinusoidal gusts at distinct frequencies. The complex-valued responses of the system to these harmonic gusts were calculated for the coupled model by solving Eq. (2.58) with an LFD solver and then stored in a snapshot matrix. Specifically, snapshots were calculated for 25 reduced frequencies linearly distributed in the range 0 to 2. The frequency range, and its upper limit in particular, was chosen as described in Section 2.3 for the expansion of the '1-cos' gust in a Fourier series in Eq. (2.61). A number of 25 harmonics were sufficient to reconstruct the '1-cos' signal accurately. Thus, 25 POD modes and their complex-conjugate were obtained as a result. They do not necessarily represent physical modes for the coupled system. No exact correspondence with flight dynamics modes is immediately identifiable. Modes can be rated in terms of energy content and the most energetic ones contain more information. In Fig. 4.12, the POD eigenvalues corresponding to the first 8 modes are depicted using a bar chart. The energy distribution shows a constant decay for each mode beyond the first and a difference of 5 orders of magnitude between the first and the eighth mode was found. The pressure component of the first mode is shown in Fig. 4.13(a). Information about pressure is concentrated around the shock-wave area on both upper and lower surface leading to a symmetric field. The shock wave is the most important feature of the flow field. The second mode is not reported since the distribution is similar to the first one. However, the third mode presents an asymmetric distribution of pressure magnitude with information spread both in the flow field as well as near the surface. POD modes, sorted by their energy contents, describe features of the flow field starting from shock wave position in the first two modes to weak pressure fluctuations in subsequent modes. The flight dynamics part of POD modes, which are reported in Tab. 4.1, is non-zero since they are calculated for the coupled system. Angular velocity and pitch rotation have an almost equal participation in the first mode whereas also the vertical velocity component is not negligible. A similar distribution is given for the second mode while the third mode is dominated by the component related to angular velocity.

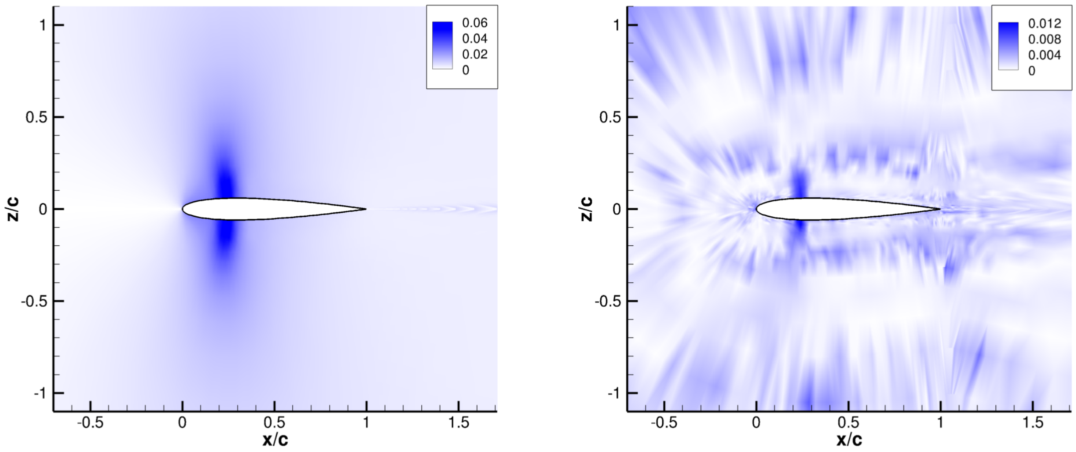

(a) POD mode 1

(b) POD mode 3

Figure 4.13: Magnitude of pressure component for two POD modes.

Table 4.1: Flight dynamics part of first three POD modes.

Component	Mode 1	Mode 2	Mode 3
vertical velocity	$-0.1081 + 0.0050\jmath$	$-0.0995 + 0.0115\jmath$	$0.0202 - 0.0147\jmath$
angular velocity	$0.3511 - 0.9364\jmath$	$0.4063 - 0.9137\jmath$	$0.5876 + 0.8092\jmath$
pitch rotation	$0.3957 + 0.1895\jmath$	$0.4501 + 0.0252\jmath$	$-0.0071 + 0.0018\jmath$

The set of POD modes resulting from the data-based identification is used to build the reduced order model by means of Eq. (3.9). In Fig. 4.14, the system's response to the encounter with a travelling '1-cos' gust with intensity $V_g = 0.1\%$ of free-stream velocity and wavelength $L_g = 10$ chord lengths is depicted. Results are reported for the reduced model built using 10 and 25 POD modes. Only vertical velocity and lift coefficient are shown since a similar agreement is obtained for all the flight dynamics degrees-of-freedom. Using the data-based ROM with 10 POD modes provides results which are qualitatively comparable to the full order reference. Underestimation of peak values and phase lag is found for both vertical velocity and lift coefficient. The error is due to the insufficient number of POD modes included in the modal basis. Additional simulations, whose results are not reported here, were performed using 5, 15, 20, 25 and 30 POD modes in order to identify the minimum number of modes which provides good accuracy. Using more than 25 POD modes did not improve results. Loads and motions are evaluated accurately for both transient decay and final steady state when 25 modes are employed as shown in Fig. 4.14. No appreciable differences were found between the reduced and full order models. The same simulation was performed with the operator-based ROM as well. Overall its results match the reference. Some differences arising in the peak values might depend on modes lacking information to completely describe the aerodynamic phenomena. This problem will be analysed in detail in the next chapter.

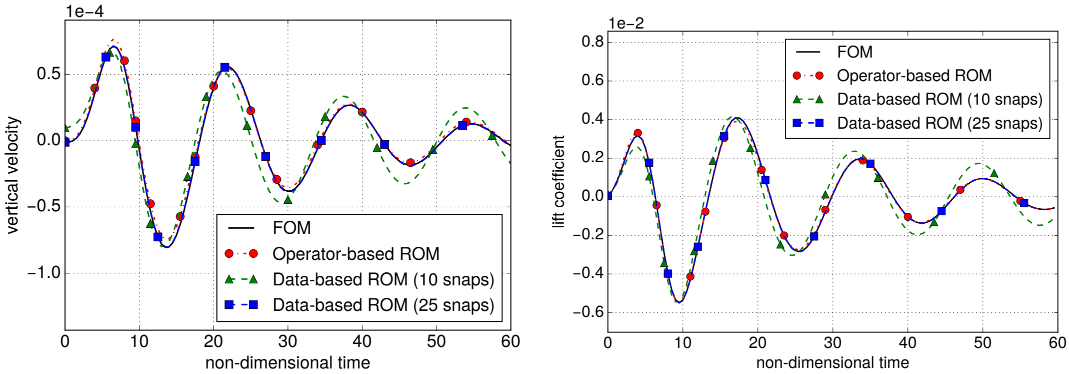

(a) Vertical velocity

(b) Lift coefficient

Figure 4.14: Response to gust encounter for '1-cos' gust of amplitude $V_g = 0.1\%$ free-stream velocity and gust wavelength of 10 chord lengths at $\mu = 100$.

4.5 Computational Cost

The computational cost for ROMs can be split in two main contributions, specifically the mode identification using LFD and the integration of ROM equations. The computational cost of one LFD solution in Eq. (2.59), which needs less than 1 m 30 s on a single Intel Xeon E3-1245 CPU, is taken as a reference. Calculating the flight dynamic modes with the operator-based identification using the Schur complement method needs 2 LFD solutions for each of 20 β-steps for a total of 40 LFD solutions (60 minutes). Solving for the adjoint eigenpairs requires only 4 additional LFD solutions since the tracing can start from direct eigenvalues. Hence, the identification with the Schur complement method requires 44 LFD solutions. Using dynamic derivatives reduces the required number of LFD solutions to 14 and the adjoint problem is solved in a negligible time since no expensive computation needs to be performed. Introducing the damping for dynamic derivatives needs 28 LFD solutions since the sampling performed for the simple dynamic derivative method must be repeated at least twice. Regarding the data-based identification, it requires a number of LFD solve equal to the number of modes, thus 25 LFD solutions were required. Concerning the second contribution which is given by the integration of ROM equations, it can be assumed negligible on any modern CPU. These numbers compare to the full order model which takes 1 h 30 m to perform a forced-motion simulation which provides the same results of an LFD solution. It needs 1 h 58 m for a single '1-cos' gust encounter. Please, note that once the reduced model is built, it can be employed to investigate multiple gust lengths thus obtaining a reduction in computational cost up to two order of magnitude. This is valid for the reduced model based on both operator-based identification and the data-based one. An application of such desirable versatility will be provided for a industry-size test case in Chapter 6.

4.6 Chapter Summary

This chapter described the application of the operator-based and data-based identification methods to a two-dimensional aerofoil test case. In particular, the size of the problem allowed for a detailed investigation of the operator-based identification with the possibility of comparing results to eigenvalue extraction using direct methods. The tracing procedure was described for two values of the mass ratio μ for which the system shows different behaviours. They correspond to two flight conditions of a small-to-medium range aircraft. The operator-based identification is easier to perform for cases when flight dynamics is a dominant aspect of the system, as it is the case for mass ratio $\mu = 100$. For those cases, both Schur complement method and dynamic derivative formulation lead to accurate results compared to the reference full order data. More challenging is the identification when the flight dynamics mode is in the pack of aerodynamic eigenvalues at $\mu = 35$. The dynamic derivative method is then used to provide an initial guess for the Schur tracing. The Schur complement method converges to the exact eigenpairs provided by the direct method for all cases analysed while limitations were found for the dynamic derivatives method.

Initial disturbance analysis are performed with the operator-based reduced model for both values of mass ratio. A good agreement was found for $\mu = 100$. Conversely, only a qualitative comparison with the full order reference can be done at $\mu = 35$. This different behaviour requires a detailed analysis which is provided in the next chapter for a more complex test case. Focusing on the case $\mu = 100$, the operator-based reduced model was expanded towards external excitation. First, a flap deflection was considered. The operator-based reduced model built with the Schur tracing is able to reproduce the full order flight dynamics response accurately. The second investigation concerned gust disturbances and the reduced model was exploited to perform gust encounter simulations including free flight effects. Overall, the operator-based ROM provided accurate results while some small discrepancies are shown in the peak values for lift coefficient. The same configuration was investigated using the data-based identification. The system response to sinusoidal gusts was sampled using an LFD approach at various frequencies and POD modes calculated. Results from this method show a very good agreement with the full order solutions.

The test case represented an effective test bed before expanding the method to larger cases. All key aspects were investigated, in particular mode identification, flight dynamics coupling with computational fluid dynamics and linearised frequency domain methods. In the next chapter, an application of the method to a more complex test case is presented. Furthermore, some open questions raised in this chapter regarding operator-based ROMs at small values of mass ratios will be addressed.

Chapter 5

Longitudinal Dynamics

Application of the mode identification and model reduction to a wing-tail configuration is exercised in this chapter. Specifically, two aerofoil geometries are combined. They represent wing and horizontal tail, respectively, to describe the dynamics representative of a large civil aircraft. Transonic aerodynamics is based on RANS equations with Spalart–Allmaras turbulence model so that viscous effects, shock waves and their mutual interactions are included in the analysis.

The horizontal degree-of-freedom plays an important role and there are two relevant flight dynamics modes, specifically short period and phugoid. The former has been already introduced in Chapter 4. Regarding the latter, it describes a motion composed of slow variations in flight speed and altitude but almost negligible changes in angle-of-attack [34, 155]. Results support the findings already shown for the aerofoil in the previous chapter and problems which arise when increasing the complexity of the model are addressed. Key challenge tackled in this chapter is mode identification and model reduction for cases when the flight dynamics eigenpairs are immersed in the cloud of fluid eigenvalues. A quasi-steady formulation, which is based on stability derivatives, is exploited to overcome this problem by providing the operator-based identification with a reliable initial guess. The majority of results has been published in a refereed journal paper [106].

5.1 Governing Equations

The equations derived in Section 2.2 are used in this chapter for longitudinal dynamics. In particular, Equations (2.38) are restated here for convenience,

$$\begin{aligned} &\frac{\mathrm{d}u^*}{\mathrm{d}\tau} + W_0^* q^* = \frac{C_x}{\pi\mu} \qquad &&\frac{\mathrm{d}w^*}{\mathrm{d}\tau} - U_0^* q^* = \frac{C_z}{\pi\mu} \\ &\frac{\mathrm{d}q^*}{\mathrm{d}\tau} = \frac{2C_m}{\pi\mu r_\alpha^2} \qquad &&\frac{\mathrm{d}\theta^*}{\mathrm{d}\tau} = q^* \end{aligned} \tag{2.38}$$

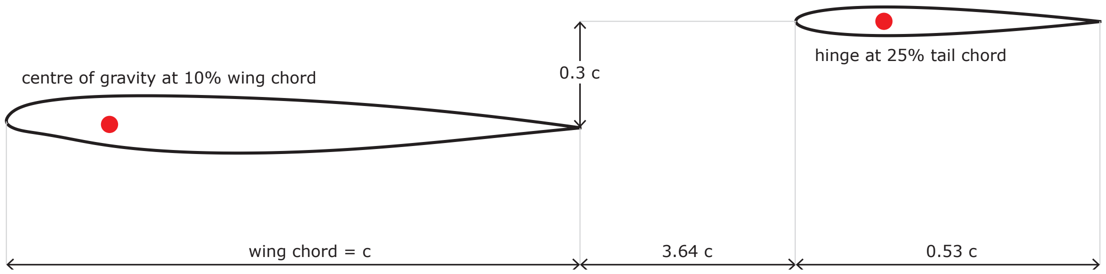

Figure 5.1: Wing-tail configuration analysed for longitudinal dynamics (not to scale).

The reference length for the non-dimensional parameters is defined as the wing semi-chord while coefficients of drag, lift and moment follow the usual convention.

5.2 Wing and Tail Configuration

The configuration investigated in this chapter is representative of the longitudinal dynamics of a large civil aircraft. The model is composed of a supercritical Crank aerofoil for the main wing and a NACA 0008 for the horizontal tail as shown in Fig. 5.1. The centre of gravity, which is also the reference point for moment calculation, is at 10% of the main wing chord. The horizontal tail hinge axis is at 25% of its chord. The RANS equations are discretised on 115,224 grid points with the far-field located 100 chord lengths away from the body. The fluid flow is transonic at Mach number of 0.75 and Reynolds number based on the chord length of the main wing of 7 million. The non-dimensional parameter $r_\alpha = 3.5$, while two values for the non-dimensional mass ratio μ are investigated, specifically $\mu = 730$ and $\mu = 73$. The former corresponds to a condition for which the flight dynamics modes are outside the cloud of the eigenvalues of the couples CFD/flight dynamic system and they are dominant modes for the system dynamics. A physical interpretation is a combination of large aircraft mass and high altitude for which the short period mode has low damping and the related eigenvalue is close to the imaginary axis of the complex plane. The mass ratio of $\mu = 73$ on the other hand corresponds to a large civil aircraft flying at about 10 km altitude.

The initial equilibrium condition is obtained with an iterative trimming procedure based on the Broyden method [27]. Target values of lift and moment coefficients, C_{L0} and C_{M0}, are chosen based on representative level flight conditions. The independent unknowns α and δ are defined as angle-of-attack and horizontal tail rotation, respectively, positive clockwise. The trim equations are written as

$$\begin{aligned} C_L(\alpha,\delta) &= C_{L0} \\ C_M(\alpha,\delta) &= C_{M0} \end{aligned} \tag{5.1}$$

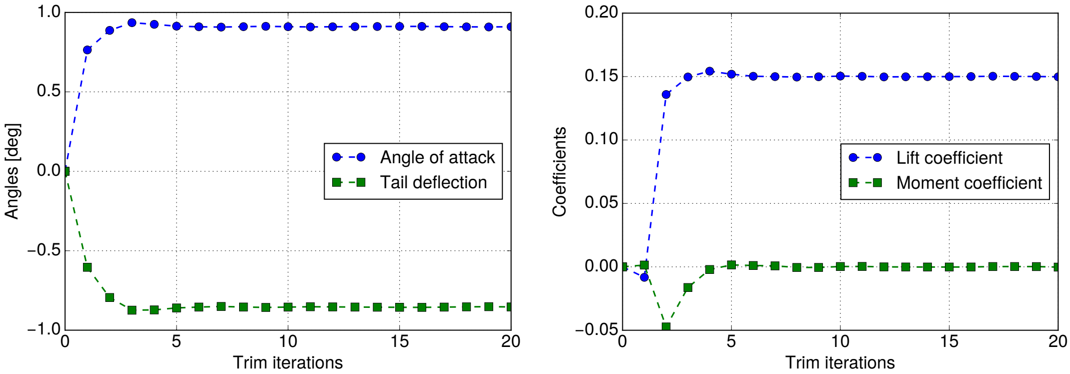

(a) Independent variables

(b) Objective functions

Figure 5.2: Convergence of trimming procedure for unknowns and objective functions.

and the Broyden method is applied to the first order Taylor expansion of these,

$$\begin{pmatrix} \frac{\partial C_L}{\partial \alpha} & \frac{\partial C_L}{\partial \delta} \\ \frac{\partial C_M}{\partial \alpha} & \frac{\partial C_M}{\partial \delta} \end{pmatrix} \begin{bmatrix} \Delta\alpha \\ \Delta\delta \end{bmatrix} = \begin{bmatrix} C_{L0} - C_L \\ C_{M0} - C_M \end{bmatrix} \tag{5.2}$$

which can be written more concisely in vector form as $J\boldsymbol{\Delta x} = \boldsymbol{\Delta F}_A$. The iterative method starts with an rough estimation of the derivative matrix J which is approximated using central finite differences with infinitesimal increment ϵ. Independent variables are altered in turns by adding $\pm\epsilon$ and a steady state computation is performed for each alteration. Values of lift and moment coefficients from steady state solutions corresponding to $+\epsilon$ and $-\epsilon$ alterations of the same independent variable are used to compute the derivatives according to the central scheme [114]. For the following trimming iterations, angle-of-attack and tail rotation are imposed with RBF mesh deformation and loads are calculated restarting the steady state computation for few iterations. An update of $\boldsymbol{\Delta x}$ is then computed. After the first iteration, the derivative matrix J is updated for the current iteration i using data from the previous step $i-1$ [27].

$$J_i = J_{i-1} + \frac{\boldsymbol{\Delta F}_A - J_{i-1}\boldsymbol{\Delta x}_i}{||\boldsymbol{\Delta x}_i||^2}\boldsymbol{\Delta x}_i^T \tag{5.3}$$

The trimming procedure ends when the norm $||\boldsymbol{\Delta x}||$ is below a defined tolerance. A thrust force is added to the horizontal direction whose value is calculated to balance the drag at equilibrium condition.

The trimming procedure was applied for values of $C_{L0} = 0.15$ and $C_{M0} = 0$. They are representative of a large civil aircraft in cruise. Values of $\epsilon = 1 \times 10^{-6}$ and a convergence tolerance of 1×10^{-6} were adopted. The evolution of the independent quantities α and δ is shown in Fig. 5.2(a). A smooth transition from zero to close-to-final values takes place in the first few iterations for both angle-of-attack and tail rotation. After 10 iterations, only tiny modifications to the value were obtained. Similarly, lift

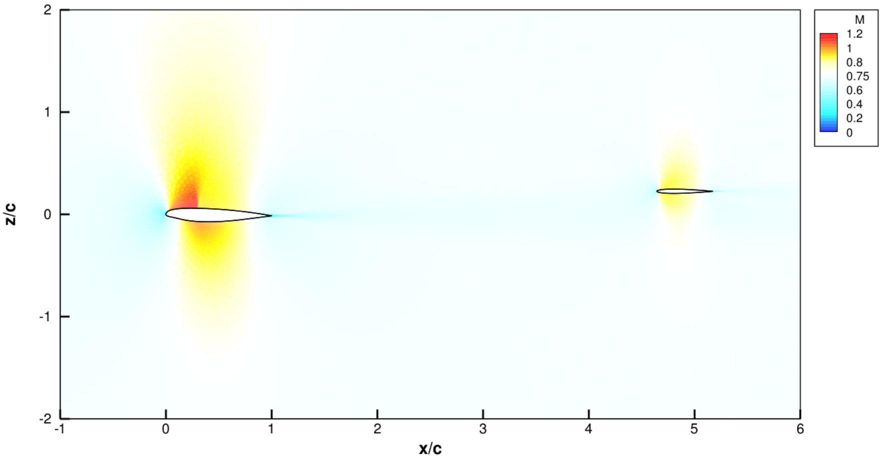

Figure 5.3: Mach number field resulting from trimming procedure.

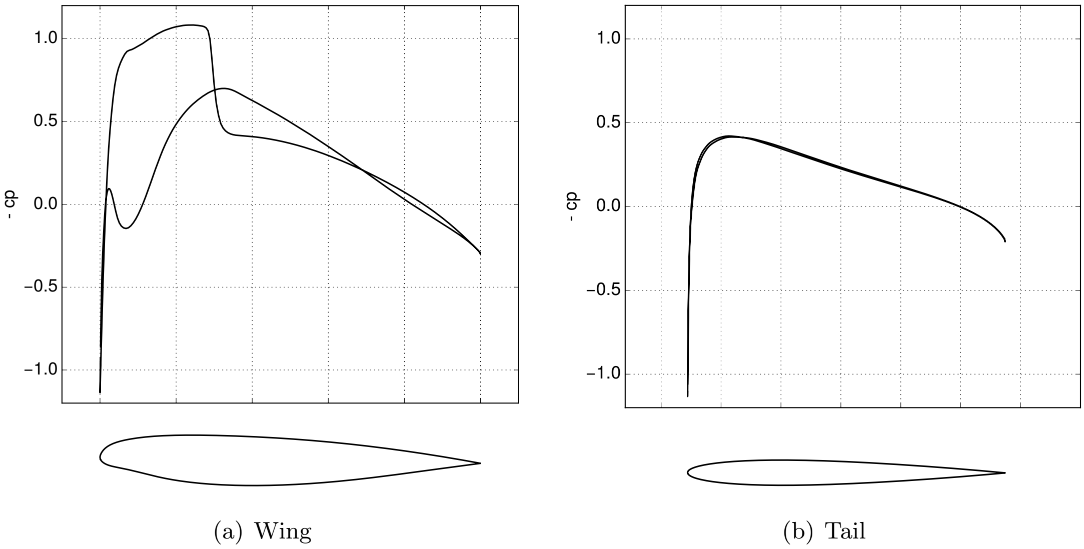

(a) Wing

(b) Tail

Figure 5.4: Pressure coefficient at steady state for Crank and NACA 0008 aerofoils.

and moment coefficients go through few initial oscillations as shown in Fig. 5.2(b). The increased angle-of-attack produces an increment in lift and alters the moment. An update to the tail rotation is needed to balance the additional moment. The convergence criterion is satisfied after 20 iterations. The converged angle of attack and tail rotation are 0.91 deg and -0.85 deg, respectively, with clockwise positive rotations.

The resulting steady flow, used as reference point for the subsequent linearisation, is shown in Fig. 5.3 plotting the Mach number field. A shock wave is clearly visible on the wing's upper surface whereas the shock is weaker on the lower one. Particular care was taken to have a shock free tail as common practice for large civil aircraft and that is achieved with an aerofoil thickness of 8%. The pressure coefficient C_p on surfaces is shown in Fig. 5.4. For the main wing in Fig. 5.4(a), the diagram is typical of a supercritical aerofoil and a shock wave is clearly identifiable on the upper surface. Regarding the tail's pressure distribution in Fig. 5.4(b), no shock wave is found. Note that despite a tail rotation of -0.85 deg, the C_p distribution is almost-symmetric and this suggests the horizontal tail is working at a very small angle-of-attack. This is due to the downwash effect which alters the effective flow incidence angle for the tail [122].

5.3 Quasi-Steady Approximation

Traditionally, flight dynamics performance of aircraft is assessed using an approach based on stability derivatives [34, 155]. While their values are computed at equilibrium points similar to LFD methods, the traditional derivatives do not take unsteady effects into account. The method provides a quick approximation of flight dynamics characteristics such as eigenvalues for handling assessment. However, its quick application (and main limitation) comes from assuming that aerodynamics is completely described by stability derivatives. This approach was applied to the test case and results are compared to the non-linear full order model based on URANS equations. Thus, the difference between the traditional formulation and the non-linear CFD-based model is highlighted. In addition, flight dynamics eigenvalues from stability derivatives will provide a good starting point to the operator-based identification described in the next section. More mathematical details and a reproduction of bibliography results for verification purposes are provided in Appendix C.

Hereafter, the traditional method is referred to as *quasi-steady* (QS). The name is taken from literature [22, p. 279] where the QS simplification assumes very slow unsteady aerodynamic phenomena. They are important at reduced frequencies very close to the zero which designates the steady state behaviour. At such low frequencies approaching zero, the dynamic derivatives are no longer complex-valued but they become real numbers, which are referred to as stability derivatives. In this context, the stability derivatives were calculated at $\mu = 73$ (representing aircraft dynamics close to cruising flight) using two strategies. First, central finite difference with two steady state computations was employed. The value of stability derivative $C_{L_\alpha} = 14.57$ corresponds to the well-known slope of the curve relating lift coefficient to angle-of-attack. This is shown in Fig. 5.5(a) for the $C_L(\alpha)$ curve as well as its linear approximation. Similarly, the evaluation of the stability derivative $C_M(\alpha)$ is reported in Fig. 5.5(b). Secondly, LFD solutions of Eq. (2.64) with a reduced frequency of zero provided the same values. Once the stability derivatives are available, flight dynamics characteristics can be evaluated.

First, approximate eigenpairs for flight dynamics modes were obtained using the stability derivatives. The short period mode and phugoid are associated to the two complex-valued eigenvalues $-0.0636 + 0.250i$ and $-0.000565 + 0.000287i$, respectively. The difference between the two modes is clear. The former has a much higher frequency and stronger damping whereas the latter shows little damping and very low frequency.

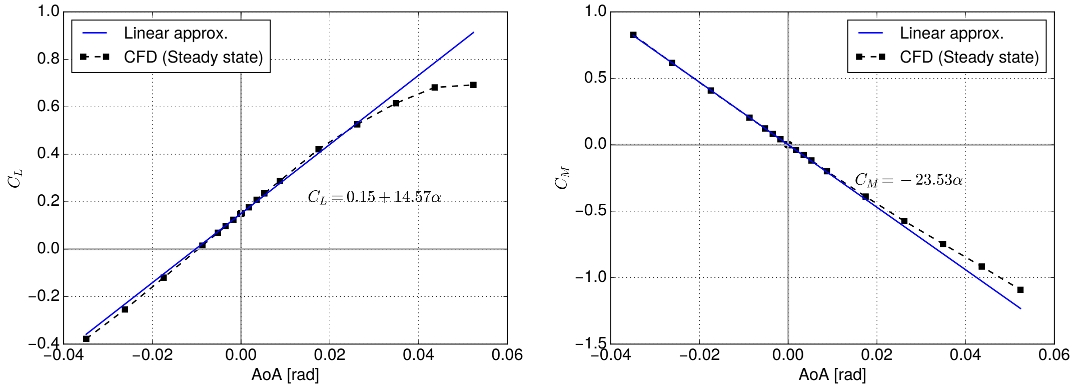

(a) Lift coefficient (b) Moment coefficient

Figure 5.5: Evaluation of stability derivative from steady state computation.

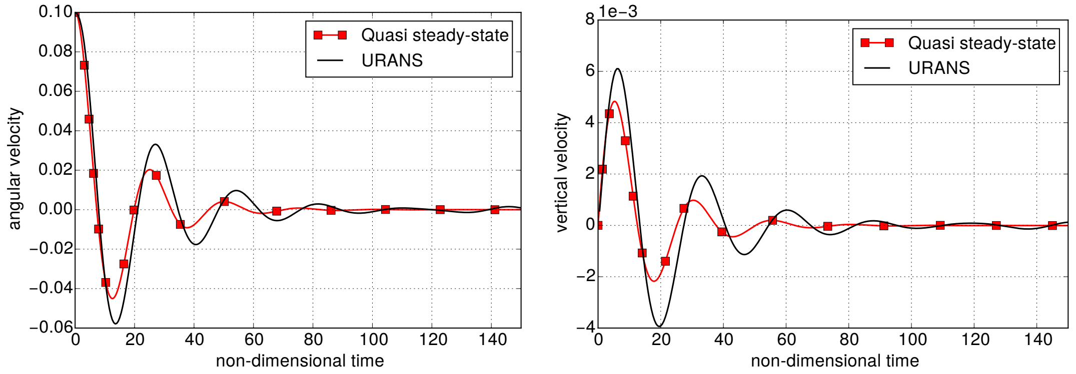

(a) Angular velocity (b) Vertical velocity

Figure 5.6: Results for initial disturbance analysis in angular velocity of $q^*(t = 0) = 0.1\,\text{deg}$. Simulation performed with QS approach and URANS.

Secondly, the stability derivatives from the QS model were exploited to integrate the flight dynamics equations in time for an initial disturbance simulation in the angular velocity with $q^*(t = 0) = 0.1\,\text{deg}$ (per non-dimensional time-unit). Results were obtained with the URANS full order model for the same excitation as well and they are summarised in Fig. 5.6. Regarding the angular velocity shown in Fig. 5.6(a), the QS curve has the same trend as the URANS reference and a similar oscillation frequency. However, the decay ratio is different and this leads to underestimation of peak values. A similar behaviour was obtained for the vertical velocity in Fig. 5.6(b). The underestimation of peak values and also a frequency shift are clearly visible. The same final equilibrium is eventually reached by both models. These differences could be related to unsteady effects not described properly using stability derivatives only.

Although the QS model shows the same trend of the URANS model, the accuracy in terms of flight dynamics response is inadequate for high-fidelity purposes. However,

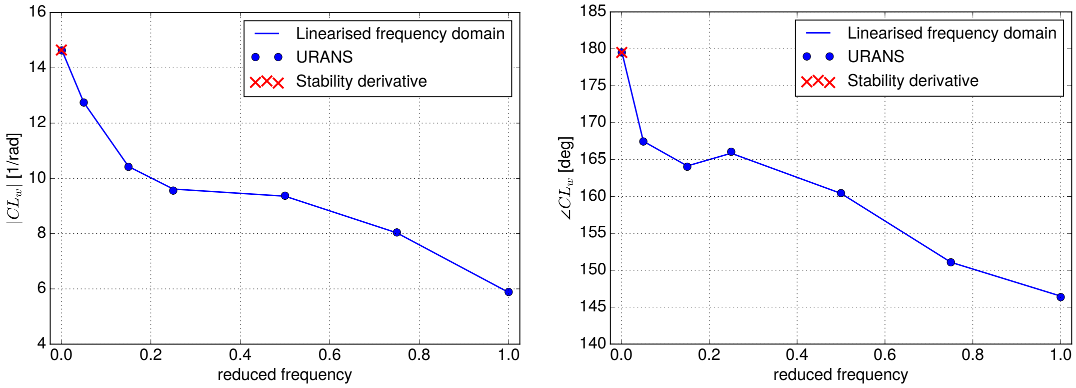

(a) Magnitude

(b) Phase in degrees

Figure 5.7: Magnitude and phase of dynamic derivative $C_{L w}$ (i.e. lift coefficient with respect to plunge) shown as representative entry of Q.

the QS model provides a starting point for the ROM. In particular, the approximate eigenpairs obtained in this section served as initial guess for the operator-based tracing.

5.4 Operator-based Identification

The operator-based identification is discussed next. The dynamic derivatives were calculated at 7 reduced frequencies in the range 0 to 1 using an LFD solver. The frequency range was chosen based on the estimation of flight dynamics eigenvalues provided by the QS method. The derivative relating lift coefficient to plunge motion is depicted in Fig. 5.7 as representative entry of the matrix Q in Eq. (3.25). It is a key entry of Q since its value can be be linked directly to the short period frequency [34]. The trend for magnitude, which is qualitatively comparable to results presented in Fig. 4.3, is characterised by a decreasing curve. Similarly, the phase is shown in Fig. 5.7(b) and it decreases as function of frequency. A local minimum is found around a reduced frequency of 0.15. Forced motion simulations were performed with URANS to verify the LFD calculations and results, which were obtained as described in Section 3.2.1, are reported in Fig. 5.7 as well. The tiny amplitude employed for the time-domain simulations is 0.0001 in order to have a linear behaviour of the system. Matching results were found for both magnitude and phase, confirming the validity of the LFD method. In addition to dynamic derivatives, the stability derivatives evaluated with the QS method in Section 5.3 are included in the plots at zero frequency. This is done to highlight the difference between static and dynamic derivatives in the context of flight dynamics since the former do not depend on the frequency.

The same frequencies were sampled at 3 different damping values in the range from -0.1 to 0 in order to include, later on, the real part of eigenvalues when calculating Q for the tracing. Figure 5.8 presents results of the mode identification for both mass cases.

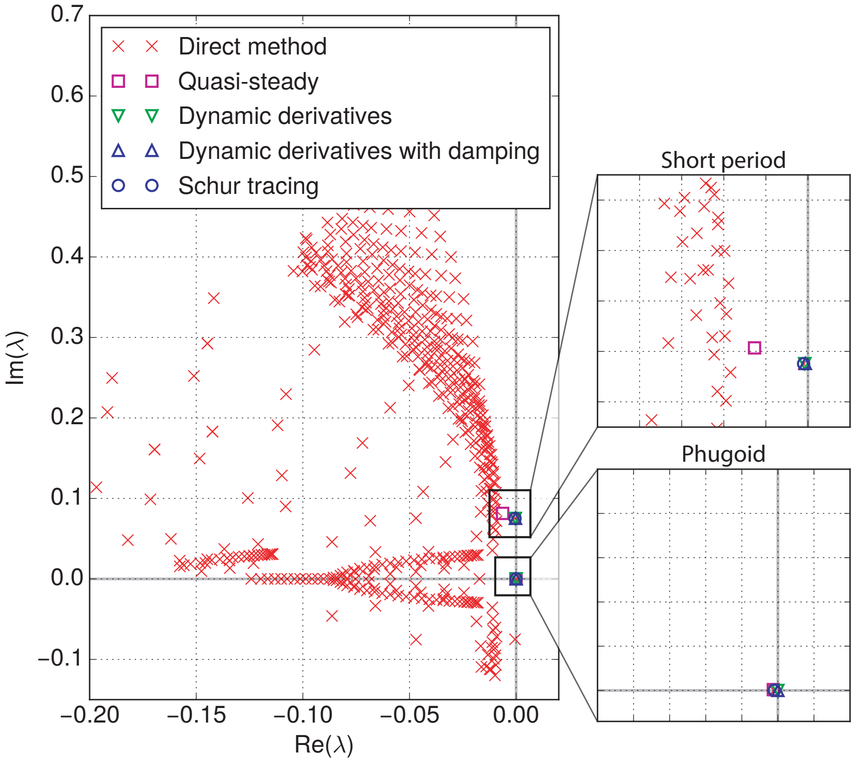

(a) Identification at $\mu = 730$

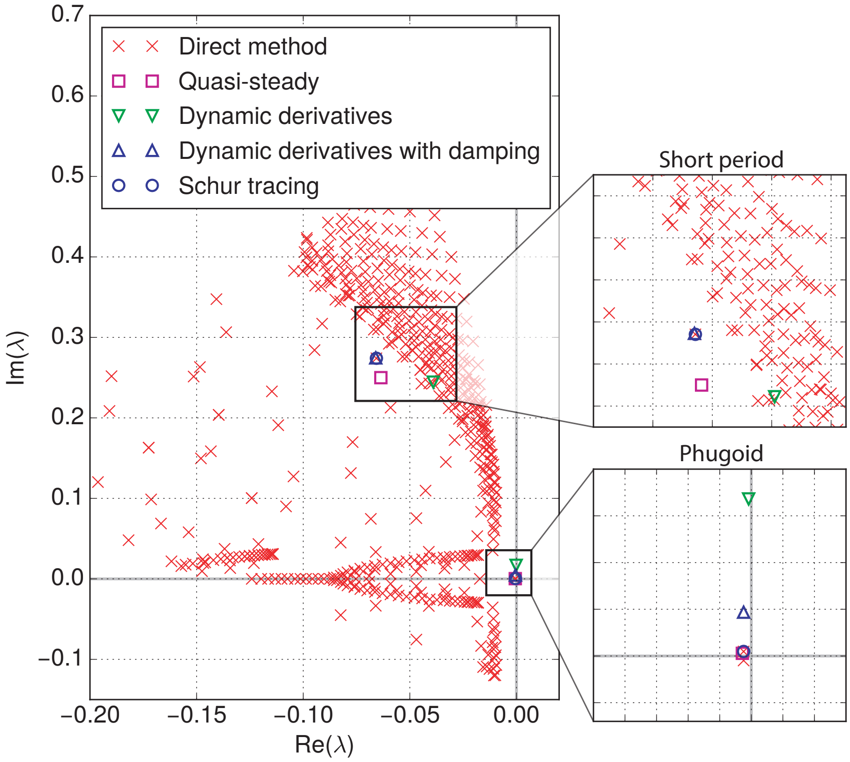

(b) Identification at $\mu = 73$

Figure 5.8: Results of operator-based mode identification compared to reference solution.

Table 5.1: Value of flight dynamics eigenvalue for mass case $\mu = 730$.

Method	**Short period**	**Phugoid**
quasi-steady	$-0.0063 + 0.0814j$	$-0.000063 + 0.0001903j$
dyn. derivatives	$-0.0004 + 0.0752j$	$-0.000001 + 0.0000011j$
dyn. derivatives with damping	$-0.0003 + 0.0752j$	$-0.000001 + 0.0000017j$
Schur tracing	$-0.0005 + 0.0751j$	$-0.000050 + 0.0000470j$

Direct methods were used to calculate some eigenvalues of the coupled Jacobian matrix which are shown as a reference solution. These reference eigenvalues were obtained using multiple shifts distributed along the positive part of the imaginary axis. The tracing procedure for the dynamic derivatives method started from approximate eigenpairs obtained with the QS approach described in Section 5.3 and depicted in the plot as well.

The short period mode was identified. The phugoid mode, which differs significantly in terms of frequency from the short period, was identified as well since the horizontal degree-of-freedom was retained. No noticeable difference was found between the three identification methods for $\mu = 730$. Assuming the dynamic derivatives are a function of frequency only is an acceptable approximation since the target eigenvalues are very close to the imaginary axis. Table 5.1 contains the eigenvalues as provided by the operator-based identification for both flight dynamics modes. Regarding the short period mode, results do not change sensibly when the damping is included. The QS method overestimates eigenvalue's real part whereas a good approximation is produced for the imaginary one. As far as the phugoid mode is concerned, eigenvalues from the dynamic derivatives methods are very similar. A large difference in order of magnitude is found for the QS method. However, it must be noted that eigenvalues for phugoid mode are very small numbers which could be affected by numerical inaccuracies.

Concerning the mass case $\mu = 73$, Figure 5.8(b) depicts a short period inside the cloud of eigenvalues. Both phugoid and short period eigenvalues are affected by an error when they are obtained with dynamic derivatives. These are calculated discarding the real part of the eigenvalue in Eq. (3.25) and this leads to underestimation of frequency and damping for the short period as well as overestimation of the phugoid frequency. Including the damping improved the results and provided an initial guess for the Schur complement method. The refinement with the Schur tracing led to the same results provided by the direct method. Specifically, the exact eigenvalues of short period and phugoid modes are $-0.0660 + 0.275i$ and $-0.000486 + 0.00469i$, respectively. A summary of results is provided with Tab. 5.2. Regarding the short period mode, identification using dynamic derivatives improves when the damping is taken into account since results are closed to the exact value provided by the Schur complement method. In addition, the QS method provides a good approximation. Results for the phugoid mode are reported as well. Using dynamic derivatives leads to the largest offset in terms of frequency whereas the inclusion of damping produces accurate results.

Table 5.2: Value of flight dynamics eigenvalue for mass case $\mu = 73$.

Method	Short period	Phugoid
quasi-steady	$-0.0636 + 0.2502j$	$-0.000565 + 0.0002872j$
dyn. derivatives	$-0.0390 + 0.2444j$	$-0.000167 + 0.0168104j$
dyn. derivatives with damping	$-0.0660 + 0.2746j$	$-0.000486 + 0.0046881j$
Schur tracing	$-0.0656 + 0.2741j$	$-0.000485 + 0.0004845j$

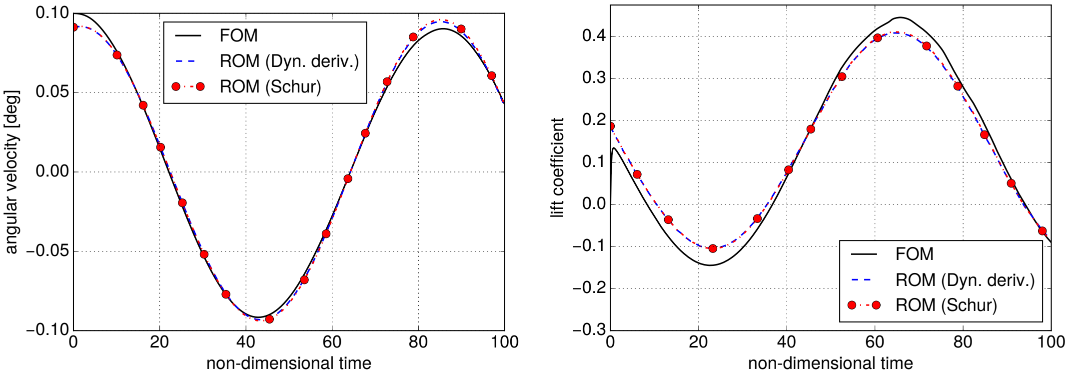

(a) Angular velocity (b) Lift coefficient

Figure 5.9: Response to initial disturbance in angular velocity of $q^* = 0.1\,\text{deg}$ for mass case $\mu = 730$.

Once direct eigenpairs are identified solving Eqs. (3.15), the corresponding adjoint ones are computed by solving Eq. (3.22) and starting from direct eigenvalues. The model reduction discussed in Chapter 3 is then applied and the number of degrees-of-freedom is reduced from 576,126 to 2. Results for an initial disturbance in the angular velocity are shown for $\mu = 730$ in Fig. 5.9. As expected for this case, full and reduced models show the same behaviour in terms of motion as presented with angular velocity in Fig. 5.9(a). Small differences are found at peak values. Similarly, lift coefficient in Fig. 5.9(b) shows a good agreement between ROM and full order model. The largest error, quantified around 3% of maximum C_L, occurs at the first oscillation. In Fig. 5.10 results for an encounter of a '1-cos' gust with an amplitude of 0.1% of the free-stream velocity and a gust wavelength of 20 wing chord lengths is reported. The small gust amplitude was chosen to excite the system in the linear regime. The system response is well reproduced by all the operator-based approaches. Small differences are found between the ROM based on dynamic derivatives and the one based on Schur tracing for vertical velocity which is shown in Fig. 5.10(a). Specifically, the largest difference of less than 1% is found in the first part of the simulation, before the first peak. A difference of 2% between full order model and ROMs is shown in the first part of the simulation, up to the first peak value, since no information is contained in the eigenpairs to represent the external disturbance. Regarding lift coefficient in Fig. 5.10(b), the build-up due to gust is not captured fully

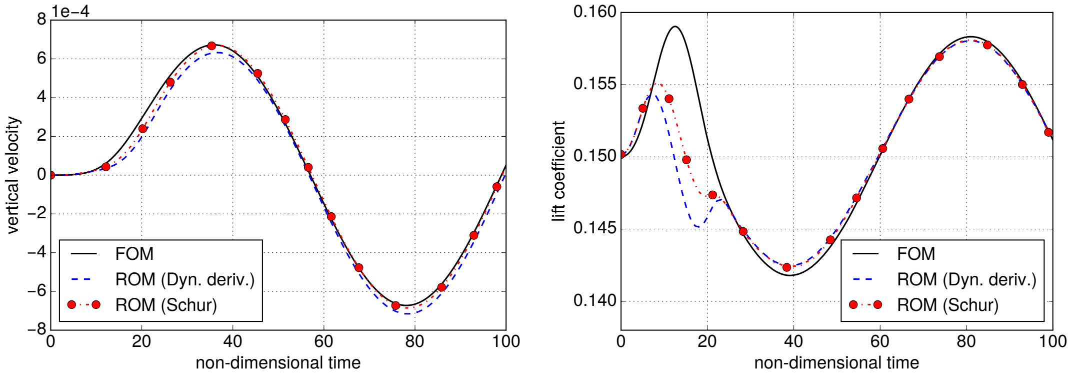

(a) Vertical velocity (b) Lift coefficient

Figure 5.10: Response to a '1-cos' gust with intensity $V_g = 0.1\%$ of the free-stream velocity and wavelength of 20 wing chords for mass case $\mu = 730$.

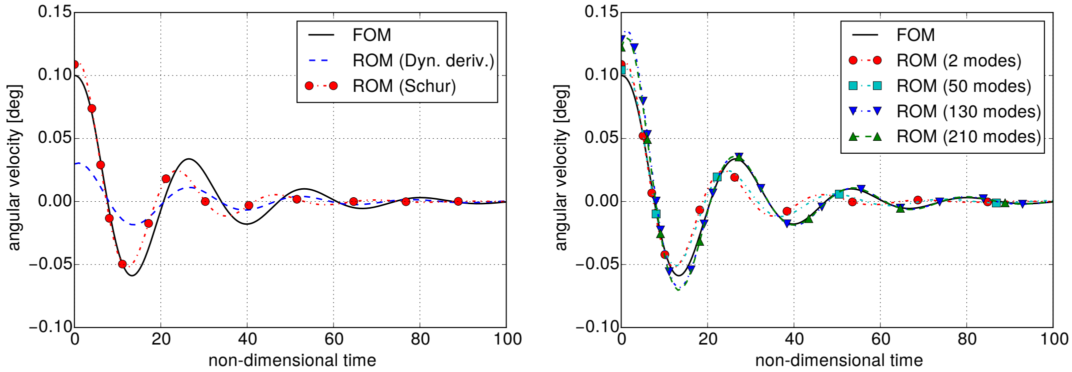

(a) ROMs built using modes from operator-based identification (b) Effect of including eigenpairs surrounding short period and phugoid

Figure 5.11: Response to initial disturbance in angular velocity of $q^*(t = 0) = 0.1\,\text{deg}$ at mass ratio $\mu = 73$.

since it is due to the external disturbance. The peak value for lift coefficient is computed with an error of 3%. However, the full order reference is reproduced accurately once the gust has passed. Overall, the ROMs match the full order results of initial disturbance and gust encounter simulations, with the limitation of lift build-up due to gust, and therefore the focus will be on the more challenging mass case $\mu = 73$ from now on.

For this case, an initial disturbance in the angular velocity of $q^*(t = 0) = 0.1\,\text{deg}$ (per non-dimensional time-unit) provides the response shown in Fig. 5.11(a). The mode identification performed while discarding the real part of the eigenvalue for the interaction matrix is not effective when the flight dynamics eigenvalues are strongly coupled (or interacting) with aerodynamics. Using the dynamic derivatives leads therefore to lower accuracy. Including the damping produces results which are very close to the ones from the exact Schur complement method. Hence, for sake of clarity only

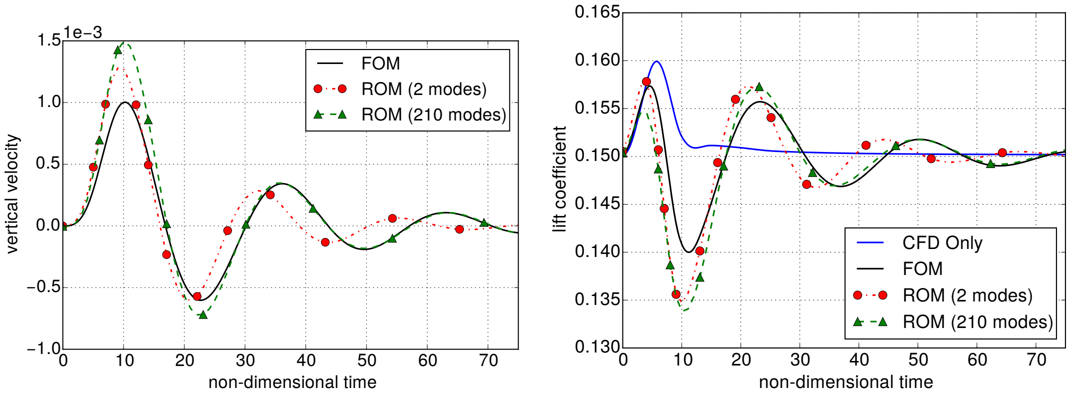

(a) Vertical velocity

(b) Lift coefficient

Figure 5.12: Response to gust encounter for a '1-cos' gust of amplitude $V_g = 0.1\%$ free-stream velocity and gust wavelength of 10 chord lengths at $\mu = 73$.

the latter will be kept in the following as reference for the operator-based identification. The comparison between full order model and ROM based on Schur tracing shows that the reduced model is able to reproduce the general trend of the system response. Initial conditions have a small offset and results match the reference when oscillations decay. However, a phase lag and an underestimation of the peak values are visible during the transient. An explanation might be that the two modes included in the modal basis contain only part of the required information.

This assumption is investigated further by calculating more eigenpairs with the direct method and including them in the modal basis. Although this cannot be used as a model reduction technique because of the prohibitive computational cost to extract eigensolutions, it does provide a posteriori confirmation. Results of the model reduction including an increasing number of modes surrounding the short period and phugoid is depicted in Fig. 5.11(b). Data for the model reduction performed with flight dynamics modes only is included as reference. Besides the two flight dynamics modes, 48 and 128 additional eigenpairs closest to the short period are subsequently added to the modal basis. Results for the transient improve gradually and with 130 modes the system response is well represented. Another set of 80 eigenpairs closest to the phugoid is then added to the modal basis, for a total of 210 modes. This further improves the results for peak values. Information about rigid-body motions is distributed in the eigenpairs surrounding the flight dynamics eigenpairs highlighting the strong coupling. Hence, the two flight dynamics modes contain only part of the information required for the model reduction. In those cases, flight dynamics modes from the operator-based identification might not be sufficient to reproduce accurately the full order results.

The analysis now proceeds with external disturbances. Results are presented in Fig. 5.12 for a '1-cos' gust with intensity $V_g = 0.1\%$ of free-stream velocity and gust wavelength $L_g = 10$ chord lengths. A preliminary comparison is made between reference results from CFD-only and coupled gust simulations. No motion is allowed for CFD-only simulations and Fig. 5.12(b) shows the lift build-up followed by a smooth decay. In contrast, results of the coupled approach produce oscillating behaviour. Regarding lift coefficient, the amplitude of the first oscillation is lower in comparison to CFD-only simulations because part of the energy goes into the rigid-body motions. The subsequent system response is composed of few decaying oscillations. The same simulation was performed with an operator-based ROM containing the short period and phugoid modes. Concerning the vertical velocity in Fig. 5.12(a), results converge to the initial value, whereas the transient is not reproduced well, which is highlighted by phase lag and underestimation of peak values. The first peak is due to the aerodynamic disturbance and it is not fully captured by the flight dynamics modes. This observation is supported in Fig. 5.12(b) for lift coefficient, where the amplitudes of the first few oscillations are not properly described either. The strategy of adding the 208 modes surrounding the short period and phugoid to the modal basis improves the results when the disturbance has passed. However, differences are still visible in the first two oscillations of vertical velocity. Subsequent fluctuations are fully captured by this reduced model as well as the asymptotic value for the final equilibrium. The same trend is visible for lift coefficient and the initial build-up is not completely reproduced. These modes, all coming from the coupled Jacobian matrix, are not able to fully reproduce the effects of a pure aerodynamic external disturbance and the first peak values are therefore not accurately captured. A possible explanation is that gusts excite an undefined number of modes which are yet not included in the modal basis. They are modes of the coupled system which mainly contain aerodynamic information. Such speculation is supported by literature studies about the model reduction of linear aerodynamic systems for which so-called gust modes can be identified with direct methods and included in the modal basis [39]. Although the identification of such modes with the operator-based method is theoretically possible, the computational cost of tracing an undefined number of modes is prohibitive when using CFD aerodynamics. Thus, an alternative method based on the data-based identification is investigated next for external disturbances and low mass ratios.

5.5 Data-based Identification

A strategy to improve the accuracy of the reduced model for external disturbances and low mass ratios is to use the data-based approach presented in Section 3.3 to calculate modes for the model reduction. The modal basis containing POD modes was computed with a number of snapshots ranging from 15 to 35. Snapshots were distributed linearly in the frequency range between 0 and 2 to investigate a typical range of gust lengths and optimisation of the sampling process is not attempted. The upper limit of the range was chosen according to the Fourier decomposition of the ‘1-cos’ gust as described in Section 2.3. Please note that in general the range’s upper limit depends on the gust

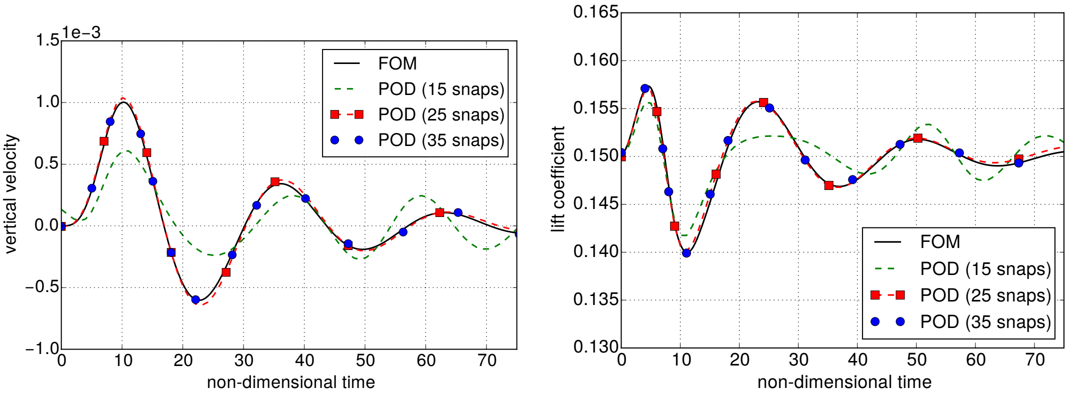

(a) Vertical velocity

(b) Lift coefficient

Figure 5.13: Response to gust encounter for a '1-cos' gust of amplitude $V_g = 0.1\%$ free-stream velocity and gust wavelength of 10 chord lengths at $\mu = 73$.

shape. Although for aeronautical applications the gust shape is defined by regulation as '1-cos' , that is not the case in general for other fields. Application to different gust shapes could require a larger (or smaller) frequency range in order to achieve an accurate reconstruction of the input signal with the Fourier decomposition as described in Section 2.3. Once the frequency range is defined, the quality of results depends on the number of snapshots used as shown in Fig. 5.13. Model reduction performed with 15 POD modes led to results not matching the full order model since a different decay rate and a phase lag are clearly identified for the vertical velocity. The values for lift are underestimated at the beginning and the subsequent oscillations are not reproduced properly. Increasing the number of snapshots provides better results and the full order results are matched with 25 POD modes. Such reduced model is capable of describing accurately the flight dynamics response and aerodynamic forces. Some minor differences arise for peak values of the vertical velocity after the first few oscillations. Although these differences are negligible, they can be eliminated by further increasing the number of snapshots up to 35. No appreciable difference is visible between the ROM with 35 POD modes and the full order model since an error of less than 0.5% is found.

The 35 POD modes can be sorted in terms of importance using the real-valued POD eigenvalues σ in Eq. (3.43). This criterion is related to the energy content of each mode. In Fig. 5.14, the POD eigenvalues corresponding to the first 15 modes are reported. The energy distribution shows a strong decay after the first 3 modes. This information can be used to perform a subsequent subselection and retain just few modes for the reduced model. In fact, the largest eigenvalue is nine orders of magnitude larger than the fifteenth mode which therefore contributes less to the ROM reconstruction. In terms of physical meaning, the interpretation of POD modes is not obvious. They describe features of the coupled system which involve fluid flow as well as free-flight phenomena. In Fig. 5.15, some POD modes are depicted using the magnitude

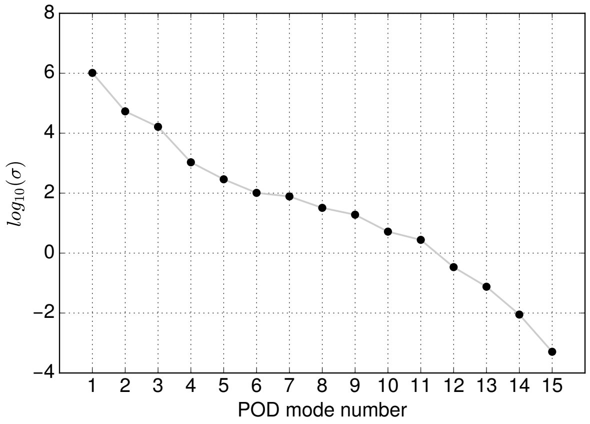

Figure 5.14: POD eigenvalues.

of the pressure component. The first mode in Fig. 5.15(a) corresponds to the most energetic one and it concerns mainly the wing's near field. A shock wave is clearly identified on the upper surface while the pressure component is larger around the tail. The distribution is mostly uniform elsewhere in the domain. A physical interpretation matches the most important feature of the transonic flow which is the shock wave. The following 3 modes are not depicted since they are similar to the first one. They gradually introduce additional features apart from the shock wave. In Fig. 5.15(b), the fifth POD mode is depicted. In terms of energy, it is associated to a value which is an order of magnitude smaller than the first mode. It clearly describes the pressure distribution on the wing lower surface. However, the information is spread elsewhere as well since flow structures involving the whole domain are shown. The fifteenth POD mode presented in Fig. 5.15(c) has an energy 1×10^9 times smaller than the first one. The pressure magnitude is spread in the flow field and it is not concentrated anywhere in particular.

The flight dynamics parts of the POD eigenvectors is obtained from the data-based identification as well since the method is applied to the coupled system. The flight dynamics parts of POD modes 1, 5, and 15 are normalised to have unitary norm and reported in Table 5.3. The largest component of mode 1 is the vertical velocity which is followed by pitch rotation. Mode 5 is mainly composed of pitch rotation and its second largest component is vertical velocity. A strong horizontal component is present as well. The dominance of vertical velocity and pitch rotation is confirmed for mode 15. In general, interpreting physical phenomena from POD modes is not trivial since they are composed of a superposition of horizontal and vertical velocity as well as pitch rotation. This is in contrast to the results from the operator-based ROM for which a clear distinction between short period and phugoid mode is possible. Sorting the POD modes by their energy contents might represent a possible way to identify the most important features of the flow field.

The data-based reduced model provides accurate results for gust encounter simulations in the linear regime. An interesting investigation concerns the applicability

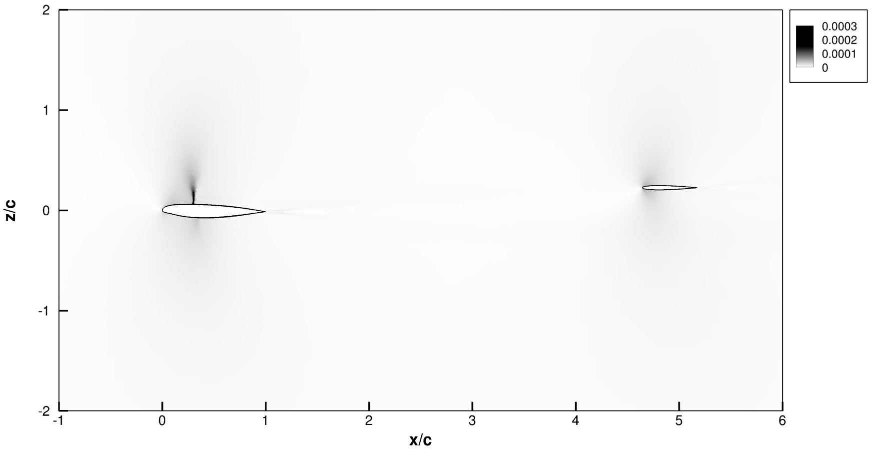

(a) Mode 1

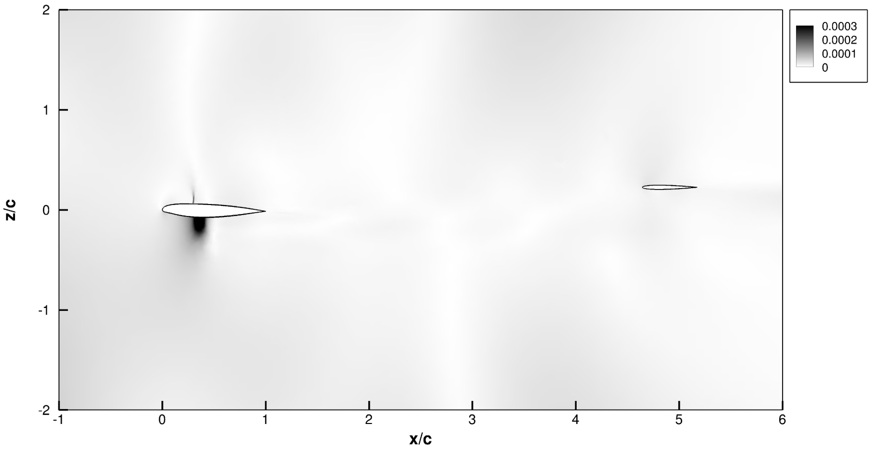

(b) Mode 5

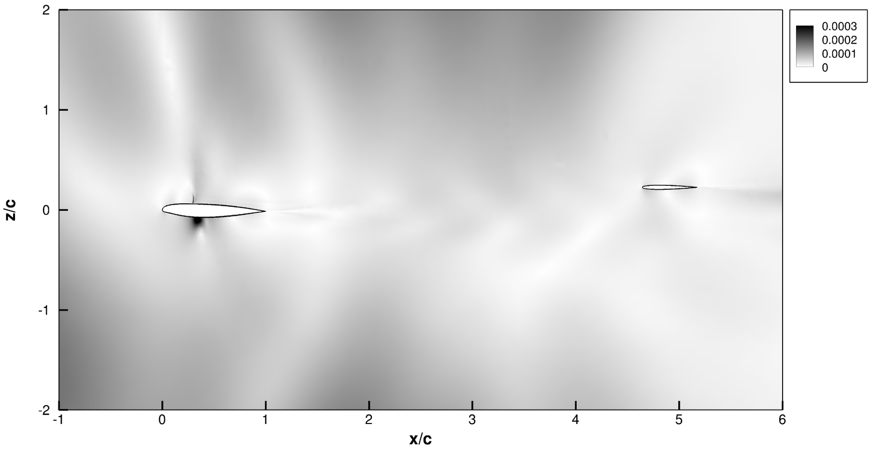

(c) Mode 15

Figure 5.15: Magnitude of pressure components of POD modes.

Table 5.3: Flight dynamics part of three POD modes.

Component	Mode 1	Mode 5	Mode 15
horizontal velocity	$-0.0002 + 0.0001j$	$0.1086 - 0.1174j$	$-0.0082 + 0.0113j$
vertical velocity	$-0.2323 + 0.7067j$	$-0.5150 + 0.2884j$	$0.7900 + 0.0079j$
angular velocity	$-0.1883 + 0.0137j$	$0.0769 - 0.0122j$	$0.0413 + 0.0524j$
pitch rotation	$0.0453 + 0.6395j$	$0.3697 - 0.6952j$	$0.6068 + 0.0546j$

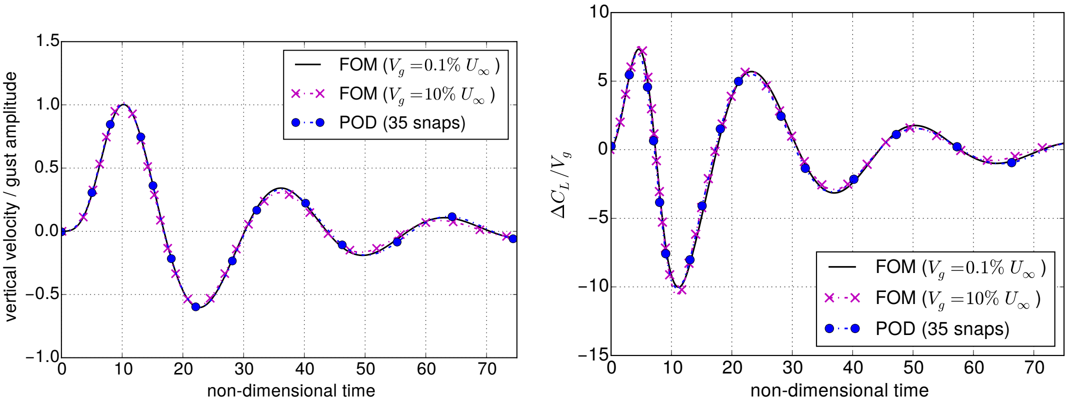

(a) Vertical velocity

(b) Lift coefficient variation

Figure 5.16: Response to gust encounter for '1-cos' gusts with amplitudes of $V_g = 0.1\%$ and $V_g = 10\%$ free-stream velocity and gust wavelength of 10 chord lengths at $\mu = 73$.

of this methodology to larger amplitude gusts. In those cases, non-linear effects are expected to take place. Although the reduced model should be compared to the full order model acting linearly only, non-linear effects were investigated by performing a '1-cos' gust simulation with a wavelength of 10 chords and a large amplitude of $V_g = 10\%$ free-stream velocity. This corresponds to an amplitude similar to EASA regulations [57]. Results are scaled by the gust amplitude and presented in Fig. 5.16 alongside the linear full order solution and the ROM curve already shown in previous plots and corresponding to an amplitude of $V_g = 0.1\%$ free-stream velocity. For this particular case, a largest difference of ±5% was found between linear and non-linear results, since non-linear effects are weak and they involve mainly peak values. The large-amplitude gust produces results which are almost proportional to the ones produced by the small-amplitude one. This suggests two considerations. First, a linear approximation can produce reliable results when investigating gusts with regulation amplitude. Secondly, the reduced model based on the data-based identification, which is not able to reproduce any non-linearity, can be accurate enough to investigate the behaviour of the system during an encounter with a certification gust. These statements are investigated further for an industry-size test case in the next Chapter 6.

5.6 Computational Cost

The computational cost of the ROM can be split in two main contributions. The first involves building the modal bases using LFD calculations for both operator-based and data-based approaches. Obtaining an LFD solution for the wing-tail configuration takes around 7 min on an Intel Xeon E3-1245 CPU (single-core) converging 8 orders of magnitude. The total CPU time is summed as 2 h for operator-based ROM with dynamic derivatives, 7 h for the one with Schur tracing refinement and 3 h for the data-based ROM with 25 samples. The second contribution is given by the integration of the ROM equations and omitted in this calculation since it is negligible. These numbers are compared to the 3 days required by one non-linear full order reference simulation coupling unsteady RANS aerodynamics and non-linear flight dynamics equations for gust encounters on the same single-core hardware. Typical parameters employed for the time-domain simulation were a non-dimensional time-step of 0.05. Convergence in dual-time was met when a residual of 1×10^{-3} was reached. The maximum number of 100 inner iterations was set and Cauchy convergence for drag and using 19 samples with a tolerance of 1×10^{-10} was enabled during inner iterations to reduce the computational time. Considering that multiple gust lengths must be analysed during aircraft design, a reduction factor of 100 can be obtained.

5.7 Chapter Summary

In this chapter, mode identification and model reduction were exploited for the longitudinal dynamics of a simplified test case describing the dynamics of a large civil aircraft. Some fundamental challenges were addressed. Specifically, identification of flight dynamics eigenpairs when they are located inside the cloud of fluid eigenvalues, for example at low values of mass ratio, was a crucial task to be addressed. It was successfully performed with a hierarchy of methods which provide an increasing level of accuracy. Tracing was applied to multiple flight dynamics modes as well. In addition, a non-trivial equilibrium condition was taken into account using a trimming procedure based on the Broyden method.

Model reduction was investigated for two parameter sets corresponding to different mass ratios. The first case concerned a condition with dominant flight dynamics modes and the operator-based method reproduced accurately the full order results for both initial disturbance and gust encounter simulations. For the second case, the flight dynamics eigenvalues were located in the cloud of aerodynamic ones. Their identification needed a procedure based on multiple steps which started from the results of the quasi-steady method and proceeded with a refinement based on dynamic derivatives and Schur complement method. The operator-based identification led to good results for initial disturbance analysis. However, results were unsatisfactory for the gust encounter simulations. An investigation showed that eigenvectors coming from the coupled Jacobian matrix do not contain enough information to fully reproduce system's response to external disturbances. Hence, the data-based identification was performed for such cases and a interpretation of the POD modes was suggested.

In conclusion, a key finding of this chapter is the reliable multi-step procedure which enables an application of the method to three-dimensional test cases such as the one described in Chapter 6. It does not need computing the full set of eigenvalues for the coupled Jacobian matrix and it is capable of identifying flight dynamics eigenpairs regardless their position in the complex plane. Based on results presented in this chapter, the application of the proposed method is summarised as follows. First, the operator-based identification is performed using dynamic derivatives calculated for reduced frequencies in the range where flight dynamics modes are expected. To speed up the procedure, the tracing can start from an approximation obtained with a quasi-steady approach. Secondly, if flight dynamics eigenvalues are far from the imaginary axis, a refinement using the Schur complement method is required. Thirdly, if the focus is on system response to external disturbance, the data-based identification can provide accurate results.

Chapter 6

Longitudinal/Lateral Dynamics

In this chapter, mode identification and model reduction technique are scaled from small-sized two-dimensional applications to a practical three-dimensional test case. Technical challenges, which arise when the investigation is scaled to large industry-relevant cases, are addressed. Specifically, performing the tracing with Schur complement method is computationally challenging and the operator-based identification is based on samples of dynamic derivatives using a linearised frequency domain solver instead. The tracing procedure was further improved to produce reliable results with a limited number of samples. In addition, large part of the eigenspectrum, easily calculated for small cases with direct methods, is now inaccessible. Although such information is not needed for the reduction per se, it provided a useful reference for comparison.

A modular approach to the model reduction was developed which is composed of three parts. First, the operator-based identification is employed for the flight dynamics modes. Results concerning aircraft's stability and handling quality are then available. Secondly, the data-based identification is applied to the aerodynamic subsystem only. Thirdly, modes coming from both operator-based identification and data-based one are included together in the modal basis for the subsequent reduction. The modularity consists in computing one or more of the three parts separately and being able to build a joint reduced model afterwards. This is a time-saving approach which makes building the reduced model for the coupled system faster. Existing software and data, which are usually available for the aerodynamic subsystem only, can be exploited and some computations concerning aerodynamics can be skipped.

Regarding the full order model, the equations of motion are used in modal form. This formulation makes the implementation easier since software infrastructure already available for structural dynamics can be exploited. Aerodynamics is provided solving RANS equations with Spalart–Allmaras turbulence model and surface displacements, calculated with the modal solver, are applied to the CFD grid using mesh deformation. The method was implemented using DLR-TAU for the aerodynamic subsystem.

The coupling between CFD and rigid-body solver was achieved within the FlowSimulator software framework [99]. An ad-hoc code was developed for the tracing and for the operator-based model reduction. Existing results and tools were exploited for the data-based identification of the aerodynamic subsystem. In particular, the computationally expensive calculation of the snapshots matrix was avoided thanks to results produced in [17] and made available by the authors. The majority of results reported in this chapter have been presented in [105].

6.1 Governing Equations in Modal Form

The modal formulation of flight dynamics equations described in Section 2.2 is exploited in this chapter for the flight dynamics model. The six modal shapes and their related generalised masses, which are needed to solve Eq. (2.47), were obtained by analysing the structural finite element model with MSC.Nastran [101]. They are used to perform the integration of Eq. (2.46), which is restated here for convenience,

$$M\frac{\mathrm{d}^2\boldsymbol{\eta}}{\mathrm{d}t^2} = \boldsymbol{F} \tag{2.46}$$

and to calculate results such as displacements and generalised forces. The mode shapes are a linear combination of rigid-body translations and rotations in the three-dimensional space. This becomes clear in Fig. 6.1. For example, mode 1 in Fig. 6.1(a) is composed mainly of yaw rotation but a translational component in the longitudinal plane is visible. Mode 4 in Fig. 6.1(d) shows roll rotation alongside vertical translation. Similarly, none of the remaining modes corresponds to pure translational or rotational modes either.

A physical interpretation of results is provided with the transformation in Eq. (2.49). An new set of 6 pure translational and rotational modes is created by prescribing unit displacements, specifically translations of 1 m in each of the three directions and rotations of 1 deg around each of the three axes according to the sign convention usually adopted in flight dynamics [34, 122], shown in Fig. 6.2. The mode shapes for the new set of modes are depicted in Fig. 6.3. Each of them corresponds to a single rigid-body degree-of-freedom. This facilitates the physical interpretation of results and it is in contrast with the set of modes in Fig. 6.1, where each mode is a linear combination of rigid motions. The Nastran modes are store in matrix Ξ, the pure rigid-body modes are stored in matrix Υ.

The transformation T in Eq. (2.49) is computed and applied to displacements and velocities as post-processing step in order to translate results from the Nastran set of modes, which are used to perform computations, to the pure rigid-body modes, which provide physical insight. The transformation is also used to obtain physical interpretations of the generalised aerodynamics force (GAF) matrix Q which is always computed using the Nastran set of modes. When the GAF matrix is translated into the pure rigid-body set of modes, it represents the ratio of aerodynamic forces with respect to the

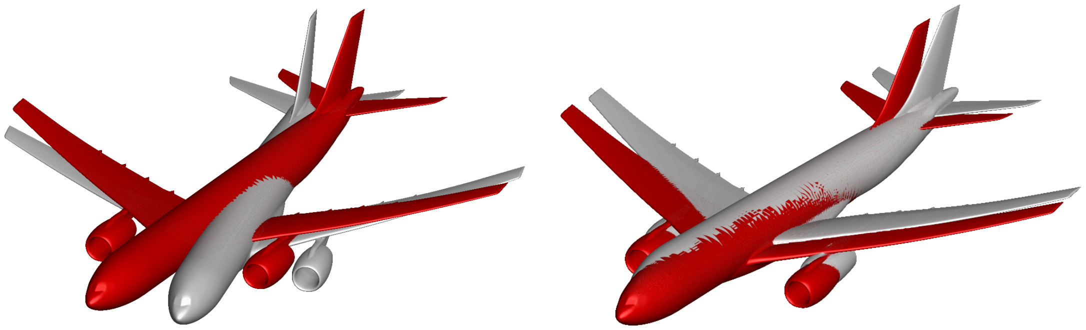

(a) Mode 1 (b) Mode 2

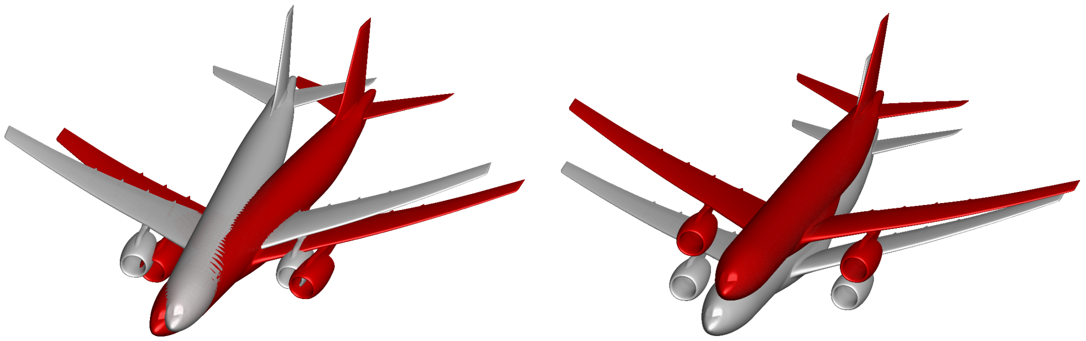

(c) Mode 3 (d) Mode 4

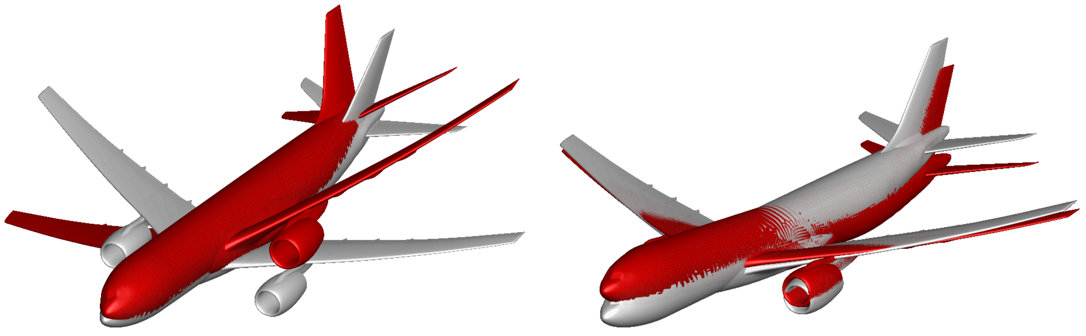

(e) Mode 5 (f) Mode 6

Figure 6.1: Rigid-boy mode shapes emerging from wind-off structural analysis. A scaling factor is applied for better visibility.

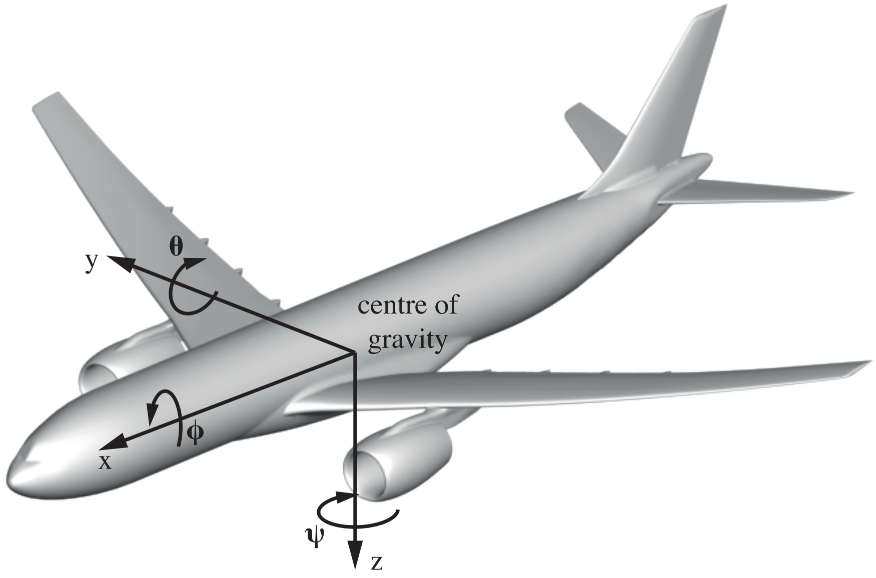

Figure 6.2: Sign convention used to present results with physical quantities.

motion in distinct directions of the reference frame shown in Fig. 6.2. Hence, its entries can be interpreted as dynamic derivatives in the traditional flight dynamics context.

6.2 Large Civil Aircraft

Results are presented for a large civil aircraft in cruise condition flying at 10 km altitude, Mach number of 0.85, Reynolds number of about 49 millions and a mean aerodynamic chord (m.a.c.) of 7 metres. The geometry is representative of a modern long-range, wide-body passenger aircraft. The mesh for CFD calculations consists of nearly 8 million points with a far field located at 77 wing m.a.c. away from the body. The steady state solution results from the iterative trimming procedure based on the Broyden method [27] already discussed in Section 5.2. Conditions for straight and level flight provide target values for lift and moment while elastic deformations are taken into account by including 94 elastic modes in the procedure. The reference point for rotation is the centre of mass. Angle of attack and horizontal tail rotation are updated iteratively to meet the trimming requirements. Thrust balances drag at the equilibrium and its orientation is assumed horizontal at all time. The CFD mesh is deformed at each iteration to account for elastic deformation. The pressure coefficient for the resulting steady state is shown in Fig. 6.4. A shock wave is clearly visible on the upper surface of the wing while the horizontal tailplane is shock free. These steady non-linearities are retained in the reduced model which describes the variations of fluid and flight dynamics unknowns around the trimmed solution.

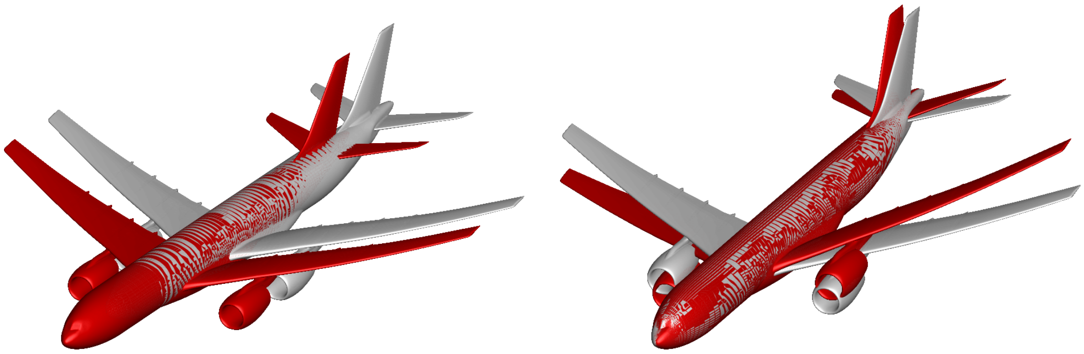

(a) X translation mode (b) Roll rotation mode

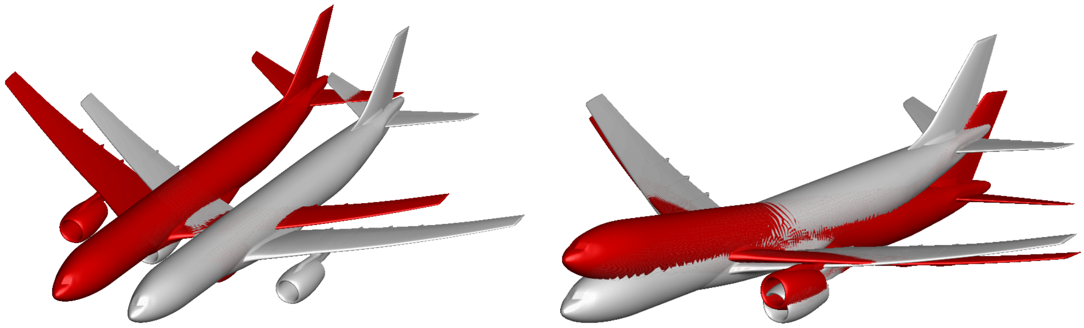

(c) Y translation mode (d) Pitch rotation mode

(e) Z translation mode (f) Yaw rotation mode

Figure 6.3: Artificial pure rigid-body mode shapes enabling physical interpretation of results. A scaling factor is applied for better visibility.

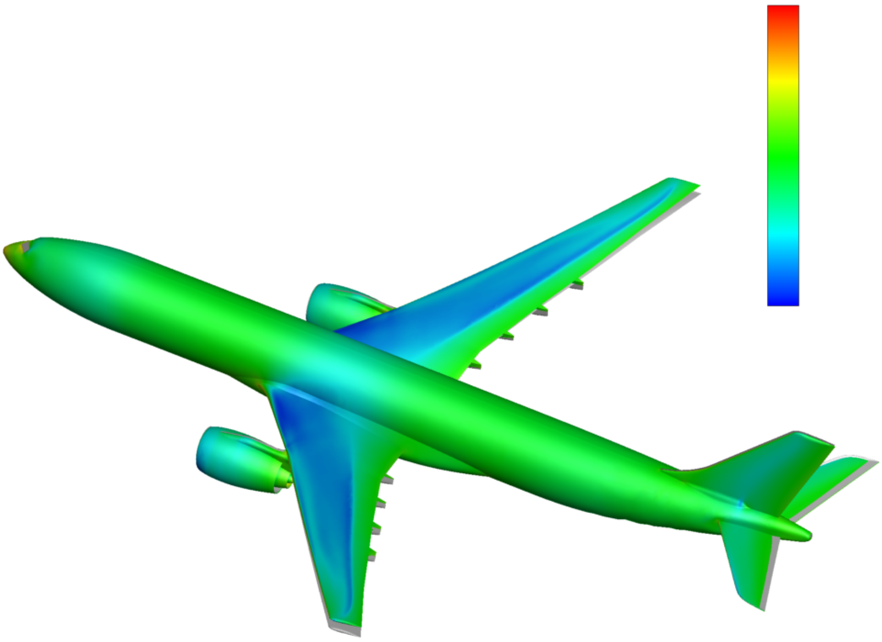

Figure 6.4: Steady state surface pressure resulting from trimming procedure and undeformed aircraft shape.

6.3 Operator-based Identification

The operator-based identification procedure is described next for flight dynamics modes. The geometry resulting from the elastic trimming is now frozen and the system assumed to evolve rigidly without any additional elastic deformation. The 6×6 GAF matrix Q in Eq. (3.25) was pre-computed in the frequency domain. For each of the 6 rigid-body modes, the right-hand side of Eq. (2.63) was produced using central finite differences and the linear system solved at the specified reduced frequencies. This corresponds to calculating the aerodynamic responses to sinusoidal rigid motions. The complex-valued flow solutions were then projected onto the generalised rigid-body modes providing the frequency response function relating the sinusoidal excitations to GAFs for the 6 modes. The results of these calculations are complex-valued GAF matrices computed at 7 positive values of reduced frequency spaced with a power law of 3 in the range $[0, 0.05]$. The upper limit was chosen based on typical frequencies of flight dynamics modes for the same class of aircraft. Magnitude and phase of two representative entries of the GAF matrix as function of frequency are depicted in Figs. 6.5(a) and 6.5(b). Equation (2.49) was used to translate the matrix into the reference frame shown in Fig. 6.2 in order to provide physical quantities.

The tracing in Eq. (3.25) leading to the flight dynamics parts of the eigensolutions of the coupled system is performed using Newton's method reported in Section 3.2.2. Cubic Hermite spline interpolation is adopted to evaluate Q at frequencies not sampled. A relaxation parameter of 0.8 is adopted for the Newton solver. The derivative $\frac{\mathsf{d}Q}{\mathsf{d}\lambda} \approx \frac{\partial Q}{\partial \omega}$ in

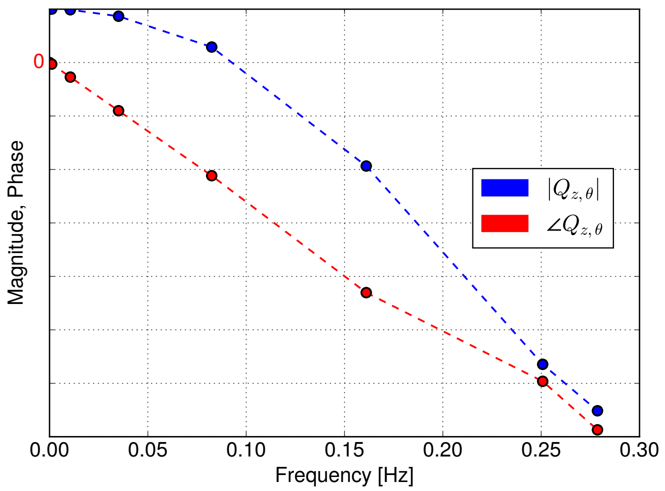

(a) Dynamic derivative relating vertical translation GAF to pitch rotation

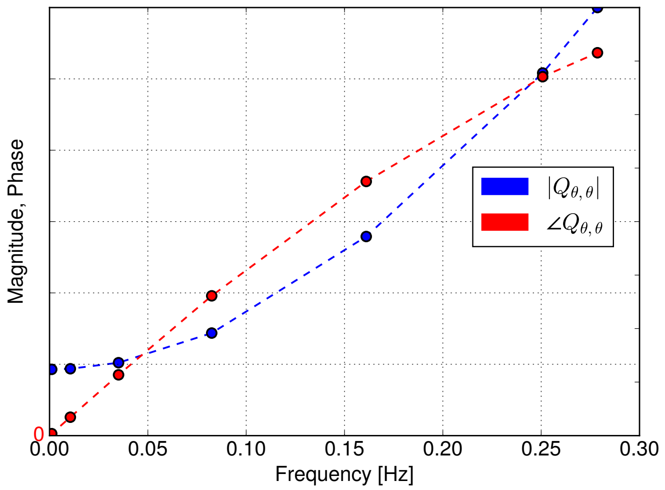

(b) Dynamic derivative relating pitch rotation GAF to pitch rotation

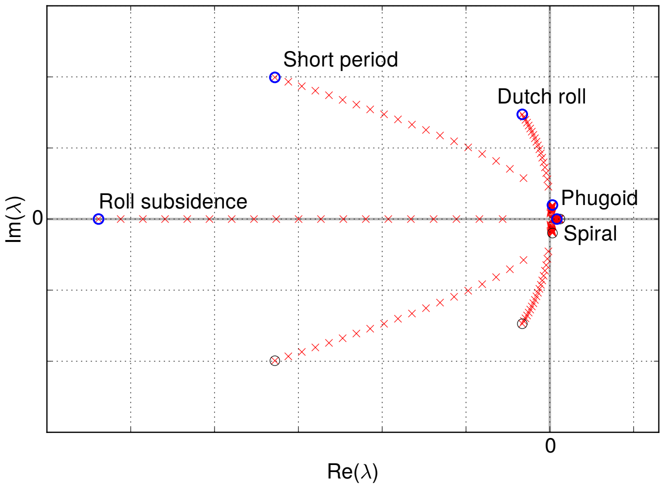

(c) Eigenspectrum showing flight dynamics eigenvalues resulting from tracing.

Figure 6.5: Operator-based identification for a large civil aircraft.

Eq. (3.40) is taken into account during the implementation to accelerate the convergence and it is calculated using central finite differences with $\epsilon = 1 \times 10^{-8}$. The procedure to solve Eq. (3.25) starts at a small value of $\beta = 0.15$ with the calculation of the initial guess, needed by Newton's method, using the quasi steady state approach described in Section 5.3. Specifically, eigensolutions of the small system in Eq. (3.25) are calculated assuming $Q = Q(\omega = 0)$ with direct methods implemented in the `eig()` function in MATLAB as previously done for the two-dimensional wing-tail configuration. It can be noticed that the entries of $Q(0)$ correspond to stability derivatives which are usually adopted to investigate the behaviour of flight dynamics systems. The eigensolutions of this simplified problem provide the initial guess for the tracing which is composed of two loops. The outer loop increases the value of β gradually in 19 steps until the coupling of flight dynamics and aerodynamics is fully taken into account at $\beta = 1$. At each value of β, the inner loop is started by the Newton solver which iterates until the norm of the residual vector reaches machine precision. The converged solution is then returned to the outer loop which will use it as initial guess to seek the eigensolution for the next β value. Calculation of eigenpairs corresponding to negative reduced frequencies are obtained by complex conjugating the ones computed at positive frequencies.

The eigenvalues resulting from the tracing are shown in the complex plane in Fig. 6.5(c). Their evolution from the rigid-body modes characterised by zero frequency and damping is clearly visible and due to the gradual inclusion of aerodynamics. The tracing procedure shows that these eigenvalues move to locations in the complex plane corresponding to real numbers as well as complex conjugate pairs and a physical interpretation can be given in terms of dynamic stability modes [34]. They are identified using their eigenvector components in addition to frequency information available in literature. For longitudinal dynamics, two oscillatory modes were expected, namely short period and phugoid. The short period corresponds to the complex-conjugate pair with the highest frequency. It describes pitch rotation and vertical velocity. Regarding the phugoid which is characterised by varying pitch rotation and horizontal speed, it must be noted that some simplifications are made in the full model since the thrust orientation does not follow the pitch rotation. Although this does not fully reflect the physical behaviour of long term dynamics, the phugoid mode can be found close to the origin having a very long period and small damping. As a result of the simplifications, the real part of its eigenvalue is a very small positive number.

Regarding lateral dynamics, three modes were expected, specifically Dutch roll, spiral and roll subsidence modes. The first one corresponds to the complex conjugate pair with the second highest frequency. It lies in the same frequency range of the short period mode but it is completely unrelated to longitudinal dynamics since it is mainly composed of roll and yaw rotations, as shown shortly. The roll subsidence mode is stable with a negative real part and zero frequency. Conversely, the real-valued spiral mode is unstable. The physical interpretation of the remaining eigenpairs is less clear compared

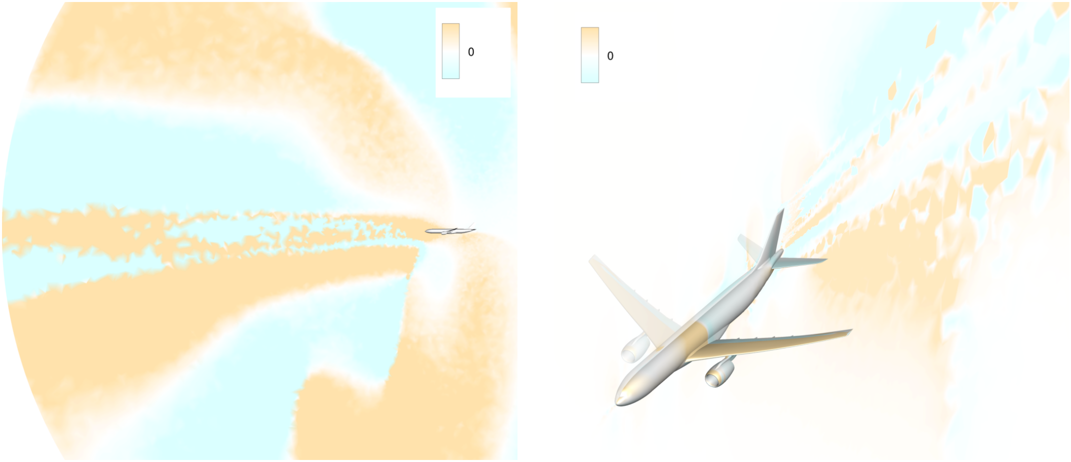

(a) Adjoint eigenvector (b) Direct eigenvector

Figure 6.6: Real part of pressure component for short period eigenvector.

with the traditional scheme. Their eigenvectors represent absolute translations which do not affect the aerodynamic response [22] and for which the eigenvalues are supposed to be zero. However, the corresponding eigenvalues are small real numbers located around the origin and their values could be affected by numerical inaccuracies.

The tracing procedure is performed for direct and adjoint problems solving Eq. (3.25). The fluid parts of direct eigenvectors are then computed with Eq. (3.13) assuming $\Re(\lambda) = 0$, to employ aerodynamics consistent with the calculation of dynamic derivatives. This simplification avoids convergence problems for the linear solver as well. Such convergence problem might arise when λ is in the cloud of the aerodynamic eigenvalues and the shifted matrix $(A_{ff} - \lambda I)$ becomes almost singular. Although computing the cloud is computationally prohibitive, the short period mode is suspected to be close to aerodynamic eigenvalues since the calculation of its fluid part by means of Eq. (3.13) was extremely difficult. Solving the linear system with $\Re(\lambda) = 0$ avoids the problem and simplifies the calculation of the eigenvectors' fluid components. However, this could lead to lower accuracy of the final reduced order model since the influence of damping on fluid part of eigenvectors is discarded.

The real parts of pressure component for the adjoint and direct fluid part eigenvectors related to the short period mode are depicted in Fig. 6.6. The adjoint one in Fig. 6.6(a) shows that most of the information is located upstream. They form an asymmetric area which extends from the aircraft to the far field. The direct eigenvector in Fig. 6.6(b) has stronger components closer to the aircraft surface and in the wake. The sign of pressure alternates leading to asymmetrical results. Physically, this suggests a mode composed of vertical translation and/or rotation in the longitudinal plane. In addition, the components of the eigenvectors show a symmetry with respect to the longitudinal plane, as expected from a longitudinal flight dynamics mode.

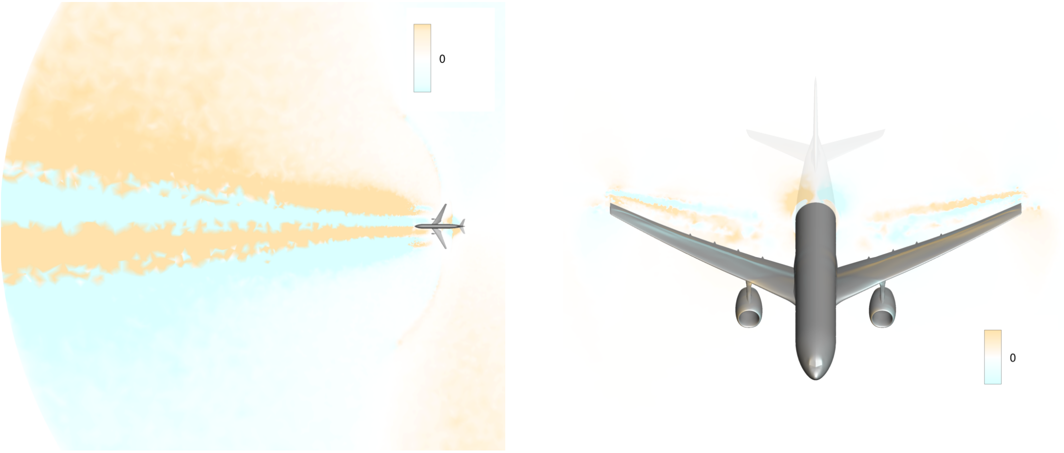

(a) Adjoint eigenvector (b) Direct eigenvector

Figure 6.7: Real part of pressure component for Dutch roll eigenvector.

Conversely, the Dutch roll, which is presented in Fig. 6.7, is a lateral mode. The pressure distribution for the direct eigenvector is now antisymmetric in the XZ plane as shown in Fig. 6.7(b). The trace of the steady-state shock wave is clearly visible on the wing's surface and the pressure distribution shows opposite signs for both wing and wake. A physical interpretation is that the Dutch roll mode rotates the aircraft in the lateral plane and pressure changes by increasing on the port and decreasing on the starboard. This is a distinctive behaviour of lateral modes. The adjoint eigenvector in Fig. 6.7(a) presents the information clustered in the region upstream the aircraft. The top view shows that pressure in regions located on the left and right of the fuselage has an antisymmetric behaviour. This confirms the findings obtained for the direct eigenvector.

Pressure components for the remaining eigenvectors are illustrated in Fig. 6.8. Regarding the phugoid, its adjoint eigenvector has most of the information upstream as shown in Fig. 6.8(a). Multiple regions can be identified where pressure alternates between positive and negative. A similar behaviour is shown for the direct eigenvector in Fig. 6.8(b). Regions of positive and negative pressure can be identified on the wing as well. Both adjoint and direct eigenvectors are symmetric with respect to the XZ plane. Compared to the short period mode in Fig. 6.6, the phugoid's pressure distribution appear more tidy. As far as the roll mode is concerned, its adjoint eigenvector is depicted in Fig. 6.8(c). It is a lateral mode and the information upstream is distributed in four bands with positive and negative pressure. In addition, lateral modes are characterized by antisymmetric distribution of the direct eigenvector and this is confirmed for the roll mode in Fig. 6.8(d). Pressure is lower in the starboard and higher in the port. This provides physical insight about how the flow is affected by the roll mode. The set of lateral and longitudinal flight dynamics modes is completed by the spiral mode. Pressure distribution for its adjoint eigenvector is shown in Fig. 6.8(e). Areas of negative and positive pressure are located upstream with a smooth transition between them. A physical interpretation is not immediate since the motion related to the spiral mode is complex and composed of roll, yaw and vertical translation. Thus, the regions highlighted by adjoint eigenvector reflect this behaviour. The corresponding direct eigenvector is illustrated in Fig. 6.8(f). In the flow field the distribution is almost antisymmetric but some small differences are present. These come from the complex motion which is not symmetrical neither in the longitudinal nor lateral plane. Similarly, pressure distribution on the wing's upper surface is not perfectly symmetric and it is composed of alternating regions of low/high pressure.

Flight dynamics parts of direct eigenvectors are discussed next. Denote $(\lambda^{(j)}, \boldsymbol{\phi}^{(j)})$ as the direct eigenpair corresponding to a mode dominated by flight dynamics contributions. Generalised displacements $\boldsymbol{\eta}^{(j)}$, which are associated with the specific mode and depend on time, are defined as

$$\boldsymbol{\eta}^{(j)}(t) = \Re(\boldsymbol{\phi}_r^{(j)} e^{\lambda^{(j)} t}) \tag{6.1}$$

Displacements $\boldsymbol{x}^{(j)}$ of the CFD mesh points are then calculated with Eq. (2.47) and they can be exploited to produce an animation for each mode which illustrates the flight dynamics part of the eigenvector. Some frames from such animations were extracted and included here. They were taken at six times linearly spaced during one period of motion in order to show changes in the aircraft position and orientation due to the specific mode. The short period mode is characterized by changes in vertical position as visible by comparing the frames in Fig. 6.9. Another component of the motion is pitch rotation which is synchronised with vertical velocity. It is clearly a longitudinal mode since no lateral motion is involved. Regarding the phugoid, it is animated in Fig. 6.10. The motion is mainly composed of horizontal translation and, to a lesser extent, pitch rotation. Some very small variations in vertical translation were found as well. The period of the phugoid is much longer in comparison with the short period's one. In Fig. 6.11, the flight dynamics part of the Dutch roll direct eigenvector is illustrated. It is a lateral mode which is composed of both roll and yaw rotations. The resulting motion is complex since a small rotation in roll is followed by an alteration of yaw and the two effects cannot be separated. Regarding its period, it has the same order of magnitude as the short period's one.

The reduced order model was then built. Note that the set of flight dynamics modes obtained with the operator-based identification comes from an eigenmode decomposition (EMD) of the Jacobian matrix. For this reason, the acronym EMD will be adopted in the following to refer to it. The modal bases in Eq. (3.4) were assembled using the adjoint and direct eigenvectors. Their complex conjugates were added, too, for a total of 12 eigenvectors, specifically three complex-conjugate pairs and six real-valued eigenvectors. The reduced model was first exploited to perform initial disturbance

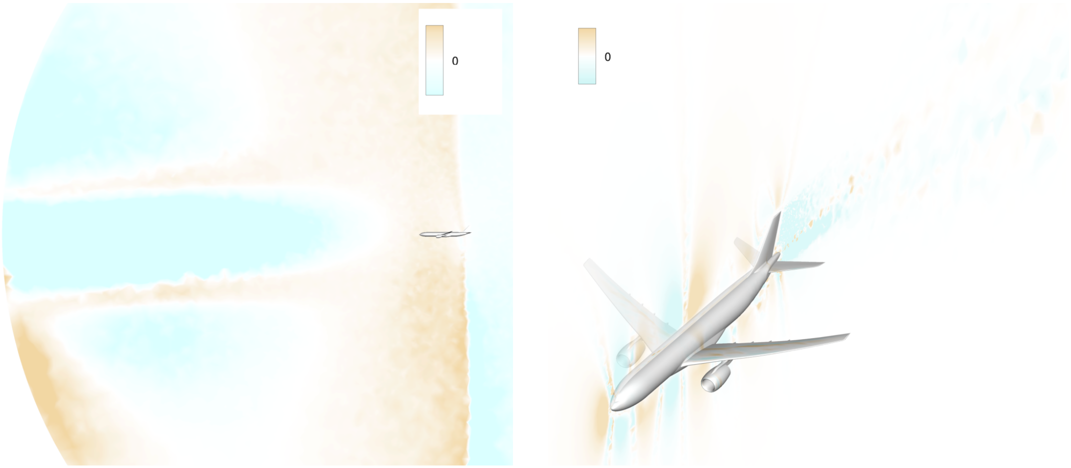

(a) Adjoint eigenvector, Phugoid mode (b) Direct eigenvector, Phugoid mode

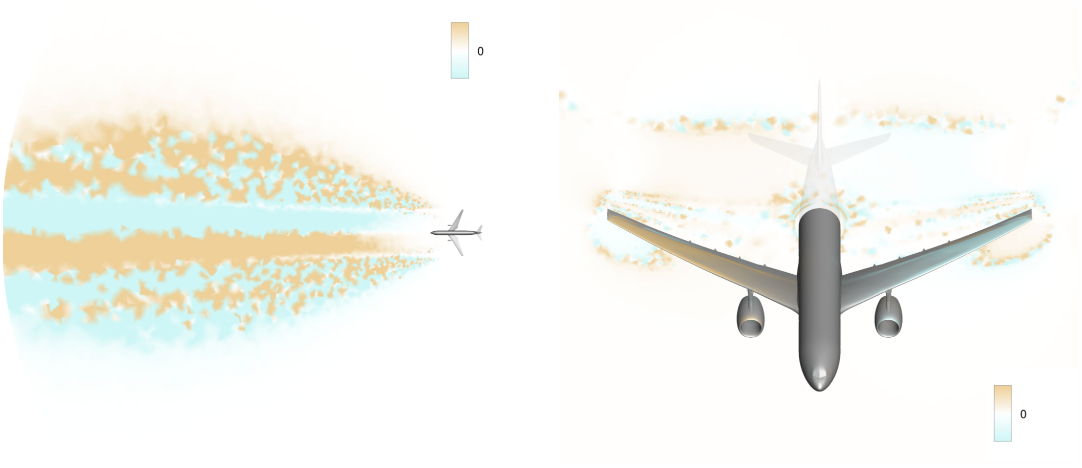

(c) Adjoint eigenvector, Roll mode (d) Direct eigenvector, Roll mode

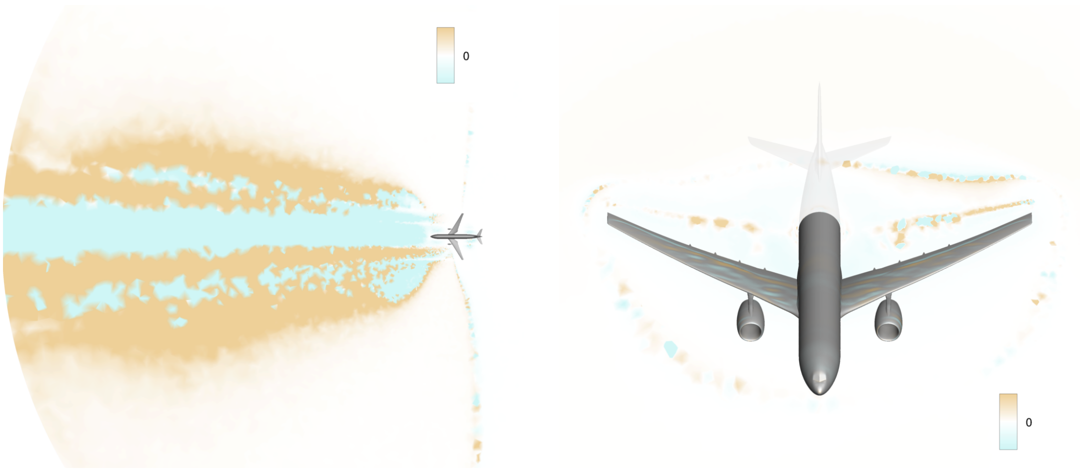

(e) Adjoint eigenvector, Spiral mode (f) Direct eigenvector, Spiral mode

Figure 6.8: Real part of pressure component for Phugoid, Roll and Spiral eigenvectors.

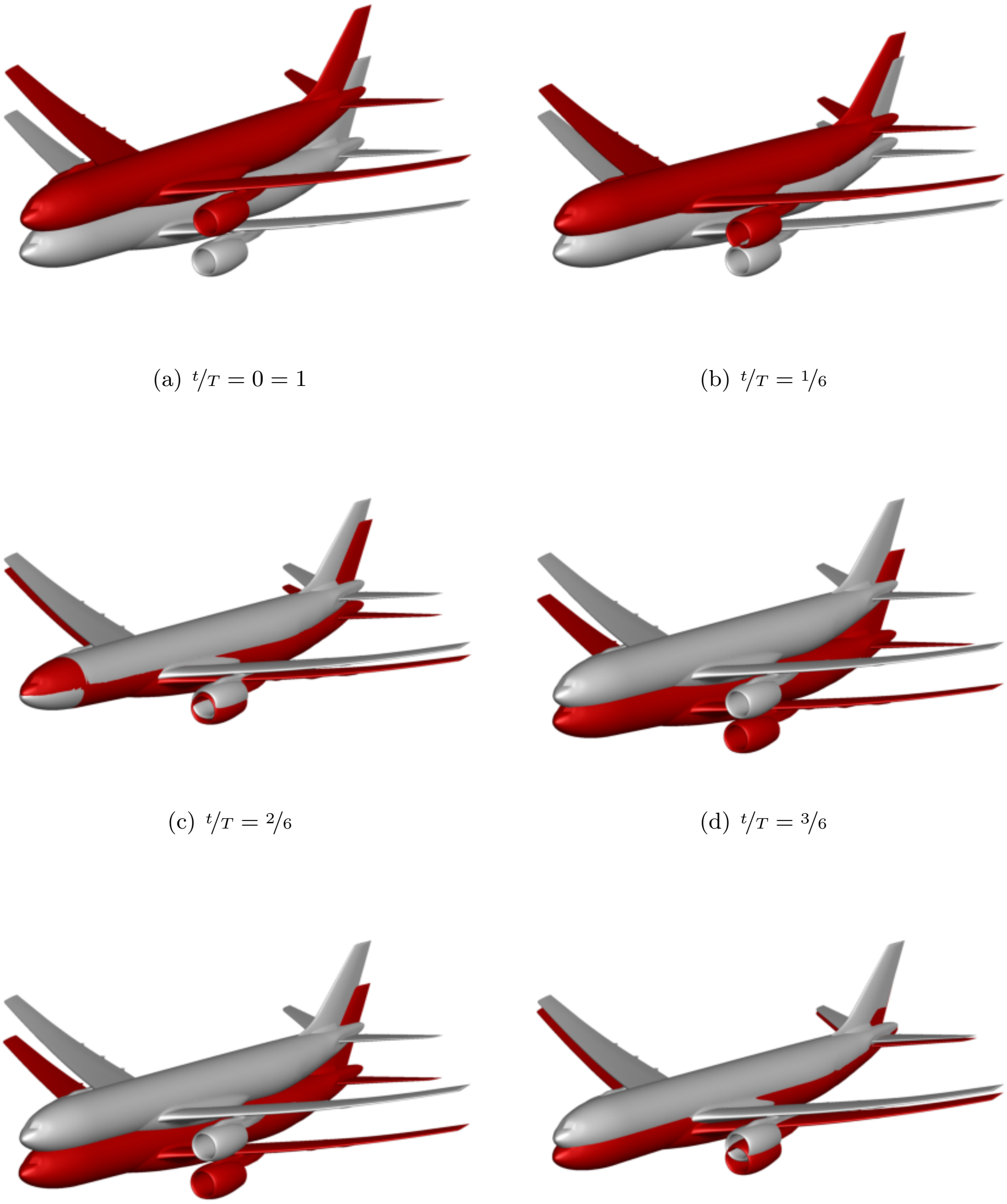

(a) $t/T = 0 = 1$

(b) $t/T = 1/6$

(c) $t/T = 2/6$

(d) $t/T = 3/6$

(e) $t/T = 4/6$

(f) $t/T = 5/6$

Figure 6.9: Flight dynamics part of short period direct eigenvector depicted as a series of snapshots taken during one period. A scaling factor is applied for better visibility.

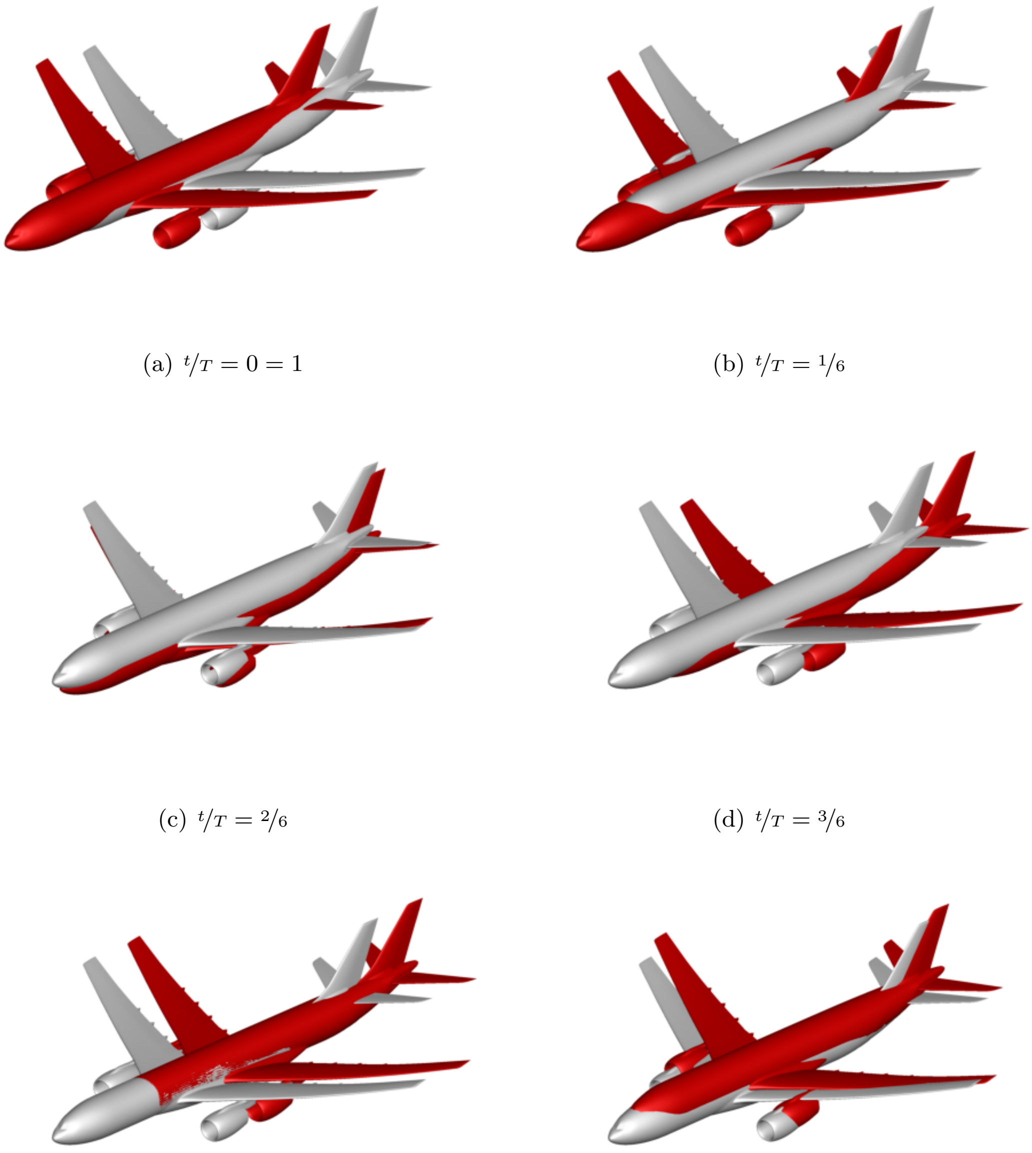

(a) ${}^{t}\!/_{T} = 0 = 1$

(b) ${}^{t}\!/_{T} = {}^{1}\!/_{6}$

(c) ${}^{t}\!/_{T} = {}^{2}\!/_{6}$

(d) ${}^{t}\!/_{T} = {}^{3}\!/_{6}$

(e) ${}^{t}\!/_{T} = {}^{4}\!/_{6}$

(f) ${}^{t}\!/_{T} = {}^{5}\!/_{6}$

Figure 6.10: Flight dynamics part of phugoid direct eigenvector depicted as a series of snapshots taken during one period. A scaling factor is applied for better visibility.

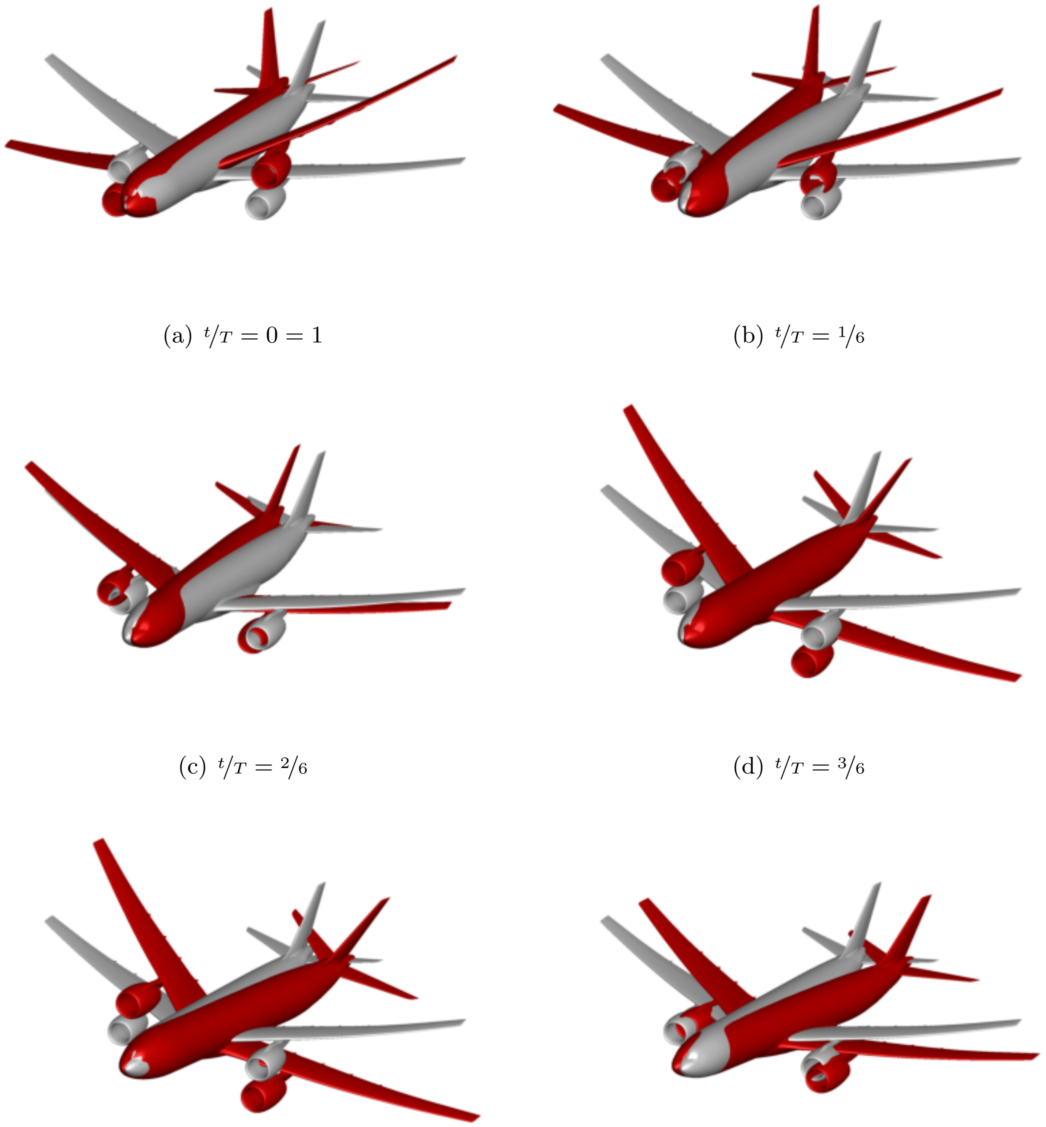

(a) ${}^{t}/_{T} = 0 = 1$

(b) ${}^{t}/_{T} = {}^{1}/_{6}$

(c) ${}^{t}/_{T} = {}^{2}/_{6}$

(d) ${}^{t}/_{T} = {}^{3}/_{6}$

(e) ${}^{t}/_{T} = {}^{4}/_{6}$

(f) ${}^{t}/_{T} = {}^{5}/_{6}$

Figure 6.11: Flight dynamics part of Dutch roll direct eigenvector depicted as a series of snapshots taken during one period. A scaling factor is applied for better visibility.

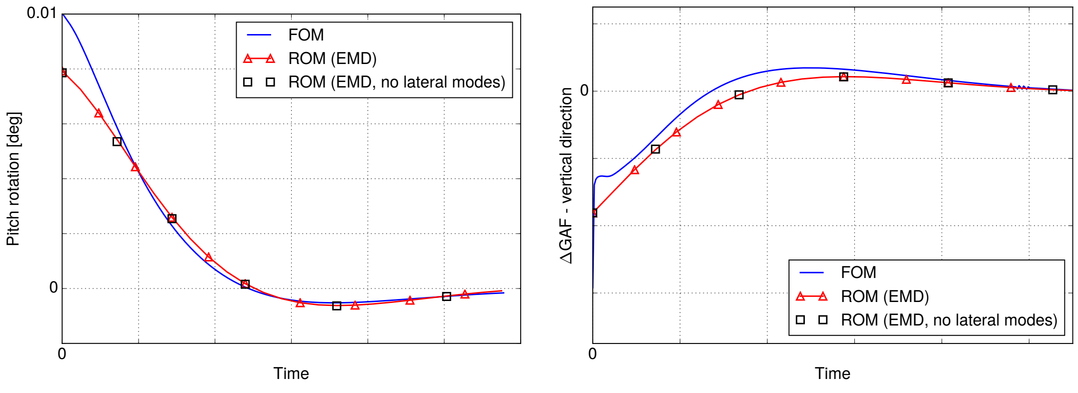

(a) Response in pitch rotation (b) GAF response in vertical direction

Figure 6.12: Results for initial disturbance of 0.01 degree in pitch degree-of-freedom. ROM includes flight dynamics modes (EMD) only.

analysis by time-integration and results are shown in Fig. 6.12 for a disturbance in the pitch rotation of 0.01 degrees. Generalised aerodynamic forces were computed during the post-processing as second derivatives of the generalised coordinates according to Eq. (2.46). Overall, full order and reduced models show a stable response as expected from the real part of the longitudinal eigenvalues. In Fig. 6.12(a) the pitch rotation is presented. Initial conditions are not fully reconstructed by the reduced model and this can be interpreted as information lost when reducing the model from about 48 million to 12 degrees-of-freedom. The trend for pitch rotation is thereafter captured accurately by the reduced model with results converging to the full order ones. In Fig. 6.12(b) a similar trend is shown for the GAF in the vertical direction. The full order model GAF shows an initial jump from a zero value followed by a slow recovery. Apart from the discrepancy in the initial conditions already discussed for the pitch rotation, the ROM results match the full order response well. Summarising, the reduced model containing 12 flight dynamics modes, specifically three complex-conjugate pairs and six real-valued eigenvectors, is able to reproduce results for initial disturbance analyses. In addition, removing the lateral flight dynamics modes from the modal bases does not affect the results for longitudinal disturbances as shown in Fig. 6.12 with an additional curve for both pitch rotation and vertical direction.

The model is subsequently expanded to account for external gust disturbances by introducing the term $\frac{\partial \boldsymbol{R}}{\partial \boldsymbol{u}_d}$ in Eq. (3.7) and defining the shape of the travelling gust with the vector $\widetilde{\boldsymbol{u}}_d$. The '1-cos' gust shape adopted for the investigation is depicted in Fig. 6.13. It extends along the lateral direction while the amplitude is applied in the vertical direction only. Results for a wavelength $L_g = 116$ m and two gust amplitudes V_{g_z} are presented in Fig. 6.14. Two curves are shown for the full order model. The first corresponds to a gust disturbance acting linearly ($V_{g_z} = 0.01\%$ of free-stream velocity) whereas the second one represents a gust amplitude as prescribed by EASA regulations

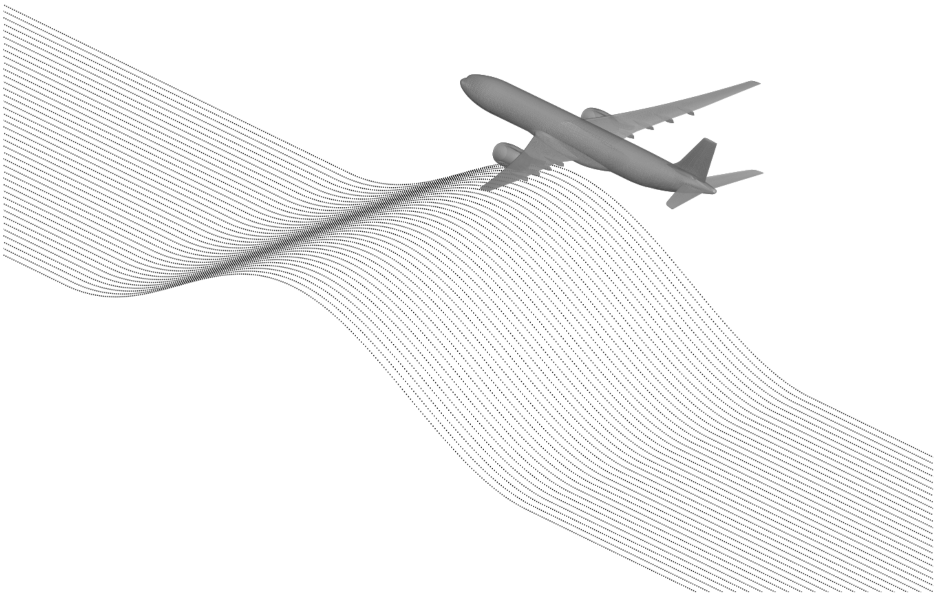

Figure 6.13: Shape of the vertical gust with gust length $L_g = 116\,\mathrm{m}$.

for the given gust length ($V_{g_z} = 6.1\%$ of free-stream velocity). Although ROM results should be compared to the linear model, including results for the certification gust helps highlighting non-linear effects. Both reference solutions show an oscillation for the pitch rotation GAF in Fig. 6.14(a). This is due to the alteration in pitching moment brought by the disturbance which is followed by a response from the stable system. Non-linear effects alter the peak values and accelerate the response decay as shown by the large amplitude gust. An offset between linear and certification gusts is visible at the end of the simulation. This depends on the tiny amplitude used for the linear excitation whose effects are dissipated more quickly and it is affected by the numerical solution scheme and chosen tolerances. The full order results are compared to the ROM which shows some discrepancies in the peak values and a phase lag. This is due to a lack of information to fully reconstruct the effect of aerodynamic disturbances. The flight dynamics eigenvectors, coming from the Jacobian matrix of the coupled system, are unable to fully account for the effects of pure aerodynamic disturbances such as gusts, as discussed in Chapter 5. When the gust has passed the aircraft, the reduced model converges to the full order results. This behaviour is confirmed by the vertical GAF in Fig. 6.14(b). The first peak, which is mainly due to the aerodynamic disturbance, is not fully predicted. Thereafter, the GAF value provided by the reduced model converges to the reference value confirming that flight dynamics modes are able to describe the system behaviour when not subject to external disturbances.

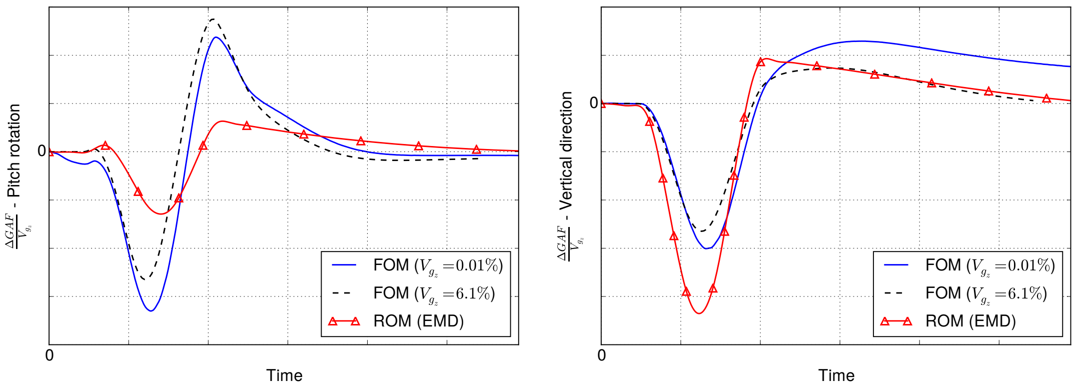

(a) GAF response in pitch rotation

(b) GAF response in vertical direction

Figure 6.14: Response to '1-cos' gust with wavelength $L_g = 116$ m and gust amplitudes $V_{g_z} = 0.01\%$ and $V_{g_z} = 6.1\%$ of free-stream velocity. ROM includes flight dynamics modes (EMD) only.

6.4 Data-based Identification

A solution to reproduce full order response to external disturbances with the reduced order model is provided with data-based identification which is described next. A snapshot matrix is populated with 20 solutions to Eq. (2.65) and their complex-conjugates, each corresponding to a harmonic fluid response for a sinusoidal gust in the reduced frequency range $[0, 2]$. The upper limit of the frequency to sample was chosen based on Fourier decomposition of the '1-cos' gust for the wavelength to be investigated. POD decomposition was applied to obtain 39 POD modes which describe the aerodynamic response only.

Considering a static aircraft, i.e. neither moving in the longitudinal nor lateral degrees-of-freedom, the reduced model containing POD modes only is capable of reproducing the full order results as presented in Fig. 6.15 for a '1-cos' gust with amplitude $V_{g_z} = 0.01\%$ of free-stream velocity and gust length $L_g = 116$ m. Regarding the lift coefficient in Fig. 6.15(a), full order results are characterised by a peak value followed by a smooth decay. The reduced model follows the reference curve and peak values as well as transient behaviour are well reproduced. A similar trend is shown for the moment coefficient in Fig. 6.15(b) which is evaluated accurately by the reduced model, confirming that the reduction with POD modes is a valid approach for the static case. These results have previously been published in [17] and made available by the authors.

The POD modes were used for the free-flight problem by adding them to the modal bases Φ and Ψ in Eq. (3.4) which were already populated with flight dynamics modes from the operator-based identification. These are now composed of flight dynamics modes identified with the operator-based method and POD modes given by the data-based identification applied to the aerodynamic subsystem only. This reduced model is denoted *joint* ROM since it results from the fusion of two parts. Approximate eigenvalues of A were obtained by calculating the eigenvalues of the reduced matrix $\Psi^H A \Phi$ and

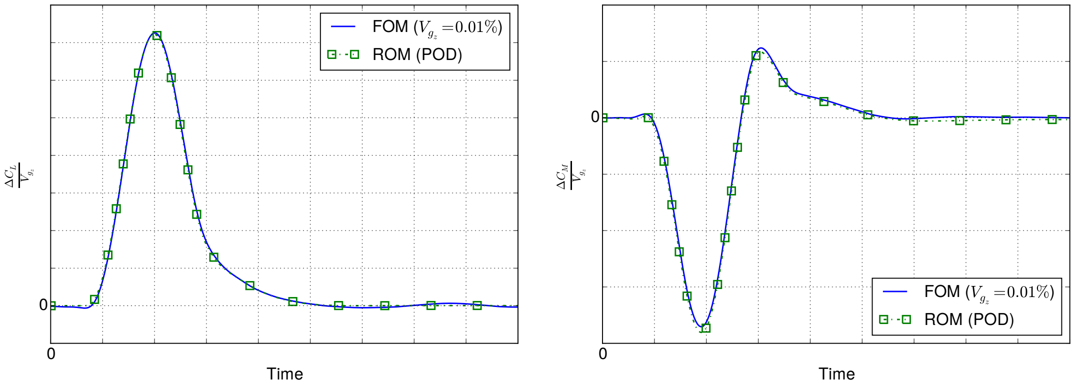

(a) Variation of the lift coefficient (b) Variation of the moment coefficient

Figure 6.15: Response to '1-cos' gust with wavelength $L_g = 116$ m and gust amplitude $V_{g_z} = 0.01\%$ of free-stream velocity for a fixed and rigid aircraft. ROM includes POD modes only.

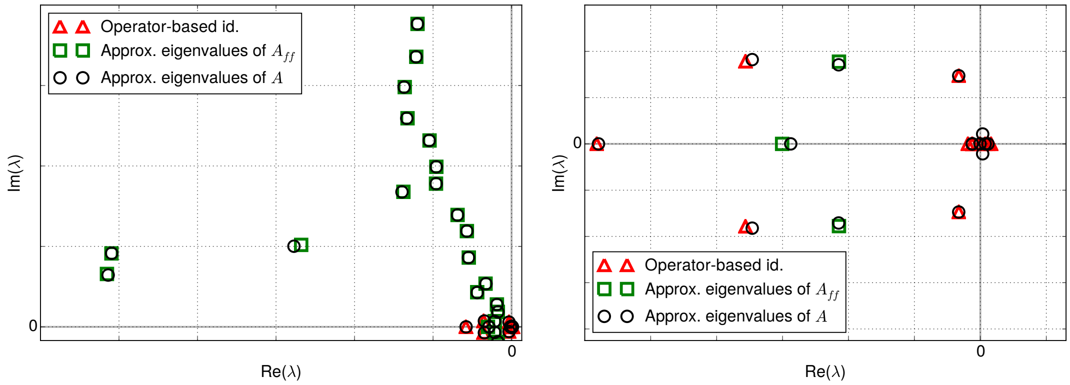

(a) Global (b) Close-up of region around origin

Figure 6.16: Eigenspectrum comparing approximate eigenvalues calculated with operator-based identification, POD and joint approaches.

results are shown in Fig. 6.16. A comparison with flight dynamics eigenvalues calculated with the operator-based identification shows that eigenvalues related to flight dynamics are affected by the coupling since they move slightly in terms of both frequency and damping. Approximate eigenvalues of A_{ff} were obtained solving the eigenproblem for $\Psi_{\text{POD}}^H A_{ff} \Phi_{\text{POD}}$ and they are reported in Fig. 6.16 as well. Their locations in the complex plane change when flight dynamics modes are added. The largest displacement of 3% was found for the flight dynamics eigenvalues. Negative imaginary parts in the global view are omitted to increase visibility.

The joint reduced model based on flight dynamics and POD modes was used to simulate an encounter with a '1-cos' gust with amplitude $V_{g_z} = 0.01\%$ of free-stream velocity and gust length $L_g = 116$ m. Results are presented in Fig. 6.17 together with

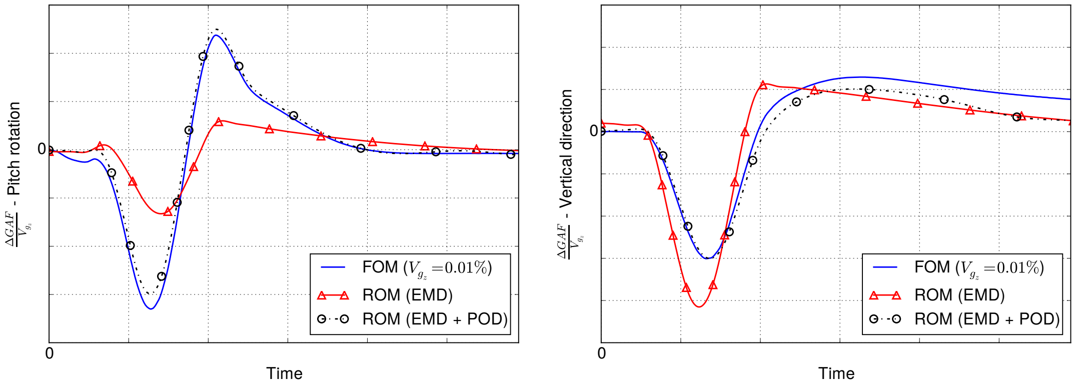

(a) GAF response in pitch rotation

(b) GAF response in vertical direction

Figure 6.17: Response to '1-cos' gust with wavelength $L_g = 116$ m and gust amplitude $V_{g_z} = 0.01\%$ of free-stream velocity. ROM includes flight dynamics (EMD) and POD modes.

the ones obtained using flight dynamics modes only in Section 6.3. Figure 6.17(a) shows a very good agreement between the full order model and ROM using flight dynamics and POD modes for the GAF in pitch rotation. The general trend is well represented and results match after the disturbance has passed the aircraft. Peak values are also well reproduced with a minor error on the first peak. The ROM behaviour is confirmed for the vertical GAF in Fig. 6.17(b) since the reference data is accurately reproduced. Thus, it can be concluded that the reduced model build using both sets of modes is able to reconstruct the system's behaviour for a small-amplitude '1-cos' gust encounter simulations. For sake of completeness, it must be noted that the differences reported in Fig. 6.14 between system's linear and non-linear response, corresponding to small and large amplitude gust encounters, are not reproduced by the linear reduced order model. Thus, the findings reported in Chapter 5 are confirmed here and the reduced model could be considered accurate enough to assess system's response to certification gusts in an industrial context.

The model reduction technique provides also a reconstruction of the flow field for each time step. This represent an advantage of this method over the approach traditionally adopted by industry for which this calculation should be performed as post-processing step. As an example, the pressure distribution at the peak value in Fig. 6.17(b) is depicted in Fig. 6.18(a). It is calculated with the joint ROM and it shows a strong shock wave on the wing upper surface. The flow field is dominated by the shock which produces the largest jump in the pressure distribution. This result is compared to the full order model which provided the reference. The difference in terms of pressure coefficient is presented in Fig. 6.18(b). The largest differences are located on the upper wing surface, close to the trailing edge. However, the maximum difference was found to be 0.05% which indicates a very good match.

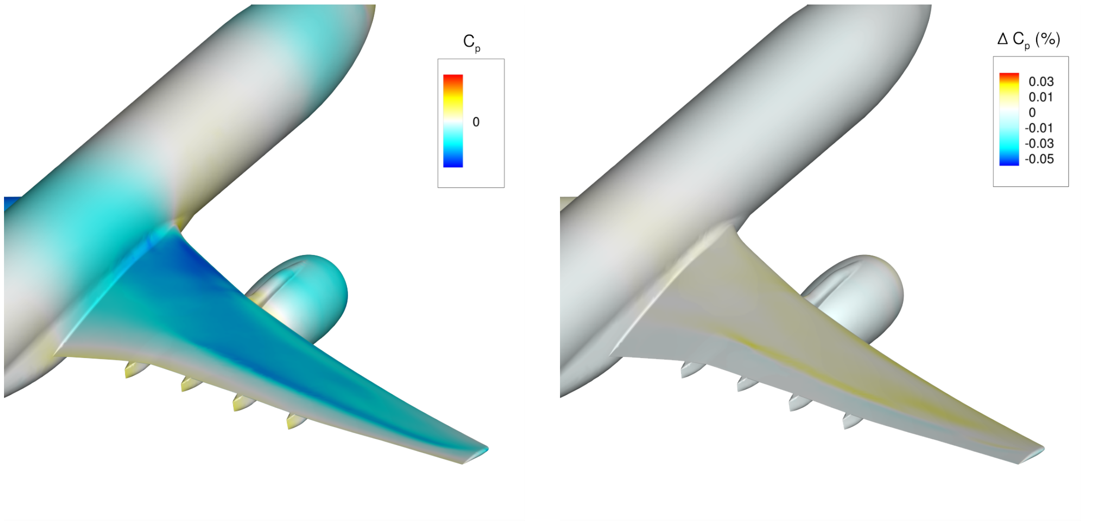

(a) Pressure coefficient distribution

(b) Difference in terms of pressure coefficient between reduced and full order models

Figure 6.18: Pressure coefficient at peak value of vertical GAF obtained from reduced order model and comparison to reference full order results.

Regarding the cost of building the reduced model for the longitudinal dynamics of the large civil aircraft, it can be split in two parts. The first is given by the operator-based identification which required the calculation of 7 GAF matrices for a total of 42 LFD solves for columns of A_{fs}. A number of 18 additional solutions are needed to obtain the direct and adjoint eigenvectors. The second part involves the evaluation of POD modes with 20 solutions of Eq. (2.65). The total cost of the ROM is estimated to be 80 LFD computations. The cost of a single full order simulation is comparable to 48 LFD solves using the same hardware configuration. However, it is highlighted here that multiple gust lengths must be investigated during the aircraft design and certification process, and each one requires an individual full order simulation. Conversely, the reduced model can be used to simulate encounter with gusts having different lengths, each at a negligible computational cost, as shown in Fig. 6.19 for a '1-cos' gust with length $L_g = 214$ m and amplitude $V_{g_z} = 0.01\%$ of free-stream velocity. Using only flight dynamics modes for the reduction leads to inaccurate results for the peak values, as already presented for the shorter gust. However, the enhanced reduced model matches the reference in terms of transient response as well as peak values for pitch rotation GAF as depicted in Fig. 6.19(a). Similar results are reported for the vertical direction GAF in Fig. 6.19(b). This confirms that the model reduction technique is a valid tool to evaluate the response of free-flying aircraft subject to gust disturbances.

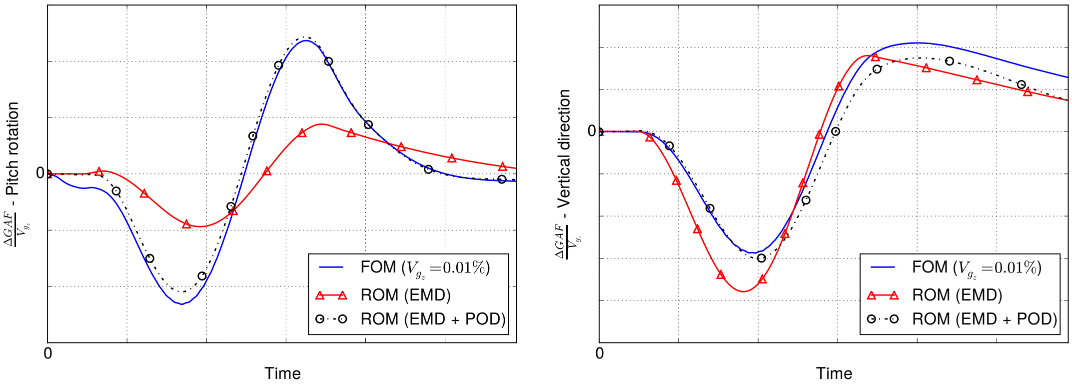

(a) GAF response in pitch rotation (b) GAF response in vertical direction

Figure 6.19: Response to '1-cos' gust with wavelength $L_g = 214$ m and gust amplitude $V_{g_z} = 0.01\%$ of free-stream velocity. ROM includes flight dynamics (EMD) and POD modes.

6.5 Model Reduction for Lateral Dynamics

So far, applications of the model reduction method concerned longitudinal dynamics. However, eigenmodes extracted with the operator-based identification contain information to represent lateral dynamics as well. The modal bases from the operator-based identification do not require any additional computation to be used for lateral dynamics. An encounter with a lateral gust is analysed in this section to demonstrate the versatility of the reduced model. This is not a comprehensive study and it represents a proof-of-concept for future applications.

The model was exploited for a '1-cos' gust with wavelength $L_g = 116$ m in the lateral direction and gust amplitude $V_{g_y} = 0.01\%$ of free-stream velocity as illustrated in Fig. 6.20. Results for the gust encounter simulations are presented in Fig. 6.21 for the GAF response in the roll and vertical velocities. The reduced model is able to reproduce accurately the lateral response in the roll motion as shown in Fig. 6.21(a). The peak value for the roll velocity is captured while reduced and full order models converge to the same value at the end of the simulation. Results for other lateral quantities are not reported since they show a similar behaviour. Lateral and longitudinal dynamics are traditionally treated independently [122] and the aircraft subject to lateral gust has a very weak response in the longitudinal dynamics as shown in Fig 6.21(b) for the vertical GAF. Although the agreement between ROM and full order model is only qualitative, note that the longitudinal response to lateral gusts is two orders of magnitude smaller than the corresponding lateral response shown in Fig. 6.21(a).

The inclusion of lateral modes in the modal bases is expected to be essential to obtain the results of Fig. 6.21(a). The effect of neglecting just one lateral mode, but retaining the others, was hence investigated. This was done to show that a key element for a successful reproduction of lateral dynamics is an accurate identification of the Dutch roll mode. A

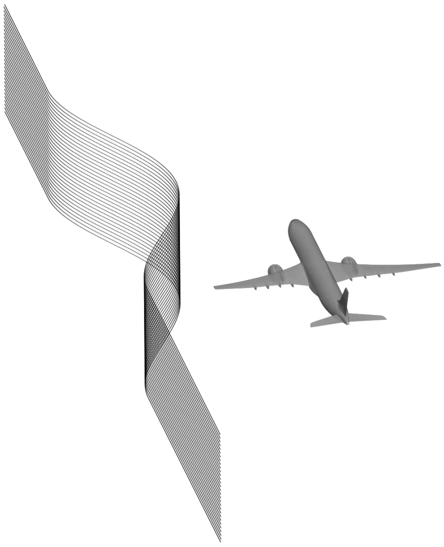

Figure 6.20: Shape of the lateral gust with gust length $L_g = 116\,\mathrm{m}$.

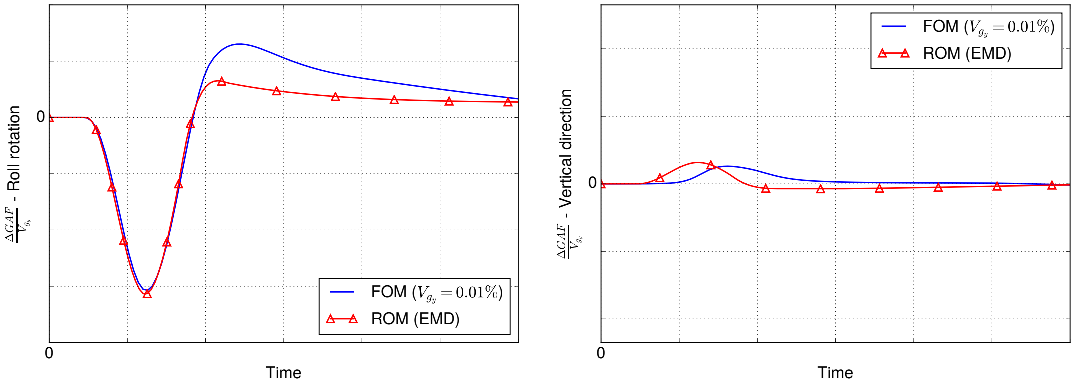

(a) GAF response in the roll rotation

(b) GAF response in the vertical direction

Figure 6.21: Response to '1-cos' lateral gust with wavelength $L_g = 116$ m and gust amplitude $V_{g_y} = 0.01\%$ of free-stream velocity. ROM includes flight dynamics modes (EMD) only.

gust encounter with the same parameters of Fig. 6.21(a) was simulated with the reduced model using modal bases containing all but the Dutch roll mode. Results are shown in Fig. 6.22 and compared to both full order reference and to the reduced model using all modes. In Fig. 6.22(a), the effect of excluding the Dutch roll mode is clearly visible on the GAF in the roll degree-of-freedom. The peak value is underestimated and the reconstruction of the transient behaviour worsened. Conversely, the Dutch roll mode does not contribute to the reconstruction of longitudinal response since very similar curves are obtained either including or excluding it from the bases as depicted in Fig. 6.22(b). Overall, this confirms that an accurate evaluation of lateral modes, in particular of the Dutch roll mode, is needed to achieve goods results for the lateral response.

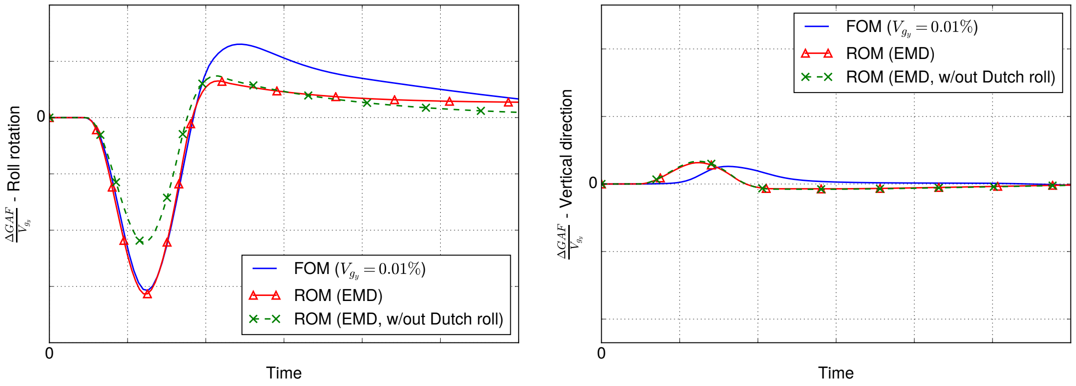

(a) GAF response in roll rotation

(b) GAF response in vertical direction

Figure 6.22: Response to '1-cos' lateral gust with wavelength $L_g = 116$ m and gust amplitude $V_{g_y} = 0.01\%$ of free-stream velocity. ROM modal bases do not include Dutch roll.

6.6 Chapter Summary

The chapter concerned the model reduction for a coupled system involving flight dynamics and computational fluid dynamics applied to a large civil aircraft. This is an upscaling of techniques already developed for two-dimensional test cases and reported in Chapters 4 and 5. In particular, the scalability of the method towards an industrial test case has been investigated. The problem of dealing with large models involving large CFD grids was tackled. A key point of the investigation is that frequency domain methods are exploited to accelerate every step of the reduced model calculation. Thus, CFD accuracy is retained and the computational cost is kept at the minimum. The key challenge of identifying flight dynamics modes regardless their position in the complex-plane was performed using dynamic derivatives distributed along the imaginary axis. Although the tracing was thus simplified, the calculation of fluid parts of eigenvectors represented a new challenge due to almost singular matrices. This was overcome by computing the LFD solution assuming $\Re(\lambda) = 0$.

The results show that the reduced model based on the operator-based identification is capable of matching the full order reference in terms of flight dynamics response. In particular, results obtained for the initial disturbance analysis highlighted the suitability of the technique for large cases as well. Results for gust encounter simulations are less accurate since the lack of aerodynamic modes leads to underestimation of peak values for flight dynamics response. This problem is solved with the data-based identification method, adopting a strategy similar to the two-dimensional test cases. The data-based identification was performed on the aerodynamic subsystem only and the POD modes were combined with modes from the operator-based identification. This allows for a modular approach where different parts of the ROM can be exploited independently or in conjunction with others, according to the need. Results were produced for two gust lengths showing a good agreement and a discussion about computational cost is provided. The last part of the chapter described a preliminary investigation towards lateral dynamics since the operator-based identification produced both longitudinal and lateral modes. A lateral gust encounter simulation was performed and results compared to the full order reference. The reduced model was capable of reproducing the lateral dynamics response accurately. This is largely due to the good accuracy obtained when evaluating the lateral modes as confirmed by an additional brief investigation.

Overall, the method has proved to be reliable and suitable for applications involving practical test cases. The modular approach based on operator-based identification with the addition of aerodynamic modes from the data-based methodology allows for multiple applications of the same ROM. For example, the operator-based ROM is suitable for stability analyses and to reproduce flight dynamics effects whereas the data-based one can be trained for various external disturbances besides gusts. Focusing on the big picture, this test case showed that this model reduction technique can enhance the current industrial practice for gust certification by including flight dynamics effects as well as unsteady CFD aerodynamics. Possible applications are rapid gust encounter simulation at the edge-of-the-envelope design.

Chapter 7

Conclusions and Outlook

Model reduction of high-fidelity systems involving both flight dynamics and aerodynamics based on computational fluid dynamics has been the aim of this thesis. This work follows a modal decomposition and projection model reduction philosophy. The specific tasks addressed here are the identification of modes for the reduction, the construction of the reduced order model and then its efficient application to gust encounter simulations. The work enables aircraft manufacturers to predict the aircraft's behaviour accurately and quickly when it is subject to gust disturbances. Thus, the aim of certification by simulation is brought closer and overall certification cost reduced. The final result will be a more efficient, cleaner aircraft whose design exploits tools first developed in this work and for which cheaper tickets have to be paid. This is the long-term vision which inspired this research and that this work contributes to. A chapter-by-chapter summary is provided next.

The high-fidelity full order model is composed of two subsystems, as described in Chapter 2, which implement aerodynamics and flight dynamics. Regarding the former, it is based on either Euler or Reynolds-averaged Navier–Stokes equations with the Spalart-Allmaras turbulence model providing a closure for the latter. Model reduction is described in Chapter 3. The full order non-linear residual function is expanded in a first-order Taylor series and the Jacobian matrix projected onto a small modal basis. The calculation of modes for the projection is achieved with either of two methods. The first one is called operator-based identification and it is based on the Schur complement of the Jacobian matrix partitioned in blocks. It is suitable to extract few eigenpairs related to flight dynamics from the coupled Jacobian matrix. The tracing is performed with Newton's method starting from rigid-body modes. The technique has previously been applied to structural dynamics problems. Here, it is improved with novel contributions for the specific computation of flight dynamics modes. A theoretical link between the Schur complement method and dynamics derivatives is derived as well. In addition, a data-based mode identification method is presented. The response of the coupled system is sampled for sinusoidal gusts at multiple frequencies using a linearised frequency domain solver. Complex-valued results are collected as columns of a snapshot matrix and proper orthogonal decomposition is applied to it. As a result, a number of POD modes equal to the number of snapshots is obtained and they are used to populate the basis for the model reduction. The data-based technique has been applied in literature to various problems. However, its frequency domain application to coupled system composed of flight dynamics and CFD aerodynamics represents a novelty.

In Chapter 4, a first application of mode identification and model reduction is presented. The coupled system is composed of a NACA 0012 aerofoil with transonic aerodynamics based on Euler equations and the focus is on short-term approximation. Full order results were reproduced accurately with the operator-based reduced model for a large value of mass ratio. A multi-step procedure is developed for cases with low values of mass ratio since the identification is significantly more challenging. It consists of exploiting dynamic derivatives to provide a starting point for a refinement stage which is performed with the Schur complement method. At the end, the method provides results comparable to the direct extraction of eigenvalues but it does not rely on any spectral information. The data-based identification was investigated as well. Based on the Fourier decomposition of the '1-cos' gust shape, a range of frequencies was identified and the sampling procedure performed for multiple sinusoidal gusts on the whole system including both aerodynamics and flight dynamics. Few tens of modes were able to produce results matching the full order model. Overall, the test case is the first application, to the author's best knowledge, of a projection reduced order model for a coupled system composed of CFD aerodynamics and flight dynamics with modes identified applying either the operator-based or the data-based technique. The list of key challenges which were tackled in Chapter 4 includes the tracing of flight dynamics modes inside the cloud of fluid modes for the operator-based identification and the sampling performed on the coupled system for the data-based one. They enable the application of both identification methods to larger test cases which are shown in the following chapters.

An application of mode identification and model reduction to longitudinal dynamics is presented in Chapter 5. The system is composed of a supercritical aerofoil and a NACA 0012 which resemble a typical wing-tail configuration for large civil aircraft. Aerodynamics is based on Reynolds-averaged Navier–Stokes equations and the equilibrium condition for the linearisation is computed with a trimming procedure based on Broyden's method. Results showing good performance of operator-based reduced model were produced at a large value of mass ratio, thus confirming the findings yielded in Chapter 4. However, such reduced models provide only a qualitative reconstruction of results at lower mass ratios. An additional investigation showed that modes coming from the Jacobian matrix cannot accurately reconstruct the response to gusts at low mass ratios since they do not contain information about any external disturbance. A solution to this problem was proposed with the data-based identification method. The coupled system was sampled at a finite number of frequencies and POD modes calculated. The results, which match the reference solution, were compared to the operator-based ones. Although almost no difference exists when flight dynamics is dominant at large values of mass ratio, results from the reduced model built using the data-based method are more accurate when flight dynamics eigenvalues are inside the aerodynamic cloud at lower mass ratios. Overall, the reduction in terms of computational time is estimated to be two orders of magnitude for this two-dimensional problem. Challenges addressed in Chapter 5 concern a more complex aerodynamics based on Reynolds-averaged Navier–Stokes equations, a non-trivial equilibrium resulting from a trimming procedure, the tracing of multiple flight dynamics modes with the operator-based method and scaling the data-based method toward larger test cases.

The model reduction method is applied to a three-dimensional industrial use case in Chapter 6. It represents a large civil aircraft flying at transonic speed. Aerodynamics is modelled with Reynolds-averaged Navier–Stokes equations with the Spalart-Allmaras model whereas flight dynamics relies on a modal formulation. Challenges depending on the large dimension of the CFD subsystem were faced. For example, no spectral information is available at all for this test case since eigenpairs extraction is prohibitive also for few eigenvalues. This is a realistic scenario for a practical application of the method. The operator-based mode identification was performed for both longitudinal and lateral flight dynamics modes. Besides short period and phugoid, modes such as Dutch roll, roll subsidence and spiral divergence were identified. Despite the short period being supposedly located inside the cloud of aerodynamic eigenvalues, the multi-step tracing approach developed in the previous Chapter 5 proved to be reliable for all flight dynamics modes. In addition, the operator-based identification provided insights about aircraft handling qualities and sensitive regions of fluid domain thanks to both adjoin and direct eigenvectors. Results calculated with the operator-based reduced model are accurate as far as initial disturbance analysis is concerned. However, results for '1-cos' gust encounters are less accurate. For them, the data-based approach was investigated as alternative. Including flight dynamics modes as well as few POD modes in the modal basis makes the reduced model capable of reproducing full order results for gust encounter simulations. A preliminary investigation for lateral gusts showed that the lateral flight dynamics modes, which were identified with the operator-based method and included in the modal basis too, proved to be sufficient to reproduce the lateral dynamics of the large civil aircraft. However, further research is still needed. A quantification of computational time needed to build and use the reduced model showed that a comparable amount of time is needed by the full order model to run a single simulation. However, a saving of up to one order of magnitude is achieved when multiple gust lengths must be investigated and this is the case during aircraft certification.

Overall, both mode identification and model reduction methods proved to be an effective way to perform quick simulations coupling flight dynamics and CFD aerodynamics, in particular for gust encounters, even when cost of building the ROM is

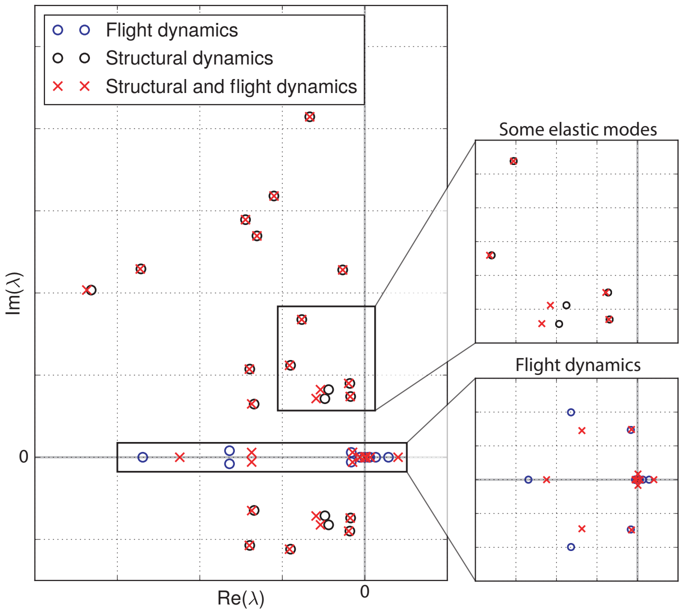

Figure 7.1: Eigenspectrum resulting from the operator-based identification for a system including aerodynamics, flight dynamics and structural dynamics.

taken into account. This represents a step toward a faster design process and brings the long-term objective of aircraft certification by simulation closer. Novel aspects of the work to the author's best knowledge are the operator-based identification for flight dynamics modes, the application of the data-based method in frequency domain to the coupled system treated as a monolithic entity and the common theoretical framework for both data-based and operator-based reduction. The test cases presented in the thesis are novel applications of model reduction to both two-dimensional and three-dimensional problems. The reduced model was able to reproduce full order results with a computational cost saving ranging from one to two order of magnitude.

7.1 Future Work

Some areas of potential future research can be identified. Further research is needed to include elastic effects in addition to flight dynamics ones since this is the ultimate certification requirement. The mutual interaction between flexible structure and flight dynamics degrees-of-freedom is expected to generate modes which describe both rigid dynamics and a deformable structure. The test case to be investigated would be the large civil aircraft described in Chapter 6. In fact, it is based on flight dynamics equations written in modal form and the software framework is designed to be able to cope with structural modes as well. Preliminary results from the operator-based identification for the system including CFD aerodynamics, flight dynamics and structural dynamics are reported in Fig. 7.1 to describe the challenges lying ahead. The spectrum depicted in Fig. 7.1 contains three sets of modes. The first one is composed of flight dynamics modes which were obtained in Chapter 6 for the rigid aircraft. The second set contains elastic modes for a static, non-moving, aircraft which were calculated by tracing the in-vacuum structural modes. They typically describe an aeroelastic system which does not include any free-flight effect. When flight dynamics and structural dynamics are included together in the same model, rigid-body and structural degrees-of-freedom interact. The operator-based identification performed on the system including aerodynamics, flight dynamics and structural dynamics returned eigenvalues which are the third set included in Fig. 7.1. They have an offset when compared to the eigenvalues obtained for the distinct models. Such difference is more evident for flight dynamics modes since their frequency and damping are both lowered. Regarding elastic modes, their frequencies are not affected significantly but their damping values are. These preliminary results show the next challenges to be faced in order to obtain a reduced model capable of including flight dynamics and CFD-based aerodynamics to perform gust encounter simulations of a flexible aircraft. In the long-term, control surfaces could be included in the reduced order model as well by building on results provided in Chapter 4 for a flap excitation. The final aim would be a quick method for gust suppression applied to flexible aircraft.

Apart from the incremental improvements described so far, additional areas of research can be identified which relate to this work. Inclusion of non-linear effects could be a promising target as shown for large amplitude gusts in both Chapters 5 and 6. In addition, fluid non-linear effects such as shock separation could be included as well. A straightforward, albeit computationally expensive, way to obtain non-linear reduced model would be to include high-order terms to the Taylor expansion of the non-linear full order residual described in Section 3.1. An example of this high-order expansion is given in [64] for non-linear structure and linear aerodynamics. Once the non-linear ROM is available, it will provide enhanced accuracy for gust encounter simulations since non-linear effects, which are present for '1-cos' gusts with certification amplitude, would be captured by the reduced model. In addition, a new scenario, i.e. dynamic manoeuvre simulations, could be investigated. In fact, the evolving flight conditions during a manoeuvre would require the non-linear ROM to be capable of taking into account large displacements.

Furthermore, the main limitation of model reduction based on operator-based identification could be tackled. Specifically, modal bases are tied to a particular flight condition and they must be recomputed when a flight parameter change [53]. However, multiple conditions must be investigated in certification context, thus multiple reduced models have to be computed. A way to alleviate this problem is highly desirable. A possible solution is the pre-computation of multiple modal bases, each one corresponding to a distinct flight condition in the range of interest. Interpolation as described in [4] could provide the reduced model with the correct modal basis for the flight condition to be investigated. Thus, a further reduction of computational cost can be reached using the tools developed in this work.

Bibliography

[1] Adrian, R., Christensen, K. and Liu, Z.-C. [2000], 'Analysis and interpretation of instantaneous turbulent velocity fields', *Experiments in Fluids* 29(3), 275–290.
doi: 10.1007/s003489900087

[2] *Air Navigation Regulations* [1919]. Accessed online on 2017-10-10.
Web: `http://www.flightglobal.com/pdfarchive/view/1919/1919%20-%200608.html`

[3] Alonso, D., Vega, J. M., Velazquez, I. and de Pablo, V. [2012], 'Reduced-order modeling of three-dimensional external aerodynamic flows', *Journal of Aerospace Engineering* 25(4), 588–599.
doi: 10.1061/(ASCE)AS.1943-5525.0000148

[4] Amsallem, D. and Farhat, C. [2008], 'Interpolation method for adapting reduced-order models and application to aeroelasticity', *AIAA Journal* 46(7), 1803–1813.
doi: 10.2514/1.35374

[5] Amsallem, D. and Farhat, C. [2012], 'Stabilization of projection-based reduced-order models', *International Journal for Numerical Methods in Engineering* 91(4), 358–377.
doi: 10.1002/nme.4274

[6] Ananthasayanam, M. [AIAA 2003-5621, 2003], Pattern of progress of civil transport airplanes during the twentieth century.
doi: 10.2514/6.2003-5621

[7] Anderson, J. D. [1995], *Computational Fluid Dynamics*, McGraw Hill.
doi: 10.1007/978-3-540-85056-4

[8] Anderson, J. D. [2005], *Introduction to flight*, McGraw-Hill.

[9] Badcock, K. J., Timme, S., Marques, S., Khodaparast, H., Prandina, M. and Mottershead, J. [2011], 'Transonic aeroelastic simulation for instability searches and uncertainty analysis', *Progress in Aerospace Sciences* 47(5), 392–423.
doi: 10.1016/j.paerosci.2011.05.002

[10] Badcock, K. J., Woodgate, M. A. and Richards, B. E. [2004], 'Hopf bifurcation calculations for a symmetric airfoil in transonic flow', *AIAA Journal* 42(5), 883–892.
doi: 10.2514/1.9584

[11] Balajewicz, M. and Dowell, E. H. [2012], 'Stabilization of projection-based reduced order models of the Navier–Stokes', *Nonlinear Dynamics* 70(2), 1619–1632.
doi: 10.1007/s11071-012-0561-5

[12] Bartels, R. E. [AIAA 2013-3044, 2013], Developing an accurate CFD based gust model for the truss braced.
doi: 10.2514/6.2013-3044

[13] Batina, J. [1993], A gridless Euler/Navier-Stokes solution algorithm for complex-aircraft applications, *in* '31st Aerospace Sciences Meeting', American Institute of Aeronautics and Astronautics, Reno, NV, U.S.A.
doi: 10.2514/6.1993-333

[14] Baur, U., Benner, P. and Feng, L. [2014], 'Model order reduction for linear and nonlinear systems: a system-theoretic perspective', *Archives of Computational Methods in Engineering* 21(4), 331–358.
doi: 10.1007/s11831-014-9111-2

[15] Bayliss, A. and Turkel, E. [1982], 'Far field boundary conditions for compressible flows', *Journal of Computational Physics* 48(2), 182–199.
doi: 10.1016/0021-9991(82)90046-8

[16] Bazilevs, Y. and Hughes, T. J. R. [2007], 'Weak imposition of Dirichlet boundary conditions in fluid mechanics', *Computers & Fluids* 36(1), 12–26.
doi: 10.1016/j.compfluid.2005.07.012

[17] Bekemeyer, P., Thormann, R. and Timme, S. [2017*a*], 'Frequency-domain gust response simulation using computational fluid dynamics', *AIAA Journal* 55(7), 2174–2185.
doi: 10.2514/1.J055373

[18] Bekemeyer, P., Thormann, R. and Timme, S. [2017*b*], 'Rapid gust response simulation of large civil aircraft using computational fluid dynamics', *The Aeronautical Journal* 121(1246), 113.
doi: 10.1017/aer.2017.104

[19] Bekemeyer, P. and Timme, S. [AIAA 2016-1485, 2016], Reduced order gust response simulation using computational fluid dynamics.
doi: 10.2514/6.2016-1485

[20] Bekemeyer, P. and Timme, S. [AIAA 2017-4361, 2017], Reduced order transonic aeroelastic gust response simulation of large aircraft.
doi: 10.2514/6.2017-4361

[21] Bird, R., Stewart, W. and Lightfoot, E. [2007], *Transport phenomena*, Wiley.

[22] Bisplinghoff, R., Ashley, H. and Halfman, R. [1955], *Aeroelasticity*, Addison-Wesley.

[23] Blazek, J. [2001], *Computational fluid dynamics: principles and applications*, Elsevier.

[24] Boeing Commercial Airplanes [2017], 'Statistical summary of commercial jet airplane accidents, 1959-2016'.

[25] Boussinesq, J. [1877], 'Essai sur la thorie des eaux courantes', *Memoires Presentes a l'Academie des Sciences de l'Institut de France* XXIII(46).

[26] Boussinesq, J. [1896], 'Theorie de l'coulement tourbillonant et tumulteur des liquides dans les lits rectiligues', *Comptes Rendus de l'Academie des Sciences de l'Institut de France* CXXII, 1293.

[27] Broyden, C. [1965], 'A class of methods for solving nonlinear simultaneous equations', *Mathematics of Computation* 19, 577–593.
doi: 10.1090/S0025-5718-1965-0198670-6

[28] Bryan, G. [1911], *Stability in aviation*, Macmillan.

[29] Bullen, N. I. [1970], Gusts, discrete and indiscrete, Technical Report C.P. 1079, Aeronautical Research Council.

[30] Buresti, G. [2015], 'A note on Stokes' hypothesis', *Acta Mechanica* 226(10), 3555–3559.
doi: 10.1007/s00707-015-1380-9

[31] Carlomagno, G. M. [2009], *Elementi di gasdinamica*, Liguori.

[32] Chen, H., Patel, V. and Ju, S. [1990], 'Solutions of Reynolds-averaged Navier-Stokes equations for three-dimensional incompressible flows', *Journal of Computational Physics* 88(2), 305–336.
doi: 10.1016/0021-9991(90)90182-Z

[33] Coleman, G. N. and Sandberg, R. D. [2010], A primer on direct numerical simulation of turbulence-methods, procedures and guidelines, Technical Report AFM-09/01a, University of Southampton, Southampton, United Kingdom.

[34] Cook, M. [2007], *Flight dynamics principles*, Elsevier.

[35] Cook, R. G. and Palacios, R. [2013], 'Robust gust alleviation and stabilization of very flexible aircraft', *AIAA Journal* 51(2), 330–340.
doi: 10.2514/1.J051697

[36] Cooper, J. [1952], 'The international air navigation conference, Paris 1910', *Journal of Air Law and Commerce* 19(2), 127–142.

[37] Cramer, E. J., Dennis, J. E., Frank, P. D., Lewis, R. M. and Shubin, G. R. [1994], 'Problem formulation for multidisciplinary optimization', *SIAM Journal on Optimization* 4(4), 754–776.
doi: 10.1137/0804044

[38] Curbastro, G. [1898], *Lezioni sulla teoria delle superficie*, Drucker.

[39] Da Ronch, A., Badcock, K. J., Wang, Y., Wynn, A. and Palacios, R. N. [AIAA 2012-4404, 2012], Nonlinear model reduction for flexible aircraft control design.
doi: 10.2514/6.2012-4404

[40] Da Ronch, A., Ghoreyshi, M. and Badcock, K. J. [2011], 'On the generation of flight dynamics aerodynamic tables by computational fluid dynamics', *Progress in Aerospace Sciences* 47(8), 597 – 620.
doi: https://doi.org/10.1016/j.paerosci.2011.09.001

[41] Da Ronch, A., McCracken, A. J., Badcock, K. J., Widhalm, M. and Campobasso, S. [2013], 'Linear frequency domain and harmonic balance predictions of dynamic derivatives', *Journal of Aircraft* 50(3), 694–707.
doi: 10.2514/1.C031674

[42] Da Ronch, A., Tantaroudas, N. D., Timme, S. and Badcock, K. J. [AIAA 2013-1492, 2013], Model reduction for linear and nonlinear gust loads analysis.
doi: 10.2514/6.2013-1492

[43] Da Ronch, A., Vallespin, D., Ghoreyshi, M. and Badcock, K. J. [2012], 'Evaluation of dynamic derivatives using computational fluid dynamics', *AIAA Journal* 50(2), 470–484.
doi: 10.2514/1.J051304

[44] Danowsky, B., Thompson, P., Farhat, C., Lieu, T., Harris, C. and Lechniak, J. [2010], 'Incorporation of feedback control into a high-fidelity aeroservoelastic fighter aircraft model', *Journal of Aircraft* 47, 1274–1282.
doi: 10.2514/1.47119

[45] Davison, E. [1966], 'A method for simplifying linear dynamic systems', *IEEE Transactions on Automatic Control* 11(1), 93–101.
doi: 10.1109/TAC.1966.1098264

[46] Day, M. A. [1990], 'The no-slip condition of fluid dynamics', *Erkenntnis* 33(3), 285–296.
doi: 10.1007/BF00717588

[47] de Boer, A., van der Schoot, M. and Bijl, H. [2007], 'Mesh deformation based on radial basis function interpolation', *Computers and Structures* 85(11-14), 784–795.
doi: 10.1016/j.compstruc.2007.01.013

[48] Delaunay, B. [1934], 'Sur la sphere vide', *Bulletin de l'Academie des Sciences de l'URSS* 7(6), 793–800.

[49] Dhole, N., Yadav, V. and Olivares, G. [2012], Certification by analysis of a typical aircraft seat, *in* '12th International LS-DYNA users conference'.
Web: `http://www.dynalook.com/international-conf-2012/automotive22-a.pdf`

[50] Dole, C. and Lewis, J. [2000], *Flight theory and aerodynamics: a practical guide for operational safety*, Wiley.

[51] Donea, J., Giuliani, S. and Halleux, J. [1982], 'An arbitrary Lagrangian-Eulerian finite element method for transient dynamic fluid-structure interactions', *Computer Methods in Applied Mechanics and Engineering* 33(1), 689–723.
doi: 10.1016/0045-7825(82)90128-1

[52] Donea, J., Huerta, A., Ponthot, J. P. and Rodrguez-Ferran, A. [2004], *Arbitrary Lagrangian-Eulerian methods*, John Wiley & Sons, Ltd., chapter 14.
doi: 10.1002/0470091355.ecm009

[53] Dowell, E. H., and Hall, K. C. [2001], 'Modeling of fluid-structure interaction', *Annual Review of Fluid Mechanics* 33(1), 445–490.
doi: 10.1146/annurev.fluid.33.1.445

[54] Drela, M. [AIAA 99-1394, 1999], Integrated simulation model for preliminary aerodynamic, structural, and control-law design of aircraft.
doi: 10.2514/6.1999-1394

[55] Duarte, F., Gormaz, R. and Natesan, S. [2004], 'Arbitrary Lagrangian-Eulerian method for Navier-Stokes equations with moving boundaries', *Computer Methods in Applied Mechanics and Engineering* 193(45), 4819 – 4836.
doi: 10.1016/j.cma.2004.05.003

[56] Dwight, R. [DLR-FB-2005-05, 2006], An implicit LU-SGS scheme for finite-volume discretizations of the Navier-Stokes equations on hybrid grids.

[57] EASA [2007], 'Certification specifications and acceptable means of compliance for large aeroplanes CS-25 amendment 15'.

[58] Euler, L. [1752], 'Principia motus fluidorum', *Novi commentarii academiae scientiarum Petropolitanae* 6, 271–311.

[59] Fornasier, L., Rieger, H., Tremel, U. and van der Weide, E. [AIAA 2002-0949, 2002], Time-dependent aeroelastic simulation of rapid manoeuvring aircraft.
doi: 10.2514/6.2002-949

[60] Frink, N. [AIAA 94-0061, 1994], Recent progress toward a three-dimensional unstructured Navier-Stokes flow solver.
doi: 10.2514/6.1994-61

[61] Fukunaga, K. [1990], *Introduction to statistical pattern recognition*, Academic Press Professional, Inc.

[62] Fultz, A. J. and Ashley, W. S. [2016], 'Fatal weather-related general aviation accidents in the United States', *Physical Geography* 37(5), 291–312.
doi: 10.1080/02723646.2016.1211854

[63] Fung, Y. [2002], *An introduction to the theory of aeroelasticity*, Dover Publications.

[64] Gai, G. and Timme, S. [2016], 'Nonlinear reduced-order modelling for limit-cycle oscillation analysis', *Nonlinear Dynamics* 84, 991–1009.
doi: 10.1007/s11071-015-2544-9

[65] Ghoreyshi, M., J. Badcock, K. and Woodgate, M. [2009], 'Accelerating the numerical generation of aerodynamic models for flight simulation', *Journal of Aircraft* 46(3), 972–980.
doi: 10.2514/1.39626

[66] Ghoreyshi, M., Jiraseck, A. and Cummings, R. [2014], 'Reduced order unsteady aerodynamic modeling for stability and control analysis using computational fluid dynamics', *Progress in Aerospace Sciences* 71, 167–217.
doi: 10.1016/j.paerosci.2014.09.001

[67] Ghoreyshi, M., Vallespin, D., Da Ronch, A., Badcock, K. J., Vos, J. and Hitzel, S. [AIAA 2010-8239, 2010], Simulation of aircraft manoeuvres based on computational fluid dynamics.
doi: 10.2514/6.2010-8239

[68] Glauert, H. [1928], 'The effect of compressibility on the lift of an aerofoil', *Proceedings of the Royal Society of London* 118(779), 113–119.
doi: 10.1098/rspa.1928.0039

[69] Hall, K. and Crawley, E. [1989], 'Calculation of unsteady flows in turbomachinery using the linearized Euler equations', *AIAA Journal* 27(6), 777–787.
doi: 10.2514/3.10178

[70] Hall, K., Thomas, J. and Dowell, E. [2000], 'Proper orthogonal decomposition technique for transonic unsteady aerodynamic flows', *AIAA Journal* 38(10), 1853–1862.
doi: 10.2514/2.867

[71] Han, Z. H., Görtz, S. and Hain, R. [2010], A variable-fidelity modeling method for aero-loads prediction, *in* 'New Results in Numerical and Experimental Fluid Mechanics', Springer Berlin Heidelberg, pp. 17–25.
doi: 10.1007/978-3-642-14243-7˙3

[72] Hassig, H. [1971], 'An approximate true damping solution of the flutter equation by determinant iteration', *Journal of Aircraft* 8(11), 885–889.
doi: 10.2514/3.44311

[73] Heinrich, R. and Reimer, L. [IFASD-2013-36B, 2013], Comparison of different approaches for gust modeling in the CFD code TAU.

[74] Hesse, H. and Palacios, R. [AIAA 2013-1895, 2013], Model reduction in flexible-aircraft dynamics with large rigid-body motion.
doi: 10.2514/6.2013-1895

[75] Hirt, C. W., Amsden, A. A. and Cook, J. [1974], 'An arbitrary Lagrangian-Eulerian computing method for all flow speeds', *Journal of computational physics* 14(3), 227–253.
doi: 10.1016/0021-9991(74)90051-5

[76] Hoblit, F. [1988], *Gust loads on aircraft: concepts and applications*, American Institute of Aeronautics & Astronautics.

[77] How, J. [2004], Aircraft dynamics, *in* 'Aircraft stability and control', MIT OpenCourseWare, Massachusetts Institute of Technology.

[78] Ishihara, T., Gotoh, T. and Kaneda, Y. [2009], 'Study of high–Reynolds number isotropic turbulence by direct numerical simulation', *Annual Review of Fluid Mechanics* 41, 165–180.
doi: 10.1146/annurev.fluid.010908.165203

[79] Jameson, A. [AIAA 91-1596, 1991], Time dependent calculations using multigrid, with applications to unsteady flows past airfoils and wings.
doi: 10.2514/6.1991-1596

[80] Jameson, A., Schmidt, W. and Turkel, E. [AIAA 1981-1259, 1981], Numerical solutions of the Euler equations by finite volume methods using Runge-Kutta time-stepping schemes.
doi: 10.2514/6.1981-1259

[81] Kaiser, C., Friedewald, D., Quero, D. and Nitzsche, J. [DLR-420161, 2016], Aeroelastic gust load prediction based on time-linearised RANS solutions.

[82] Kaiser, C., Thormann, R., Dimitrov, D. and Nitzsche, J. [DLR-370189, 2015], Time-linearised analisys of motion-induced and gust-induced airloads with the DLR-TAU code.

[83] Kalashnikova, I. and Arunajatesan, S. [2012], A stable Galerkin reduced order model (ROM) for compressible flow, *in* '10th World Congress on Computational Mechanics', Sao Paulo, Brazil, pp. 1399–1423.
doi: 10.5151/meceng-wccm2012-18407

[84] Katz, J. and Plotkin, A. [2001], *Low-Speed Aerodynamics*, Cambridge Aerospace Series, 2 edn, Cambridge University Press.
doi: 10.1017/CBO9780511810329

[85] Kennett, D., Timme, S., Angulo, J. and Badcock, K. [2012*a*], 'An implicit meshless method for application in computational fluid dynamics', *International Journal for Numerical Methods in Fluids* 71, 1007–1028.
doi: 10.1002/fld.3698

[86] Kennett, D., Timme, S., Angulo, J. and Badcock, K. [2012*b*], 'Semi-meshless stencil selection for anisotropic point distributions', *International Journal of Computational Fluid Dynamics* 26(9-10), 463–487.
doi: 10.1080/10618562.2012.744450

[87] Kermode, A., Barnard, R. and Philpott, D. [2006], *Mechanics of Flight*, Pearson Prentice Hall.

[88] Krantz, S. [1999], *Handbook of complex variables*, Birkhäuser Boston.

[89] Küssner, H. G. [1936], 'Zusammenfassender bericht über den instationären auftrieb von flügeln', *Luftfahrtforschung* 13(12), 410–424.

[90] Landwehr, U. and Vettel, M. [2016], 'Adams simulation saves 3 million euro by replacing physical testing in aircraft certification'.
Web: `http://files.mscsoftware.com/sites/default/files/cs_airbus2_ltr_w.pdf`

[91] Launder, B. and Spalding, D. [1974], 'The numerical computation of turbulent flows', *Computer Methods in Applied Mechanics and Engineering* 3(2), 269–289.
doi: 10.1016/0045-7825(74)90029-2

[92] Lawson, C. and Hanson, R. [1995], *Solving least squares problems*, Society for Industrial and Applied Mathematics.
doi: 10.1137/1.9781611971217

[93] LeGresley, P. and Alonso, J. [AIAA 00-33879, 2000], Airfoil design optimization using reduced order models based on Proper Orthogonal Decomposition.
doi: 10.2514/6.2000-2545

[94] Lodato, G., Domingo, P. and Vervisch, L. [2008], 'Three-dimensional boundary conditions for direct and large-eddy simulation of compressible viscous flows', *Journal of Computational Physics* 227(10), 5105–5143.
doi: 10.1016/j.jcp.2008.01.038

[95] Lucia, D. J. and Beran, P. S. [2003], 'Projection methods for reduced order models of compressible flows', *Journal of Computational Physics* 188(1), 252 – 280.
doi: 10.1016/S0021-9991(03)00166-9

[96] Martins, J. and B. Lambe, A. [2013], 'Multidisciplinary design optimization: a survey of architectures', *AIAA Journal* 51(9), 2049–2075.
doi: 10.2514/1.J051895

[97] McCracken, A., Timme, S. and Badcock, K. [2012], Accelerating convergence of the CFD linear frequency domain method by a preconditioned linear solver, *in* 'ECCOMAS 2012 - European Congress on Computational Methods in Applied Sciences and Engineering', Vienna, Austria.

[98] McDonald, P. W. [ASME 71-GT-89, 1971], The computation of transonic flow through two-dimensional gas turbine cascades.
doi: 10.1115/71-GT-89

[99] Meinel, M. and Einarsson, G. [2010], The FlowSimulator framework for massively parallel CFD applications, *in* 'State of the Art in Scientific and Parallel Computing', Reykjavik, Island.

[100] Michler, A. [2011], 'Aircraft control surface deflection using RBF-based mesh deformation', *International Journal for Numerical Methods in Engineering* 88(10), 986–1007.
doi: 10.1002/nme.3208

[101] MSC Software Corporation [2012], *MSC.Nastran Reference Handbook - Aeroelastic Analysis Users Guide*, 68 edn.

[102] Mukerji, S. [1997], Turbulence computations with 3-D small-scale additive turbulent decomposition and data-fitting using chaotic map combinations, PhD thesis, University of Kentucky, Lexington, KY (United States).
doi: 10.2172/666048

[103] Neumann, J. and Mai, H. [2013], 'Gust response: simulation of an aeroelastic experiment by a fluid-structure interaction mehod', *Journal of Fluids and Structure*

38, 290–302.
doi: 10.1016/j.jfluidstructs.2012.12.007

[104] Newmark, N. [1959], ‘A method of computation for structural dynamics.’, *Journal of Engineering Mechanics* 85(3), 67–94.

[105] Pagliuca, G., Bekemeyer, P., Thormann, R. and Timme, S. [IFASD-2017-148, 2017], Model reduction for gust load analysis of free-flying aircraft.

[106] Pagliuca, G. and Timme, S. [2017], ‘Model reduction for flight dynamics simulations using computational fluid dynamics’, *Aerospace Science and Technology* 69, 15–26.
doi: 10.1016/j.ast.2017.06.013

[107] Pagliuca, G. and Timme, S. [AIAA-2016-3850, 2016], Flight dynamics mode identification and model reduction using computational fluid dynamics.

[108] Palacios, R. and Cesnik, C. E. S. [AIAA 2005-1945, 2005], Static nonlinear aeroelasticity of flexible slenderwings in compressible flow.
doi: 10.2514/6.2005-1945

[109] Parameswaran, V. and Baeder, J. D. [1997], ‘Indicial aerodynamics in compressible flow - direct computational fluid dynamic calculations’, *Journal of Aircraft* 34(1), 131–133.
doi: 10.2514/2.2146

[110] Patil, M. and Hodges, D. [2006], ‘Flight dynamics of highly flexible flying wings’, *Journal of Aircraft* 43(6), 1790–1798.
doi: 10.2514/1.17640

[111] Penrose, R. [1955], ‘A generalized inverse for matrices’, *Mathematical Proceedings of the Cambridge Philosophical Society* 51(3), 406–413.
doi: 10.1017/S0305004100030401

[112] Pratt, K. G. [1953], A revised formula for the calculation of gust loads, Technical Report TN-2964, National Advisory Committee for Aeronautics.

[113] Pullin, D. I. and Wang, Z. J. [2004], ‘Unsteady forces on an accelerating plate and application to hovering insect flight’, *Journal of Fluid Mechanics* 509, 1–21.
doi: 10.1017/S0022112004008821

[114] Quarteroni, A., Saleri, F. and Gervasio, P. [2010], *Scientific computing with MATLAB and Octave*, Springer.

[115] Raveh, D. E. and Karpel, M. [2000], 'Nonlinear design loads for maneuvering elastic aircraft', *Journal of Aircraft* 37(2), 313–318.
doi: 10.2514/2.2595

[116] Raymer, D. [1989], *Aircraft design: a conceptual approach*, American Institute of Aeronautics and Astronautics.

[117] Reimer, L., Ritter, M., Heinrich, R. and Kruger, W. [AIAA 2015-2455, 2015], CFD-based gust load analysis for a free-flying flexible passenger aircraft in comparison to a DLM-based approach.
doi: 10.2514/6.2015-2455

[118] Reynolds, O. [1895], 'On the dynamical theory of incompressible viscous fluids and the determination of the criterion', *Philosophical Transactions of the Royal Society of London* 186, 123–164.

[119] Ricciardi, A. P., Patil, M. J. and Canfield, R. A. [2013], 'Evaluation of quasi-static gust loads certification methods for high-altitude long-endurance aircraft', *Journal of Aircraft* 50(2), 457–468.
doi: 10.2514/1.C031872

[120] Rodden, W. and Bellinger, E. D. [1988], 'Unrestrained aeroelastic divergence in a dynamic stability analysis', *Journal of Aircraft* 19(9), 796–797.
doi: 10.2514/3.61559

[121] Rodden, W. and Giesing, J. P. [1970], 'Application of oscillatory aerodynamic theory to estimation of dynamic stability derivatives', *Journal of Aircraft* 7(3), 272–275.
doi: 10.2514/3.56736

[122] Roskam, J. [1995], *Airplane flight dynamics and automatic flight controls*, Roskam Aviation and Engineering Corporation.

[123] Saad, Y. and Schultz, M. H. [1986], 'GMRES: A generalized minimal residual algorithm for solving nonsymmetric linear systems', *SIAM Journal on Scientific and Statistical Computing* 7(3), 856–869.
doi: 10.1137/0907058

[124] Safonov, M. G. and Chiang, R. Y. [1989], 'A Schur method for balanced-truncation model reduction', *IEEE Transactions on Automatic Control* 34(7), 729–733.
doi: 10.1109/9.29399

[125] Schwamborn, D., Gerhold, T. and Heinrich, R. [2006], The DLR-TAU code: recent applications in research and industry, *in* 'European Conference on Computational Fluid Dynamics'.

[126] Selig, M. S. [AIAA 2010-7635, 2010], Modeling full-envelope aerodynamics of small UAVs in realtime.
doi: 10.2514/6.2010-7635

[127] Shearer, C. M. and Cesnik, C. E. S. [2007], 'Nonlinear flight dynamics of very flexible aircraft', *Journal of Aircraft* 44(5), 1528–1545.
doi: 10.2514/1.27606

[128] Silva, W. [1993], 'Application of nonlinear systems theory to transonic unsteady aerodynamic responses', *Journal of Aircraft* 30(5), 660–668.
doi: 10.2514/3.46395

[129] Silva, W. and Bartels, R. [2004], 'Development of reduced-order models for aeroelastic analysis and flutter prediction using the CFL3Dv6.0 code', *Journal of Fluids and Structure* 19(6), 729–745.
doi: 10.1016/j.jfluidstructs.2004.03.004

[130] Sirovich, L. [1987], 'Turbulence and the dynamics of coherent structures, Parts I-III', *Quarterly of Applied Mathematics* 45(3), 561–590.

[131] Slotnick, J., Khodadoust, A., Alonso, J., Darmofal, D., Gropp, W., Lurie, E. and Mavriplis, D. [NASA/CR-2014-218178, 2013], CFD vision 2030 study: a path to revolutionary computational aerosciences, Technical report, NASA Langley Research Center.

[132] Spalart, P. and Allmaras, S. [1994], 'A one equation turbolence model for aerodynamic flows', *Recherche Aerospatiale* 1, 5–21.
doi: 10.2514/6.1992-439

[133] Stickan, B., Dillinger, J. and Schewe, G. [2014], 'Computational aeroelastic investigation of a transonic limit-cycle-oscillation experiment at a transport aircraft wing model', *Journal of Fluids and Structures* 49, 223–241.
doi: 10.1016/j.jfluidstructs.2014.04.014

[134] Stroscher, F., Sika, Z. and Petersson, O. [2013], 'Reduced order model of a blended wing body aircraft configuration', *Progress in Flight Dynamics, GNC and Avionics* 6, 635–650.
doi: 10.1051/eucass/201306635

[135] Taira, K., Brunton, S., Dawson, S., Rowley, C., Colonius, T., J. McKeon, B., Schmidt, O., Gordeyev, S., Theofilis, V. and Ukeiley, L. [2017], 'Modal analysis of fluid flows: an overview', *AIAA Journal* 55(12), 4013–4041.
doi: 10.2514/1.J056060

[136] Taylor, G. I. [1935], 'Statistical theory of turbulence', *Proceedings of the Royal Society of London* 151(873), 421–444.
doi: 10.1098/rspa.1935.0158

[137] Tennekes, H. and Lumley, J. L. [1972], *A first course in turbulence*, MIT press.

[138] Theodorsen, T. [1935], General theory of aerodynamic instability and the mechanism of flutter, Technical report, NACA Report 496.

[139] Thormann, R., Bekemeyer, P. and Timme, S. [ECCOMAS-5441, 2016], Reduced order modelling of gust analysis using computational fluid dynamics.

[140] Thormann, R., Pagliuca, G. and Timme, S. [IFASD-2017-195, 2017], Influence of gust modelling on free-flight aerofoils.

[141] Thormann, R. and Widhalm, M. [2013], 'Linear-frequency-domain predictions of dynamic-response data for viscous transonic flows', *AIAA Journal* 51(11), 2540–2557.
doi: 10.2514/1.J051896

[142] Timme, S., Badcock, K. J. and Da Ronch, A. [IFASD-2013-36A, 2013], Linear reduced order modelling for gust response analysis using the DLR-TAU code.

[143] Timme, S., Marques, S. and Badcock, K. J. [2011], 'Transonic aeroelastic stability analysis using a Kriging-based Schur complement formulation', *AIAA Journal* 49(6), 1202–1213.
doi: 10.2514/1.J050975

[144] Tipler, P. and Mosca, G. [2004], *Physics for scientists and engineers*, Physics for Scientists and Engineers, W. H. Freeman.

[145] Turner, M., Clough, R., Martin, H. and Topp, L. [1956], 'Stiffness and deflection analysis of complex structures', *Journal of the Aeronautical Sciences* 23(9), 805–823.
doi: 10.2514/8.3664

[146] Vallespin, D., Badcock, K. J., Da Ronch, A., White, M. D., Perfect, P. and Ghoreyshi, M. [2012], 'Computational fluid dynamics framework for aerodynamic model assessment', *Progress in Aerospace Sciences* 52, 2–18.
doi: 10.1016/j.paerosci.2011.12.004

[147] Vos, J., Rizzi, A., Darracq, D. and Hirschel, E. [2002], 'Navier–Stokes solvers in European aircraft design', *Progress in Aerospace Sciences* 38(8), 601–697.
doi: 10.1016/S0376-0421(02)00050-7

[148] Wagner, H. [1925], ‘Uber die entstehung des dynamischen auftriebes von tragflgeln’, *ZAMM - Journal of Applied Mathematics and Mechanics* 5(1), 17–35.
doi: 10.1002/zamm.19250050103

[149] Walker, P. [1932], Experiments on the growth of circulation about a wing with a description of an apparatus for measuring fluid motion, Technical report, Air Ministry - Aeronautical Research Committee.

[150] Widhalm, M., Hubner, A. R. and Thormann, R. [2012], Linear frequency domain predictions of dynamic derivatives for the DLR F12 wind tunnel model, *in* ‘ECCOMAS 2012 - European Congress on Computational Methods in Applied Sciences and Engineering’, Vienna, Austria.

[151] Wilcox, D. [1994], *Turbulence Modeling for CFD*, DCW Industries, Incorporated.

[152] Wilcox, D. C. [1988], ‘Reassessment of the scale-determining equation for advanced turbulence models’, *AIAA Journal* 26(11), 1299–1310.
doi: 10.2514/3.10041

[153] Willcox, K. and Megretski, A. [2003], Fourier model reduction for large-scale applications in computational fluid dynamics, *in* ‘SIAM Conference on Applied Linear Algebra’, Williamsburg, VA.

[154] Winther, B. A., Goggin, P. J. and Dykman, J. R. [2000], ‘Reduced-order dynamic aeroelastic model development and integration with nonlinear simulation’, *Journal of Aircraft* 37(5), 833–839.
doi: 10.2514/2.2677

[155] Wright, J. and Cooper, J. [2007], *Introduction to aircraft aeroelasticity and loads*, Wiley.

[156] Xu, S., Timme, S. and Badcock, K. [2016], ‘Enabling off-design linearised aerodynamics analysis using Krylov subspace recycling technique’, *Computer and Fluids* 140, 385–396.
doi: 10.1016/j.compfluid.2016.10.018

[157] Zang, T. A., Dahlburg, R. B. and Dahlburg, J. P. [1992], ‘Direct and large-eddy simulations of three-dimensional compressible Navier-Stokes turbulence’, *Physics of Fluids* 4(1), 127–140.
doi: 10.1063/1.858491

[158] Zbrozek, J. K. [1960], The relationship between the discrete gust and power spectra presentations of atmospheric turbulence, with a suggested model of low-altitude turbulence, Technical Report R.M. 3216, Aeronautical Research Council.

Appendix A

Derivation of Aerodynamic Equations

Behaviour of any fluid flows is governed by three principles: conservation of mass, Newton's second law, which equates force to the product of mass times acceleration, and conservation of energy [7]. These principles are expressed mathematically with a set of equations named after two scientists from the 19th century who made seminal contribution to fluid dynamics, specifically Claude–Louis Navier and Sir George Gabriel Stokes. Solving Navier–Stokes equations provides flow properties, such as density or enthalpy, in various points of the flow field. Deriving such equations from first principles is not a trivial task [23].

Two mathematical formulations, specifically integral and differential, can be obtained to describe the same problem and the two strategies to derive them are schematically depicted in Fig. A.1. Equations for mass, momentum and energy conservation are translated into integral or differential equations adopting either a finite control volume or infinitesimal element model. These models use an Eulerian and Lagrangian reference frame, respectively. Choosing one of the two models determines the final form of the equations. Differences between the two models are described graphically in Fig. A.2. The first one, which uses an Eulerian formulation, is based on the idea of a finite control volume $\mathcal{V}$ which is a finite region of the flow domain with an arbitrary shape. The surface surrounding the volume is called control surface and indicated with S. Assuming the control volume fixed in space, the fluid flows through the control surface. The second method, which uses a Lagrangian formulation, is described in Fig. A.2(b) and it is based on an infinitesimal element which moves following the flow. Denote t_1 and t_2 two values of time. The element is located at two different points in the space since its path defines a streamline as shown in the picture. Properties such as volume and energy change, too, and element's velocities $\boldsymbol{V}_1$ and $\boldsymbol{V}_1$ can differ in terms of magnitude and direction. However, its mass, i.e. the number of flow particles forming the infinitesimal element, is constant.

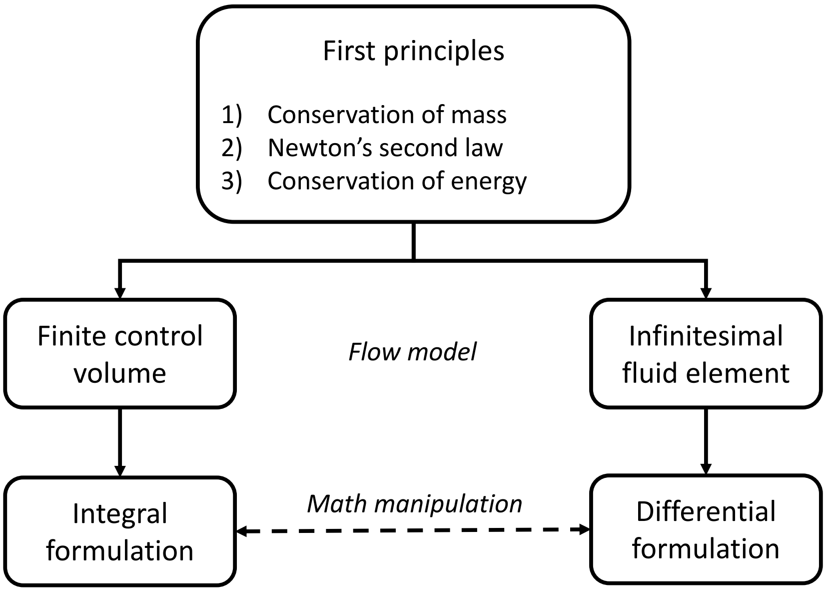

Figure A.1: Derivation of Navier–Stokes equation.

The derivation of Navier–Stokes equations is described next for the finite control volume. The physical principle of conservation for a generic quantity U is obtained by equating the net flow out of the control surface to the time ratio of change of U inside the control volume. Denote $\mathrm{d}S$ an infinitesimal area on the control surface S and $\boldsymbol{n}$ as the corresponding unitary normal vector. The conservation equation of U is

$$\frac{\partial}{\partial t}\iiint_{\mathcal{V}} U\ \mathrm{d}\mathcal{V} + \iint_S (\boldsymbol{F}_C - \boldsymbol{F}_D)\cdot\boldsymbol{n}\ \mathrm{d}S = \iiint_{\mathcal{V}} Q_{\mathcal{V}}\ \mathrm{d}\mathcal{V} + \iint_S \boldsymbol{Q}_S\cdot\boldsymbol{n}\ \mathrm{d}S \tag{A.1}$$

where $\mathcal{V}$ is the finite control volume, $\boldsymbol{F}_C = U\boldsymbol{V}\cdot\boldsymbol{n}$ is the convective flux, $\boldsymbol{F}_D = k\boldsymbol{\nabla}\boldsymbol{V}\cdot\boldsymbol{n}$ is the diffusive flux with coefficient k, $Q_{\mathcal{V}}$ is the volume source and $\boldsymbol{Q}_S$ is the surface source[1]. Replacing the scalar quantity U with density, leads to the mass conservation equation (also known as continuity equation),

$$\frac{\partial}{\partial t}\iiint_{\mathcal{V}} \rho\ \mathrm{d}\mathcal{V} + \iint_S \rho(\boldsymbol{V}\cdot\boldsymbol{n})\ \mathrm{d}S = 0 \tag{2.1}$$

where ρ and $\boldsymbol{V}$ are density and Cartesian velocity vector on the control surface, respectively. Volume and surface sources of mass are not possible and diffusive flux of mass is zero as well. Hence, only the convective flux $\boldsymbol{F}_C = \rho\boldsymbol{V}\cdot\boldsymbol{n}$ affects the time ratio of the mass.

To apply the conservation law in Eq. (A.1) to momentum, which is defined as the vector quantity $\rho\boldsymbol{V}\ \mathrm{d}\mathcal{V}$, a generalization of Eq. (A.1) with tensor calculus is needed [38]. Specifically, fluxes and surface source term are expressed by means of second order tensors. The convective flux is $\overline{\overline{\boldsymbol{F}}}_C = -\rho\boldsymbol{V}\boldsymbol{V}$ where the tensor $\boldsymbol{V}\boldsymbol{V}$ represents the

---

[1] The divergence theorem is adopted so that $\iiint_{\mathcal{V}}(\boldsymbol{\nabla}\cdot\bullet)\ \mathrm{d}\mathcal{V} = \iint_S \bullet\cdot\boldsymbol{n}\ \mathrm{d}S$ for a vector $\bullet$.

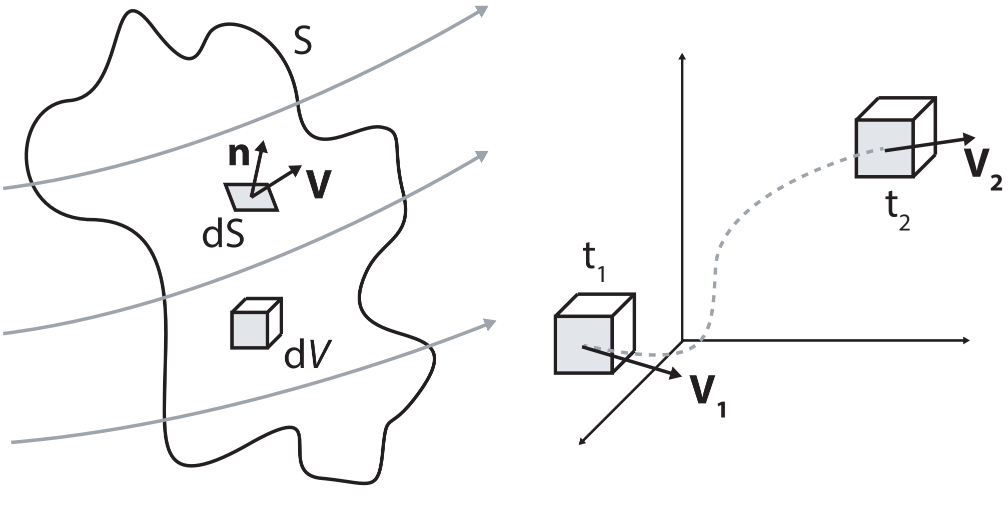

(a) Finite volume (b) Infinitesimal element

Figure A.2: Two points-of-view to derive Navier–Stokes equations.

momentum flux per unit mass[2]. No diffusive flux for momentum is possible. Regarding the volume source term $\boldsymbol{Q}_{\mathcal{V}}$, it is given by external body forces $\rho\boldsymbol{f}_{ext}$ per unit mass applied to the control volume. The surface source term accounts for surface forces per unit mass by introducing in the equation pressure p and surface stress tensor $\overline{\overline{\tau}} \cdot \boldsymbol{n}$. The tensor $\overline{\overline{\tau}}$ has size 3×3 and it includes elements accounting for both shear and normal stresses in three dimensions. The resulting equation is

$$\begin{aligned}\frac{\partial}{\partial t}\iiint_{\mathcal{V}} \rho\boldsymbol{V}\ \mathrm{d}\mathcal{V} + \iint_{S} \rho\boldsymbol{V}(\boldsymbol{V}\cdot\boldsymbol{n})\ \mathrm{d}S = \\ \iiint_{\mathcal{V}} \rho\boldsymbol{f}_{ext}\ \mathrm{d}\mathcal{V} - \iint_{S} p\boldsymbol{n}\ \mathrm{d}S + \iint_{S} \overline{\overline{\tau}}\cdot\boldsymbol{n}\ \mathrm{d}S\end{aligned} \tag{2.2}$$

The energy conservation principle from thermodynamics is translated into an integral equation by applying Eq. (A.1) to the total energy per unit mass E. It is defined as the sum of internal energy e and kinetic energy $\frac{\boldsymbol{V}^2}{2}$. The convective flux for total energy is then $\boldsymbol{F}_C = \rho E\boldsymbol{V}$. Fourier's law of heat conduction [144] is adopted for the diffusive flux $\boldsymbol{F}_D = -k\boldsymbol{\nabla}T$ with temperature T and fluid's conductivity coefficient k. Regarding the volume source per unit mass, $Q_{\mathcal{V}}$, it accounts for both possible heat sources $\dot{q}$ and the work done by body forces $\rho\boldsymbol{f}_{ext}\cdot\boldsymbol{V}$. The surface source term $\boldsymbol{Q}_S$ is the sum of the time rate of work done by the pressure force per unit mass (-$p\boldsymbol{V}$) and by the shear

---

[2] The tensor product between a vector $\boldsymbol{a}$ with size N and a vector $\boldsymbol{b}$ with size M is a second order tensor $\overline{\overline{C}}$ with $C_{ij} = a_i b_j$ and $i \in [0, N]$, $j \in [0, M]$. More details in [21, App. A].

stresses ($\overline{\overline{\tau}} \cdot \boldsymbol{V}$). The resulting equation for energy conservation is

$$\begin{aligned} &\frac{\partial}{\partial t} \iiint_{\mathcal{V}} \rho E \,\mathrm{d}\mathcal{V} + \iint_S \rho E (\boldsymbol{V} \cdot \boldsymbol{n}) \,\mathrm{d}S - \iint_S k (\boldsymbol{\nabla} T \cdot \boldsymbol{n}) \,\mathrm{d}S = \\ &\qquad \iiint_{\mathcal{V}} \left(\rho \boldsymbol{f}_{ext} \cdot \boldsymbol{V} + \dot{q}\right) \,\mathrm{d}\mathcal{V} - \iint_S p \boldsymbol{V} \cdot \boldsymbol{n} \,\mathrm{d}S + \iint_S (\overline{\overline{\tau}} \cdot \boldsymbol{V}) \cdot \boldsymbol{n} \,\mathrm{d}S \end{aligned} \tag{2.3}$$

Equations (2.1), (2.2) and (2.3) are an integral form of Navier–Stokes equations for a fixed control volume. Alternative formulations, which are not reported here for sake of brevity, are needed when the control volume is either in a moving reference frame or it deforms. An overview of such equations is available in [23, App. A.4].

The derivation of Navier–Stokes equation in differential form is limited here to the mass continuity equation without loss of generality. The starting point is the infinitesimal fluid element which moves following the flow, Fig. A.2(b). Its constant mass is defined as product of density and infinitesimal volume, $\delta m = \rho \delta \mathcal{V}$. The substantial derivative[3] of the mass is zero by definition.

$$\frac{\mathrm{D}\delta m}{\mathrm{D}t} = \rho \frac{\mathrm{D}\delta \mathcal{V}}{\mathrm{D}t} + \delta \mathcal{V} \frac{\mathrm{D}\rho}{\mathrm{D}t} = 0 \tag{A.2}$$

It can be proven [7] that $\frac{1}{\delta \mathcal{V}} \frac{\mathrm{D}\delta \mathcal{V}}{\mathrm{D}t} = \boldsymbol{\nabla} \cdot \boldsymbol{V}$ and the mass conservation equation becomes

$$\frac{\mathrm{D}\rho}{\mathrm{D}t} = -\rho \boldsymbol{\nabla} \cdot \boldsymbol{V} \tag{A.3}$$

The same procedure adopted for mass continuity provides equations for both momentum and energy, resembling the strategy adopted in the previous paragraph for integral equations. Although the complete derivation is skipped, the resulting set of differential equations is reported here

$$\frac{\mathrm{D}\rho}{\mathrm{D}t} = -\rho \boldsymbol{\nabla} \cdot \boldsymbol{V} \tag{2.4}$$

$$\rho \frac{\mathrm{D}\boldsymbol{V}}{\mathrm{D}t} = -\boldsymbol{\nabla} p + \boldsymbol{\nabla} \overline{\overline{\tau}} + \rho \boldsymbol{f}_{ext} \tag{2.5}$$

$$\rho \frac{\mathrm{D}}{\mathrm{D}t} \left(e + \frac{\boldsymbol{V}^2}{2} \right) = \rho \dot{q} + \boldsymbol{\nabla} \cdot (k \boldsymbol{\nabla} T) - \boldsymbol{\nabla} \cdot (p \boldsymbol{V}) + \boldsymbol{\nabla} \cdot \left(\overline{\overline{\tau}} \boldsymbol{V} \right) + \rho \boldsymbol{f}_{ext} \cdot \boldsymbol{V} \tag{2.6}$$

They represent the Navier–Stokes equations in a differential formulation and they are analogous to Eqs. (2.1-2.3). Specifically, Eq. (2.4) expresses mass conservation, Eq. (2.5) is the momentum equation and Eq. (2.6) imposes energy conservation.

Although integral and differential formulations are mathematically connected, some differences can be found. The integral form allows discontinuities inside the control

---

[3] The substantial derivative of a scalar quantity U is defined as $\frac{\mathrm{D}U}{\mathrm{D}t} = \frac{\partial U}{\partial t} + \boldsymbol{V} \cdot \boldsymbol{\nabla} U$. More details in [7, Ch. 2].

volume. In fact, their presence does not affect the integration process. Conversely, the differential formulation assumes that flow properties are differentiable and, hence, no discontinuities are allowed. In practice, this aspect must be taken into account when dealing with discontinuities such as shock waves. The two formulations lead to different CFD implementations and one of the two can be more suitable for a given problem since it can avoid, for example, phenomena such as numerical oscillations [7].

Euler equations

Another set of aerodynamic equations, which is exploited in this work, was proposed by Leonhard Euler who first described them in his work *Principia motus fluidorum*, written in Latin and presented at the Royal Academy of Prussia in Berlin on August 31, 1752 [58]. Although Euler equations historically precede the Navier–Stokes ones, they can be derived from the latter assuming an adiabatic and inviscid fluid. For example, dropping all the terms concerning viscosity and thermal effects in Eq. (2.4-2.6) leads to their differential form

$$\begin{aligned}
\frac{\mathrm{D}\rho}{\mathrm{D}t} &= -\rho\boldsymbol{\nabla}\cdot\boldsymbol{V} \\
\rho\frac{\mathrm{D}\boldsymbol{V}}{\mathrm{D}t} &= -\boldsymbol{\nabla}p+\rho\boldsymbol{f} \\
\rho\frac{\mathrm{D}}{\mathrm{D}t}\left(e+\frac{\boldsymbol{V}^2}{2}\right) &= \rho\dot{q}-\boldsymbol{\nabla}\cdot(p\boldsymbol{V})+\rho\boldsymbol{f}\cdot\boldsymbol{V}
\end{aligned} \tag{A.4}$$

Such equations represent a simplification of Navier–Stokes ones which discard viscous effects. It is a valid assumption when applied to cases, for example, of fluid flows with very high Reynolds numbers for which the boundary layer is very thin [23]. Shock waves are still captured by solving Euler equations. However, interesting phenomena such as interaction of boundary layer with shock waves cannot be simulated.

Appendix B

Verification of Mode Tracing

The tracing procedure was applied in Chapters 4, 5 and 6 to identify flight dynamics modes and the same implementation was verified by reproducing literature results. In particular, a test case involving rigid-body and structural degrees-of-freedom was chosen to perform a flutter analysis. It is a well-known case since its theoretical background is given in [120] and results can be reproduced with an input file for Nastran which is available in the MSC.Nastran handbook [101, Ch. 8, Example HA145A].

The configuration is composed of a lumped mass and an aerodynamic body connected by means of linear and rotational springs as shown in Fig. B.1. This resembles a wing and fuselage configuration. The system can translate freely in the vertical direction and the three degrees-of-freedom for the system are y (fuselage vertical translation), h (relative distance between wing and fuselage) and α (wing rigid rotation). Denote m and m_f the wing and fuselage masses, respectively. The dimensional equations describing system's dynamics are

$$\begin{aligned} m_f\ddot{y} - k_h h &= -m_f g \\ m\ddot{y} + m\ddot{h} + S_\alpha\ddot{\alpha} + k_h h &= -mg - L(t) \\ S_\alpha\left(\ddot{y} + \ddot{h}\right) + I_\alpha\ddot{\alpha} + k_\alpha\alpha &= -S_\alpha g + M(t) \end{aligned} \tag{B.1}$$

where k_h is the linear spring constant, k_α is the rotational spring constant, g is the gravitational acceleration, S_α is the static moment around the elastic axis and I_α is the inertia around the same axis. Aerodynamic lift and moment are denoted L and M, respectively, and they are assumed to be function of time. The uncoupled wing plunging and pitching frequencies are ω_h and ω_α, respectively. The non-dimensional velocity, also known as reduced velocity, is defined as $U^* = \frac{U}{b\omega_\alpha}$ where b is the wing semi-chord and U is the dimensional free-stream velocity. Values for structural parameters were taken directly from [120] in non-dimensional form or from [101] in imperial units.

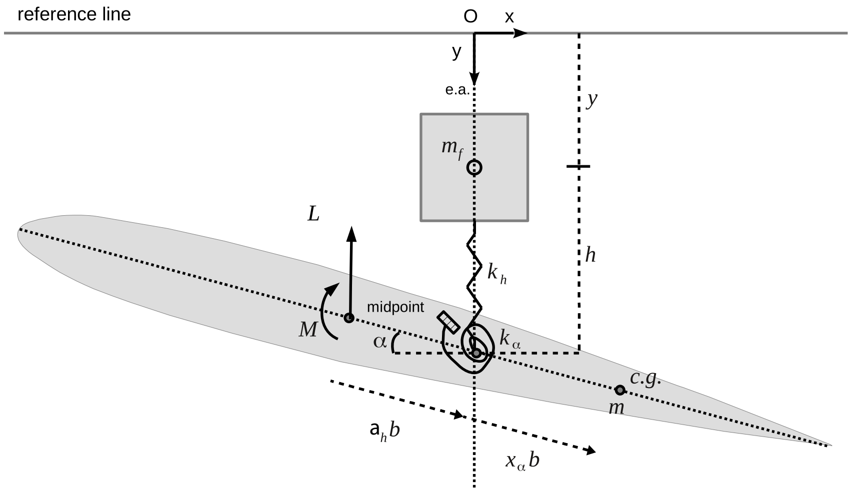

Figure B.1: Configuration for the body-free flutter analysis.

Equations (B.1) are translated in Laplace domain and the set is rewritten in matrix form for the tracing as

$$\Big[A_{rr}(\beta U^*) - \lambda I + CQ\Big]\phi_r^{(j)} = 0 \tag{B.2}$$

which is a formulation very similar to Eq. (3.25). The matrix A_{rr} depends on the reduced velocity and the tracing is performed by changing β. The first guess needed by Newton's solver to trace structural eigenpairs is given by structural modes and frequencies in vacuum. The tracing starts from the rigid-body modes for the flight dynamics ones. Flutter point is identified by checking real parts of the structural eigenvalues since a positive value indicates an unstable system.

Three aerodynamic models were adopted to calculate the matrix Q. First, Theodorsen's model was implemented [138]. It is a well-known model for incompressible flow which is widely adopted by the aeroelastic research community [22]. It provides expressions for lift and moment coefficients directly in frequency domain by introducing the complex-valued Theodorsen function. In this case, the matrix Q in Eq. (B.2) depends on frequency only and the tracing method reduces to the p-k method traditionally used for flutter analysis [72]. Secondly, Wagner's time-domain aerodynamic model was implemented. It assumes unsteady, incompressible and inviscid flows [148] and it predicts aerodynamic performance of an accelerating flat plate with great accuracy as reported in [113] and demonstrated experimentally in [149]. When Wagner's model is used, the term Q in Eq. (B.2) depends on both frequency and damping. The tracing corresponds to the p method for flutter analysis [72]. Thirdly, CFD aerodynamics based on Euler equations was adopted. Specifically, the same combination of grid and solver exploited to produce results in Chapter 4 was adopted for this case too. The grid is showed in Fig. 4.1(a) while the steady state solution

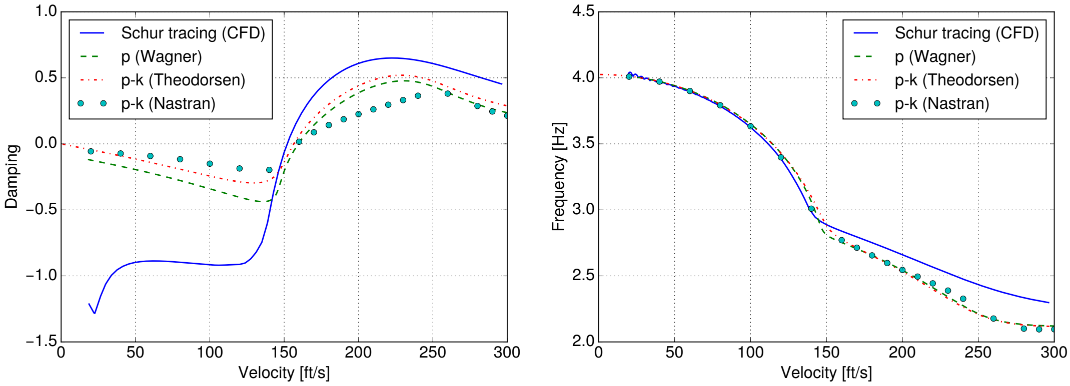

(a) Damping

(b) Frequency

Figure B.2: Results from the body-free flutter analysis.

in depicted in Fig. 4.1(b). An exact formulation for matrix CQ is used, specifically $CQ = -A_{rf}\left(A_{ff} - \lambda I\right)^{-1} A_{fr}$, and it is computed on the fly during the tracing so that the formulation coincides with the Schur complement method [143].

Results from the tracing performed with all the three methods are shown with a V-g plot in Fig. B.2(a) for the fluttering mode. They are compared to the reference values provided by Nastran. Regarding CFD aerodynamics, the critical speed is evaluated to be 153 ft/s. The tracing started at 18 ft/s with an increment of 4 ft/s up to 300 ft/s and each step converged with a residual of 1×10^{-12}. These results compare successfully to the ones provided by the p-k method implemented with Theodorsen aerodynamics. The tracing started at 0 ft/s for the latter method and no structural damping was introduced. The crossing happened at 156.5 ft/s. Regarding the Wagner model for the p method, the real part of the eigenvalue is taken into account when calculating the aerodynamic forces. As a consequence, the slope of the curve at the flutter point is different. In the end, a flutter speed of 159.6 ft/s was found. All these values are compared to the results from Nastran which adopts an approximation of the Theodorsen function [63]. The flutter speed is estimated in 158.6 ft/s and it corresponds to the bibliography value found in [120]. In conclusion, the tracing was successful for all the aerodynamic models and a largest error of 3% with respect to the reference was found in the flutter speed calculation. Differences in the curve slopes in Fig. B.2(a) highlight the different nature of the aerodynamic tools. However, the critical speed is not affected because zero damping is assumed at flutter point. Regarding frequencies in Fig. B.2(b), a very good agreement was found between results from the tracing and the literature reference.

Overall, the purpose of verify the correct implementation of the Newton's method was fulfilled. The theoretical formulation presented in Eqs. (3.34-3.41) was implemented and verified by solving Eq. (B.2) for a literature case using multiple aerodynamic tools. Results confirmed the correct implementation and the reliability of the method.

Appendix C

Short Period and Phugoid Approximation

Flight dynamics modes such as short period and phugoid can be estimated using stability derivatives [34, 155]. This represents the traditional approach which is independent from the aerodynamic model as long as the stability derivatives are available. Such model served in this work as verification for the CFD methods and to estimate flight dynamics eigenvalues as discussed in Section 5.3. In this appendix, its implementation is described and the model is verified by reproducing bibliography results in both time and Laplace domain.

The external forces and moment in Eq. (2.37) are expanded with Bryan's approach [28]. They become

$$\begin{aligned} F_x &= X_u u + X_{\dot{u}}\dot{u} + X_w w + X_{\dot{w}}\dot{w} + X_q q + X_{\dot{q}}\dot{q} + X_\theta \theta + X_{\dot{\theta}}\dot{\theta} + X_\delta \delta + X_\eta \eta \\ F_z &= Z_u u + Z_{\dot{u}}\dot{u} + Z_w w + Z_{\dot{w}}\dot{w} + Z_q q + Z_{\dot{q}}\dot{q} + Z_\theta \theta + Z_{\dot{\theta}}\dot{\theta} + Z_\delta \delta \\ M_y &= M_u u + M_{\dot{u}}\dot{u} + M_w w + M_{\dot{w}}\dot{w} + M_q q + X_{\dot{q}}\dot{q} + M_\theta \theta + M_{\dot{\theta}}\dot{\theta} + M_\delta \delta \end{aligned} \tag{C.1}$$

and two additional external forces are added to account for engine thrust η and control surface deflection δ. Thus, the flight dynamics equations (2.37) for longitudinal dynamics are rewritten in matrix form as

$$\begin{pmatrix} m - X_{\dot{u}} & -X_{\dot{w}} & -X_{\dot{q}} & 0 \\ -Z_{\dot{u}} & m - Z_{\dot{w}} & -Z_{\dot{q}} & 0 \\ -M_{\dot{u}} & -M_{\dot{w}} & I_y - M_{\dot{q}} & 0 \\ 0 & 0 & 0 & 1 \end{pmatrix} \begin{bmatrix} \dot{u} \\ \dot{w} \\ \dot{q} \\ \dot{\theta} \end{bmatrix} = \begin{pmatrix} X_u & X_w & X_q & 0 \\ Z_u & Z_w & Z_q & 0 \\ M_u & M_w & M_q & 0 \\ 0 & 0 & 0 & 0 \end{pmatrix} \begin{bmatrix} u \\ w \\ q \\ \theta \end{bmatrix}$$

$$+ \begin{pmatrix} 0 & 0 & -mW_e & -mg\cos\theta_0 \\ 0 & 0 & mU_e & -mg\sin\theta_0 \\ 0 & 0 & 0 & 0 \\ 0 & 0 & 1 & 0 \end{pmatrix} \begin{bmatrix} u \\ w \\ q \\ \theta \end{bmatrix}$$

$$+ \begin{pmatrix} X_\delta \\ Z_\delta \\ M_\delta \\ 0 \end{pmatrix} \delta + \begin{pmatrix} X_\eta \\ 0 \\ 0 \\ 0 \end{pmatrix} \eta \tag{C.2}$$

They can be integrated in time to simulate an initial disturbance analysis or a response to elevator deflection. Alternatively, they can be translated in Laplace domain for an eigenvalue analysis. Discarding inputs and focusing on the homogeneous form, the eigenvalue problem becomes

$$(A - \lambda I)\,\boldsymbol{w}_r = 0 \tag{C.3}$$

where the Jacobian matrix A is obtained from Eq. (C.2) as

$$A = \begin{pmatrix} m - X_{\dot{u}} & -X_{\dot{w}} & -X_{\dot{q}} & 0 \\ -Z_{\dot{u}} & m - Z_{\dot{w}} & -Z_{\dot{q}} & 0 \\ -M_{\dot{u}} & -M_{\dot{w}} & I_y - M_{\dot{q}} & 0 \\ 0 & 0 & 0 & 1 \end{pmatrix}^{-1} \begin{pmatrix} X_u & X_w & X_q - mW_e & -mg\cos\theta_0 \\ Z_u & Z_w & Z_q + mU_e & -mg\sin\theta_0 \\ M_u & M_w & M_q & 0 \\ 0 & 0 & 1 & 0 \end{pmatrix} \tag{C.4}$$

with θ_0 indicating the pitch angle at equilibrium conditions. This model was implemented in Python and it requires the stability derivatives as input.

Two cases are reported here as verification of the implementation. The first one is taken from [155, p. 269]. The velocity is $U_\infty = 175\,\text{m/s}$ with air density $\rho = 1.10\,\text{kg/m}^3$, mass $m = 10000\,\text{kg}$, inertia $I_y = 144000\,\text{kgm}^2$ and gravitational acceleration $g = 9.81\,\text{m/s}^2$. The aerodynamic coefficients are provided for wing $C_{L\alpha w} = 4.5\,\text{rad}^{-1}$, tail $C_{L\alpha t} = 3.2\,\text{rad}^{-1}$, elevator $C_{L\alpha e} = 1.5\,\text{rad}^{-1}$ and the drag coefficient $C_D = 0.1$. The geometry of the aeroplane is defined by wing chord $c = 2\,\text{m}$, wing surface $S_w = 30\,\text{m}^2$ and tail surface $S_t = 7.5\,\text{m}^2$ while the three-dimensional effects are taken into account with a downwash factor $k_e = 0.35$. The distance between

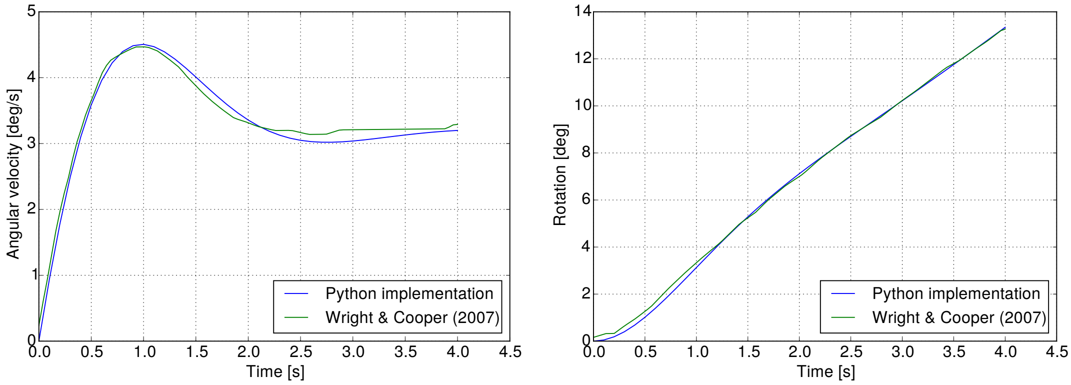

(a) Angular velocity (b) Pitch rotation

Figure C.1: Results of operator-based mode identification compared to reference solution provided in [155].

the centre of gravity and the wing aerodynamic centre is denoted L_w while L_t is the corresponding distance for the tail. The derivatives in Eq. (C.1) are expressed by means of a combination of geometric quantities as well as wing and tail aerodynamic coefficients. As a result the only non-zero derivatives are

$$\begin{aligned}
Z_w &= -\frac{1}{2}\rho U_\infty \left(S_w C_{L\alpha w} + S_t C_{L\alpha t}(1-k_e) + S_w C_D\right) \\
Z_q &= -\frac{1}{2}\rho U_\infty S_t C_{L\alpha t} L_t \\
Z_\delta &= -\frac{1}{2}\rho U_\infty^2 S_t C_{L\alpha e} \\
M_w &= +\frac{1}{2}\rho U_\infty \left(S_w C_{L\alpha w} L_w - S_t C_{L\alpha t}(1-k_e) L_t\right) \\
M_q &= -\frac{1}{2}\rho U_\infty S_t C_{L\alpha t} L_t^2 \\
M_\delta &= -\frac{1}{2}\rho U_\infty^2 S_t C_{L\alpha e} L_t
\end{aligned} \tag{C.5}$$

and this formulation allows for a short-term approximation involving the short period mode only. Results are provided in literature for the response to 1 deg elevator deflection and a comparison is provided in Fig. C.1 for the angular velocity and pitch rotation. The response matches for both quantities while a similar agreement was obtained for the other flight dynamics unknowns. The short period frequency was estimated in 0.3 Hz with Eq. (C.3).

The second case chosen for the verification was taken from [34, p. 106]. Parameters are given in imperial units with $\rho = 0.00238\,\mathrm{slug/ft^3}$, velocity $U_\infty = 305\,\mathrm{ft/s}$, mass $m = 746\,\mathrm{slugs}$, inertia $I_y = 65000\,\mathrm{slug/ft^2}$ and gravitational constant $g = 32.2\,\mathrm{ft/s^2}$.

Table C.1: Stability derivatives taken from [34, p. 106]

Variable	Horizontal force X	Vertical force Z	Moment M
u	-26.26 slug/s	-159.64 slug/s	0
w	79.82 slug/s	-328.24 slug/s	-1014 slug ft/s
$\dot{w}$	0	0	-36.4 slug ft/s
q	0	0	-18135 slug ft^2/s
η	0	-16502 slug ft/s^2/rad	-303575 slug ft/s^2/rad

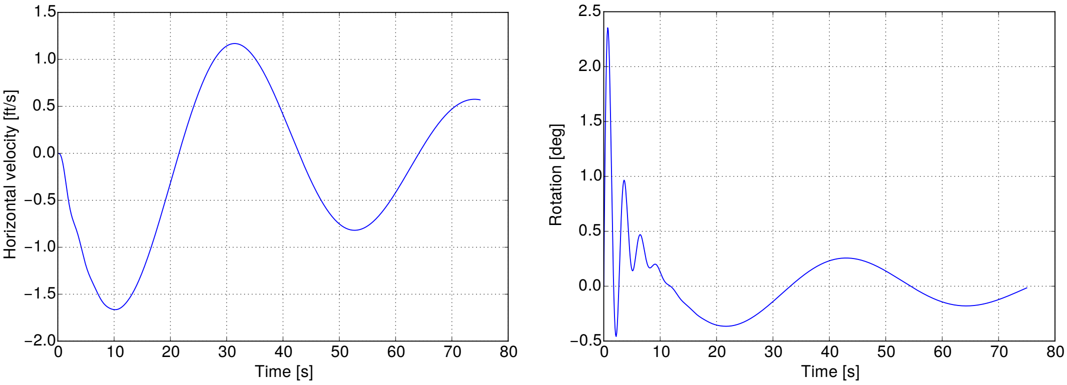

(a) Horizontal velocity

(b) Pitch rotation

Figure C.2: Time-domain integration performed using the results reproduced from [34].

Values of the stability derivatives are provided and reported in Table C.1 for reference. Notice that some of the derivative in the horizontal direction $X_\square$ are available. This allows for the calculation of the phugoid mode. Solving Eq. (C.3) for this case, lead to two pairs of complex-conjugate eigenvalues, specifically

$$\begin{aligned}\lambda_{SP} &= -0.44586984133 \pm 2.16437192886i \\ \lambda_{Ph} &= -0.0166306948626 \pm 0.147431081456i\end{aligned} \tag{C.6}$$

The first one, λ_{SP}, has a frequency of 0.34 Hz and it is associated with the short period mode. The second one has a frequency which is lower by an order of magnitude and it correspond to the phugoid mode. Their values are provided by the bibliographic reference as solutions of the equation $(s^2 + 0.033s + 0.022)(s^2 + 0.893s + 4.884)$ where s is a complex variable. They are $s_1 = -0.0165 \pm 0.1474i$ and $s_2 = -0.4465 \pm 2.164i$ and they match the results obtained from the model. Equations (C.2) were then integrated in time for an initial disturbance in angular speed of $q = 0.01$ rad/s and results are shown in Fig. C.2. Short term oscillations are visible in Fig. C.2(b). These are given by the short period mode and they quickly disappear because of the large damping. Slower oscillations with a longer period are instead associated with the phugoid mode. They involve the long-term dynamics and affect the horizontal speed as shown in Fig. C.2(a).